
**Development of Novel Time-Domain
Electromagnetic Methods for Offshore
Groundwater Studies: A Data Application from
Bat Yam, Israel**

Inaugural-Dissertation

zur Erlangung des Doktorgrades
der Mathematisch-Naturwissenschaftlichen Fakultät
der Universität zu Köln

vorgelegt von

Amir Haroon

aus Nürnberg

Köln 2016

Gutachter: Prof. Dr. B. Tezkan
Prof. Dr. A. Junge

Tag der mündlichen Prüfung: 07.12.2016

Abstract

Recent marine long-offset transient electromagnetic (LOTEM) measurements yielded the offshore delineation of a fresh groundwater body beneath the seafloor in the region of Bat Yam, Israel. The LOTEM application was effective in detecting this freshwater body underneath the Mediterranean Sea and allowed an estimation of its seaward extent. However, the measured data set was insufficient to understand the hydrogeological configuration and mechanism controlling the occurrence of this fresh groundwater discovery. Especially the lateral geometry of the freshwater boundary, important for the hydrogeological modelling, could not be resolved. Without such an understanding, a rational management of this unexploited groundwater reservoir is not possible.

Two new high-resolution marine time-domain electromagnetic methods are theoretically developed to derive the hydrogeological structure of the western aquifer boundary. The first is called Circular Electric Dipole (CED). It is the land-based analogous of the Vertical Electric Dipole (VED), which is commonly applied to detect resistive structures in the subsurface. Although the CED shows exceptional detectability characteristics in the step-off signal towards the sub-seafloor freshwater body, an actual application was not carried out in the extent of this study. It was found that the method suffers from an insufficient signal strength to adequately delineate the resistive aquifer under realistic noise conditions. Moreover, modelling studies demonstrated that severe signal distortions are caused by the slightest geometrical inaccuracies. As a result, a successful application of CED in Israel proved to be rather doubtful.

A second method called Differential Electric Dipole (DED) is developed as an alternative to the intended CED method. Compared to the conventional marine time-domain electromagnetic system that commonly applies a horizontal electric dipole transmitter, the DED is composed of two horizontal electric dipoles in an in-line configuration that share a common central electrode. Theoretically, DED has similar detectability/resolution characteristics compared to the conventional LOTEM system. However, the superior lateral resolution towards multi-dimensional resistivity structures make an application desirable. Furthermore, the method is less susceptible towards geometrical errors making an application in Israel feasible.

In the extent of this thesis, the novel marine DED method is substantiated using several one-dimensional (1D) and multi-dimensional (2D/3D) modelling studies. The main emphasis lies on the application in Israel. Preliminary resistivity models are derived from the previous marine LOTEM measurement and tested for a DED ap-

plication. The DED method is effective in locating the two-dimensional resistivity structure at the western aquifer boundary. Moreover, a prediction regarding the hydrogeological boundary conditions are feasible, provided a brackish water zone exists at the head of the interface.

A seafloor-based DED transmitter/receiver system is designed and built at the Institute of Geophysics and Meteorology at the University of Cologne. The first DED measurements were carried out in Israel in April 2016. The acquired data set is the first of its kind. The measured data is processed and subsequently interpreted using 1D inversion. The intended aim of interpreting both step-on and step-off signals failed, due to the insufficient data quality of the latter. Yet, the 1D inversion models of the DED step-on signals clearly detect the freshwater body for receivers located close to the Israeli coast. Additionally, a lateral resistivity contrast is observable in the 1D inversion models that allow to constrain the seaward extent of this freshwater body.

A large-scale 2D modelling study followed the 1D interpretation. In total, 425 600 forward calculations are conducted to find a sub-seafloor resistivity distribution that adequately explains the measured data. The results indicate that the western aquifer boundary is located at 3600 m - 3700 m before the coast. Moreover, a brackish water zone of $3 \Omega\text{m}$ to $5 \Omega\text{m}$ with a lateral extent of less than 300 m is likely located at the head of the freshwater aquifer. Based on these results, it is predicted that the sub-seafloor freshwater body is indeed open to the sea and may be vulnerable to seawater intrusion.

Zusammenfassung

Eine vorangegangene marine Long-Offset Transient-Elektromagnetische (LOTEM) Messung in der Gegend von Bat Yam, Israel, verdeutlichte die Abgrenzung eines Grundwasserkörpers unter dem Meeresboden. Die LOTEM-Anwendung konnte diesen Grundwasserkörper unter dem Mittelmeer detektieren und die Ausdehnung eingrenzen. Der gemessene Datensatz ist jedoch nicht ausreichend, um die hydrogeologische Konfiguration und den Mechanismus nachzuvollziehen, die für das Auftreten dieses Grundwasserreservoirs verantwortlich sind. Vor allem die laterale Geometrie der Aquiferkante, die für die hydrogeologischen Modellierung relevant ist, konnte nicht aufgelöst werden. Ohne dieses Verständnis ist eine Bewirtschaftung des ungenutzten Grundwasserreservoirs nicht möglich.

Zwei neue hochauflösende marine zeitbereichs-elektromagnetische Methoden sind theoretisch entwickelt worden, um die hydrogeologische Struktur der westlichen Aquiferkante abzuleiten. Die erste Methode ist der Circular Electric Dipole (CED). Diese Sendekonfiguration ist das Analog-Verfahren zum Vertical Electric Dipole (VED). Dieser wird häufig zum Detektieren schlechtleitender Strukturen im Untergrund angewandt. Obwohl der CED im Ausschaltsignal eine hohe Detektierbarkeit zeigt, um den submarinen Grundwasserkörper zu erkunden, wurde eine praktische Anwendung in der Studie nicht durchgeführt. Es wurde festgestellt, dass das CED-Verfahren unter einer unzureichenden Signalstärke leidet, die das Detektieren des Grundwasserleiters unter realistischen Rauschbedingungen nicht ermöglicht. Darüber hinaus zeigen theoretische Modellierungen, dass starke Signalverzerrungen durch die geringste geometrische Ungenauigkeit verursacht werden. Daher erschien eine erfolgreiche Anwendung von CED in Israel nicht erfolgsversprechend.

Ein zweites Verfahren namens Differential Electric Dipole (DED) wurde als Alternative zu der CED-Methode entwickelt. Im Vergleich zu dem herkömmlichen LOTEM-System, das einen horizontalen elektrischen Dipol-Sender verwendet, besteht der DED-Sender aus zwei horizontalen elektrischen Dipolen in einer Inline-Konfiguration. Theoretisch weist der DED zu dem herkömmlichen System vergleichbare Detektierbarkeit und Auflösungseigenschaften gegenüber 1D Leitfähigkeitsstrukturen auf. Die höheren lateralen Auflösungseigenschaften für mehrdimensionale Widerstandsstrukturen machen eine Anwendung jedoch erstrebenswert. Darüber hinaus ist das Verfahren für geometrische Fehler weniger anfällig als das CED-Verfahren, was eine praktische Anwendung in Israel möglich macht.

Im Umfang dieser Arbeit wird das neue DED-Verfahren mit mehreren eindimension-

alen und mehrdimensionalen Modellierungsstudien untersucht. Der Schwerpunkt liegt auf der Anwendung in Israel. Vorläufige Widerstandsmodelle sind aus der früheren LOTEM Messung abgeleitet worden und werden für eine DED-Anwendung getestet. Das DED-Verfahren lokalisiert die zweidimensionale Widerstand-Struktur auf der westlichen Aquiferkante. Außerdem ist eine Vorhersage über die hydrogeologischen Randbedingungen möglich, sofern sich eine Brackwasserzone an der Spitze der Aquiferkante befindet.

Erste DED-Messungen wurden in Israel im April 2016 durchgeführt. Der erfasste Datensatz ist der erste seiner Art. Die gemessenen Daten wurden prozessiert und mittels 1D Inversion interpretiert. Das angestrebte Interpretations-Ziel konnte aufgrund der unzureichenden Datenqualität der Ausschaltssignale nicht durchgeführt werden. Dennoch konnten 1D Inversions-Modelle der Einschaltssignale eindeutig den Grundwasserkörper detektieren. Außerdem ist ein lateraler Widerstandscontrast in den 1D Inversions-Modellen zu beobachten, der auf eine seewärtige Abgrenzung dieses Grundwasserkörpers hinweist.

Die 1D Inversions-Modelle wurden als Grundlage für eine großangelegte 2D Modellierungsstudie verwendet. Insgesamt wurden 425 600 Vorwärtsrechnungen durchgeführt, um ein zweidimensionales Widerstandsmodell herzuleiten, das die gemessenen Daten adäquat erklärt. Die Ergebnisse zeigen, dass sich die westliche Aquiferkante 3600 m bis 3700 m vor der Küste befindet. Darüber hinaus ist eine Brackwasserzone von 3 Ω m bis 5 Ω m mit einer lateralen Ausdehnung von weniger als 300 m an der Spitze des Grundwasser-Aquifers wahrscheinlich. Mit diesen Ergebnissen kann vorhergesagt werden, dass der Grundwasserkörper zum Meer hin womöglich offen, und somit für das Eindringen von Meerwasser anfällig ist.

Contents

List of Figures	xi
List of Tables	xvii
1 Introduction	1
2 State of Research & Motivation	5
2.1 The Coastal Aquifer of Israel	5
2.1.1 EM Surveys in Israel	7
2.1.2 Hydrogeological Modelling Studies	9
2.2 Marine EM Applications	10
2.3 Motivation of the Presented Thesis	11
3 Theory of the Applied EM Methods	13
3.1 Time-Domain Electromagnetic Methods	14
3.1.1 Circular Electrical Dipole	17
3.1.2 Differential Electrical Dipole	18
3.2 Quasi-static Maxwell's Equations	20
3.3 The Layered Full-Space Model	22
3.3.1 TE and TM Mode	22
3.3.2 1D Forward Operator: Ideal CED	24
3.3.3 1D Forward Operator: Approximated CED and DED	27
3.3.4 Fast Hankel Transformation	29
3.3.5 Code Verification	30
3.4 System Response	31
4 1D-Inversion Theory	33
4.1 General Terms of 1D-Inversion	33

4.2	Non-Linear Inverse Problems	34
4.2.1	Data and Model Parameter Transformation	35
4.2.2	Data Fit	36
4.3	Marquardt Inversion	37
4.3.1	Eigenvalue Analysis	39
4.3.2	Importances	40
4.3.3	Equivalent Models using Monte-Carlo	41
4.4	Occam Inversion	41
4.5	Calibration Factor	43
5	1D Modelling Studies	45
5.1	Background EM Noise Model	46
5.2	Layered Aquifer	47
5.2.1	Detectability of the Aquifer	48
5.2.2	Influence of the Sea-Air Interface	58
5.2.3	Parameter Resolution of the Aquifer	61
5.2.4	Conclusions: Layered Aquifer	65
5.3	Geometrical Errors	66
5.3.1	Non-Verticality	67
5.3.2	Internal Transmitter Symmetry	70
5.3.3	1D Inversion of Geometrically Distorted Data	74
5.4	Summary of 1D Modelling	76
6	2D/3D Modelling of Resistive Formations	79
6.1	3D Forward Operator	80
6.1.1	Grid Design	83
6.1.2	Convergence of the Solution	86
6.2	The 2D Aquifer Model	89
6.2.1	Constructing the Bathymetry Model	90
6.2.2	The Aquifer Boundary	96
6.2.3	1D Inversion of synthetic 2D data	102
6.2.4	Conclusions: 2D Aquifer Model	103
6.3	Signal-Variations of resistive 3D Targets	105
6.4	Summary of 2D/3D Modelling	108

7	Field Survey & Data Processing	111
7.1	Field Survey	111
7.1.1	The DED System	112
7.1.2	Measurement Procedure	113
7.1.3	Field Setup	114
7.1.4	Issues during Data Acquisition	116
7.2	Data Processing	116
7.2.1	Digital Filtering	119
7.2.2	Cutting & Levelling	122
7.2.3	Cluster Analysis	122
7.2.4	Log-Gating and Gate-Stacking	124
7.3	Background Noise Measurements	127
7.4	Field Data	129
7.5	Summary of the Field Survey and Data Processing	131
8	1D Inversion of Field Data	133
8.1	Evaluation of the Current Signals	134
8.1.1	Comparison of Current Signals	134
8.1.2	Significance of the resistive Aquifer	140
8.1.3	Summary of Current Signal Comparison	142
8.2	1D Inversion of all Stations	142
8.2.1	Importances and Resolution Analysis	145
8.2.2	Validating the Results	147
8.3	Calibration Factor	148
8.4	Summary of 1D Inversion	150
9	2D Modelling of Measured Data	153
9.1	2D Interpretation Procedure	155
9.2	Best Fit Models	156
9.2.1	Aquifer Depth, Resistivity and Boundary Position	156
9.2.2	Boundary Shape	166
9.2.3	Summary of 2D Modelling	168
10	Summary & Conclusion	171

Bibliography	175
A Setup and Nomenclature	185
B 1D Inversion - Extended	187
C 2D Modelling of Field Data - Extended	193
D Electric Fields of CED and DED	195
E Acknowledgements	199

List of Figures

2.1	Map of the coastal aquifer of Israel.	6
2.2	Cross section of the coastal aquifer in Israel.	7
2.3	Results of TDEM measurements along the coastal plain of Israel. . .	8
2.4	1D Occam inversion results from LOTEM.	9
2.5	Hydrogeological modelling study from the Palmahim disturbance. . .	10
3.1	Marine TD-CSEM setup	14
3.2	Square wave current signals.	15
3.3	Step-on and step-off electrical fields.	16
3.4	Sketch of the real and the ideal CED	17
3.5	Schematic of a seafloor-based DED system	19
3.6	Layered earth model consisting of N layers below the source and M layers above	23
3.7	Illustration of the current density \mathbf{j} and magnetic flux density \mathbf{b} for TE mode on the left and TM mode on the right (<i>Weidelt, 1986</i>).	24
3.8	CED transients calculated with three different algorithms at an offset of 200 m from the CED centre	31
5.1	Exemplary transients and associated noise models for marine LOTEM measurements in Israel	47
5.2	Layered aquifer model applied for 1D modelling studies	48
5.3	Step-off transient for a layered aquifer model in the shallow sea environment	50
5.4	Step-on transient for a layered aquifer model in the shallow sea environment	52
5.5	Layered earth model in a deep ocean of 3000 m.	54
5.6	Step-off transient for a layered aquifer model in the deep sea environment	55

5.7	Step-on transient for a layered aquifer model in the deep sea environment	56
5.8	1D resistivity models used to investigate the influence of the airwave .	59
5.9	Impulse response of different resistivity models to study the airwave. .	60
5.10	Synthetic data calculated for a shallow marine model.	62
5.11	Eigenparameter analysis for synthetic LOTEM, DED and CED data .	63
5.12	Schematic of non-verticality configuration for VED, CED and DED transmitters	68
5.13	Non-verticality effect of VED (a and d), CED (b and e) and DED (c and f)	69
5.14	Relative errors displayed as a function of tilt-angle and time for a VED source	70
5.15	Geometrical error study investigating dipole movements of (a) LOTEM, (b) DED, and (c) CED	70
5.16	Transients and relative errors investigating geometrical errors and displayed for LOTEM, CED and DED	72
5.17	RMS errors displayed as a function of geometrical error	73
5.18	1D Occam inversion model for distorted step-off data	74
5.19	1D Occam inversion model for distorted step-on data	75
6.1	Example of a Yee-grid cell	81
6.2	Geometry for averaging conductivities with current flow in x-direction	82
6.3	Finite difference grid of a CED transmitter.	84
6.4	Finite difference grid of a DED transmitter	85
6.5	Grid checks for CED and DED transmitters using one-dimensional resistivity models	87
6.6	Output parameters (a) RES, (b) PROGN and (c) EPS	88
6.7	Sketches of the true, approximated 2D and 1D bathymetry models . .	90
6.8	Synthetic transients of a 2D bathymetry model	91
6.9	Study of 2D bathymetry model using 1D forward modelling	93
6.10	1D Marquardt inversion of different 2D bathymetry models	95
6.11	Schematic sketches of the 2D resistivity model used for modelling. In (a) the aquifer is blocked to the sea and no seawater encroachment occurs. In (b), seawater intrusion is occurring without a mixed-water zone ahead. In (c), a brackish water zone is located ahead of the freshwater body.	97
6.12	DED profile plots for three different aquifer models	98

6.13	DED transients at selected stations for the three different aquifer models	99
6.14	DED profile plots for the Intrusion and Blockage model aquifer excluding the bathymetry	101
6.15	1D Occam R1 inversion models of synthetic 2D data.	103
6.16	3D modelling study representing a hydrocarbon saturated formation .	106
6.17	Profile plots of CSEM, VED, DED and CED for a hydrocarbon resistivity model	107
7.1	Sketch of the applied DED-transmitter/receiver system	112
7.2	Impressions during the field survey	114
7.3	Map of the survey area near the coastline of Bat Yam, Israel	115
7.4	In-line DED electric field data measured during the test measurements in Cuxhaven, Germany. The power spectra of the recorded time series is displayed in (a). All recorded channels are displayed in (b) and the shifted time-series is displayed in (c).	117
7.5	(a) Power spectra and (b) time series segment of electrical field data measured at station p16NR. In blue, the raw data is displayed, in orange the filtered data.	120
7.6	(a) Power spectra and (b) time series segments of electrical field data measured at station p11FR. The data was filtered multiple times using the three-point filter starting from period lengths of 18 s (orange) and incrementally decreasing to period lengths of 2 s (light blue). This approach is used to minimise the long-periodic noise.	121
7.7	Cluster analysis of measured DED data	123
7.8	Normal probability plots at a selected intermediate time of $t = 0.2512$ s	124
7.9	Exemplary illustration of how data is log-gated using the data acquired at station p16NR	125
7.10	Comparison between log-gated/gate-stacked data and smoothed data	127
7.11	Background EM noise measurements from station p12NR	128
7.12	Processed transients at station p03FR	129
7.13	Processed transient of Rx1 (FR) and Rx2 (NR) plotted against the position along the profile	130
7.14	Profile plots of the data measured at the far receiver for selected time points.	131
8.1	Inversion models obtained from the step-on transient at station p03FR	135
8.2	Inversion models obtained from the step-off transient at station p03FR	136
8.3	Models obtained from the joint inversion at station p03FR	137
8.4	Graphical SVD-analysis of the weighted Jacobian	138

8.5	Modelling studies investigating the significance of the resistive aquifer layer	141
8.6	Occam Inversion models for Step-On signals of roughness 1 (top) and 2 (bottom) plotted against the receiver positions along the profile . .	143
8.7	Marquardt inversion models for Step-On signals plotted against the receiver positions along the profile	144
8.8	Data fit of inversion models at selected stations	144
8.9	SVD analysis for selected Marquardt inversion models	145
8.10	Modelling studies investigating the significance of the resistive aquifer layer	147
8.11	Occam R2 and Marquardt inversion models obtained for free (red lines) and fixed (black lines) calibration factors at stations p04FR, p08FR and p16NR displayed in a, b and c, respectively	149
9.1	The 2D model consisting of five model parameters	153
9.2	Scatter plots of the model parameters ρ_1 , ρ_2 , d_1 and d_2 vs. the χ . . .	157
9.3	Distribution of model parameter combinations for the 2D model acquired for transients of Zone A	158
9.4	Measured and calculated transients for all equivalent models obtained in Zone A	159
9.5	Accumulation of models with $\chi \leq 1$ to identify the most likely boundary position	160
9.6	Scatter plots of the model parameters ρ_1 , ρ_2 , d_1 and d_2 vs. the χ for equivalent models obtained in Zone B.	161
9.7	Data fit of profile plots for selected delay-times of 3.2 ms and 8.0 ms .	162
9.8	Equivalence domain in dependency of three model paramters for $x_a = 3600$ m and $x_a = 3700$ m	164
9.9	Measured and calculated transients for all equivalent models obtained in Zone B	165
9.10	The 2D model consisting of five model parameters	166
9.11	Data fits of data from Zone B for possible western aquifer boundary conditions.	167
9.12	Final 2D resistivity model for offshore Bat Yam, Israel	169
B.1	SVD analysis for several stations along the profile.	187
B.2	SVD analysis for several stations along the profile.	188
B.3	Inversion models of step-on signals for stations p01FR through p09FR in (a) through (h), respectively.	189

B.4	Inversion models of step-on signals for stations p10FR through p17NR in (a) through (h), respectively.	190
B.5	Joint-Inversion models of step-on/off signals for stations p01FR through p09FR in (a) through (h), respectively.	191
B.6	Joint-Inversion models of step-on/off signals for stations p10FR through p17NR in (a) through (h), respectively.	192
C.1	χ -errors for all equivalent models along the profile	193
C.2	Distribution of CF values at each station in Zone B	193
D.1	Total electric field for CED step-on at selected times	195
D.2	Total electric field for CED step-off at selected times	196
D.3	Total electric field for DED step-on at selected times	197
D.4	Total electric field for DED step-off at selected times	198

List of Tables

6.1	True water depths for the three exemplary transmitter positions.	94
8.1	Importances of model parameters from the Marquardt inversion: 0 - 0.5 poorly resolved (-). 0.51 - 0.7 (o) moderately resolved. 0.71 - 1.0: well resolved (+). The CF is kept fixed at 1 for all inversion models.	139
8.2	Importances of model parameters from the Marquardt inversion: 0 - 0.5 poorly resolved (-). 0.51 - 0.7 (o) moderately resolved. 0.71 - 1.0: well resolved (+).	146
9.1	Model parameters tested in the 2D modelling study to fit the measured DED data. For the stations of Zone B, all combinations of five parameters are tested. Stations of Zone A are only tested for the resistivity and thickness parameters.	155
9.2	Model parameter variation for the 2D modelling study to fit the measured data.	169
A.1	Information to receiver positions from the measurements.	185

Introduction

Electromagnetic (EM) induction methods are commonly applied to determine the resistivity distribution within the subsurface. In principle, these methods can distinguish a target formation from its surroundings if a resistivity contrast exists. In terms of studying the salinity of groundwater aquifers in coastal regions, EM methods are particularly effective, as the pore-fluid salinity has a direct influence on the electrical resistivity. The resistivity of water decreases with increasing salinity. In Israel, *Goldman et al.* (1988) quantifies the resistivity of seawater saturated sediments to be between $0.5 \Omega\text{m}$ and $1.5 \Omega\text{m}$. Freshwater saturated sediments will have resistivity values of greater $10 \Omega\text{m}$ (*Kafri and Goldman, 2006*).

An onshore time-domain EM (TDEM) application along the coastal plain of Israel investigated the resistivity values of the lower coastal sub-aquifers (*Kafri and Goldman, 2006*). Direct borehole salinity/conductivity measurements confirmed that regions of increased resistivity are linked to aquifer systems occupied with fresh to brackish water, whereas areas of low resistivity contained mainly saline water. The largest region of interest is a 20 km long transect known as the Palmahim Disturbance, located between the cities of Ashdod in the South and Bat Yam in the North. Marine Long Offset Transient Electromagnetic (LOTEM) measurements conducted by the Institute of Geophysics and Meteorology (IGM) at the University of Cologne, confirmed the offshore extent of this freshwater body to approximately 3.5 km from the coastline (*Lippert et al., 2012; Lippert, 2015*). However, the measurements could not explain why this region of the lower coastal sub-aquifer contains fresh groundwater. The insufficient lateral resolution of the applied LOTEM method, in addition to the sparse data density around the western aquifer boundary prohibited an adequate assessment of the transition zone between the freshwater aquifer and seawater saturated sediments.

A further attempt to answer this question was granted in January 2014 by the German Research Foundation (DFG) in a project called: “Marine Circular Electric Dipole (MCED): An innovative electromagnetic method used for the exploration of groundwater resources”. The presented thesis is conducted in the framework of this three-year project. The initial consideration of the project intended the application of a method called marine Circular Electric Dipole (CED). *Mogilatov and Balashov* (1996) introduced this method for land-based EM applications as an alternative to the Vertical Electrical Dipole (VED) to avoid the necessity of using boreholes. Their applied CED transmitter antenna consists of eight horizontal electric dipoles (HEDs) arranged in a star-shaped pattern around a common central

electrode. The excited EM field for a surface-based CED is analogous to that of a VED. The land-based application utilises a transmitter with several hundred metres radii in addition to mobile magnetic field receivers to map three-dimensional resistivity structures (*Helwig et al.*, 2010a,b). The intended marine application aimed at decreasing the transmitter radius to approximately 10 m, while using electric field receivers at short-offsets of approximately 50 m. The advantage of such application is the enhanced lateral resolution compared to the marine LOTEM method (*Haroon et al.*, 2013). Theoretically, the acquired step-off signal can clearly distinguish between different hydrogeological structures at the sub-seafloor freshwater aquifer boundary. However, the intention of applying the MCED had to be abandoned in August 2014, due to the insights gained during theoretical modelling studies. These proved that the complex structure of the CED transmitter is extremely susceptible towards geometrical inaccuracies. Even small deviations of several millimetres cause pronounced distortions in the received signal. These modelling studies are found in *Haroon et al.* (2016) and are presented and elaborately discussed in the extent of this thesis.

To minimise the distortions caused by these geometrical errors, it was decided to simplify, and elongate the CED transmitter. The result is a completely new transmitter antenna consisting of two HEDs in an in-line configuration that share a common central electrode. This novel EM method is called Differential Electrical Dipole (DED). Compared to the standard in-line LOTEM application, DED has an enhanced lateral resolution, especially in the short-offset configuration (*Haroon et al.*, 2016).

In the framework of this thesis, extensive theoretical modelling studies are conducted investigating the advantages and disadvantages of CED and DED compared to the conventional LOTEM and VED methods. An excerpt of these studies is published in *Haroon et al.* (2016) for a hydrocarbon application. The main focus of this thesis lies on studying the signal characteristics for the expected groundwater model in Israel, including detectability, resolution and signal distortion caused by geometrical inaccuracy. Moreover, the lateral resolution characteristics of DED are investigated using a 2D resistivity model. As an application of CED proved to be impractical, the 2D modelling studies focus mainly on the application of DED. However, an excerpt of the lateral resolution capabilities of CED is found in *Goldman et al.* (2015) and *Haroon et al.* (2016).

One interesting aspect that evolved in the extent of the theoretical modelling studies is the noticeable difference between step-on and step-off transients for seafloor-based EM systems within shallow marine settings. It appears that the received signals of either current excitation are sensitive towards different model parameters, provided the seawater layer above the transmitter/receiver system is shallow. This effect is independent of the current excitation and also applies for LOTEM signals. The differences of both signal types are emphasised in all modelling studies conducted in the context of this thesis.

The first marine DED measurements were conducted in April 2016 with the partners at EcoOcean, who were responsible for all technical issues concerning the research vessel “Mediterranean Explorer”. During the four-day measurement, 22 receiver sta-

tions were acquired along the profile of *Lippert (2015)*. Issues arose at five receiver stations, which are therefore not considered in the interpretation. The acquired data is processed and interpreted using newly developed processing and 1D inversion software¹. It is shown using synthetic data, that the acquired step-on signal retrieves a realistic sub-seafloor resistivity structure if certain conditions regarding the bathymetry are respected. The 1D inversion of the measured data will therefore indicate if the DED method can detect the resistive sub-seafloor aquifer.

Subsequently, a multi-dimensional interpretation of the measured DED data is sought. A multi-dimensional time-domain inversion software for marine DED is presently not available. Recently, *Yogeshwar (2014)* applied 2D inversion on measured in-loop TDEM data based on the code of *Martin (2009)*. However, this algorithm is designed for surface-based sources and has not been applied for marine LOTEM or DED data sets. Therefore, a large-scale 2D modelling study is realised to fit the measured DED step-on data. The main objectives yield the delineation of the aquifer boundary, including shape and hydrogeological structure. In total, over 425 600 forward calculations are carried out on the HP-Cluster at the University of Cologne. An ensemble of resistivity models that best describes the measured data set is found and evaluated.

Finally, the results are summarised and evaluated in connection to the first marine DED application. An outlook for necessary developments is given to improve the acquisition and interpretation process in the future.

Thesis Overview

The presented thesis has the following structure. First, the scientific background of groundwater studies in Israel and marine EM applications is presented. This overview includes previous EM applications in the region (*Kafri and Goldman, 2005, 2006; Lippert, 2015*) and groundwater flow studies (*Amir et al., 2013*). Furthermore, the standard marine EM application is introduced. The development of a new application technique is motivated based on the limitations of the existing EM systems within shallow water. Finally, the objectives of this thesis are motivated and classified on the basis of the current state of research. In Chapter 3 and Chapter 4, the basic theory of the applied EM methods and inversion techniques are introduced. In Chapter 5, a one-dimensional earth model is assumed and several modelling studies are realised. Detectability, resolution and geometrical errors of the novel methods are investigated and compared to the conventional marine EM systems. The 2D submarine aquifer model of *Lippert (2015)* is incorporated into the theoretical assessment of the DED method in Chapter 6. The multi-dimensional forward modelling is performed with `s1dmem3t` from *Druskin and Knizhnerman (1994)*. Chapter 7 through 9 deal with the DED application in Israel and the subsequent data analysis. In Chapter 10, a conclusion of the presented work is given along with an outlook of necessary future DED developments.

¹Technically, only the forward solutions for CED and DED are newly developed. These are implemented in the existing 1D inversion software MARTIN of C. Scholl.

Preliminary Notes

The presented work will stick to the following convention. Unless stated otherwise, all presented electric fields are source current normalised. Although they are displayed in V/m, the correct dimensions should actually read V/Am. To avoid confusion, I renounce from this terminology. Furthermore, all vectors are written in bold lower-case letters, whereas matrices are displayed in bold upper-case letters. This also applies to the vector quantities in the EM theory.

The modelling studies presented in this thesis are largely based on the resistivity models derived by *Lippert* (2015). I therefore recommend reading his work prior to this one.

State of Research & Motivation

The following chapter will give an overview of the scientific background to motivate the developments made in the context of this thesis. First, the groundwater situation in Israel is presented emphasising the coastal aquifer and the phenomenon of the sub-seafloor freshwater body around the Palmahim Disturbance. Several studies have been published regarding the coastal aquifer of Israel. The first section of this chapter constrains to the previous work of *Kafri and Goldman* (2005, 2006) and *Lippert* (2015). A brief review of the geophysical groundwater studies performed by the IGM Cologne in Israel is given. Groundwater flow simulations conducted by *Amir et al.* (2013) are introduced for two possible aquifer scenarios in the Palmahim region. The first assumes an aquifer that is open to seawater intrusion, the second a closed aquifer scenario. The derived subsurface salinity distribution of *Amir et al.* (2013) motivates an EM application to delineate the hydrogeological structure of the seawater/freshwater interface. The conventional marine EM methods are introduced, focussing mainly on the limitations in shallow sea environments. Based on these limitations, the development of novel time-domain EM methods is justified, as they will help to distinguish between the two aquifer scenarios. Taking the presented scientific background into account, the main objectives of this thesis are explained.

2.1 The Coastal Aquifer of Israel

Groundwater reservoirs in coastal regions are particularly vulnerable to contamination due to the continuing natural threat of seawater rise. Anthropogenic influences, caused by the increased urbanisation, also lead to a deterioration in groundwater quality. In Israel, this situation is pronounced as population steadily increases, while the coastal regions of the Mediterranean Sea are already densely populated. Furthermore, the coastal aquifer is one of only three national water system reservoirs (*Kafri and Goldman*, 2006). The salinity content of this aquifer has increased in the last decades due to over exploitation, anthropogenic pollution and artificial recharge (*Amir et al.*, 2013; *Kafri and Goldman*, 2006).

Displayed in Fig. 2.1 is the southern and central coastal aquifer of Israel that extends from Hadera in the North to the Gaza Strip in the South. It is replenished by the mountainous aquifer and drains into the Mediterranean Sea. The lateral extent of the aquifer from the Mediterranean Sea to the foothills is between 8 km in the North, and 30 km in the South with a thickness of 200 m or less

(Amir *et al.*, 2013). The aquiferous units consist mainly of sand and calcareous sandstone that are separated by aquicludeal clay formations near the coast, which thin out towards the East. As displayed in Fig. 2.2, the aquifer is generally divided into four sub-aquifers named A, B, C and D from top to bottom. The upper sub-aquifers A and B, are phreatic. Due to the saline water detected in these depth intervals, the basic assumption is that sub-aquifers A and B are prone to seawater encroachment throughout the entire Israeli coastal plain. Kapuler and Bear (1970) assume that this also applies to the lower sub-aquifers. However, Kolton (1988) challenges their assumption, stating that the lower sub-aquifers (C and D) thin out towards the Mediterranean Sea in the West and pass into a continuous shale sequence that blocks the lower sub-aquifers from seawater intrusion. His theory is based on the Nordan 4 Wildcat borehole located between Ashqelon and Gaza (see Fig. 2.1), which shows a thick continuous shale sequence below the upper sub-aquifers (Kafri and Goldman, 2006). Kafri and Goldman (2006) summarise observations that support the described possibilities of Kolton (1988) and Kapuler and Bear (1970). For instance, the water age obtained from the lower sub-aquifers is older than that of the upper ones, indicating restricted interaction. This may suggest that the lower aquifers are confined, whereas the upper aquifers are prone to seawater intrusion. Yet, the lower sub-aquifers are intruded by salt water in many areas along the coastal plain of Israel, suggesting that all sub-aquifers are open to the sea.

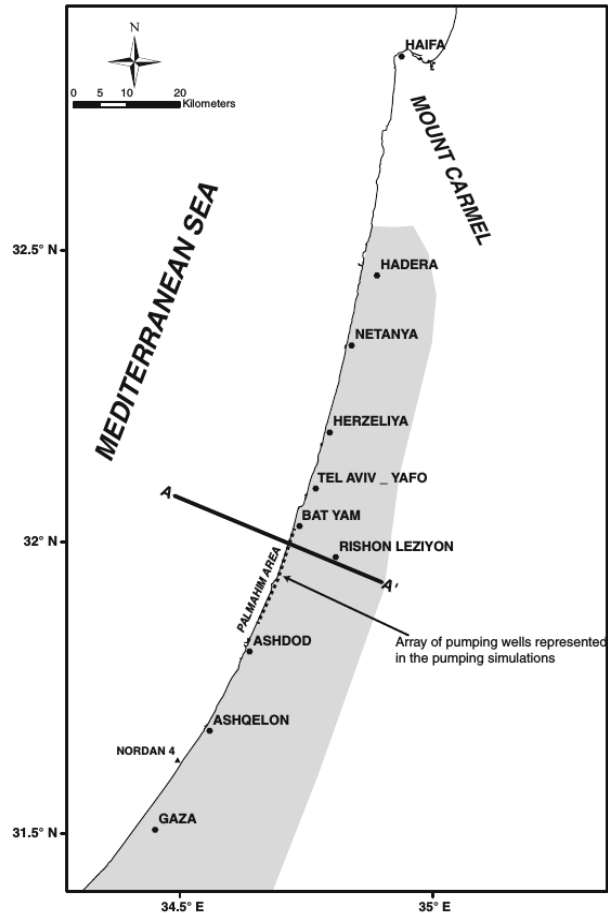


Figure 2.1: Map of the coastal aquifer in Israel (grey area) showing the Palmahim area. The cross section A - A' is studied in a 2D hydrogeological groundwater flow simulation presented in Section 2.1.2, investigating which hydrogeological condition enables the existence of fresh groundwater in the lower sub-aquifers (Amir *et al.*, 2013).

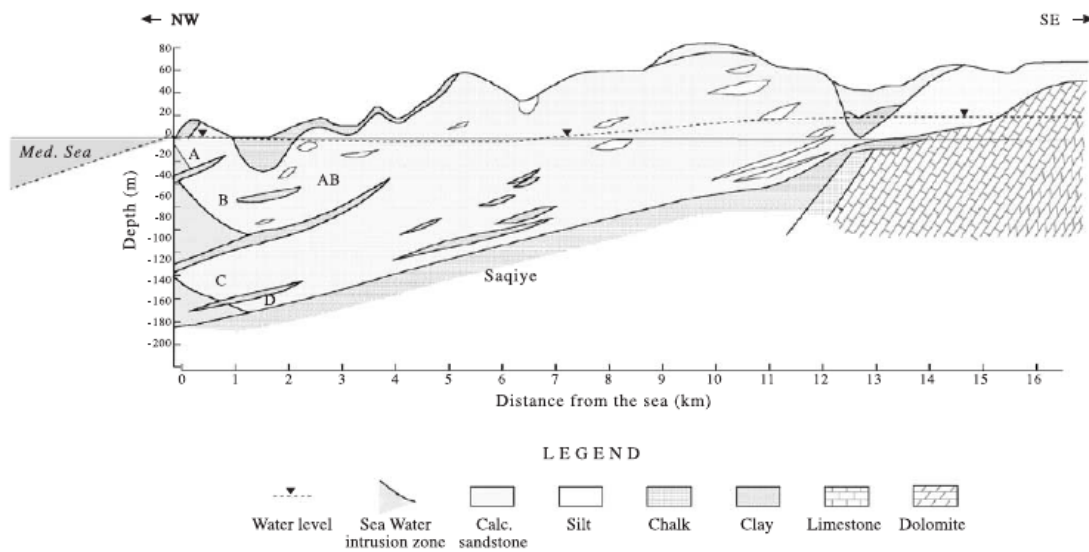


Figure 2.2: Typical cross section of the coastal aquifer in Israel (Kafri and Goldman, 2005). Near the coastline, the coastal aquifer is divided into four separate sub-aquifers named A through D. The intermediate clay formations thin out towards the land. The lower aquifer is bounded by the Saqiye clay formation.

2.1.1 EM Surveys in Israel

TDEM methods are useful for groundwater studies due to the relationship between pore-water salinity and the corresponding electrical resistivity. Saltwater saturated sediments found in the coastal regions are less resistive compared to the same sediments saturated with fresh water. Therefore, areas of increased resistivity values within the depth range of the lower sub-aquifers indicate the presence of brackish or fresh water. First groundwater TDEM experiments in Israel are presented by Goldman *et al.* (1988), studying the freshwater/seawater interface in northern Israel. These measurements are followed by Nuclear Magnetic Resonance (NMR) measurements for groundwater exploration (Goldman *et al.*, 1994). The IGM Cologne actively started investigating the groundwater situation in Israel by applying the LOTEM method in northern Israel (Scholl, 2005). Later, Kafri and Goldman (2006) published work on the coastal aquifer south of Tel Aviv, which motivated a further IGM study in Israel (Lippert, 2015) and the presented thesis.

Kafri and Goldman (2006) conducted several TDEM measurements along the coastal plain of Israel, investigating the resistivity (salinity) of the lower coastal sub-aquifers. An excerpt of their study is presented in Fig. 2.3. The authors correlated their findings to borehole data, which found regions within the central and southern coastal aquifer that are occupied with fresh water. The largest region is a 20 km long strip located south of Tel Aviv and north of Ashdod, generally referred to as the Palmahim Disturbance. These fresh water findings are related to the assumption that the lower sub-aquifers are locally blocked to the sea.

The IGM Cologne started a joint project with the Israel Oceanographic and

Limnological Research (IOLR) and the Geophysical Institute of Israel (GII) that was funded by the German Federal Ministry of Education and Research (BMBF) and the Israeli Ministry of Science, Technology and Space (MOST) between 2008 and 2011 to explore the westward extent of the lower sub-aquifers in the Palmahim area underneath the Mediterranean Sea. In the extent of this project, marine LOTEM measurements were conducted along a transect running perpendicular to the coastline off the shore of Bat Yam, Israel. The full interpretation of the acquired data set is found in *Lippert (2015)*. The following is an excerpt of his main findings to motivate the applications conducted in the extent of this thesis.

Displayed in Fig. 2.4 are 1D Occam inversion models obtained from marine LOTEM data. Clearly, the marine LOTEM measurements were effective in detecting the sub-seafloor aquifer off the coastline of Bat Yam, Israel (*Lippert, 2015*). Furthermore, the application was also effective in restraining the lateral extent of the sub-seafloor aquifer, predicting the western boundary to be located between 3.25 – 3.65 km from the coastline. The results enabled preliminary hydrogeological modelling based partly on still unknown assumptions (*Amir et al., 2013*). This includes the location and nature of the western aquifer boundary that could not yet be assessed due to the insufficient lateral resolution of the LOTEM method. *Lippert (2015)* applies synthetic modelling studies to show that marine LOTEM is capable of differentiating between the hydrogeological structures at the aquifer boundary, provided a sufficient data density, and knowledge about the exact boundary position is available. However, the exact position of the boundary was not known prior to the LOTEM campaigns and is still vague within a range of about 400 m. An EM data set with a sufficient station density is needed, preferably using a method with high lateral resolution, to further constrain the boundary position and gain information regarding the hydrogeological structure of the aquifer transition zone.

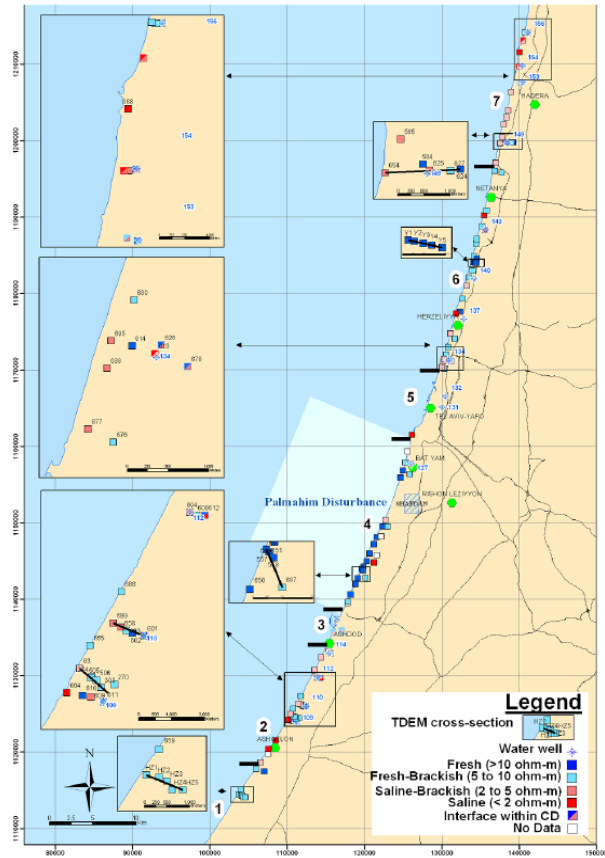


Figure 2.3: Map of southern Israel including TDEM stations investigating the resistivity in the depth range of the lower sub-aquifers C and D (*Kafri and Goldman, 2006*).

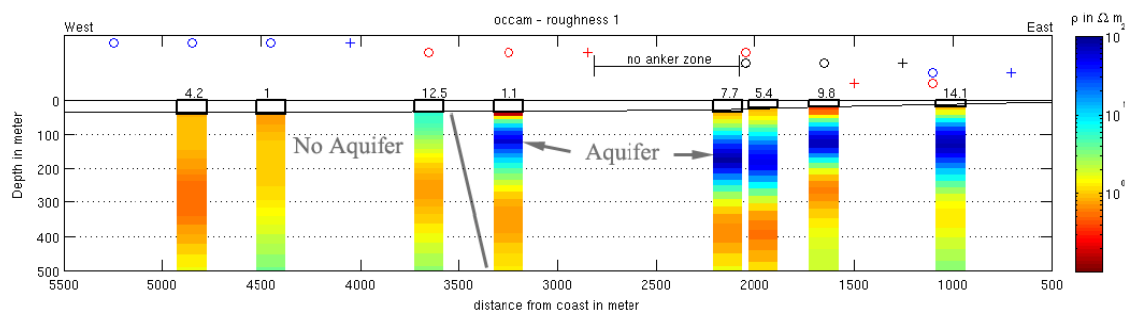


Figure 2.4: 1D Occam inversion results obtained from marine LOTEM measurements (modified after Lippert (2015)). A resistive layer interpreted as the subsurface freshwater body extends to approximately 3.25–3.65 km from the coastline.

2.1.2 Hydrogeological Modelling Studies

Hydrogeological modelling studies were performed in the extent of the BMBF-MOST project by Amir *et al.* (2013). The following is only an excerpt of the hydrogeological simulation. As displayed in Fig. 2.5, the authors differentiated between two possible aquifer scenarios. The first scenario, displayed in the top images of Fig. 2.5, assumes an aquifer system where the lower sub-aquifers are open to the sea. The second scenario assumes an aquifer system that is closed to the sea by a sharp boundary located 9 km before the coast. Note, Amir *et al.* (2013) did not take the LOTEM results of Lippert (2015) into account, else the aquifer boundary would be located closer to the shoreline.

The simulations show the steady state condition for a hydraulic conductivity of $K = 0.001$ m/day in the separating layers. The necessary conditions for a freshwater occurrence at the shoreline are investigated. For the selected hydraulic conductivity, both aquifer scenarios satisfy this occurrence. However, a gradual salinity gradient is pronounced for the open aquifer scenario, whereas the closed aquifer scenario is characterised by a sharp salinity transition reproducing the shape of the initial model. In this case a vertical boundary. The differences in the salinity variations may produce a measurable EM signature, provided the lateral resolution of the applied EM method is sufficiently high.

Based on these hydrogeological flow simulations, three possible resistivity models are derived for the 2D modelling studies. These are displayed in Fig. 6.11 and will be explained in detail in the corresponding section. Basically, the first two models exemplify either a closed aquifer scenario with a vertical boundary or a partially closed scenario with a typical wedge-shaped boundary. The third model exemplifies the open aquifer scenario with a zone of decreased salinity (resistivity) at the head of the saltwater/freshwater interface. If an apparent DED response is measurable between the three models is extensively studied in Chapter 6.

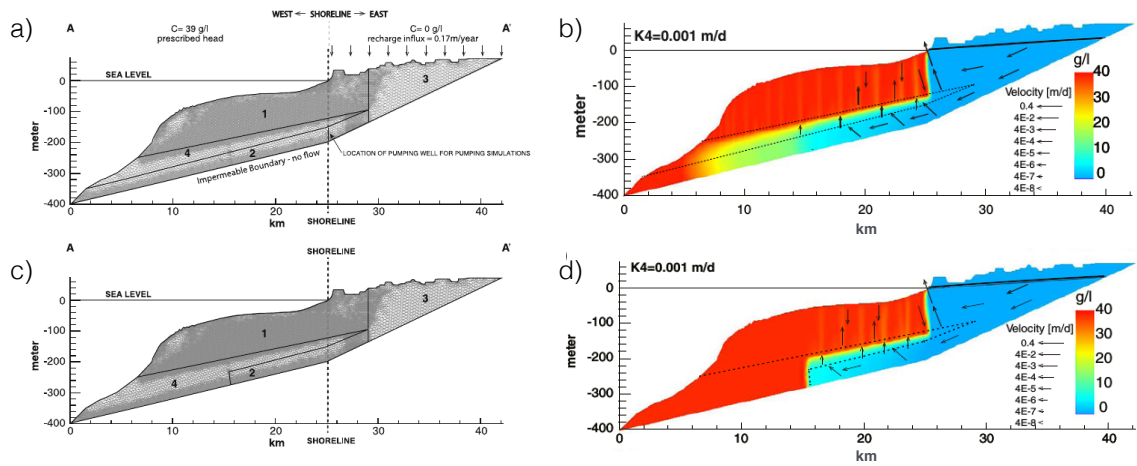


Figure 2.5: Hydrogeological modelling study for a schematic cross section of the coastal aquifer in the Palmahim region. The left column displays the cross section A - A' from Fig. 2.1 for (a) an open-aquifer scenario and (c) a closed-aquifer scenario. The four subdomains are 1) the upper aquifers A and B, 2) the lower aquifers C and D, 3) the undivided coastal aquifer and 4) the separating clay layers. The images on the right display the modelling results for a hydraulic conductivity of $K = 0.001$ m/day for (b) an open-aquifer scenario and (d) a closed-aquifer scenario. The colours correspond to the salinity of the contained water, which is related to the resistivity value. Images are modified after Amir et al. (2013).

2.2 Marine EM Applications

The idea of using electromagnetic (EM) methods to study sub-seafloor resistivity structures dates back to Cagniard (1953). He proposed using the Magnetotelluric (MT) method as a tool to study the resistivity structure beneath the seafloor. Since then, numerous publications proposed the application of a horizontal electrical dipole transmitter with a continuous, low frequency wave excitation along with seafloor based receivers to map the sub-seafloor resistivity structure, e.g. Filloux (1967); Cox et al. (1986); Constable and Cox (1996). This method became generally known as the frequency-domain controlled source electromagnetic (FD-CSEM or just CSEM) method. The main advantage of CSEM is the exceptional detectability towards resistive layers. Consequently, the method has become quite popular in hydrocarbon prospecting ever since Ellingsrud et al. (2002) first applied CSEM on an offshore oil field. A review of the CSEM method is found in Constable (2010).

CSEM experiments are generally difficult to conduct in shallow-sea environments due to the saturation of the acquired signal at large offsets, known as the airwave effect (Chen and Alumbaugh, 2011). As a consequence, CSEM loses its sensitivity towards the resistive layers in the subsurface. Different strategies have been developed to account for the effect of the airwave. For example, Chen and Alumbaugh (2011) present three strategies to mitigate the effect of the airwave: (1) EM bucking, (2) $dE/dFreq$ and (3) MT impedance stripping. However, these approaches are often inaccurate due to simplified assumptions and are sometimes controversial.

CSEM applications in the time-domain, generally referred to as TD-CSEM or marine LOTEM (only in Cologne) are also applied frequently, e.g. *Schwalenberg et al.* (2010); *Hunziker et al.* (2011); *Hölz et al.* (2015); *Lippert* (2015). The advantage of an application in the time-domain is that the airwave can be separated in the early time data (*Ziolkowski and Wright*, 2007). A detailed analysis between TD-signals and FD-signals for shallow water experiments is given by *Weiss* (2007). He shows that the signature of the target formation in the subsurface is not necessarily masked by the signature of the airwave in the TD-signal. Further applications use a VED transmitter, which excites an EM field that is independent of the airwave (*Haland et al.*, 2012; *Singer and Atramonova*, 2013; *Helwig et al.*, 2013). Note, the airwave is only present in five of six electromagnetic field components using a HED source (*Weidelt*, 2007) and remains absent in the vertical electrical field. Due to reciprocity, this also applies to VED transmitters.

Recently, first applications using VED sources have been published (*Holten et al.*, 2009; *Helwig et al.*, 2013). These applications constrain to measuring vertical electric fields at the receiver, as they are less prone to errors caused by non-verticality. This effect is investigated by *Goldman et al.* (2015), who show that VED measurements require perfectly vertical transmitters/receivers to avoid parasitic effects from contributing to the acquired signal. Even small deviations may result in strong distortions in the acquired signal. Furthermore, the application of VED in shallow water is problematic due to the limited extent of the vertical source. Unless very large current amplitudes are applied, the acquired signal will generally exhibit a poor signal-to-noise ratio (SNR). For applications in Israel, a VED source is not feasible due to the limited extent of the water column (< 40 m).

2.3 Motivation of the Presented Thesis

The presented work is completed in the framework of the DFG project (GZ:TE 170/19-1) “Marine Circular Electric Dipole (MCED): An innovative electromagnetic method used for the exploration of groundwater resources”. The original goals of the project include the development of a new MCED system. An application of MCED in Israel shall clarify if the lower sub-aquifers (C and D) are indeed open or closed to seawater intrusion. During the theoretical developments prior to the first intended measurement, modelling studies proved that an application is not feasible in the extent of the project due to various technical issues. These will be elaborately explained in Chapter 5 of this thesis. As a result, an alternative method called Differential Electric Dipole (DED) is developed to resolve the hydrogeological structure of the sub-seafloor aquifer.

A seafloor-towed transmitter and receiver system is built at the Institute of Geophysics and Meteorology, Cologne, Germany. Compared to the previous marine LOTEM measurements, where the offset between transmitter and receiver was not stringently known, a fixed-offset system is developed to minimise the geometrical errors and increase the accuracy of the measurement. Additionally, new transmitter (ZT30: Zonge International) and receiver (KMS-820: KMS Technologies) devices are implemented into system. The latter required the development of a new time-

series processing software. The processing steps are explained and illustrated in Chapter 7. Test measurements were conducted in Cuxhaven - Sahlenburg (January 2016) to test the system and the developed software, but are not addressed in the framework of this thesis.

The content of the presented work deals with the practical and theoretical development of the marine CED and DED methods. This includes the development of a 1D forward algorithm for both methods, which is implemented in the existing 1D inversion software “Marine TEM Inversion Program - MARTIN” of C. Scholl. Theoretical studies are realised using 1D modelling and 3D modelling with `s1dmem3t` of *Druskin and Knizhnerman* (1994). For the latter, a new finite-difference grid generator is developed to accompany the discretisation of the CED transmitter. Ultimately, only DED is applied during the measurements in Israel due to the complexity and geometrical issues concerning the CED.

The first marine DED measurement was conducted in April 2016 with the following aims:

1. Feasibility study of the new marine DED system.
2. Validating the results previously obtained by marine LOTEM. Is a resistive layer detectable in the vicinity of the coastline using marine DED?
3. Locate the position of the western aquifer boundary more accurately compared to the marine LOTEM measurements.
4. Investigate the hydrogeological structure at the aquifer boundary to draw conclusions about the possible seawater intrusion scenarios.

The acquired data is processed and interpreted using the developed software. Subsequently, a large-scale 2D modelling study is conducted to fit the measured data using the 1D inversion results as a basis. The parameter space is systematically investigated between minimum and maximum values for each model parameter. The final 2D results are presented as an ensemble of models that best describe the measured data set.

The projected goal of this work is to present a fully functional marine DED system that is applicable in the shallow marine environment. Furthermore, software developments shall allow an interpretation of the measured data with the ultimate goal of applying marine DED in other coastal regions in the future.

Theory of the Applied EM Methods

The basic theory of TDEM methods is based on the electromagnetic diffusion equation in conductive media. The electrical conductivity or its inverse, the electrical resistivity are the essential physical material property to which the applied TDEM methods are sensitive. The propagation of electric current through the earth is generally classified into three mechanisms: electrolytic, electronic and dielectric conduction (*Telford et al.*, 1976). In the coastal regions of Israel, mainly sedimentary rocks are found. The current propagation is therefore dictated by electrolytic (ionic) conduction, where the resistivity of the porous rock varies with the mobility and concentration of the dissolved ions. The controlling factors are the state of the pores, and the amount and conductivity of the contained fluid. Resistive fluids like hydrocarbons or fresh water increase the sediment resistivity and can be targeted using TDEM methods (*Gehrmann*, 2014). In comparison, sedimentary rocks saturated with salt water will have much lower resistivity values (*Darnet et al.*, 2010). Consequently, TDEM methods are not only effective in hydrocarbon exploration, e.g. *Ellingsrud et al.* (2002), but are also commonly applied for groundwater studies in coastal regions, e.g. *Kafri and Goldman* (2006).

The empirical formula of Archie (*Archie*, 1942) relates the resistivity of a fully saturated host medium ρ_0 to the resistivity of the contained pore fluid ρ_w with

$$\rho_0 = a\phi^{-m}\rho_w, \quad (3.1)$$

for clean sands. This relationship was developed for clay-free sands only, but is commonly used to analyse marine sediments that contain fair amounts of clay. In Eq. (3.1), ϕ is the porosity and a is a coefficient introduced by *Winsauer et al.* (1952) that is theoretically equal to one, but practically not equal to one. m is a further empirical Archie parameter (*Spangenberg*, 2001). Small values of a and m describe sediments with well-interconnected pore spaces, as ρ_0 then decreases. If we assume that a , ϕ and m remain constant for a specific rock formation and degree of saturation, and solely the resistivity of the pore fluid ρ_w dictates the value of ρ_0 , then TDEM methods can determine if the porous rock formation contains fresh water or salt water.

In the following, marine TDEM applications are introduced both practically and theoretically. The main emphasis lies on the novel CED and DED methods studied

in the extent of this thesis. The general concepts of EM applications are found in *Ward and Hohmann (1988)*. The specific theory of a HED source in a layered marine environment is found in *Edwards (1997)*. The CED method is presented by *Mogilatov (1992)*, *Mogilatov and Balashov (1996)* and *Haroon et al. (2016)*. The theory to VED and loop sources in a layered marine environment are found in *Scholl and Edwards (2007)* and *Swidinsky et al. (2012)*, respectively.

The basic principles and source current excitations of TDEM methods are introduced. Subsequently, Maxwell's quasi-static equations are used to derive the basic diffusion equation. A simplified one-dimensional (1D) earth model, consisting of stratified layers of homogeneous conductivity is introduced and the forward solution of a CED and DED source located on any layer boundary is derived. The forward operator is described regarding its implementation in the 1D inversion software **MARTIN**. The implementation is verified using comparative modelling studies with existing software (*Mogilatov and Zlobinsky, 2008*). Finally, the system response is addressed.

3.1 Time-Domain Electromagnetic Methods

In the following, the basic principles of TD-CSEM in the marine environment are described. The general description is extended to the specific EM sources developed in the context of this thesis.

As illustrated in Fig. 3.1, a seafloor-based marine TD-CSEM system generally consists of a HED transmitter along with several electric field receivers at fixed offsets in an in-line configuration. The injected source current is often a square-wave signal

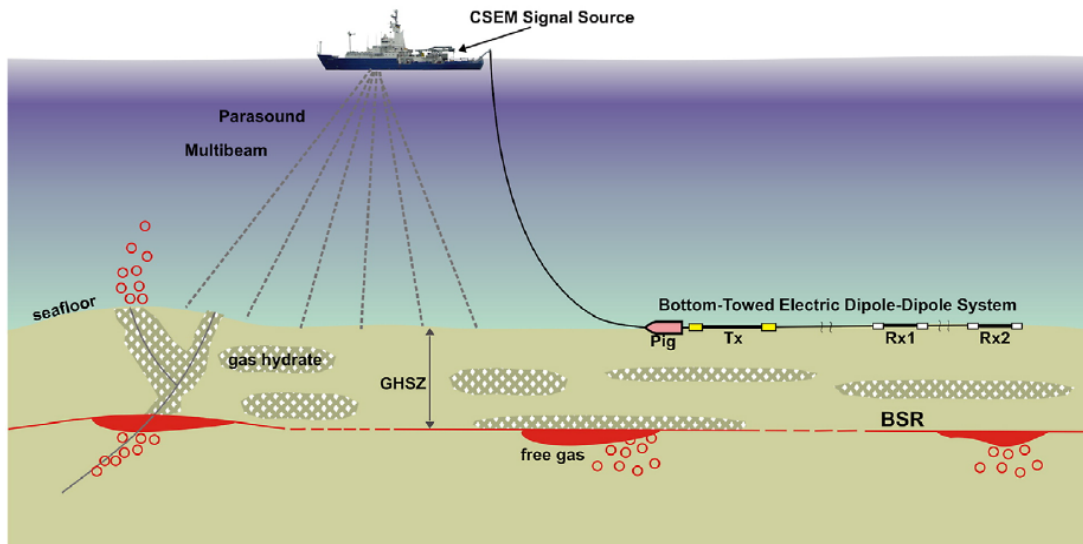


Figure 3.1: Schematic setup of a typical TD-CSEM measurement applied in the marine environment. The system consists of a HED transmitter accompanied by electrical field receivers in an in-line configuration (*Schwalenberg et al., 2010*).

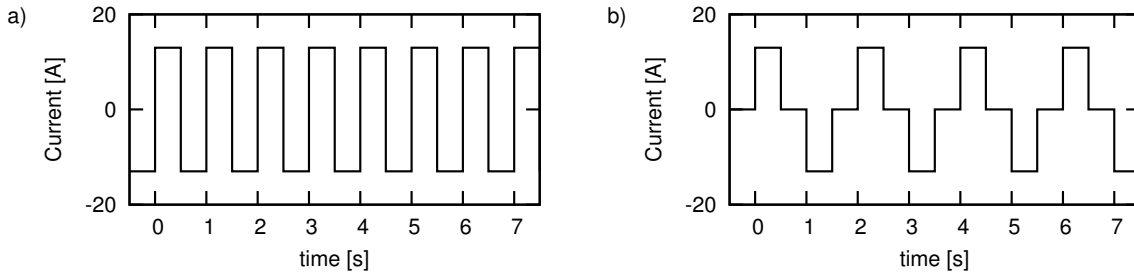


Figure 3.2: Square wave current signals for (a) 100% and (b) 50% duty cycle with current amplitudes of 13 A and a period of 1 s and 2 s, respectively.

with either 100% duty cycle displayed in Fig. 3.2a, or a 50% duty cycle displayed in Fig. 3.2b. The term duty cycle refers to the percentage in which the transmitter is in an active state. At each station, the ship will stop and measure for several minutes to ensure decent data quality (*Schwalenberg et al., 2010*). The system positioning is commonly maintained using acoustic transponders in the leading weight (PIG).

As mentioned, two types of current signals are often applied. These are displayed in Fig. 3.2. For a 100% duty cycle signal, the transmitter switches the polarity directly without an intermediate pause. These polarity switches are generally interpreted as step-on signals with a twofold current amplitude. In this case, it is assumed that the transmitter is inactive at $t < 0$ s and is switched on at $t = 0$ s. In contrast, the 50% duty cycle signal has intermediate phases between polarity switches, where no current is transmitted. Accordingly, both step-on and step-off transients are obtained when applying a 50% duty cycle. A step-off transient is constant at $t < 0$ s and decays after the transmitter is turned off at $t = 0$ s. The relationship between step-on f^{On} and step-off f^{Off} signals is expressed as

$$f^{Off} = f^{DC} - f^{On}, \quad (3.2)$$

where f^{DC} describes the signal at the direct current (DC) level.

Marine TD-CSEM applications generally apply a 100% duty cycle signal due to the increased SNR. The resulting signals are interpreted as a step-on transients, e.g. *Schwalenberg and Engels (2011)*. An interpretation of step-off signals is only feasible when applying a 50% duty cycle. This approach is commonly applied for in-loop TEM measurements (*Asten, 1987*) due to two particular technicalities. First, the step-off function of modern transmitter systems is generally quicker and cleaner compared to the step-on function (*Lippert, 2015*). Second, the DC plateau is not completely constant, but actually oscillates around a particular value. These oscillations may appear in form of noise at the receiver. In this case a step-off signal is more robust, as no primary EM field superimposes the measured signal. Particularly magnetic field measurements benefit from the characteristics of a step-off current signal. Appropriately, *Lippert (2015)* interpreted step-off signals in a marine LOTEM experiment, where magnetic fields were also measured.

Exemplary step-on and step-off transients are illustrated in Fig. 3.3 by blue and red lines, respectively. The DC level is displayed by a dashed black line. The time

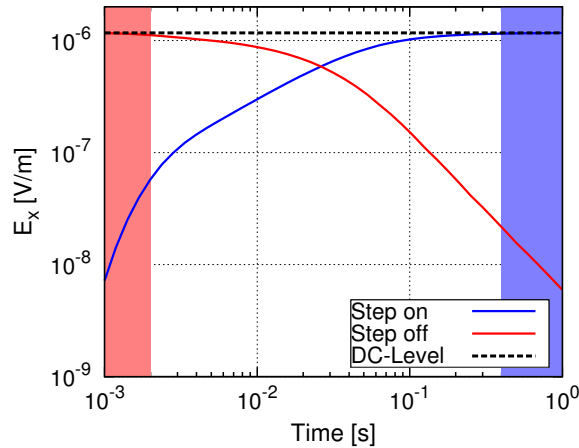


Figure 3.3: Exemplary electric field for a step-on (blue) and step-off (red) current excitation. The DC level is displayed by a black dashed line. The quasi-DC ranges of the respective transients are displayed by blue and red background colours.

range in which the corresponding signal is in the quasi-DC range is marked by the respective background colours. In general, the step-on signal is characterised by an increase of signal amplitude that is dependent on the subsurface resistivity structure. A more resistive subsurface will result in a steeper increase of the acquired signal. Alternatively, the step-off signal begins at the DC level and decays proportionally to the subsurface resistivity structure. A more resistive subsurface will cause a steeper decay of the signal amplitude.

One issue that is brought into conjunction with step-off signals is the poor SNR at late times. Unfortunately, the response of the respective target formation often appears at these late times. Therefore, the step-on signal is usually applied in marine TD-CSEM measurements, as SNR is a common issue, especially if deep resistive targets are investigated. The studies presented in this thesis will demonstrate that the signals of step-on and step-off for shallow sea EM applications are sensitive towards different model parameters. This phenomenon has not been thoroughly investigated in literature and is evaluated using 1D/2D resistivity models in the extent of this thesis.

In recent years, marine TD-CSEM applications did not confine to the application of HED sources. *Goldman et al. (2015)* states that the relative target response towards an intermediate resistive layer, embedded in a conductive background, is increased if a VED source is applied. The authors base their arguments on the two separate modes of the EM field within a 1D background environment. Commonly these are referred to as the transverse electric (TE) mode and transverse magnetic (TM) mode. A detailed description of the TE and TM mode is found in Chapter 3.3.1 of this thesis. Any EM application using a HED transmitter with horizontal electric field receivers is considered bimodal, since both modes are excited. Unimodal applications either use a VED source for a pure TM field or Vertical Magnetic Dipoles (VMD) for a pure TE field (*Goldman et al., 2015*). Generally, the horizontal electric fields of a VED source are more sensitive towards a resistive intermediate layer compared to the unimodal TE field system or even the bimodal TD-CSEM system. However,

VED applications are difficult to conduct at shallow sea, primarily due to the limited extent of the water column. Issues such as non-verticality and SNR are pronounced in these specific settings. Alternatives to the conventional methods are therefore needed, particularly for marine EM studies in coastal regions. The development of such methods is the primary aim of the presented thesis.

3.1.1 Circular Electrical Dipole

The CED method was introduced as the analogue of VED for land-based measurements to avoid the necessity of drilling boreholes (*Mogilatov, 1992*). The signal of a surface-based CED is analogous to that of a VED under the condition

$$(Id_z)_e h = \frac{I_0 b^2}{4}, \quad (3.3)$$

where Id_z describes the dipole moment of a VED source located at depth $h \rightarrow 0$ m below the surface. I_0 and b describe the disc current and radius of the CED source, respectively (*Mogilatov and Balashov, 1996*).

A CED application was practically realised by *Mogilatov and Balashov (1996)*. Theoretically, the CED transmitter consists of a continuum of ‘outer electrodes’ with one polarity, arranged in a concentric circle around an electrode with the other polarity (see Fig. 3.4-right). In theory, this type of current excitation is described by the radial current sheet with an inner radius a and an outer radius b . Under practical considerations, this type of source is hardly feasible due to inhomogeneous coupling conditions for the large outer ring-electrode (*Helwig et al., 2010b*). However, *Mogilatov and Balashov (1996)* show that a sufficient CED approximation is achieved by applying eight outer electrodes arranged symmetrically around the mutual central electrode (see Fig. 3.4-left). The current between the inner and outer electrodes

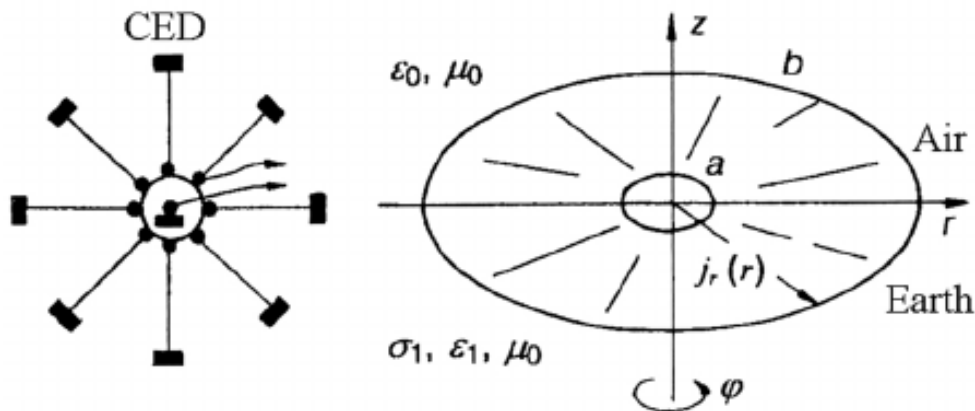


Figure 3.4: The real (left) and the ideal (right) CED comprising two concentric electrode systems with inner radius a and outer radius b (*Mogilatov and Zlobinsky, 2014*).

flows through insulated wires, meaning that the CED transmitter can be seen as a composition of eight HED sources.

One known shortcoming of CED is the strict criterion of equal current amplitudes in each of the horizontal dipoles. This cumbersome task is solved by applying a special transmitter system that regulates the current in each arm individually (*Mogilatov and Balashov*, 1996; *Helwig et al.*, 2010a). In marine applications, this is less of an obstacle due to the homogeneous coupling conditions in the surrounding seawater (*Haroon et al.*, 2016). Equal current amplitudes in each arm can be maintained by increasing the resistance within each dipole to a higher value compared to the expected contact resistance at the electrodes.

One characteristic of CED that is commonly applied in land-based measurements is the complete absence of a vertical magnetic field at the surface of a stratified, one-dimensional subsurface. Past applications of CED made use of this characteristic using large transmitter systems of several 100 m to 1 km radius, along with mobile receivers to map 3D resistivity structures in predominantly 1D background environments, e.g. *Mogilatov and Balashov* (1996) and *Helwig et al.* (2010b).

Although this approach is effective as a mapping tool on land, a marine CED application in this form would require the installation of a large transmitter of several hundred meters radii on the seafloor. For the EM prospecting campaign in Israel, this type of application is ineffective. An easier implementation is theoretically suggested by *Goldman et al.* (2015): A small mobile transmitter of several tens meter radii, applied together with mobile electric field receivers located at short offsets. This will allow the system to have the necessary mobility to investigate the resistivity structure along a profile. The propagation of the total electric field for a seafloor-based CED within a shallow marine environment is illustrated in Appendix D.

In the following, modelling studies will investigate the effectiveness of the short-offset CED application, while concurrently emphasising its restrictions.

3.1.2 Differential Electrical Dipole

The application of a marine DED system is an entirely novel approach. Until present, applications of the land-based equivalent referred to as counter lines have been applied in Russia together with CED. However, publications do not exist in western journals¹. The DED transmitter can be seen as a simplification of CED, consisting of only two HED sources arranged in-line with a common central electrode. The current in each dipole flows in opposite directions. The excited total electric field is illustrated in Appendix D. The central electrode has one polarity, whereas the two outer electrodes have the other one (see Fig. 3.5). Unlike CED, the excited EM field of DED is bimodal, consisting of both TE and TM mode. The sensitivity towards resistive layers in a one dimensional earth is, therefore, comparable to a HED transmitter. However, the excited field is more focussed underneath the DED transmitter compared to a HED, resulting in a higher resolution towards multi-

¹Personal communication with V. Mogilatov.

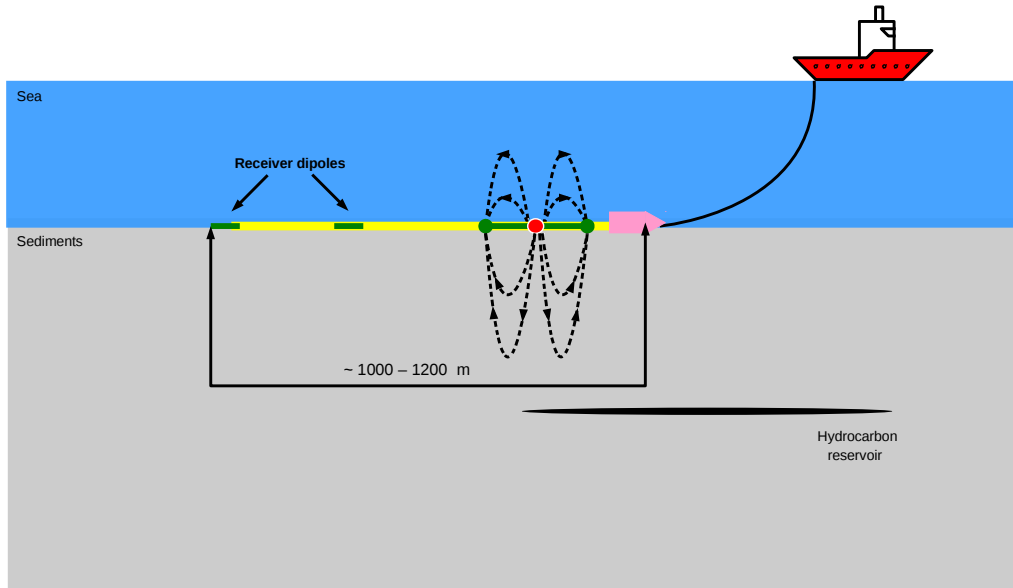


Figure 3.5: Schematic of a seafloor-based DED system. The transmitter consists of two horizontal electric dipoles in an in-line configuration with opposite current amplitudes. The displayed dashed lines represent the excited current system in the xz -plane (Haroon *et al.*, 2016).

dimensional resistivity structures (Haroon *et al.*, 2016).

Theoretically, Davydycheva and Rykhliniski (2011) discuss the application of a focussed-source EM (FSEM) system that resembles the DED in the so-called axial setup. The theoretical background and DC current patterns for FSEM are found in Davydycheva *et al.* (2006). Similar approaches referred to as Differentially-Normalised EM (DNEM) are presented in Russian literature, e.g. Bubnov *et al.* (1984); Legeydo *et al.* (1990, 1997); Mandelbaum *et al.* (2002). The elementary difference to DED is that the differential field is obtained through post-processing of the measured dipole receiver signals. The DED current pattern is directly of differential nature through the three-electrode transmitter. DNEM and FSEM experiments for hydrocarbon exploration are published by Veeken *et al.* (2009); Davydycheva and Rykhliniski (2009).

Similar to CED, the drawback of DED applications are the complicated measurement procedures. In order to obtain a clean differential signal, dipole moments need to be identical. This can be a challenging task, especially in marine measurements. Exact positioning is often difficult to control, and as a result, signal distortions caused by geometrical inaccuracies may become relevant. Therefore, signal distortions caused by these geometrical errors are emphasised in the presented thesis. Furthermore, marine DED is a completely novel method with little preceding literature. The presented studies in this thesis aim to investigate the excited DED signal in one-dimensional and multi-dimensional background environments. The method is studied with respects to strengths and weaknesses in comparison to marine LOTEM (TD-CSEM), CED and VED.

3.2 Quasi-static Maxwell's Equations

All EM methods in geophysics are based on a set of equations referred to as Maxwell's equations. These are the governing equations of all electromagnetic phenomena. The following derivations are based on a simplification, where displacement currents are neglected. This approximation is generally valid in time and frequency domain EM, if reasonably large conductivity values are studied. In the coastal environment of Israel, this assumption is valid for all expected resistivity values. Maxwell's equations then simplify to a set of uncoupled, first order, linear differential equations generally referred to as Maxwell's quasi-static equations. In differential form, these are expressed as

$$\nabla \times \mathbf{e} = -\partial_t \mathbf{b} \quad (3.4)$$

$$\nabla \times \mathbf{h} = \mathbf{j} \quad (3.5)$$

$$\nabla \cdot \mathbf{b} = 0 \quad (3.6)$$

$$\nabla \cdot \mathbf{d} = q \quad (3.7)$$

where \mathbf{e} in V/m is the electric field, \mathbf{h} in A/m the magnetic field, \mathbf{b} in Vs/m² the magnetic field flux density, \mathbf{d} in As/m² the electric displacement field, \mathbf{j} in A/m² the current density and q in As/m³ the electric charge density. The conventional forms of Maxwell's equations are based on experiments (*Ward and Hohmann, 1988*). Faraday's law of induction describes how a time varying magnetic field $\partial_t \mathbf{b}$ generates an electric eddy field. Amperes' law links the current density \mathbf{j} to the curl of the magnetic field intensity \mathbf{h} .

Equation (3.4) through Eq. (3.7) are uncoupled differential equations of five vector functions, \mathbf{e} , \mathbf{b} , \mathbf{h} , \mathbf{d} and \mathbf{j} (*Ward and Hohmann, 1988*). These can be coupled through the following constitutive relations and Ohm's law.

$$\mathbf{d} = \epsilon \mathbf{e} \quad (3.8)$$

$$\mathbf{b} = \mu \mathbf{h} \quad (3.9)$$

$$\mathbf{j} = \sigma \mathbf{e} \quad (3.10)$$

The parameters ϵ , μ , σ describe the dielectric permittivity, the magnetic permeability and the electric conductivity, respectively. These material properties are generally tensors that are dependent on time, temperature, pressure, etc., but are seen in the following derivations as scalar functions. This assumption holds in linear, isotropic and homogeneous media.

Provided \mathbf{e} and \mathbf{h} are piecewise continuous, Eq. (3.4) through Eq. (3.10) can be used to express Maxwell's equations outside of the source as

$$\nabla \times \nabla \times \mathbf{e} = -\mu\sigma\partial_t \mathbf{e} \quad (3.11)$$

$$\nabla \times \nabla \times \mathbf{h} = -\mu\sigma\partial_t \mathbf{h}. \quad (3.12)$$

For an arbitrary vector field \mathbf{a} , the vector identity $\nabla \times \nabla \times \mathbf{a} = \nabla \nabla \cdot \mathbf{a} - \nabla^2 \mathbf{a}$ can be used to convert Eq. (3.11) and Eq. (3.12) to

$$\nabla^2 \mathbf{f} - \mu\sigma \partial_t \mathbf{f} = 0, \quad \mathbf{f} \in \{\mathbf{e}, \mathbf{h}\} \quad (3.13)$$

This equation describes the propagation of the EM field due to electric conduction and is referred to as the diffusion equation. It is a second order, linear differential equation that leads to the attendant lack of resolution for EM prospecting methods in real earth materials (*Ward and Hohmann, 1988*). The 1D version in the frequency domain is expressed as

$$\partial_{zz} \mathbf{f} - i\omega\mu\sigma \mathbf{f} = 0. \quad (3.14)$$

The positive solution of Eq. (3.14) for a plane wave propagating in z -direction shows that for a real quantity β , $e^{-\beta z}$ gets smaller as z gets larger (*Ward and Hohmann, 1988*). In this case β is defined as

$$\beta = \sqrt{\frac{\omega\mu\sigma}{2}}. \quad (3.15)$$

The solution represents an attenuation of the EM field with increasing depth. The field amplitude is reduced by factor of $1/e$ at a distance within the medium, described by skin depth. The latter is defined as,

$$\delta = \frac{1}{\beta} = \sqrt{\frac{2}{\omega\mu\sigma}}. \quad (3.16)$$

A second basic 1D solution of Eq. (3.13) is for impulsive electric and magnetic fields at $z = 0$ m (*Ward and Hohmann, 1988*). For this specific case, the positive solution is written as

$$\mathbf{f} = \mathbf{f}_0^+ \frac{(\mu\sigma)^{1/2} z}{2\pi^{1/2} t^{3/2}} e^{-\mu\sigma z^2/4t}. \quad (3.17)$$

By calculating the derivative of Eq. (3.17) with respect to z and setting it to zero, the diffusion depth,

$$\delta_D = \sqrt{\frac{2t}{\sigma\mu}} \quad (3.18)$$

is derived. It describes the depth of the maximum wave amplitude to a certain time t (*Ward and Hohmann, 1988*). *Spies (1989)* shows that the depth of investigation for several electromagnetic sounding methods is dependent on the transmitter moment, noise levels and the resistivity of the subsurface. He concludes that for transient measurements, a buried inhomogeneity can be detected under about one diffusion depth.

To investigate the arrival time of certain signal contributions, the travel velocity of the EM field in conductive media is often considered. Following *Ward and Hohmann* (1988), the derivative of Eq. (3.18) with respect to time is the velocity of the maximum field amplitude within a conductive media. It is calculated according to

$$v = \frac{1}{\sqrt{2\sigma\mu t}}. \quad (3.19)$$

The maximum field amplitude has a higher travel velocity within a more resistive subsurface. For a receiver located at a fixed offset to the transmitter, a signal will be registered at earlier delay times if a resistive aquifer is present within the subsurface. Yet, a shallower seawater column above the measurement system will cause the same effect. If the signal contributions of the resistive aquifer and the air-sea interface overlap will be investigated in the Chapter 5.

3.3 The Layered Full-Space Model

One of the simplest ways of discretising the subsurface resistivity structure is based on the assumption that the resistivity only varies with depth $\rho = \rho(z)$. Thereby, the conductive earth is composed of a given number of horizontally stratified layers with certain thickness, resistivity and anisotropy values. The following derivation of the radial electrical field for a CED and DED current excitation will assume a layered full-space, consisting of N -layers below the source and M -layers above (see Fig. 3.6). The source and receivers may be located on any arbitrary boundary.

The objective of the following section is to deduce expressions for the radial electrical field given a specified source current. In this sense, the expressions for a DED and CED source are presented. The DED transmitter is composed of two in-line HED sources with opposite currents. Therefore, the 1D forward solution of DED is merely computed using superposition of two HED transmitters of opposite polarity and adjusted offsets to the receiver. In comparison, two methods can be used to discretise a CED transmitter: (1) CED transmitter consisting of eight HED's referred to as the approximated solution or (2) by a radial current sheet describing the ideal CED solution (see Fig. 3.4).

For a stratified 1D earth model, the EM field can be separated into two modes commonly referred to as the TE and TM mode. These are characterised by the absence of either the vertical magnetic field (TM mode) or vertical electric field (TE mode). The attributes of these two modes are briefly explained.

3.3.1 TE and TM Mode

Displayed in Fig. 3.7 are the current densities and corresponding magnetic field flux densities for the TE and TM mode (*Weidelt*, 1986)². The TE mode is characterised by electrical currents flowing in horizontal plane that couple purely by induction

²Note that the TE mode is sometimes referred to the poloidal magnetic (PM) mode.

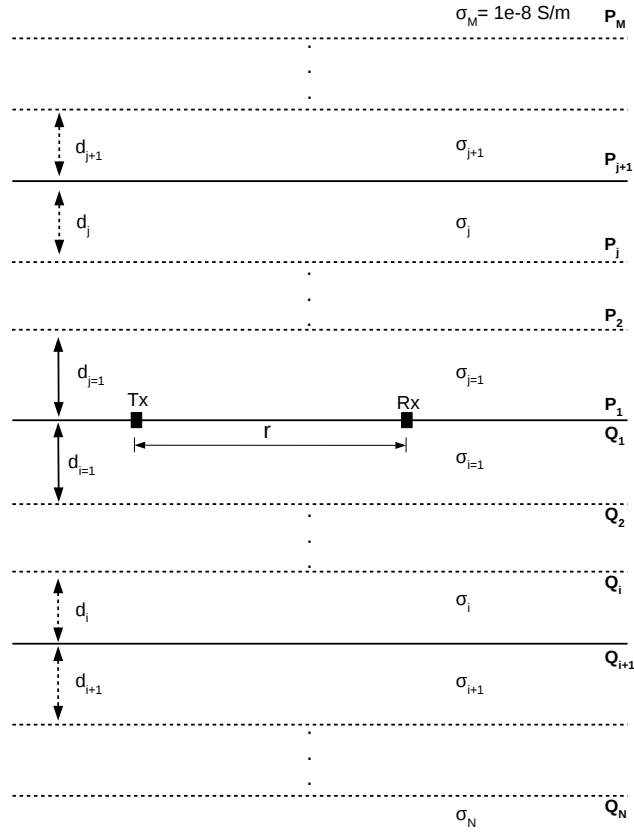


Figure 3.6: Layered earth model consisting of N layers below the source and M layers above. Each layer has a thickness d and a conductivity σ . The position of the transmitter and receiver at offset r are illustrated by black markers. P and Q describe the transfer functions at each layer boundary above and below the transmitter, respectively. Further explanations are given in the text.

(Chave and Jones, 2012). The TM mode is associated with vertical electric currents systems that run perpendicular to the subsurface resistivity structure. The latter exists if the source is galvanically coupled to the subsurface, e.g. grounded electric dipole source. Furthermore, a non-conducting layer will decouple the TM mode so that only horizontal currents exist below (Weidelt, 1986).

The EM field of a HED source consists of both modes. Other source types may be unimodal consisting of either TM mode (VED or CED) or TE mode (VMD). It is quite commonly known that both modes are influenced by the resistivity structure with depth. However, as studied by Chave (1984), large differences in the sensitivity exist between both modes if an intermediate resistive layer embedded in a conductive background is considered. The TE mode is hardly affected by a thin resistive layer, whereas the TM mode is strongly perturbed (Ferguson and Edwards, 1994). Consequently, resistive layers are commonly studied using EM methods that excite either a bimodal field or an unimodal TM mode field.

The idea of applying a pure TM mode method, e.g. VED has gained interest in recent years despite the difficulties in the application procedure. One exceptional feature of the TM mode is that it is unaffected by the airwave. Marine applications

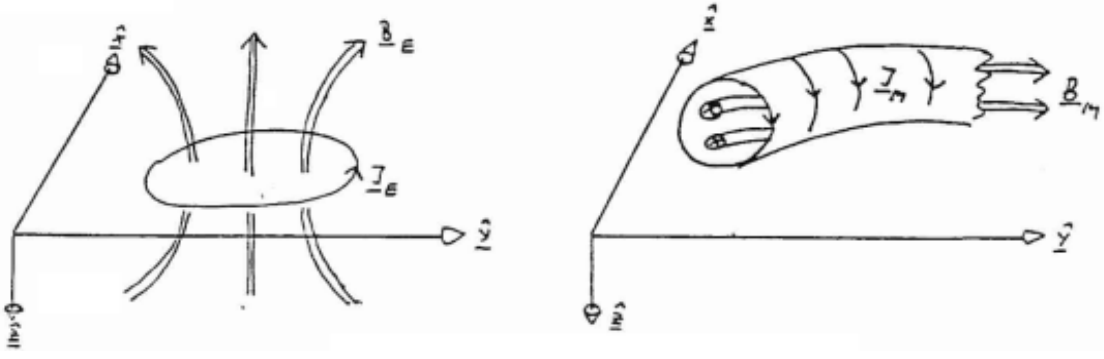


Figure 3.7: Illustration of the current density \mathbf{j} and magnetic flux density \mathbf{b} for TE mode on the left and TM mode on the right (Weidelt, 1986).

are therefore even more desirable, especially at shallow sea. The idea of applying a CED in coastal regions originates from these arguments. Note, this also applies for DED, although the excited EM field is considered bimodal. The main objective of a CED/DED application is to achieve an increased sensitivity towards an intermediate resistive layer.

In the following section, the field expressions for the ideal CED, the approximated CED and the DED source are derived. These are based on the literature of *Edwards* (2005) for bimodal sources, *Scholl and Edwards* (2007) for TM mode sources and *Swidinsky et al.* (2012) for TE mode sources. The ideal CED is derived first, due to the simplicity of deriving a unimodal TM mode field. The TE mode is required for the calculation of the approximated CED and DED. It is derived in an analogous way and is included in the field expressions at the appropriate time.

3.3.2 1D Forward Operator: Ideal CED

Due to the azimuthal symmetry of the problem, the EM field of an ideal CED is sufficiently described by assuming $e_\phi = 0$ and $b_r = b_z = 0$. Furthermore, the curl of an arbitrary vector \mathbf{v} in cylindrical coordinates is defined as

$$\nabla \times \mathbf{v} = \left(\frac{1}{r} \partial_\phi v_z - \partial_z v_\phi \right) \hat{\mathbf{e}}_r + (\partial_z v_r - \partial_r v_z) \hat{\mathbf{e}}_\phi + \frac{1}{r} (\partial_r r v_\phi - \partial_\phi v_r) \hat{\mathbf{e}}_z, \quad (3.20)$$

where $\hat{\mathbf{e}}_r$, $\hat{\mathbf{e}}_\phi$ and $\hat{\mathbf{e}}_z$ are the corresponding unit vectors.

Applying these relations on the laws of Faraday and Ampere, the azimuthal magnetic field flux density $b_\phi(r, z)$ satisfies the Helmholtz equation

$$\partial_{rr} b_\phi(r, z) + \frac{1}{r} \partial_r b_\phi(r, z) - \frac{1}{r^2} b_\phi(r, z) + \partial_{zz} b_\phi(r, z) = \alpha^2 b_\phi(r, z), \quad (3.21)$$

with $\alpha^2 = s\mu_0\sigma$ within all source free layers of conductivity σ and $s = i\omega$ describes the Laplace coefficient³. A Hankel transform is defined relating the fields $b_\phi(r, z)$

³Note, the TE-Mode is solved using the identical equation with $e_\phi(r, z)$ instead of $b_\phi(r, z)$

and $b_\phi(k, z)$ as,

$$b_\phi(r, z) = \int_0^\infty k b_\phi(k, z) J_1(kr) dk \quad (3.22)$$

where J_1 is a Bessel function of the first kind, order one. Substituting Eq. (3.22) into Eq. (3.21) and solving the derivatives with respect to r and z results in the following relation (excluding the integrals)

$$\left[k^2 J_1''(kr) + \frac{k}{r} J_1'(kr) - \frac{1}{r^2} J_1(kr) \right] b_\phi(k, z) + \partial_{zz} b_\phi(k, z) J_1(kr) = \alpha^2 b_\phi(k, z) J_1(kr). \quad (3.23)$$

Using the relation for differentiating Bessel functions found in *Abramowitz and Stegun* (1972), Eq. 9.1.1, p. 358, the square bracket in Eq. (3.23) is compressed to equal $-k^2 J_1(kr)$ (*Swidinsky et al.*, 2012), yielding the second order differential equation

$$\partial_{zz} b_\phi(k, z) - \theta^2 b_\phi(k, z) = 0, \quad (3.24)$$

with $\theta^2 = k^2 + \alpha^2$. Consequently, every layer of constant conductivity within the full-space model has a solution of Eq. (3.24), which can be written as

$$b_{\phi,i}(k, z) = U \cosh(\theta_i z) + W \sinh(\theta_i z). \quad (3.25)$$

U and W are functions that are independent of z and constrained by the boundary conditions (*Swidinsky et al.*, 2012). The radial electric field e_r is related to the azimuthal magnetic field component b_ϕ through Ampere's Law (Eq. (3.5)). In the Laplace domain, e_r is therefore defined as

$$\mu e_{r,i}(k, z) = -\frac{\theta_i}{\sigma_i} [U \sinh(\theta_i z) + W \cosh(\theta_i z)] \quad (3.26)$$

with the conductivity of layer i being $\sigma_i = 1/\rho_i$ and $\mu = \mu_0$. Two transfer functions $Q = \mu e_r/b_\phi$ and $P = -\mu e_r/b_\phi$ are introduced for the layers below and above the source, respectively. Each transfer function is calculated separately beginning with the uppermost and lowermost half-spaces for P and Q , respectively. Following *Scholl and Edwards* (2007), U and W are eliminated from Eq. (3.25) and Eq. (3.26). The upward recursion relationship for Q at layer i is obtained by

$$Q_i(k) = \frac{\theta_i}{\sigma_i} \left[\frac{\sigma_i Q_{i+1} + \theta_i \tanh(\theta_i d_i)}{\theta_i + \sigma_i Q_{i+1} \tanh(\theta_i d_i)} \right]. \quad (3.27)$$

Q_i and Q_{i+1} are the values of the transfer function at the top and the bottom of the i^{th} layer, where d_i is the corresponding layer thickness. The transfer function Q_1 just underneath the CED source is obtained by successive applications of Eq. (3.27) starting from the top of the lowermost terminating half-space where

$$Q_N(k) = \frac{\theta_N}{\sigma_N}. \quad (3.28)$$

Similarly to Q , the transfer function P for the layers above the transmitter is calculated by

$$P_j(k) = \frac{\theta_j}{\sigma_j} \left[\frac{\sigma_j P_{j+1} + \theta_j \tanh(\theta_j d_j)}{\theta_j + \sigma_j P_{j+1} \tanh(\theta_j d_j)} \right], \quad (3.29)$$

where P_j and P_{j+1} are the values of the transfer function at the bottom and top of the j^{th} layer, respectively. The transfer function P_1 just above the CED source is obtained by successive applications of Eq. (3.29) starting from the bottom of the uppermost half-space (generally the air layer),

$$P_M(k) = \frac{\theta_{Air}}{\sigma_{Air}} \quad (3.30)$$

where $\sigma_{Air}^{-1} = \rho_{Air} = 10^8 \Omega\text{m}$. Outside of the source, the transfer functions P and Q are continuous across all boundaries, as e_r and b_ϕ are also continuous. At the source, the following boundary conditions have to be considered (*Mogilatov, 1996*). The radial electric field e_r is continuous through the plane, whereas the azimuthal magnetic field b_ϕ is not due to the effects of the source. The amount by which the magnetic field above the source differs from the magnetic field below the source δb_ϕ can be expressed as

$$\delta b_\phi(k) = \mu e_r(k) \left[\frac{P_1 + Q_1}{P_1 Q_1} \right]. \quad (3.31)$$

Following *Mogilatov (1996)*, the influence of the source is

$$\delta b_\phi(k) = \mu \int_0^\infty j_r(r) \cdot r \cdot J_1(kr) dr. \quad (3.32)$$

Mogilatov and Balashov (1996) define the current density function $j_r(r)$ for a radial current sheet with inner radius a and outer radius b to be,

$$j_r(r) = \begin{cases} \frac{I_0}{2\pi r s} & \text{if } a \leq r \leq b \\ 0 & \text{else} \end{cases}$$

where I_0 is the maximum current amplitude. By inserting this relation into Eq. (3.32), *Mogilatov and Balashov* (1996) show that $\delta b_\phi(k)$ is expressed as

$$\delta b_\phi(k) = \frac{I_0 \mu}{2\pi s} \int_a^b J_1(kr) dr = \frac{I_0 \mu}{2\pi s k} \left[J_0(ka) - J_0(kb) \right]. \quad (3.33)$$

This expressions describes the source excitation for a pair of grounded electrodes. Thereby, the inner electrode has a radius of a and the outer electrode a radius of b . This expression is further simplified by assuming that the inner electrode is approximated as a point electrode ($a \rightarrow 0$) and, therefore $J_0(ka) = 1$. For the purposes of this study, it is sufficient to assume that the offset between transmitter and receiver is much larger than the transmitter radius. Therefore, $b \ll r$ and $J_0(kb) \approx 1 - k^2 b^2 / 4$. These relations are inserted into Eq. (3.31) to obtain our final field expression for radial electric field

$$e_r(r) = \frac{I_0 b^2}{8\pi s} \int_0^\infty J_1(kr) k^2 \frac{P_1 Q_1}{P_1 + Q_1} dk. \quad (3.34)$$

The Hankel transform and Laplace transform in Eq. (3.34) are evaluated by using appropriate digital filters as described in *Johansen and Sørensen* (1979) and *Christensen* (1990). In Chapter 3.3.4, a description of the applied Fast Hankel algorithm is given.

3.3.3 1D Forward Operator: Approximated CED and DED

The EM field of a CED and also DED source situated on any vertical boundary of a layered earth model may also be derived by superposition of horizontal electrical dipoles, each with a different location and orientation to the receiver. In this case, the field is bimodal and both TE and TM modes are calculated for each HED component.

The Laplace transform of an electric field, measured for a single HED transmitter at offset r is given by

$$e(s) = \frac{I \cdot dl}{2\pi s} [F_{TE}(s) + F_{TM}(s)], \quad (3.35)$$

where $I \cdot dl/s$ is the moment of the transmitter dipole with length dl and current amplitude I . As mentioned, the electric field of a HED source is a superposition of $F_{TE}(s)$ and $F_{TM}(s)$, which are the Laplace transforms of the TE and TM-Mode, respectively (*Edwards and Chave, 1986*). Following *Edwards (2005)*, $F_{TE}(s)$ and $F_{TM}(s)$ for an inline geometry are expressed as

$$F_{TE}(s) = -\frac{s}{r} \int_0^{\infty} J_1(kr) \frac{\hat{P}_1 \hat{Q}_1}{\hat{P}_1 + \hat{Q}_1} dk \quad (3.36)$$

$$F_{TM}(s) = -\int_0^{\infty} k J_1'(kr) \frac{P_1 Q_1}{P_1 + Q_1} dk \quad (3.37)$$

where P , Q , \hat{P} and \hat{Q} are transfer functions of the EM field polarisations. The functions P and Q follow the TM mode derivations presented in the preceding section. \hat{P} and \hat{Q} are calculated similarly to the P and Q functions in the preceding section, where

$$\hat{P}_j(k) = \frac{\mu_0}{\theta_j} \left[\frac{\theta_j \hat{P}_{j+1} + \mu_0 \tanh(\theta_j d_j)}{\mu_0 + \theta_j \hat{P}_{j+1} \tanh(\theta_j d_j)} \right] \quad (3.38)$$

and

$$\hat{Q}_i(k) = \frac{\mu_0}{\theta_i} \left[\frac{\theta_i \hat{Q}_{i+1} + \mu_0 \tanh(\theta_i d_i)}{\mu_0 + \theta_i \hat{Q}_{i+1} \tanh(\theta_i d_i)} \right]. \quad (3.39)$$

The functions \hat{Q}_1 and \hat{P}_1 are again obtained by the upward and downward recursion relation for the layers below and above the source. The corresponding starting values are $\hat{Q}_N = \mu_0/\theta_N$ and $\hat{P}_M = \mu_0/\theta_M$.

An approximated CED transmitter consist of eight horizontal electrical dipoles, six of which also contain a broadside component. Thereby, the electrical field is still calculated according to Eq. (3.35), but alternative definitions of $F_{TE}(s)$ and $F_{TM}(s)$ are needed:

$$F_{TE}(s) = s \int_0^{\infty} k J_1'(kr) \frac{\hat{P}_1 \hat{Q}_1}{\hat{P}_1 + \hat{Q}_1} dk \quad (3.40)$$

and

$$F_{TM}(s) = \frac{1}{r} \int_0^{\infty} J_1(kr) \frac{P_1 Q_1}{P_1 + Q_1} dk. \quad (3.41)$$

All other transmitter-receiver geometries are obtained through a linear combination of the in-line and broadside geometries (*Edwards, 2005*). The forward solution is calculated for several frequencies in the frequency-domain for each of the eight transmitter dipoles and subsequently added. Afterwards, the solution is transformed into the space-domain by solving the Hankel transform and subsequently into the time-domain using a Hankel transform of half-integer order (*Scholl and Edwards, 2007*).

The radial electric field of a DED source is calculated using superposition of two in-line HED's with opposite current amplitudes and adjusted offsets. In this case, only Eq. (3.36) and Eq. (3.37) are needed for an undistorted DED. Similar to the approximated CED, the field is calculated for several frequencies and transformed into the space and time-domain. This can be done using a so-called fast Hankel Transformation explained in the following section.

3.3.4 Fast Hankel Transformation

The integrals above are commonly evaluated using digital filter technique proposed by *Ghosh (1971)*. For an arbitrary kernel function or forward operator $f(k)$, the integral of the form

$$F(r) = \int_0^{\infty} f(k) J_1(kr) dk \quad (3.42)$$

can be discretely evaluated by using a vector \mathbf{h} , of predetermined linear filter coefficients. For a filter vector \mathbf{h} of length n , Eq. (3.42) is ultimately approximated using (*Key, 2012a*)

$$rF(r) \approx \sum_{i=1}^n f(b_i/r) h_i, \quad (3.43)$$

where $b_i = k_i r = e^{ai}$. In this case, a is the spacing coefficient and $i = -l, -l+1, \dots, l$ with $l = (n-1)/2$ (*Key, 2012a*). Due to the decrease of computational expense, this method is generally referred to as the Fast Hankel Transform. Different methods to optimise the filter coefficients have been published, e.g. by *Guptasarma and Singh (1997)*. Additionally, *Sorensen and Christensen (1994)* show an approach to handle the problem-specific EM integral for a finite electrical dipole source. The applied coefficients in MARTIN were calculated by C. Scholl in 2006, but no indication regarding the method are given.

3.3.5 Code Verification

The 1D forward operator for an ideal CED, approximated CED and DED transmitter is implemented in the 1D inversion software `MARTIN` of Carsten Scholl. The following section will compare the solutions of a CED step-off response to the existing algorithm of *Mogilatov and Zlobinsky* (2014). The latter can only calculate step-off responses of an ideal CED. Therefore, the comparison is confined only to the step-off response. An additional comparison to the approximated CED will give insight regarding the accuracy of the implemented algorithm for an ideal CED. The latter code is independent of the $b \ll r$ assumption, but may have inaccuracies due to the superposition of the many individual dipole components. Additionally, as HEDs are used to approximate the source, TE contributions may also affect the signal at late times.

For CED, a violation of $b \ll r$ of the approximated Bessel function in Eq. (3.34) may affect the early times of the step-off transient. In Fig. 3.8, a comparison between the three algorithms is presented for four different b/r -ratios. Note, the offset between the centre of the transmitter and electric field receiver is constant at 200 m and only the transmitter radius is varied between values of 5 m, 10 m, 20 m and 50 m. A ratio at which the b/r -approximation holds for this particular model and transmitter configuration is obtained.

The transients displayed in Fig. 3.8 show the calculated signals of the *Mogilatov and Zlobinsky* (2014) code (labelled `mogilatov`), and the ideal and approximated CED solutions (labelled accordingly) for the r/b -ratios of 40, 20, 10 and 4. The relative errors of all transients are illustrated beneath each image and are displayed as percentile values, accordingly. The markers represent comparisons of the ideal/approximated CED to the *Mogilatov-Code*. The solid purple line represents the relative difference of the ideal and approximated CED solution.

For b/r -ratios smaller than $1/4$ displayed in Fig. 3.8a through Fig. 3.8c, the results of all algorithms are generally consistent. However, features are apparent at intermediate to late times, which seem to be independent of the selected ratio. These oscillations affect both CED solutions implemented in `MARTIN`. The relative differences to the solution of *Mogilatov and Zlobinsky* (2014) reach values of approximately 4%. As they are independent of the selected ratio, they appear to be of systematic nature between the two program packages. Which solution is ultimately more accurate is difficult to assess and can only be determined using analytical solutions.

The solutions of an ideal CED computed using `MARTIN` becomes inaccurate at early times for $b/r = 1/4$ (see Fig. 3.8d). Relative errors of approximately 7% are reached compared to the *Mogilatov-Code* at times of $t < 2 \cdot 10^{-3}$ s. This value is even surpassed when comparing the ideal CED to the approximated CED, both obtained with `MARTIN`. In this case, it is advisable to use the approximated CED solution, as it is more consistent with the results obtained by the *Mogilatov and Zlobinsky* (2014) code.

A code verification for DED is conducted by simply using superposition of two HED sources. The results do not differ considerably to a comparison with `sldmem3t`. Therefore, they are neglected here, but can be examined in the grid checks in Fig. 6.5.

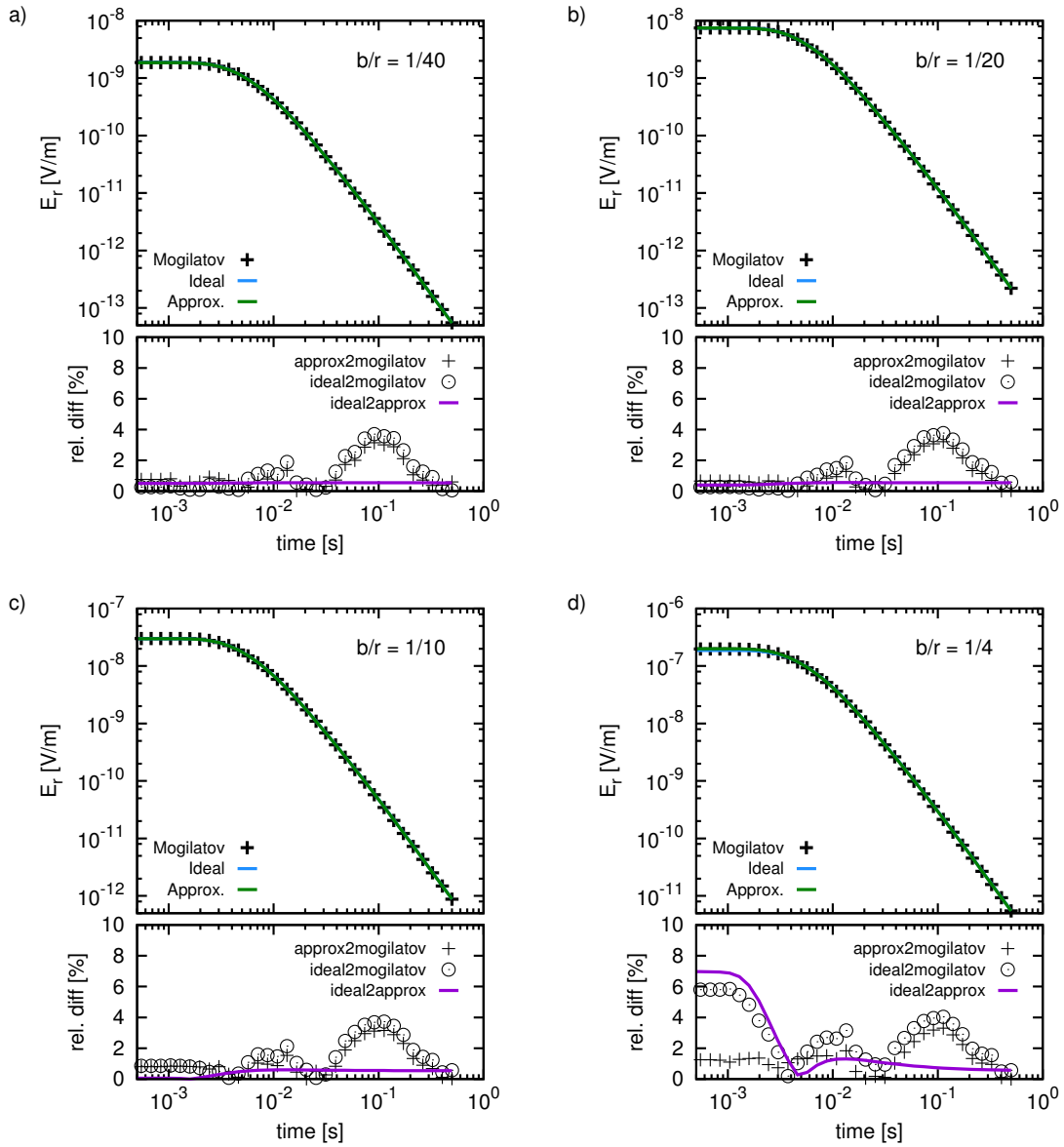


Figure 3.8: CED transients calculated with three different algorithms at an offset of 200 m from the CED centre. The ratio b/r varies from top to bottom from (a) 1/40, (c) 1/20, (e) 1/10 and (g) 1/4. The bottom images of each plot display the relative differences of the transients with respects to each other.

3.4 System Response

The calculated forward solutions cannot be compared with the measured data directly. The measurement is performed at discrete time points and not continuously. Therefore, the measured data is composed of an input signal originating from the earth, combined with the effects of the data generation process (*Strack, 1992*). The latter is often referred to as the system response. The influences of a system response are summarised by *Strack (1992)*, including deviation from a step function, polarisation effects, inductance in the transmitter wire, misalignment of the receiver, A/D converters, etc. Formally, the influence of the system response $s(t)$ on the measured

data $d(t)$ is seen as a convolution

$$d(t) = f(t) * s(t), \quad (3.44)$$

where $f(t)$ is the response of the earth.

Two separate strategies, largely depending on the applied measurement system are followed when dealing with the system response. The first strategy is mainly applied for in-loop TEM applications, where the step-off current function resembles a linear ramp (*Martin*, 2009). This can be treated by using a parameterised deconvolution on the measured data *Hanstein* (1992). Subsequently, the calculated forward response is directly compared to the data. This approach is unstable for LOTEM applications (*Hördt*, 1989). Consequently, the system response is often measured in the direct vicinity of the transmitter antenna. The time derivative of the measured system response is then incorporated through a convolution with the calculated data. Subsequently, a comparison to the measured data is feasible.

For the applied studies, the calculated data from **MARTIN** is convolved with the measured system response. This step is realised for 1D inversion using **MARTIN**, and also prior to comparing the results of the 2D modelling study with the measured data. For the latter case, a program called **MAXPROC**⁴ is used.

⁴Program to process data calculated by SLDMEM3t - A. Hoerd

1D-Inversion Theory

For a layered full-space model, the synthetic response of a DED or CED transmitter located at any layer boundary is calculated using the forward solution presented in the preceding chapter. This forward response is used in the 1D inversion process to search for a layered earth model that best explains the measured data and the *a priori* knowledge. In our specific case, the water depth and the water resistivity. The following section will exhibit the basic principles of the inversion algorithms implemented in the software **MARTIN**. Specifically, these are the inversion schemes of Occam, Marquardt and a hybrid Marquardt-Monte-Carlo scheme. Additionally, a singular value decomposition (SVD) of the weighted Jacobian is presented as a tool to analyse the model parameter resolution of the Marquardt inversion. Many of the presented principles are found either in textbooks such as *Menke* (1984), or have been presented in previous dissertations, e.g. *Scholl* (2005), or published in scientific literature, e.g. *Edwards* (1997).

The notation for the inversion theory is as follows. Scalar values are written in lowercase and uppercase letters, vectors in bold lowercase letters and matrices in bold uppercase letters. Entries of matrices are written in capital letters with indices.

4.1 General Terms of 1D-Inversion

The data vector $\mathbf{d} \in [N \times 1]$ contains the processed data sampled at time points t_1, \dots, t_N . The model parameters are contained in the model parameter vector $\mathbf{p} \in [M \times 1]$. For 1D inversion of time-domain EM data, \mathbf{p} generally consists of layer resistivity and layer thickness values. In the interpretation of measured data, the transmitter and receivers are located on the seafloor, where water depth and water resistivity are treated as *a priori* information. Only the sub-seafloor resistivity structure is unknown. For K number of layers underneath the seafloor, the parameter vector \mathbf{p} consists of $M = 2K - 1$ entries.

The relationship between the data vector \mathbf{d} and model vector \mathbf{p} is simply given through the forward operator \mathbf{f} that maps the model space to the data space. Hence, $\mathbf{f} : \mathbb{R}^M \rightarrow \mathbb{R}^N$. The forward operator \mathbf{f} is expressed as a $N \times M$ coefficient matrix if the model parameters have a linear relationship to the measured data. For non-linear problems, the forward operator remains a function of \mathbf{p} and a different approach is necessary.

Is $N > M$, the inversion problem is considered overdetermined. In this case, no exact/unique solution exists. Otherwise, the problem is either underdetermined for $N < M$ or even-determined $N = M$. For the former, an infinite amount of models exists that essentially explain the data. The latter has exactly one exact solution. TDEM data is rarely independent, meaning that the 1D inversion problem is not considered to be overdetermined although the number of data points exceed the amount of model parameters. For TDEM applications, some model parameters are better resolved than others. Consequently, the inversion problem is often considered to be mixed-determined and a least-squares solution is used to minimise the data cost-function Φ_d , where

$$\Phi_d = [\mathbf{W}\mathbf{d} - \mathbf{W}\mathbf{f}(\mathbf{p})]^T [\mathbf{W}\mathbf{d} - \mathbf{W}\mathbf{f}(\mathbf{p})], \quad (4.1)$$

with data error weighting matrix $\mathbf{W} = \text{diag}(1/\Delta d_1, \dots, 1/\Delta d_N)$. The data error Δd_i is estimated according to the processing steps presented in Chapter 7.2. The classical approach is to find the extremal values of $\Phi_d(\mathbf{p})$ by searching for vectors \mathbf{p} where

$$\frac{\partial \Phi_d(\mathbf{p})}{\partial \mathbf{p}} = 0. \quad (4.2)$$

For linear methods, this step can be undertaken directly. However, as EM induction methods are non-linear, the forward operator has to be linearised before Eq. (4.1) is minimised. This is explained in the following.

4.2 Non-Linear Inverse Problems

TDEM is a non-linear inversion problem meaning that the forward operator $\mathbf{f}(\mathbf{p})$ has a non-linear dependency on \mathbf{p} . The problem is linearised by calculating the first order Taylor expansion for small model perturbations $\delta\mathbf{p}$ around a starting model \mathbf{p}_0 , where $\mathbf{f}(\mathbf{p}) = \mathbf{f}(\mathbf{p}_0 + \delta\mathbf{p})$ and

$$\mathbf{f}(\mathbf{p})|_{\mathbf{p}=\mathbf{p}_0} = \mathbf{f}(\mathbf{p}_0) + \mathbf{J}|_{\mathbf{p}=\mathbf{p}_0} \delta\mathbf{p}. \quad (4.3)$$

The matrix $\mathbf{J} \in [N \times M]$ is referred to as the Jacobian matrix with the form

$$J_{ij} = \left. \frac{\partial f_i(\mathbf{p})}{\partial p_j} \right|_{\mathbf{p}=\mathbf{p}_0}. \quad (4.4)$$

By substituting Eq. (4.3) into Eq. (4.1), the following relation is obtained:

$$\Phi_d = [\mathbf{W}\mathbf{d} - \mathbf{W}(\mathbf{f}(\mathbf{p}_0) + \mathbf{J}\delta\mathbf{p})]^T [\mathbf{W}\mathbf{d} - \mathbf{W}(\mathbf{f}(\mathbf{p}_0) + \mathbf{J}\delta\mathbf{p})]. \quad (4.5)$$

This equation is simplified by introducing the data difference vector $\delta\mathbf{d} = \mathbf{d} - \mathbf{f}(\mathbf{p}_0)$. Consequently, Eq. (4.5) is rearranged to

$$\Phi_d = (\delta \mathbf{d} - \mathbf{J}\delta \mathbf{p})^T \mathbf{W}^2 (\delta \mathbf{d} - \mathbf{J}\delta \mathbf{p}), \quad (4.6)$$

with $\mathbf{W}^2 = \mathbf{W}^T \mathbf{W}$. The data cost function Φ_d of Eq. (4.6) is now minimised by calculating the derivative with respect to $\delta \mathbf{p}$ and setting it to zero. This leads to

$$\mathbf{J}^T \mathbf{W}^2 \mathbf{J} \delta \mathbf{p} = \mathbf{J}^T \mathbf{W}^2 \delta \mathbf{d}. \quad (4.7)$$

Rearranging for $\delta \mathbf{p}$ results in the normal equation for an unconstrained least-squares inversion.

$$\delta \mathbf{p} = (\mathbf{J}^T \mathbf{W}^2 \mathbf{J})^{-1} \mathbf{J}^T \mathbf{W}^2 \delta \mathbf{d} \quad (4.8)$$

The model update $\delta \mathbf{p}$ in Eq. (4.8) provides an improvement of the starting model \mathbf{p}_0 . It is generally referred to as the Gauss-Newton or unconstrained least-squares solution. However, because \mathbf{f} is linearised using the first order Taylor expansion by dropping higher order terms, $\Phi_d(\mathbf{p}_0 + \delta \mathbf{p})$ will generally not reach the minimum. Therefore, $\mathbf{p}_1 = \mathbf{p}_0 + \delta \mathbf{p}_0$ is used as an initial guess for the next iteration step and a new model update is calculated according to,

$$\mathbf{p}_{n+1} = \mathbf{p}_n + \delta \mathbf{p}_n \quad (4.9)$$

The model update for the n^{th} iteration step is calculated according to

$$\delta \mathbf{p}_n = (\mathbf{J}_{n-1}^T \mathbf{W}^2 \mathbf{J}_{n-1})^{-1} \mathbf{J}_{n-1}^T \mathbf{W}^2 \delta \mathbf{d}_{n-1}, \quad (4.10)$$

where $\mathbf{J}_{n-1} = \mathbf{J}|_{\mathbf{p}=\mathbf{p}_{n-1}}$ and $\delta \mathbf{d}_{n-1} = \mathbf{d} - \mathbf{f}(\mathbf{p}_{n-1})$.

The model updates reduce the cost function so that $\Phi_d(\mathbf{p}_{n+1}) < \Phi_d(\mathbf{p}_n)$. This iterative process is repeated until a truncation criterion, i.e. maximum number of iterations, or acceptable error threshold is reached. This procedure is generally described as the Gauss Newton (GN) scheme.

The drawback of this procedure is the requirement of a sufficient starting model to reach the global minimum. Also, in case $\mathbf{J}^T \mathbf{W}^2 \mathbf{J}$ is singular or nearly singular, the solution fails, or the update may overshoot the linear range due to instability of the solution (*Meju, 1994*). The model update vector $\delta \mathbf{p}$ will have huge entries leading to solutions which are far away from the initial guess. The first order Taylor-expansion is no longer valid, thus making it a diverging solution (*Scholl, 2005*). Consequently, regulations are generally introduced to limit the step size and counteract the possible divergence of the solution.

4.2.1 Data and Model Parameter Transformation

The approximation in Eq. (4.3) is only good when changes in the model response are dependent linearly on \mathbf{p} (*Scholl and Edwards, 2007*). This is only valid for small perturbations of the model parameter vector. To increase the linearity of the

problem, both \mathbf{f} and \mathbf{p} are transformed either logarithmically (if no sign-reversals are expected) or transformed using the area sine hyperbolic (arsinh) transform, in order to force the dependency to be closer to linear (*Scholl and Edwards, 2007*). The 1D inversion presented in this thesis uses an arsinh-transform on the data vectors, defined as:

$$f_i \rightarrow \tilde{f}_i = \operatorname{arsinh}(f_i/s) = \ln(f_i/s + \sqrt{(f_i/s)^2 + 1}). \quad (4.11)$$

The transform behaves in a logarithmic manner if f_i is much larger than the scaling parameter s or much smaller than $-s$. The scaling parameter is set to 1% of the maximal absolute value of the transient \mathbf{f} (*Scholl and Edwards, 2007*).

The model parameter vector is simply transformed using the natural logarithm, as all model parameters are defined as positive quantities:

$$p_j \rightarrow \tilde{p}_j = \log(p_j). \quad (4.12)$$

The transformation of the model and data vectors will generally lead to a faster convergence of the solution (*Meju, 1994*) and have a higher inversion stability (*Petry, 1987*). The data/model parameter transformation require an adjustment of the Jacobian matrix. Following *Scholl and Edwards (2007)*, the entries of the arsinh-transformed Jacobian are calculated as

$$\tilde{J}_{ij} = \frac{\partial \tilde{f}_i}{\partial \log p_j} = \left(\frac{\partial \log p_j}{\partial p_j} \right)^{-1} \frac{\partial \tilde{f}_i}{\partial f_i} \frac{\partial f_i}{\partial p_j} = \frac{p_j}{\sqrt{f_i^2 + s^2}} \frac{\partial f_i}{\partial p_j}, \quad (4.13)$$

for $i = 1, \dots, N$ and $j = 1, \dots, M$.

The calculation of the data misfit is adjusted for inversion using transformed data/model parameters. This is described in the following section.

4.2.2 Data Fit

The quantity that describes the fit between measured and calculated data is generally described by either the χ -error, or the Root Mean Square (RMS). As confusion may arise concerning the definition of either, the following interpretation will confine to a data fit using the χ -error. Using Eq. (4.1), the fit is calculated for the data cost function Φ_d , where

$$\chi = \sqrt{\frac{\Phi_d}{N}} = \sqrt{\frac{1}{N} \sum_{i=1}^N (d_i - f_i(\mathbf{p}))^2 \cdot W_{ii}^2}. \quad (4.14)$$

W_{ii} are the diagonal entries of a weighting matrix. In the simplest case, these entries are the reciprocal values of the data error estimates. Generally, an optimal fit is reached if $\chi = 1$. In this case, the χ -error states that the measured data is fitted within the estimated error bounds. A fit of less than one implies over-fitted data, or

an over-estimation of the data errors. However, as Eq. (4.14) averages over all data points of the transient, a value of $\chi \leq 1$ may also be reached if some data points are over fitted, whereas others are under fitted. Therefore, the inversion results presented in the extent of this thesis will also include the residual error (ϵ), defined as

$$\epsilon_i = \frac{d_i^{calc} - d_i^{meas}}{\Delta d_i^{meas}}. \quad (4.15)$$

The residual error is calculated at each time sample. It is meant to display the data fit as a function of time. The interpreter can observe if the transient is sufficiently fitted, or rather irregularly fitted.

One aspect that has to be considered for transformed data/model parameter vectors are the adjustments to the weighting matrix in order to maintain the criterion of an ideal fitting equalling $\chi = 1$. *Scholl* (2001) shows explicitly how this is done for a log transformation. An arsinh-transform is slightly different. The entries of the weighting matrix for an arbitrary data transform are expressed as

$$W_{ii} = \frac{1}{\Delta d_i} \left(\frac{\partial \tilde{d}_i}{\partial d_i} \right)^{-1}, \quad (4.16)$$

where an arsinh-transformation has the relation

$$\left(\frac{\partial \tilde{d}_i}{\partial d_i} \right) = \frac{1}{\sqrt{d_i^2 + s^2}} \Rightarrow W_{ii} = \frac{\sqrt{d_i^2 + s^2}}{\Delta d_i}. \quad (4.17)$$

Provided $s \ll |d_i|$, the diagonal elements of the weighting matrix contain the reciprocal values of the relative data errors, which coincides with a logarithmic data transformation. The data fit of transformed data/parameters is calculated according to Eq. (4.14), where $d_i \rightarrow \tilde{d}_i$ and $f_i(\mathbf{p}) \rightarrow \tilde{f}_i(\mathbf{p})$.

A data transformation is conducted for 1D inversion, but neglected in the 2D modelling study presented in Chapter 9. No data transformation was necessary, as the best fit models are obtained through a brute-force modelling approach. The data fit is therefore calculated according to Eq. (4.14), where the weighting matrix contains the reciprocal values of the error estimates.

4.3 Marquardt Inversion

The Marquardt-Levenberg method, also called damped least squares inversion is based on the concept of *Levenberg* (1944) and was enhanced by *Marquardt* (1963). The algorithm is applied for inversion problems with a distinct number of layers, where both layer resistivity and thickness are accounted for in the inversion. Compared to the Gauss-Newton method, an additional constraint is introduced that limits the variation of $\delta \mathbf{p}$. The constraint increases the numerical stability of the inversion

and reduces the influence of unimportant or irrelevant model parameters. Following *Strack* (1992), the normal Eq. (4.10) is modified to

$$\delta \mathbf{p}_n = (\mathbf{J}_{n-1}^T \mathbf{W}^2 \mathbf{J}_{n-1} + K^2 \mathbf{I})^{-1} \mathbf{J}_{n-1}^T \mathbf{W}^2 \delta \mathbf{d}_{n-1}, \quad (4.18)$$

where \mathbf{I} is the identity matrix and K^2 the damping factor. The additional term limits the length of the model update vector depending on the value of K^2 .

Equation (4.18) is often calculated using Singular Value Decomposition (SVD) introduced by *Lanczos* (1964). He shows that any $N \times M$ -matrix \mathbf{A} can be split up using SVD as

$$\mathbf{A} = \mathbf{U} \mathbf{S} \mathbf{V}^T. \quad (4.19)$$

The orthogonal matrix $\mathbf{U} \in \mathbb{R}^{N \times N}$ consists of eigenvectors that span the data space. The columns of \mathbf{U} contain the individual eigenvectors of $\mathbf{A} \mathbf{A}^T$. The orthogonal matrix $\mathbf{V} \in \mathbb{R}^{M \times M}$ spans the model space and consists of the eigenvectors from the matrix $\mathbf{A}^T \mathbf{A}$. This matrix can be used to investigate the model parameter resolution. The matrix $\mathbf{S} \in \mathbb{R}^{N \times M}$ is a diagonal eigenvalue matrix. The diagonal elements S_{ii} contain the non-negative roots of the eigenvalues of $\mathbf{A}^T \mathbf{A}$ and are called singular values. These are arranged in decreasing order (*Menke*, 1984). If matrix \mathbf{A} of $\text{rank}(\mathbf{A}) = p \leq \min(M, N)$, then p number of non-zero singular values exist. For the majority of 1D EM inversion problems, the decomposition of \mathbf{A} is reduced to $\mathbf{U} \mathbf{S} \mathbf{V}^T = \mathbf{U}_p \mathbf{S}_p \mathbf{V}_p^T$ where $\mathbf{U} \in \mathbb{R}^{N \times p}$, $\mathbf{S} \in \mathbb{R}^{p \times p}$ and $\mathbf{V} \in \mathbb{R}^{p \times p}$. Due to simplicity, the terminology will remain \mathbf{U} , \mathbf{S} and \mathbf{V} , although the non-zero matrices are meant.

The SVD is applied to the weighted Jacobian defined as $\mathbf{J}_w = \mathbf{W} \mathbf{J}$. Equation (4.18) can be expressed in terms of SVD as (*Lines and Treitel*, 1984)

$$\begin{aligned} \delta \mathbf{p}_n &= \mathbf{V} \underbrace{(\mathbf{S}^2 + K^2 \mathbf{I})^{-1} \mathbf{S}^T \mathbf{S} \mathbf{S}^{-1} \mathbf{U}^T \mathbf{W}}_{\mathbf{T}} \delta \mathbf{d}_{n-1} \\ &= \mathbf{V} \mathbf{T} \mathbf{S}^{-1} \mathbf{U}^T \mathbf{W} \delta \mathbf{d}_{n-1}, \end{aligned} \quad (4.20)$$

with the diagonal damping matrix \mathbf{T} , that has the values

$$T_{ii} = \frac{S_{ii}^2}{S_{ii}^2 + K^2}, \quad (4.21)$$

or, if the values are normed by the maximal singular value S_{11}

$$T_{ii} = \frac{\lambda_i^2}{\lambda_i^2 + \nu^2}, \quad (4.22)$$

with $\nu = K/S_{11}$ is a relative singular value threshold (RSVT) and $\lambda_i = S_{ii}/S_{11}$. Parameter combinations with singular values smaller than ν are less important for the data fitting (*Hoerdt et al.*, 1992). The value of ν is generally set to 0.1 to begin the inversion process and is decreased in the inversion process to allow less important

parameter combinations to become relevant. According to *Hoerdt et al.* (1992) and *Jupp and Vozoff* (1975a), the smallest allowed value of ν should equal the mean noise floor of the data. A threshold of $\nu^2 = 0$ results in the Gauss-Newton method explained previously. For $\nu^2 > 0$, the Lagrange factor counteracts a divergence of the solution as the additional value in the denominator prevents a division by values close to zero. If the algorithm fails to find a better model, one can increase the size of ν resulting in a decrease of step-size (*Scholl*, 2005). In-turn, a model update can be found. However, model improvements may become too small to be regarded as relevant.

Jupp and Vozoff (1975a) define a class of inversion procedures by setting

$$T_{ii} = \frac{\lambda_i^{2C}}{\lambda_i^{2C} + \nu^{2C}}. \quad (4.23)$$

For LOTEM, the inversion is termed Marquardt-Levenberg method of second order, meaning a value of $C = 2$ is commonly used (*Strack*, 1992).

A clear drawback of the Marquardt inversion scheme is the dependency on the initial model (*Petry*, 1987). The algorithm will tend to find a local minimum for an arbitrarily chosen starting model. A sufficient initial guess of the model parameters including the number of true layers is required.

4.3.1 Eigenvalue Analysis

As stated in Eq. (4.3), small variations in the model parameter vector $\delta\mathbf{p}$ are related to changes in the data $\delta\mathbf{f}$ by the first term of the Taylor expansion as

$$\delta\mathbf{f} = \mathbf{J}\delta\mathbf{p}. \quad (4.24)$$

By applying SVD on the Jacobian matrix \mathbf{J} , one can show that the importance of each eigenvalue parameter (EV_{par}) is determined by the value of the corresponding singular value contained in \mathbf{S} (*Hölz et al.*, 2015). Hence, Eq. (4.24) can be rewritten as,

$$\mathbf{U}^T \delta\mathbf{f} = \mathbf{S}\mathbf{V}^T \delta\mathbf{p}. \quad (4.25)$$

The \mathbf{V} -matrix contains the so-called eigenparameters (EPs), with which an analysis of original parameter combinations can be resolved by the data, is realised (*Scholl and Edwards*, 2007). Additionally, *Edwards* (1997) shows that each eigenparameter (EP) can be expressed as stated above provided each datum f_i has an independent error estimate e_i of unity. Following *Edwards* (1997), the EP standard error $\Delta(EV_{par})$ is computed by calculating the reciprocal of the corresponding eigenvalue.

$$\Delta(EV_{par}) = \mathbf{S}^{-1} \quad (4.26)$$

Additionally, a coarse upper bound of the standard error Δ_{max} of the original pa-

parameter p_j can be computed using the entries of the \mathbf{V} -matrix and the corresponding eigenvalues as

$$\Delta_{max}(p_j) = \sum_{k=1}^M \left| \frac{V_{jk}}{S_{kk}} \right|. \quad (4.27)$$

The theory of the error calculation in a model parameter is only valid for linear changes. Consequently, Δ_{max} needs to be smaller than unity. Is the standard error of the coarse upper bound predicted to be larger than unity, a nonlinear technique has to be adopted to find the correct error bound. In this case, the value of Δ_{max} will determine if a parameter is resolved by the data in the scope of the linearised analysis.

When interpreting the resolution characteristics of measured or calculated data, the following convention is often used. The entries of the \mathbf{V} -matrix are displayed as circles with radii proportional to the weight. Positive values are illustrated as solid black circles, whereas negative weights are displayed by white circles. The fractional standard error of each eigenparameter $\Delta(EV_{par})$ is displayed along the bottom of each image and is reference for the relevance of each EP. The coarse upper bound Δ_{max} is displayed for each row of the \mathbf{V} -matrix and gives insight if an original model parameter is resolved or not. Further explanations regarding the model parameter resolution are given in the corresponding sections.

4.3.2 Importances

A further approach to analyse the resolution of a specific model parameter is to use the so-called model parameter importances. Through the transformation of \mathbf{T} using

$$\mathbf{R} = \mathbf{VT}, \quad (4.28)$$

a diagonal matrix \mathbf{R} is derived containing the damping factors of the original parameters (*Hoerdt et al.*, 1992; *Strack*, 1992). These are generally referred to as the importances where

$$\text{Imp}_i = R_{ii} \quad \text{with } 0 \leq \text{Imp}_i \leq 1. \quad (4.29)$$

A model parameter has a large influence on the data fit if the importance is close to one. Smaller values indicate a smaller influence of the corresponding model parameter on the data fit. For the sake of quantification, the suggested approach of *Lippert* (2015) is followed. A model parameter is well resolved for importances between 0.71 and 1, moderately resolved for importances of 0.5 to 0.7 or poorly resolved for importances smaller than 0.5.

4.3.3 Equivalent Models using Monte-Carlo

Two models are said to be equivalent if their response is identical within a certain error bound (*Spies and Frischknecht, 1991*). For grounded-dipole systems, the radial electric field is strongly dependent on the transverse resistance ($\rho \cdot d$) of a K-type section (intermediate resistive layer). This may result in many different model parameter combinations achieving similar data fitting. Also, poorly resolved parameters that are not supported by the data may increase the equivalence.

Often an uncertainty remains about the recovered electrical conductivity model. To counteract this uncertainty, several so-called global algorithms are applied that try to find a global minimum of the misfit or sample the complete probability distribution. One popular method is the Markov-Chain Monte Carlo scheme that has been applied on time-domain marine CSEM data (*Gehrmann, 2014*). The inversion approach is based on a Metropolis-Hastings algorithm that samples the probability distribution by a random walk through the model parameter space. The probability density is obtained through an ensemble of accepted models. This approach has been developed for CED and DED data, but is not presented in the scope of this thesis due to inefficiencies in runtime. Future applications of this software are desirable to investigate the equivalence domain in a more sophisticated manner.

Alternatively, equivalent models are calculated based on the hybrid Marquardt Monte-Carlo inversion scheme presented by *Scholl (2005)*. Model parameters of a preliminary resistivity model or best fit Marquardt inversion model are perturbed randomly by a certain percentage value. If the data fit is within an acceptable range, the model is accepted. If not, a Marquardt inversion is performed using the perturbed model and the steps are repeated.

The result of the hybrid Marquardt Monte-Carlo inversion is an ensemble of accepted models. If these models exhibit large variations within a certain model parameter, it is perceived as poorly resolved. In the reversed case, where only small variations are visible within the equivalent models, the corresponding model parameter is well resolved. The equivalent models calculated at each station are displayed with the individual inversion results that are mainly found in Appendix B.

4.4 Occam Inversion

Due to the strong dependency of the Marquardt inversion towards the initial guess, a further inversion algorithm is generally applied prior to the Marquardt inversion. This inversion scheme is referred to as Occam inversion, which was first introduced for EM by *Constable et al. (1987)*. The concept is based on finding the smoothest model that fits the data within a reasonable tolerance. The features of the model depart from the simplest case only if it is necessary to fit the data.

Typically the subsurface is divided into a large number of layers (≥ 15) with fixed thickness values. The model vector \mathbf{p}^* is only dependent on the resistivity values of the individual layers $\mathbf{p}^* = (\rho_1, \dots, \rho_k)^T$, but remains independent of the layer thickness. A homogeneous half-space is commonly chosen as an initial model, as the

inversion algorithm will only introduce resistivity contrasts if they are necessary to explain the data. The model update $\delta\mathbf{p}_n^*$ is then expressed as

$$\delta\mathbf{p}_n^* = (\mathbf{J}_{n-1}^T \mathbf{W}^2 \mathbf{J}_{n-1} + \lambda \mathbf{P}^T \mathbf{P})^{-1} (\mathbf{J}_{n-1}^T \mathbf{W}^2 \delta\mathbf{d}_{n-1} - \lambda \mathbf{P}^T \mathbf{P} \mathbf{p}_{n-1}^*), \quad (4.30)$$

where $\mathbf{P} = \mathbf{R}$ or $\mathbf{P} = \mathbf{R}^2$ are the two separate roughness constraints R_1 and R_2 . These constraints are defined as either the first, or second order derivative of \mathbf{p}^* with respect to depth (*Constable et al.*, 1987). In terms of matrix operations, the constraints \mathbf{R}_1 and \mathbf{R}_2 are calculated as

$$\mathbf{R}_1 = \mathbf{p}^{*T} \mathbf{R}^T \mathbf{R} \mathbf{p}^*, \quad (4.31)$$

and

$$\mathbf{R}_2 = \mathbf{p}^{*T} (\mathbf{R}^2)^T \mathbf{R}^2 \mathbf{p}^*. \quad (4.32)$$

Where $\mathbf{R} \in [K \times K]$ has the form

$$\mathbf{R} = \begin{bmatrix} 0 & 0 & 0 & \dots & 0 & 0 \\ -1 & 1 & 0 & \dots & 0 & 0 \\ 0 & -1 & 1 & \dots & 0 & 0 \\ \vdots & & \ddots & \ddots & & \vdots \\ 0 & 0 & 0 & \dots & -1 & 1 \end{bmatrix}. \quad (4.33)$$

When applying roughness R_1 , the resulting model is generally very smooth. Accordingly, the resistivity contrast between neighbouring layers will be small. For roughness R_2 , the resistivity contrast is uniform, meaning that the curvature will be small. In both cases, sudden resistivity jumps are punished by the constraints. They will also suppress layers that have a large resistivity contrast, but a small thickness compared to the surrounding layers.

An approximate depth of investigation is where the inversion models of roughness R_1 and roughness R_2 drift apart. The R_1 constraint will force the model to converge to one resistivity, whereas the R_2 constraint will compel the curvature to a specific value, causing the model to steadily increase/decrease. Therefore, at a depth where the data has no more influence on the model, the estimated resistivity profiles based on R_1 and R_2 will drift apart.

The Lagrange factor λ is interpreted as a smoothing parameter (*Constable et al.*, 1987) that controls the influence of the Occam constraints. Is λ large, the roughness will decrease and a very smooth model is expected. Conversely, if $\lambda \rightarrow 0$, the roughness term is hardly important in the minimisation problem. The model will fit the data without considering the roughness constraints. In the program **MARTIN**, the size of λ between consecutive iterations is controlled by a multiplier $c \in [0, 1]$.

At the start of the inversion, λ is an arbitrary high value defined by the interpreter. At every iteration, the inversion routine searches for a λ which minimizes the misfit

(*Constable et al.*, 1987). A large damping is required at the early stage of the inversion. As the inversion advances, less smoothing is needed (*Jupp and Vozoff*, 1975a) and thus, the values of λ decrease. *Farquharson and Oldenburg* (2004) propose to limit the decrease of λ between iterations to counteract the development of additional structure in the model. *Scholl* (2005) implemented this idea into **Emuplus** and **MARTIN**. If λ_n was set to $c\lambda_{n-1}$, and the resulting model would meet the chosen convergence criteria, then c is halved. *Farquharson and Oldenburg* (2004) recommend a value of $c \in [0.01, 0.5]$ for Occam's inversion.

4.5 Calibration Factor

A calibration factor (CF) is often applied in order to fit the measured data. The CF is treated as a scalar, time-independent inversion parameter with which the calculated data is multiplied. Hence, the form of the transient does not change in the double-logarithmic representation. *Hördt* (1989) and *Hördt and Scholl* (2004) show that shallow geological three-dimensional structures underneath the receivers may distort the measured LOTEM signal. Lateral inhomogeneities may cause current channeling that also rectify the application of a CF in inversion. These shallow structures result in a shift of the whole transient to a higher or lower voltage. However, *Hördt and Scholl* (2004) state this is often only valid within a certain time range of the transient. Receiver misalignment, improper definition of gain, receiver area, topography, current, offsets, etc. are often also accounted for using a CF (*Strack*, 1992).

Newman (1989) concludes that this scaling allows for acceptable fits to the measured data and an accurate interpretation of the deeper geological sections. Generally, it is desirable to fit the data with a CF of close to one as the measured transient is then solely represented by the model parameters of the subsurface. The CF is either treated as a free inversion parameter or fixed. In case of the former, the CF is transformed logarithmically. If the parameter vector is displayed as $\mathbf{p} = (\log \rho, \log \mathbf{d}, \log CF)$, a smooth model with $CF = 1$ satisfies the requirement $\partial \mathbf{p} = 0$ (*Kalscheuer*, 2004). Therefore, it is desirable to fit the data with a calibration factor close to 1, so that the data is solely explained by the model parameters: layer resistivity ρ_i and layer thickness d_i .

1D Modelling Studies

Marine EM methods are often applied to detect resistive formations, e.g. hydrocarbon reservoirs embedded in conductive background sediments (*Eidesmo et al.*, 2002). Although these formations have finite lateral extents, they are often considered as stratified layers with no horizontal boundaries. EM studies in deep-sea environments (water depths of 1000 m or more) commonly apply the FD-CSEM method, as it is effective and well developed. However, the method lacks efficiency in shallow water (water depths of 100 m - 300 m), primarily due to the signature of the air-sea interface. This so-called airwave signature dominates the signal at large offsets, resulting in limited sensitivity towards the sub-seafloor resistivity structure (*Connell and Key*, 2013). As an alternative, shallow sea EM applications are usually conducted in the time-domain, where the airwave effect is less relevant (*Weiss*, 2007). For example, a marine LOTEM application conducted in very shallow water (water depths of 50 m or less) is found in *Lippert* (2015). In the following chapter, the time-domain DED and CED methods are examined for shallow sea applications using 1D modelling studies.

To begin, the detectability characteristics of DED and CED for a sub-seafloor aquifer model are presented and compared to standard in-line TD-CSEM. In the following, TD-CSEM will be referred to as marine LOTEM or just LOTEM following the convention at the IGM Cologne. As the step-on/off signals exhibit different detectability characteristics in shallow sea environments, the study is repeated for greater water depths prior to investigating the influence of the airwave. Subsequently, the model parameter resolution is studied and compared using SVD-analysis.

The second part of this chapter deals with errors caused by geometrical distortions of the CED and the DED transmitter antennas. It is known, that CED measurements are susceptible towards symmetry distortions (*Haroon et al.*, 2016). To quantify these errors for the investigated resistivity model in Israel, a 1D forward algorithm is developed that takes the transmitter distortions into account. Two different geometrical inaccuracies of the transmitter system are simulated. First, the effect generally referred to as non-verticality is studied. This effect is especially prominent in the application of VED's (*Goldman et al.*, 2015). Therefore, a comparison between CED, DED and VED is made. Second, errors for geometrically distorted CED and DED transmitters are studied and analysed. The obtained results show that CED is not applicable at the present time with the intended short-offset configuration due to the strong susceptibility towards these geometrical distortions.

5.1 Background EM Noise Model

The limiting factor of any EM survey is the background electromagnetic noise. Quantifying the EM noise and the typical nature of the noise is crucial when assessing theoretical modelling studies. The quality of the acquired signal dictates the success of any controlled source EM measurement. In case of poor signal-to-noise ratios (SNR), dipole moment and acquisition times may need to be adjusted to improve the data quality. Admittedly, these adjustments are limited by the characteristics of the existing equipment. For example, electrical current amplitudes of several thousand Amperes are not feasible using the available ZT-30 transmitter. Also, transmitter dipoles extending over several kilometres are too laborious to handle during field measurements. Therefore, a decent noise evaluation will indicate if measurements are actually feasible beforehand. This is especially important when applying novel EM prospecting methods for the first time.

For the following modelling studies, the noise model of *Lippert (2015)* is used as a reference. The noise level is estimated from actual measurements conducted in Israel during the 2011 campaign. It should be noted, that new transmitter and receiver instruments were purchased in the extent of this project resulting in better data quality due to larger current amplitudes and faster recording characteristics. Consequently, the reference noise model is considered to be rather pessimistic. It is used in conjunction with the theoretical modelling studies to estimate the SNR of each method. Preliminary estimations about the minimum number of necessary stacks to resolve the freshwater aquifer can also be made.

The SNR of acquired TDEM data is generally improved by repeating single observations at one site. The final transient is obtained using robust stacking methods of many single measurements (*Hanstein, 1996*). The relationship by which the SNR improves is expressed as

$$\frac{s_0}{n_0} = \sqrt{N} \frac{s}{n}, \quad (5.1)$$

where s_0/n_0 is the SNR of a single measurement, s/n the final SNR after stacking and N the total number of single observations.

Current normalised error floors are shown for all relevant modelling studies. These error floors are additionally normalised by either $\sqrt{500}$ or $\sqrt{5000}$, representing 500 and 5000 repetitions of single measurements, respectively. *Munkholm and Auken (1996)* investigated cultural EM noise for TEM measurements and found a \sqrt{t} relationship for Gaussian distributed noise in processed and binned TEM data. However, due to the applied hardware and subsequent data processing scheme of *Lippert (2015)*, no evidence of this time-dependency is noticeable in his marine LOTEM data. Therefore, *Lippert (2015)* suggests a time-independent noise model.¹

Figure 5.1 shows exemplary data from marine LOTEM (*Lippert, 2015*). The markers represent exemplary LOTEM data for a broadside (left) and an in-line configuration

¹Noise measurements conducted in the extent of this project show a time-dependency, but only at late times. This noise model is used in the interpretation of the measured data.

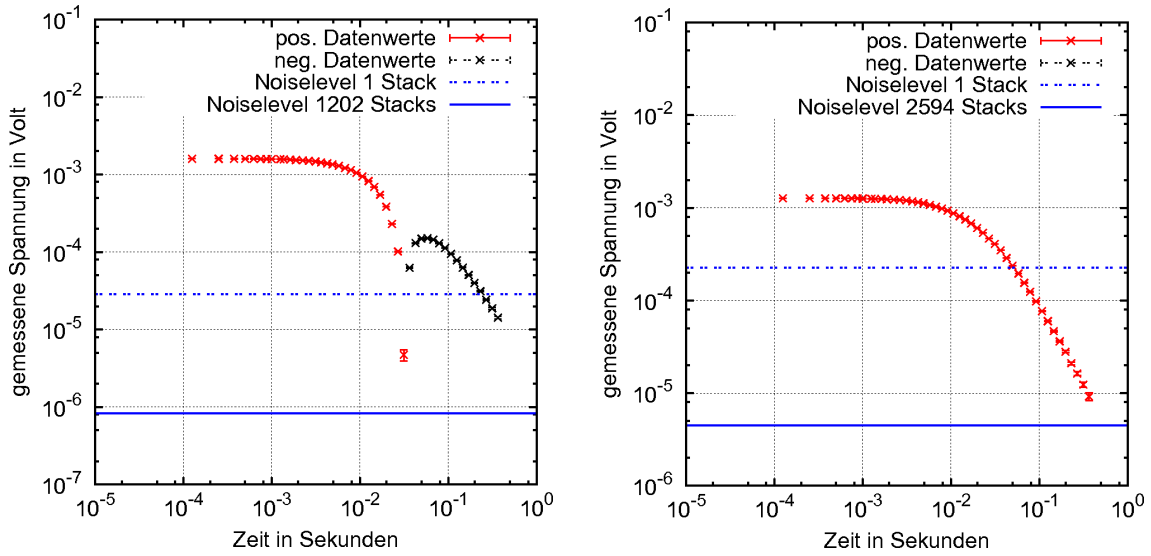


Figure 5.1: Exemplary transients (red and black markers) and the associated noise models (dashed and solid blue line) for measured voltages in the broadside (left) and in-line (right) configuration (Lippert, 2015).

(right). The solid blue represents the error floor after stacking, the dashed blue line the error floor for a single measurement derived from Lippert (2015). Note, measured voltages are displayed, which are normalised by the receiver length to obtain the electric fields. The average current normalised noise floor of the displayed transients is between $3 \cdot 10^{-7}$ V/m and $2 \cdot 10^{-6}$ V/m for a single observation, depending on the location and day of measurement. The applied reference noise model assumes the worst case scenario with a noise floor of $s_0/n_0 = 10^{-6}$ V/m.

5.2 Layered Aquifer

In the following modelling study, the resistive freshwater aquifer is assumed to be a horizontal layer with infinite lateral dimensions, embedded between two conductive layers. Generally, these simplified models are used to investigate the signal characteristics of the applied EM methods. It should be pointed out that one primary aim of a CED and DED application in Israel is to obtain information regarding the multi-dimensional transition zone at the western aquifer boundary. Therefore, the following theoretical studies may seem only partly relevant for the actual application. However, they are by no means redundant, as they are used to investigate different signal characteristics of the excited EM field, e.g. detectability, SNR, resolution, geometric errors, etc. Furthermore, DED and CED are both not commonly applied in the marine environment. Therefore, little is known regarding their signal characteristics. Accordingly, the 1D modelling studies are essential to study the characteristics in transient behaviour for CED and DED transmitters, especially in comparison to the conventional LOTEM application.

To conduct this study, a mean subsurface resistivity model is derived from the

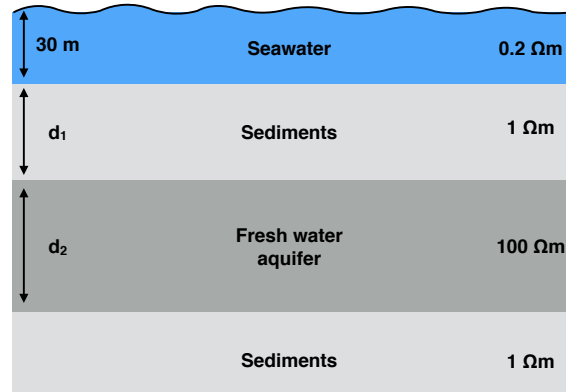


Figure 5.2: Layered earth model applied for the subsequent 1D modelling studies. A resistive aquifer of 100 Ωm and thickness d_2 is embedded in marine sediments of 1 Ωm at a depth of d_1 . Transmitter and receiver are located on the seafloor.

1D inversion results of the marine LOTEM data (Lippert, 2015). Unless stated otherwise, a water depth (d_w) of 30 m is used for all modelling studies. Both, transmitter and electric field receiver are located on the seafloor at an offset of 580 m, corresponding to one of the applied offset during the field measurements. The resistive sub-seafloor freshwater aquifer with a constant resistivity of 100 Ωm is embedded in marine sediments of 1 Ωm. In the first study, the depth and thickness of the aquifer are varied. If not specified otherwise, the aquifer is considered to be 100 m thick, embedded at a depth of 70 m beneath the seafloor.

The forward modelling studies are conducted for step-on and step-off current excitations. The modelling studies assess which current signal is more suitable in terms of SNR, detectability (Section 5.2.1) and resolution towards the freshwater aquifer. Moreover, a joint interpretation of both signals has not been conducted in marine EM applications. In Section 5.2.3, SVD-analysis is applied to analyse if a joint interpretation of step-on and step-off signals will offer a more reliable subsurface resistivity model compared to the single interpretation of either.

5.2.1 Detectability of the Aquifer

This first investigation focuses on studying one very basic feature of EM methods called detectability. This feature is often used to theoretically assess if a method is able to distinguish between the signal of a target layer and the signal caused by the background environment. In some cases, the signal caused by the latter is also referred to as geological noise (Goldman *et al.*, 2015). To be more specific: Is the signal of the resistive freshwater aquifer distinguishable from the signal of the conductive marine sediments? If yes, how do alterations in aquifer depth and aquifer thickness change the detectability?

Detectability is simply referred to as the signal of a model including the target layer normalised by the signal of the background model (no target). Thus, some literature also refers to detectability as the normalised response, e.g. Swidinsky *et al.* (2012). In the following, both forms are used to describe the modelled data. Note,

a high normalised response does not necessarily imply a quantitative delineation of the target parameters, i.e. thickness, depth and resistivity. Instead, it merely illustrates if the applied method sufficiently detects the resistive aquifer (*Goldman et al.*, 2015). Further issues that may be relevant when trying to resolve model parameters from actual field data, i.e. SNR, equivalence, etc. are neglected in this very simplistic approach. For a better assessment of the calculated transients, the current normalised noise floor at a certain number of stacks (see Section 5.1) will be displayed in all relevant figures.

In the following, detectability studies are performed in a very general manner using only one transmitter-receiver configuration. Specifically, an offset of 580 m is used for DED and LOTEM, corresponding to the offset applied in the marine DED measurement in Israel. The transmitter lengths of the DED and LOTEM are considered to be 400 m. For clarification, each dipole of the DED transmitter is 200 m in length. On the contrary, marine CED is intended to be a short offset method. Thus, dipole lengths $dl = 9$ m and an offset of 50 m are considered. All displayed signals are current normalised to 1 A. The chosen time range of the study ranges from 10^{-3} s to 10^0 s for DED and LOTEM, and 10^{-5} s to 10^0 s for CED.

A common scheme is used for all figures shown in the detectability study. For example, Fig. 5.3 and Fig. 5.4 show the transients of a switch-off and switch-on excitation for LOTEM, DED and CED in the left, centre and right column, respectively. Beneath each sub-image of the modelled transients, the detectability is plotted with colours and line patterns corresponding to the respective transients displayed in the subfigure directly above. The figures containing the calculated signals in a double-logarithmic representation also show the assumed SNR at 500 and 5000 stacks. These are plotted with black dashed lines and labelled accordingly. For better reference, the normalised response images have a red box that represents a 20% threshold. A sufficient detectability is only achieved if the plotted lines are outside the box for a certain time range. Note, this 20% threshold is subjective and may vary within the literature. In the top row of each figure, the thickness of the aquifer is varied, while its depth remains constant at 70 m beneath the seafloor. The resulting signals are illustrated by purple, green, blue and black transients denoting a 50 m, 100 m, 200 m and infinite, half-space aquifer thickness, respectively. The middle row displays variations of the aquifer depth while the aquifer thickness remains constant at 100 m. These transients are all displayed in the same colour, but with different line patterns. The depth of the aquifer is varied between values of 40 m, 70 m and 100 m displayed by dashed, solid and dotted lines, respectively. The solid line in the second row is identical to the green line of the top row. The bottom row displays the variations of both aquifer depth and thickness, corresponding to the colours and patterns of the top two rows.

Step-Off Signals

Figure 5.3 shows calculated transients of a step-off current excitation for LOTEM (left), DED (centre) and CED (right). The current normalised signal amplitudes of LOTEM are larger compared to the other methods and range from 10^{-6} V/m at

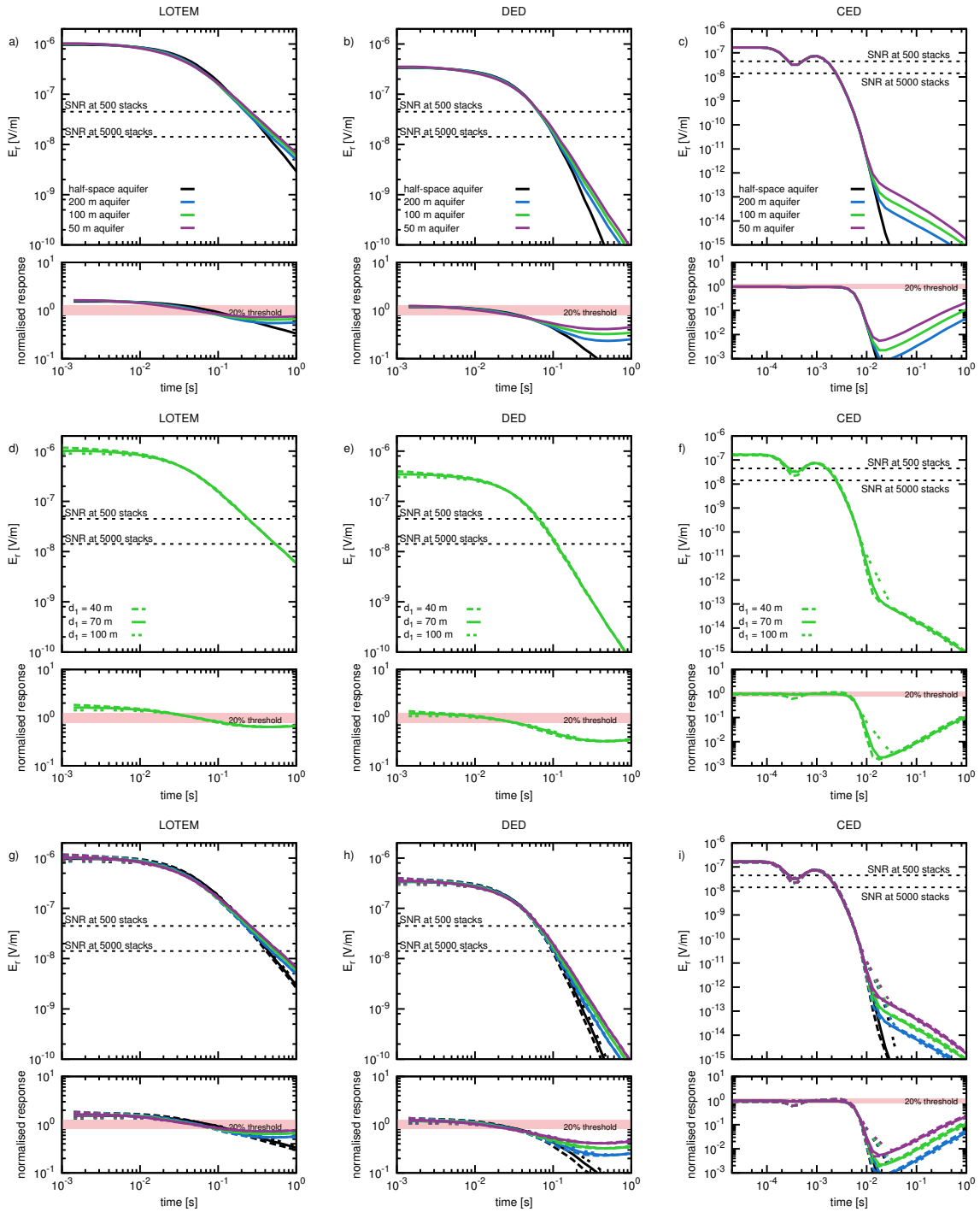


Figure 5.3: Step-off response for the resistivity model displayed in Fig. 5.2 using LOTEM, DED and CED displayed in left, centre and right columns, respectively. In (a) - (c), the thickness of the resistive aquifer is varied, while keeping the depth constant at 70 m beneath the seafloor. In (d) - (f) the depth of the aquifer is varied, while keeping the aquifer thickness constant at 100 m. In (g) - (i), a combination of (a) to (f) is given for each method, respectively. The calculated transient for a given model is displayed in the top subfigures the normalised response underneath.

early times to approximately 10^{-9} V/m at late times. If current amplitudes exceeding 10 A are used, less than 1000 stacks are sufficient to surpass the expected noise floor, even at late times. In comparison, the DED signals displayed in Fig. 5.3b are approximately half an order of magnitude smaller at early times ($t < 1e^{-2}$ s), and almost two orders of magnitude smaller at late times ($t > 1e^{-1}$ s). Consequently, the signal falls below the assumed noise floor at much earlier times and is more difficult to measure. Correspondingly, more single observations are required for DED measurements to achieve the same SNR as LOTEM, provided all other influences remain consistent. The benefit of DED is the improved detectability and, additionally, the dispersiveness of the transients for different aquifer thicknesses. Especially the latter feature is a technical improvement to LOTEM. However, if SNR is also considered, a cost-benefit analysis should essentially be taken into account as additional stacking time is financially expensive. CED is clearly the best method in terms of detectability, but also worst in terms of SNR. Actually, the extremely poor SNR of CED makes an application doubtful. Unless transmitting currents of several thousand Ampere are used, a CED application using a small, mobile transmitter seems unrealistic considering the background noise. In this case it is also questionable if a stable current amplitude and a clean ramp function can be achieved.

Summarising the results of Fig. 5.3a through Fig. 5.3c, it is reasonable to say that all three methods are effective in terms of detecting the resistive freshwater aquifer. The normalised response is outside of the 20% threshold, implying a sufficient response. CED shows the highest detectability compared to the other two methods, especially at late times of the step-off response. The detectability values reach the third order of magnitude making CED incomparable to the other methods. Furthermore, a clear distinction between different aquifer thicknesses is feasible using CED. In comparison, the normalised response of DED and LOTEM behave differently. The DC level dictates the very early times of all step-off signals, but is insensitive towards different aquifer thicknesses. Consequently, all transients containing the resistive aquifer are shifted by the same value to a higher DC-voltage, merely indicating a more resistive subsurface. The transients are practically identical at early times, suggesting that little information regarding the aquifer-thickness is contained in the DC voltages. At intermediate and late times, the signal decay shows dependencies towards different aquifer thicknesses. This is where DED has slight advantages over LOTEM, as the calculated transients disperse more distinctly. Based on this result, one could assume that DED has an improved sensitivity towards the aquifer thickness.

The second row of Fig. 5.3 shows transients for aquifer depth-variations between values of 40 m, 70 m and 100 m. Only CED shows minor variations in transient decay at approximately $t = 10^{-2}$ s. LOTEM and DED are rather insensitive towards the variations in aquifer depth. Surprisingly, the normalised response indicates that each method is indeed capable of detecting the resistive layer, but no apparent response caused by the aquifer depth-variation is noticeable. Consequently, the step-off signals of DED and LOTEM are practically indifferent towards variations of aquifer-depth. This subject is revisited in the subsequent analysis of step-on signals.

The bottom row of Fig. 5.3 illustrates all combinations displayed in the upper two rows. Bundles of same-coloured transients indicate the superior dispersiveness

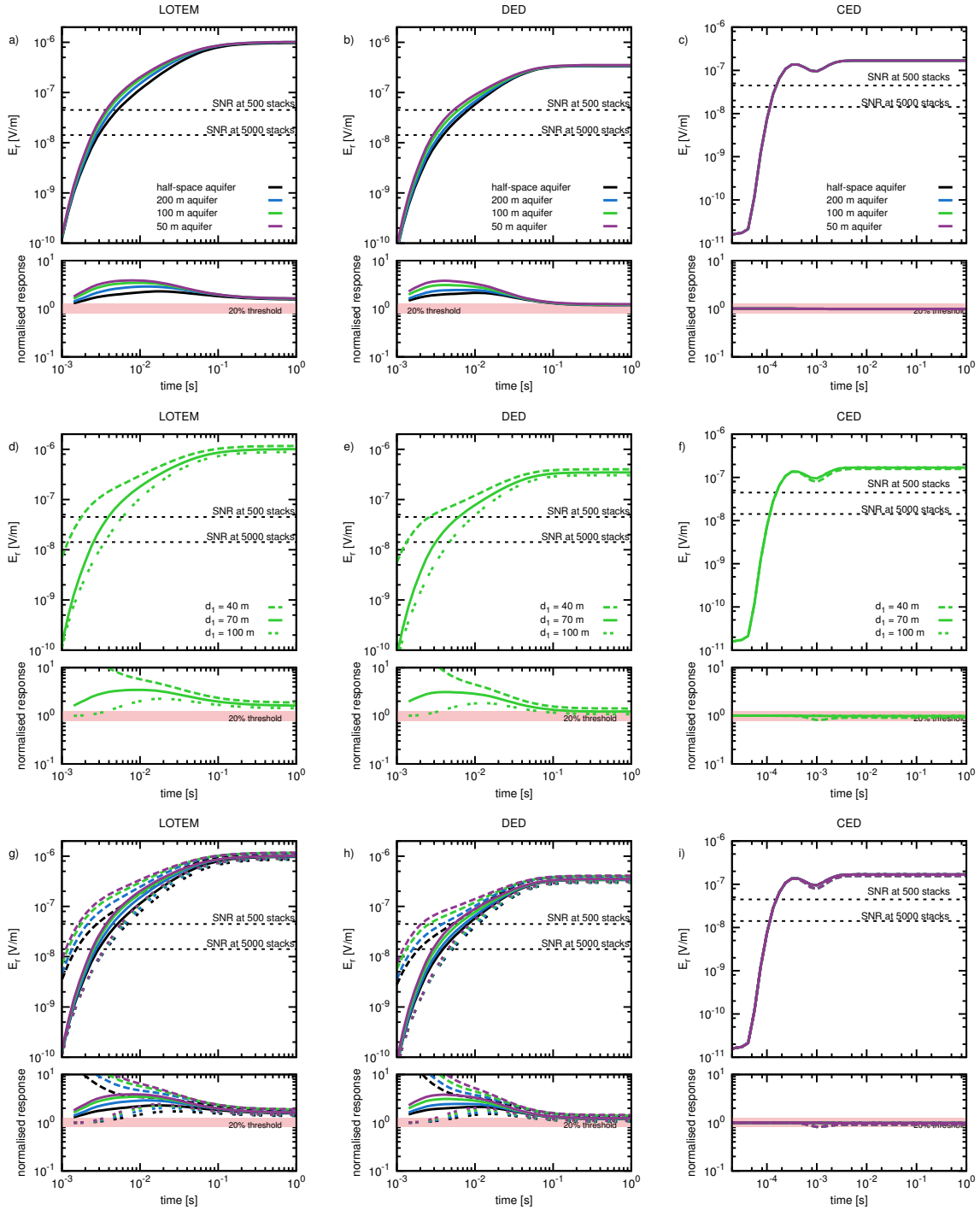


Figure 5.4: Step-on response for the resistivity model displayed in Fig. 5.2 using LOTEM, DED and CED displayed in left, centre and right columns, respectively. In (a) - (c), the thickness of the resistive aquifer is varied, while keeping the depth constant at 70 m beneath the seafloor. In (d) - (f) the depth of the aquifer is varied, while keeping the aquifer thickness constant at 100 m. In (g) - (i), a combination of (a) to (f) is given for each method, respectively. The calculated transient for a given model is displayed in the top subfigures the normalised response underneath.

caused by aquifer thickness variations. In contrast, bundles of transients with the same pattern but different colours would indicate an increased detectability towards the aquifer depth variations. However, this is not the case here.

The results indicate a slight advantage of DED compared to LOTEM in terms of detectability. However, the signal amplitudes of LOTEM surpasses DED and CED by several orders of magnitude. Especially, the applicability of CED is questionable due to the poor SNR at late times.

Step-On Signals

In Fig. 5.4, the detectability study of a sub-seafloor aquifer in the shallow marine environment is repeated for step-on signals. The signals increase with time, depending on the resistivity structure of the subsurface. Compared to the step-off signals displayed in Fig. 5.3, the detectability of each method is different. Conspicuously, the CED method shows absolutely no detectability towards the resistive aquifer (see Fig. 5.4i). Primarily, this is attributed to the DC level that dictates the transient after approximately 5 ms. Due to the intended short-offset CED system, the geometric spreading is too small to detect the resistive aquifer. The aquifer response is smothered by the DC voltage. Larger offsets would considerably improve the normalised response of CED at the expense of the SNR. In comparison, LOTEM and DED exhibit a high detectability towards the resistive aquifer embedded in conductive sediments between 2 ms and approximately 30 ms. The normalised responses of both methods are comparable showing a sufficient detectability and dispersiveness for different aquifer thicknesses. The aquifer footprint of the DED signal seems to arrive several ms before LOTEM, but also ends sooner. Additionally, the signal amplitudes of DED are approximately half an order of magnitude smaller in comparison. However, for step-on signals SNR is less relevant, as the aquifer footprint lies above the required noise floor at 5000 stacks.

The depth-variations of the aquifer (second row of Fig. 5.4) show remarkable results. The step-on signals of LOTEM and DED disperse for different aquifer depths implying a higher detectability of the aquifer depth. This is surprising, keeping in mind that step-off signals showed little dependency towards the aquifer depth. Generally, the step-on signal arrives sooner at the receiver with larger amplitudes for a shallower aquifer. Moreover, the detectability is also larger for shallower targets. This is further analysed in the following.

Preliminary Results to Detectability

Based on these preliminary 1D detectability studies, the following preliminary conclusions can be made:

- For one-dimensional resistivity models in shallow marine environments, the detectability of LOTEM and DED do not differ considerably. The DED application has slight advantages in terms of detectability in the step-off signal. In

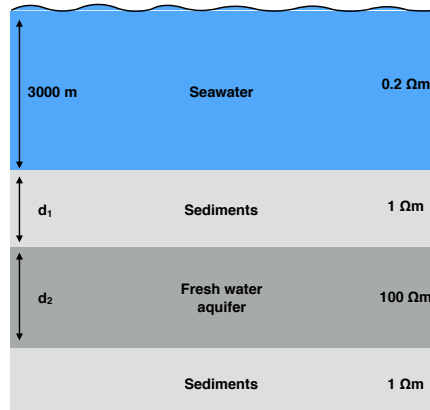


Figure 5.5: Layered earth model applied for 1D detectability studies. A resistive aquifer of 100 Ωm and thickness d_2 is embedded in marine sediments of 1 Ωm at a depth of d_1 . In comparison to Fig. 5.2, the water depth was increased to 3000 m. Transmitter and receiver are located on the seafloor.

turn, LOTEM is comparable in step-on and is additionally superior in terms of SNR.

- The step-on signal of DED and LOTEM is superior to the step-off signal, as both aquifer depth and thickness are detectable. This does not apply to CED, where the step-off signal is clearly better.
- The applicability of CED is hardly justifiable due to the poor SNR for step-off and poor detectability for step-on. Current amplitudes of several thousand Amperes are needed to reach signal amplitudes of $E_r = 10^{-11}$ V/m at late times. For the considered noise model, these amplitudes still lie approximately three orders of magnitude below the SNR at 5000 stacks.

The differences in detectability between step-on and step-off signals are one of the main findings in the preceding studies. It is probable that these differences are related to the influence of the air-sea interface. Accordingly, the study is repeated for the identical resistivity models in water depths of 3000 m, where the air-sea interface has no influence in the considered time range.

Deep-Water Aquifer

The interaction of the EM field at the air-sea interface has a significant contribution to the acquired signal in shallow sea measurements. Moreover, it is likely that this interaction is accountable for the differences in detectability between the current signals. To investigate this influence, the thickness of the water column is increased to 3 km (see Fig. 5.5). The preceding detectability studies are repeated for this altered model and displayed in Fig. 5.6 and Fig. 5.7 for step-off and step-on signals, respectively.

As displayed in Fig. 5.6 and Fig. 5.7, the removal of the airwave has a large influence on the modelled signals. Primarily, the DC level of all transients is considerably

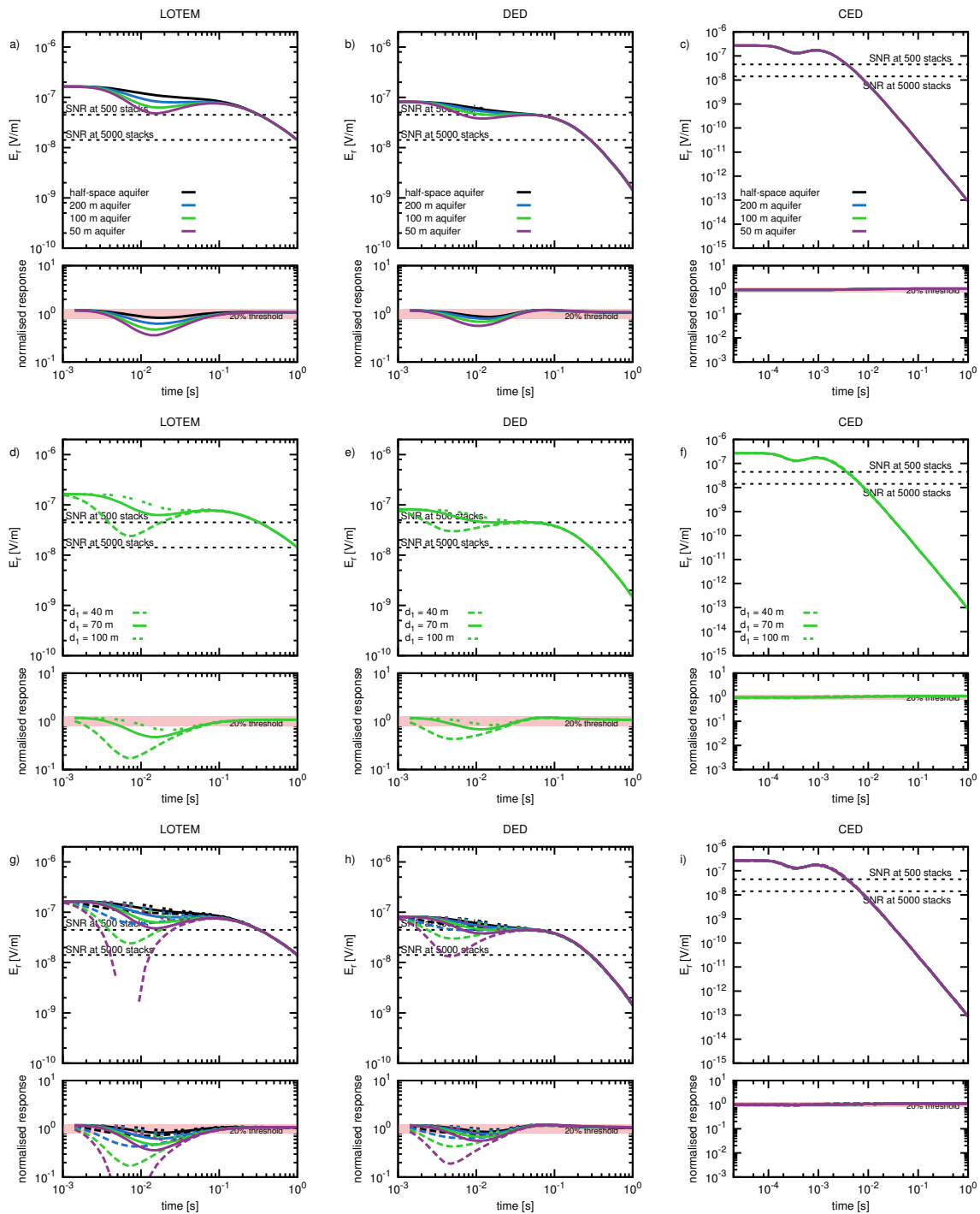


Figure 5.6: Step-off response for the resistivity model displayed in Fig. 5.5 using LOTEM, DED and CED displayed in left, centre and right columns, respectively. In (a) - (c), the thickness of the resistive aquifer is varied, while keeping the depth constant at 70 m beneath the seafloor. In (d) - (f) the depth of the aquifer is varied, while keeping the aquifer thickness constant at 100 m. In (g) - (i), a combination of (a) to (f) is given for each method, respectively. The calculated transient for a given model is displayed in the top subfigures the normalised response underneath.

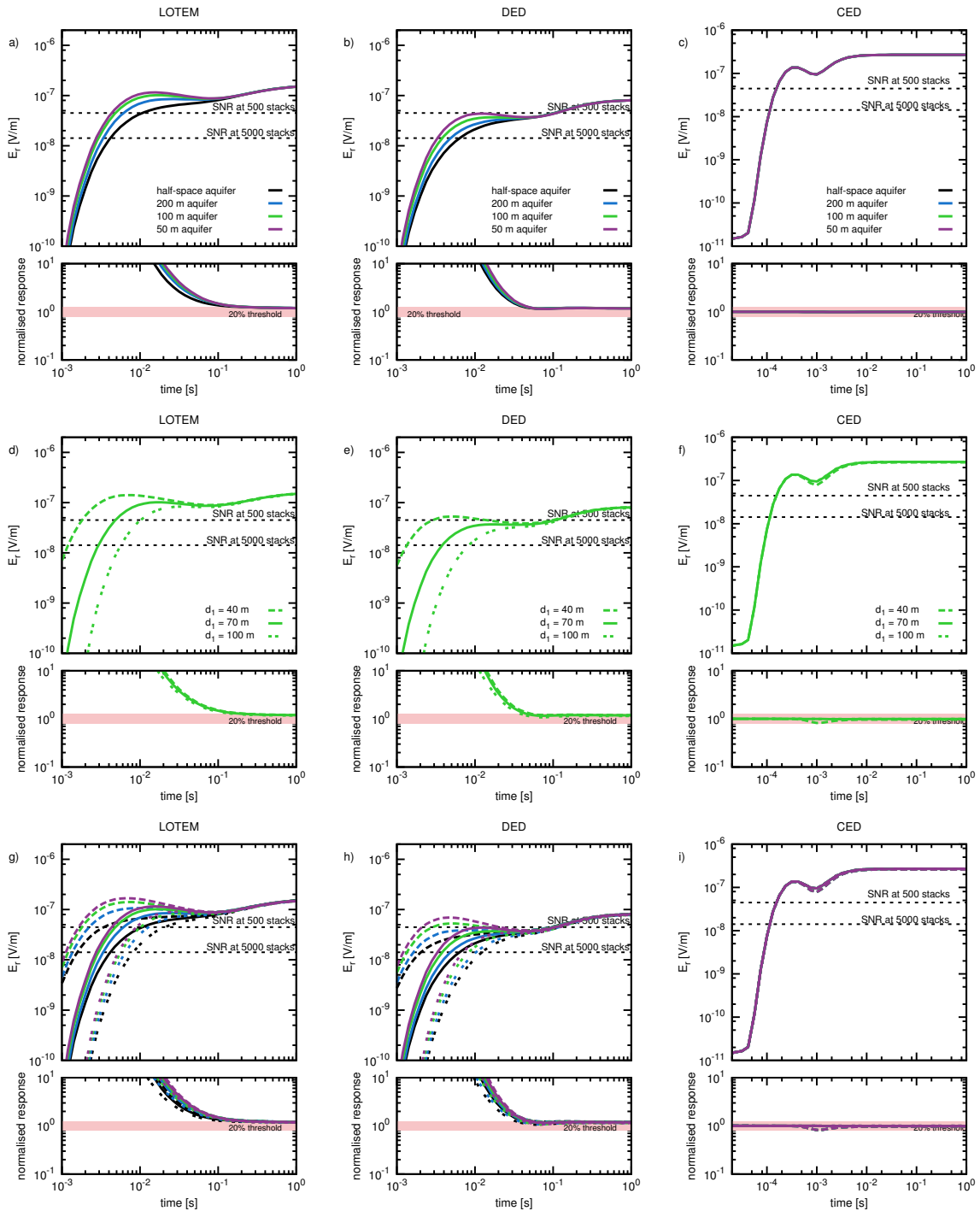


Figure 5.7: Step-on response for the resistivity model displayed in Fig. 5.5 using LOTEM, DED and CED displayed in left, centre and right columns, respectively. In (a) - (c), the thickness of the resistive aquifer is varied, while keeping the depth constant at 70 m beneath the seafloor. In (d) - (f) the depth of the aquifer is varied, while keeping the aquifer thickness constant at 100 m. In (g) - (i), a combination of (a) to (f) is given for each method, respectively. The calculated transient for a given model is displayed in the top subfigures the normalised response underneath.

lower. Furthermore, the aquifer footprint is apparent at the same delay times in the step-on/off signals. This was not the case in the shallow-water model, where the aquifer footprint for the step-off signal was distinct at late-times. Also, LOTEM and DED are sensitive towards both aquifer thickness and aquifer depth in both current step signals. The LOTEM step-off signals of the deep-water model are superior to the other methods in terms of signal amplitude and detectability. In comparison, the CED signal cannot detect the resistive aquifer, which is again attributed the intended short-offset configuration. For larger offsets, the detectability characteristics of CED are improved at the expense of a SNR decrease. Thus, the poor signal amplitudes of CED may still prohibit an application. In case of step-on, the detectability characteristics of LOTEM and DED are nearly identical.

The question arises of why the detectability of step-on/off signals are more alike compared to the shallow-water model. Particularly because a step-on signal can be transformed into a step-off signal through the DC level, independent of the underlying resistivity model. Presumably, the answer is associated to the increased DC voltages, which prohibit the detection of the aquifer depth variations in the shallow marine environment. For the latter case, the signal amplitude of DC is approximately one order of magnitude larger compared to deep water setting. In addition, DC measurements are rather insensitive to variations in model parameters for one transmitter-receiver configuration. Solely, the presence of the resistive aquifer in the subsurface is detectable using DC voltages. Therefore, the aquifer footprint at early times is masked by the DC contribution of the signal.

Discussion on Detectability

Typically, step-on signals are applied during LOTEM measurements due to the advantages in terms of the SNR characteristics. Therefore, step-on signals are also often used in simplified detectability studies. However, step-on signals may also be used in the detectability study although step-off signals are measured, e.g. *Lippert* (2015). Primarily, this is due to sign-reversals that appear in certain configurations of a step-off signal, which may obscure the detectability study. A large normalised response around a sign-reversal does not necessarily indicate a sufficient detectability, but is rather attributed numerical inaccuracies of the code. Yet, the presented study shows that it is advisable to examine both current signals, as they exhibit differences in detectability for different model parameter variations.

The common characteristic of both signals is that they are able to detect the presence of the resistive aquifer. This basic detectability feature is comparable for LOTEM and DED. An application of either method is therefore desirable to investigate the resistive freshwater aquifer. In theory, the CED method shows the highest response towards the resistive layer in the step-off signal, but lacks the necessary SNR to be considered for a potential application. The signals are four to five orders of magnitude below those of LOTEM and DED, making an application rather idealistic at the present time. Consequently, a further interpretation of the CED signals for the freshwater aquifer model is neglected in the extent of this thesis. Additionally, the geometrical error analysis conducted in Section 5.3.2 will show that a marine CED application has further disadvantages compared to the other two methods.

The signals of DED and LOTEM are similar for one-dimensional resistivity models. Slight differences in amplitudes and transient decay are noticeable for both step-on and step-off signals. Generally, the transients of the step-off signal disperse more for DED if the aquifer thickness is varied. For variations in aquifer depth within shallow marine settings, LOTEM and DED step-off transients are similar. However, if the influence of the air-sea interface is removed, the step-off signal of either method is again sensitive towards variations in aquifer depth. In contrast, the step-on signal shows differences in transient behaviour if either thickness and/or depth of the aquifer are varied in both shallow and deep sea environments. In this case, LOTEM and DED are almost identical.

A possible explanation for the differences between shallow- and deep-sea signals is given by the amplitude of the DC voltages that superimposes the step-off signal at early times. At the arrival of the aquifer footprint, the step-off transient is still in the quasi-DC range. Consequently, the aquifer footprint is masked by the DC contribution at early times and no sensitivity towards aquifer depth is noticeable at shallow sea. Surprisingly, the aquifer response is then shifted towards the late times of the step-off transient. Appropriately, these late times are sensitive towards aquifer thickness variations. In contrast, the aquifer footprint is apparent in the step-on signals depending on the depth of the aquifer. At the investigated offset of 580 m, the aquifer response arrives before the signal reaches the DC level. Accordingly, the aquifer footprint is not masked by the latter. In the case of a deep-sea environment, the DC voltages are comparable to the voltages of the aquifer footprint, and as a result, seem to be less relevant. In the following section, the effect of the air-sea interface is studied to substantiate this hypothesis.

The results of the detectability study have a direct impact on the interpretation of the measured data. Presently, one type of transmitter signal is commonly used for interpretation. For example, the interpretation of *Lippert (2015)* is based only on the step-off current signals due to the cleaner step-function of the transmitter signal. *Moghadas et al. (2015)* or *Gehrmann et al. (2015)* present applications where only step-on signals are applied. The presented theoretical study indicates that it may be advisable for future shallow marine EM applications to apply a 50% duty cycle and subsequently use both step-functions in a joint interpretation. This approach will also be further investigated in the extent of this thesis.

5.2.2 Influence of the Sea-Air Interface

The influence of the air-sea interface on the detectability characteristics of a resistive sub-seafloor aquifer are partly investigated in the preceding section. The following study will further address this issue. *Edwards (1997)* proposes to interpret marine TD-CSEM (LOTEM) data by using arrival times that he defines as the first maximum of the differentiated step response. The resulting impulse response gives insights regarding the arrival times of different signal contributions. For example, *Weiss (2007)* applied this approach to decompose the signal of a hydrocarbon model into its basic contributions. For the case presented in this thesis, the field calculated at the receiver (offset of 580 m) will generally have three main contributions. (1)

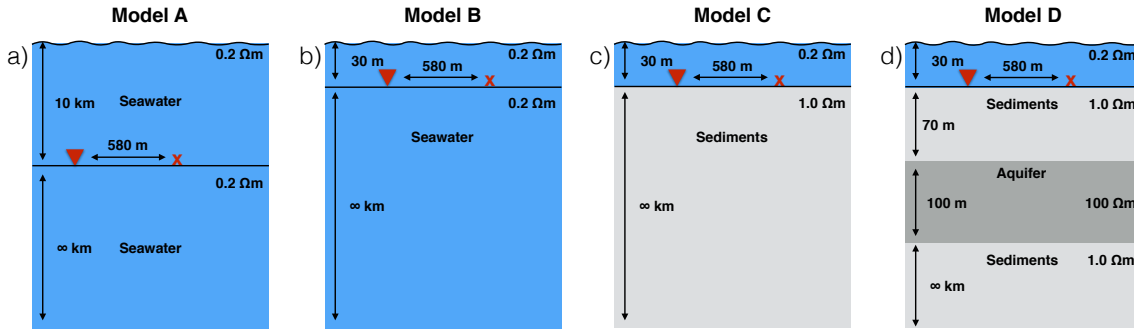


Figure 5.8: Four different 1D resistivity models to investigate the effect of the airwave. (a) a full-space model consisting of a 10 km thick seawater layer above the transmitter and a homogeneous half-space of seawater with 0.2 Ωm . (b) The model consists of a 30 m seawater layer above the transmitter and a homogeneous seawater layer below the transmitter taking the air-sea interface into account. (c) The seawater below the transmitter is replaced by marine sediments of 1 Ωm . (d) The resistive aquifer of 100 Ωm is included in the model to investigate the interaction of the resistive layer mode with the airwave.

The contribution of the direct way through the water and/or sediments. (2) The contribution of the energy traveling upward from the transmitter along the sea-air interface and downward towards the receiver. (3) The contribution of the resistive layer in the subsurface. Thereby, the four models displayed in Fig. 5.8 are used to depict the information of each signal contribution. By differentiating each calculated signal with respect to time, the arrival times of different signal contributions can be assessed. As the signals of LOTEM and DED are similar in terms of detectability, the following study will only take DED signals into account. CED is also neglected, as it is not affected by the airwave.

It should be mentioned, that after differentiating the signal, step-on and step-off signals are equivalent, where

$$\partial_t E_r^{\text{on}} = \underbrace{\partial_t E_r^{\text{DC}}}_{=0} - \partial_t E_r^{\text{off}} = -\partial_t E_r^{\text{off}}. \quad (5.2)$$

Therefore, the conclusions made in the following modelling study apply to both types of current excitations.

Model A, displayed in Fig. 5.8a, consists of a 10 km thick seawater layer above and below the transmitter. The impulse response of will show the arrival time of the energy travelling through the conductive saltwater. Model B also consists of two seawater layers. However, the transmitter and receiver are located 30 m from the sea-surface. Since the energy travelling along the air-sea interface will arrive at much earlier delay-times compared to the energy travelling through the seawater, Model A and Model B are used to obtain the arrival time of the airwave. Model C takes the marine sediments into account. The energy travelling through these sediments arrives at the receiver after the airwave, but ahead of the contribution travelling

through the seawater. Finally, Model D takes the energy travelling through the resistive aquifer into account often referred to as the resistive layer mode *Weidelt* (2007).

The time derivatives of the radial electric fields are displayed in Fig. 5.9a and Fig. 5.9c. Also, the calculated transients are plotted in Fig. 5.9b and Fig. 5.9d for better reference. The transients in the right images are colour coded with their respected impulse response in the left images. The top row shows signals of Models A and B. As mentioned, the response including the air-sea interface (blue) arrives at earlier delay-times. Due to the insulating characteristics of the air, the EM field diffuses practically at the speed of light and is hardly attenuated at the air-sea interface, resulting in earlier arrival times and larger signal amplitudes compared to the energy travelling through the conductive seawater (red curve).

Model B is also included in Fig. 5.9c and Fig. 5.9d. Here, Model A is neglected due to the small amplitude of the impulse response that is hardly recognisable compared to the other signals. The impulse response of Model C and Model D are displayed in green and black, respectively. The second maximum of the green curve describes the arrival of the energy travelling directly through the sediments, which are more conductive than the air. This response is less attenuated compared to the airwave. The most prominent signal is associated with the resistive layer mode (black curve). Compared to the response of the airwave, the arrival times of the resistive layer mode are similar, which may imply that the aquifer response is masked by the airwave contribution. However, Fig. 5.9d clearly shows that the resistive layer mode is clearly distinguishable from the airwave. Accordingly, the black curve in Fig. 5.9c indicates that the resistive aquifer is observable in the time range from 2 ms to approximately 30 ms, which coincides with the detectability studies shown in Fig. 5.4.

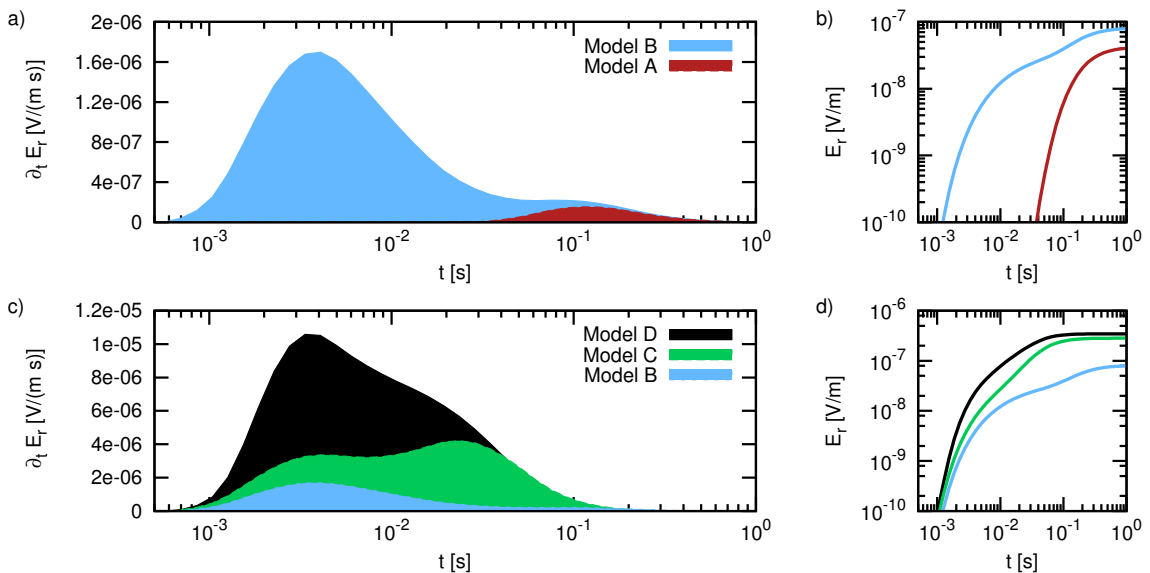


Figure 5.9: Airwave study using the impulse response (a) and (c) of signals calculated for the models displayed in Fig. 5.8. Additionally, the calculated signals at an offset of 580 m are displayed in (b) and (d) for better reference. Transients are colour-coded with their respective impulse response.

Studying the influence of the air-sea interface on the calculated data also gives insights regarding the differences in detectability of step-on and step-off signals. The study shows that the aquifer footprint in the data is expected at delay-times of 30 ms or earlier. Moreover, the signal of the resistive layer mode is small compared to the maximum amplitude of the step-on transient (DC level). As a reminder, the DC voltages mask the aquifer response at early times in the step-off signal. These are useful to detect the presence of a resistive layer in the subsurface, but have little sensitivity towards alterations in aquifer depth and thickness.

5.2.3 Parameter Resolution of the Aquifer

The detectability and airwave studies revealed some interesting aspects concerning the transient behaviour of LOTEM and DED. Three main questions arise that will be further investigated in the following sections.

1. Detectability characteristics differ in the shallow marine environment depending on the type of transmitter signal. The question remains if this also applies to the model parameter resolution?
2. In comparison to LOTEM, DED shows enhanced detectability towards variations in aquifer thickness in the step-off response. Does this indicate a higher resolution towards this model parameter?
3. The normalised response of step-on and step-off signals is different for shallow marine resistivity models. Can a joint interpretation of both signals enhance the resolution towards all parameters of the subsurface resistivity model?

In the following, a SVD-analysis is used to study the model parameter resolution for LOTEM, DED and CED under realistic noise conditions. The study aims at discussing the above-mentioned aspects.

The reference noise model is applied to the data to simulate realistic noise conditions. The noise model is assumed to be uncorrelated and normally distributed at each time sample. The noise vector $\mathbf{e}(t)$ is thereby expressed as

$$\Delta d(t_i) = [0.01 \cdot e_r(t_i) + \frac{1}{\sqrt{N}} \cdot \frac{s_0}{n_0}] / I \quad (5.3)$$

where $e_r(t_i)$ is the radial electric field at each interpolated time point t_i . As the implemented forward operator of the developed code calculates current normalised signals, the noise floor is additionally divided by a current amplitude of 13 A, agreeing with the current amplitudes applied in field measurements. Following *Hölz et al.* (2015), the left term of the noise contribution in Eq. (5.3) describes the relative error expressed as the percentage of the amplitude and is assigned a value of 1%. The second contribution is considered the noise floor of the instrumentation, which prevents unrealistically small voltages at either early or late times. In the following study, this contribution is assumed to be time-independent

following the studies of *Lippert* (2015). For the subsequent modelling studies, a noise floor at 3000 stacks is assumed. Therefore, the left right of Eq. (5.3) is $1/(I \cdot \sqrt{N}) \cdot s_0/n_0 = 1/(13 \cdot \sqrt{3000}) \cdot 10^{-6} \text{ V}/(\text{Am})$.

The transients for the standard 1D resistivity model with $\rho_i = [1 \text{ } \Omega\text{m}, 100 \text{ } \Omega\text{m}, 1 \text{ } \Omega\text{m}]$ and $d_i = [70 \text{ m}, 100 \text{ m}]$ using the corresponding error estimations are display in Fig. 5.10. The top row shows the step-on signals of LOTEM, DED and CED in a, b and c, respectively. The bottom row shows the corresponding step-off signals. The time-independent noise floor at 3000 stacks is displayed in each plot by a black dashed line and labelled accordingly. The time ranges and TX-RX configurations corresponds to the ones used in the detectability studies. In terms of SNR, LOTEM is superior to DED and CED. Data points below the noise floor (not displayed in Fig. 5.10) are excluded from the following study. Consequently, the CED transients are clearly handicapped due to the poor SNR of the signal. Partly, this also applies to the step-off signal of DED, where the last seven data points are neglected due to the poor SNR.

The SVD-analysis of the weighted Jacobian follows the theory described in Section 4.3.1. The results of the SVD-analysis for different transmitters and current signals are displayed in Fig. 5.11. The images contain the relative weights of the original parameters displayed with circles of different radii. The size and colour of each circle symbolises the value and sign of the corresponding coefficient. Black circles

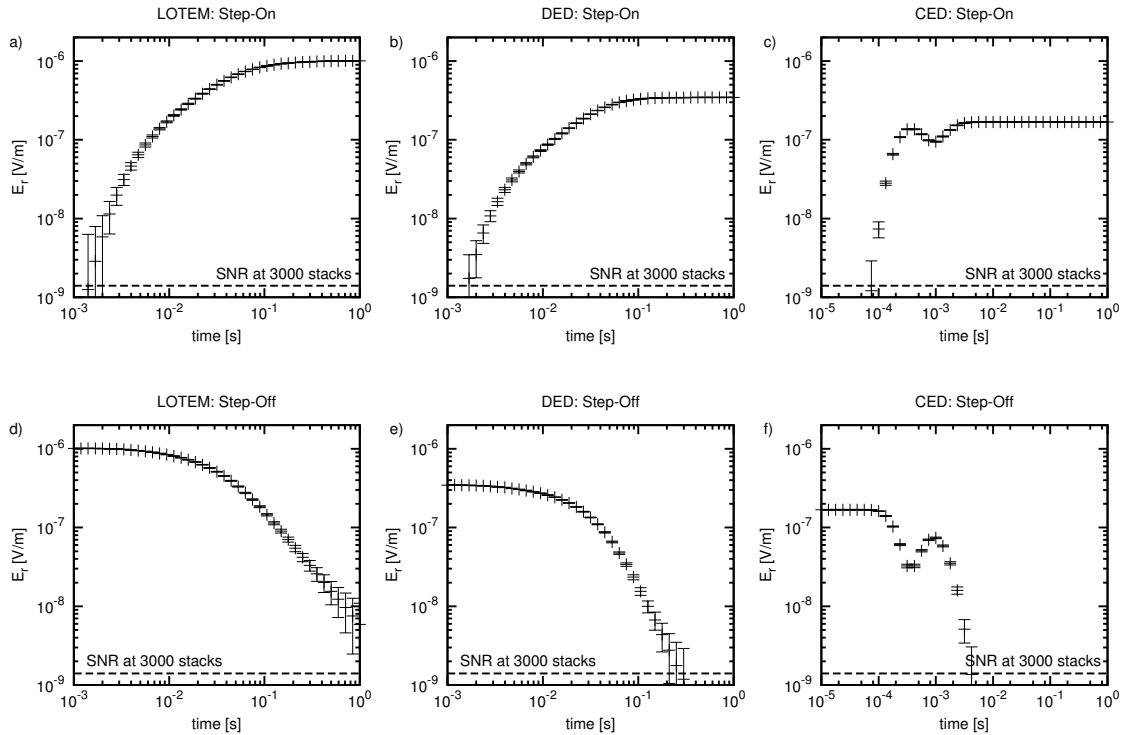


Figure 5.10: Synthetic data calculated for a shallow marine model with a water depth of 30 m consisting of three layers. The resistivity distribution is 1 Ωm , 100 Ωm and 1 Ωm with thicknesses of 70 m and 100 m. A realistic noise model was derived from LOTEM data at 3000 stacks using Eq. (5.3).

correspond to positive, white circles to negative coefficients. For example, the first column of Fig. 5.11a can also be expressed as the linear combination of logarithmic values and reads as follows:

$$EP1 = 0.65 \cdot \log(\rho_1) + 0.02 \cdot \log(\rho_2) - 0.06 \cdot \log(\rho_3) - 0.75 \cdot \log(d_1) - 0.04 \cdot \log(d_2) \quad (5.4)$$

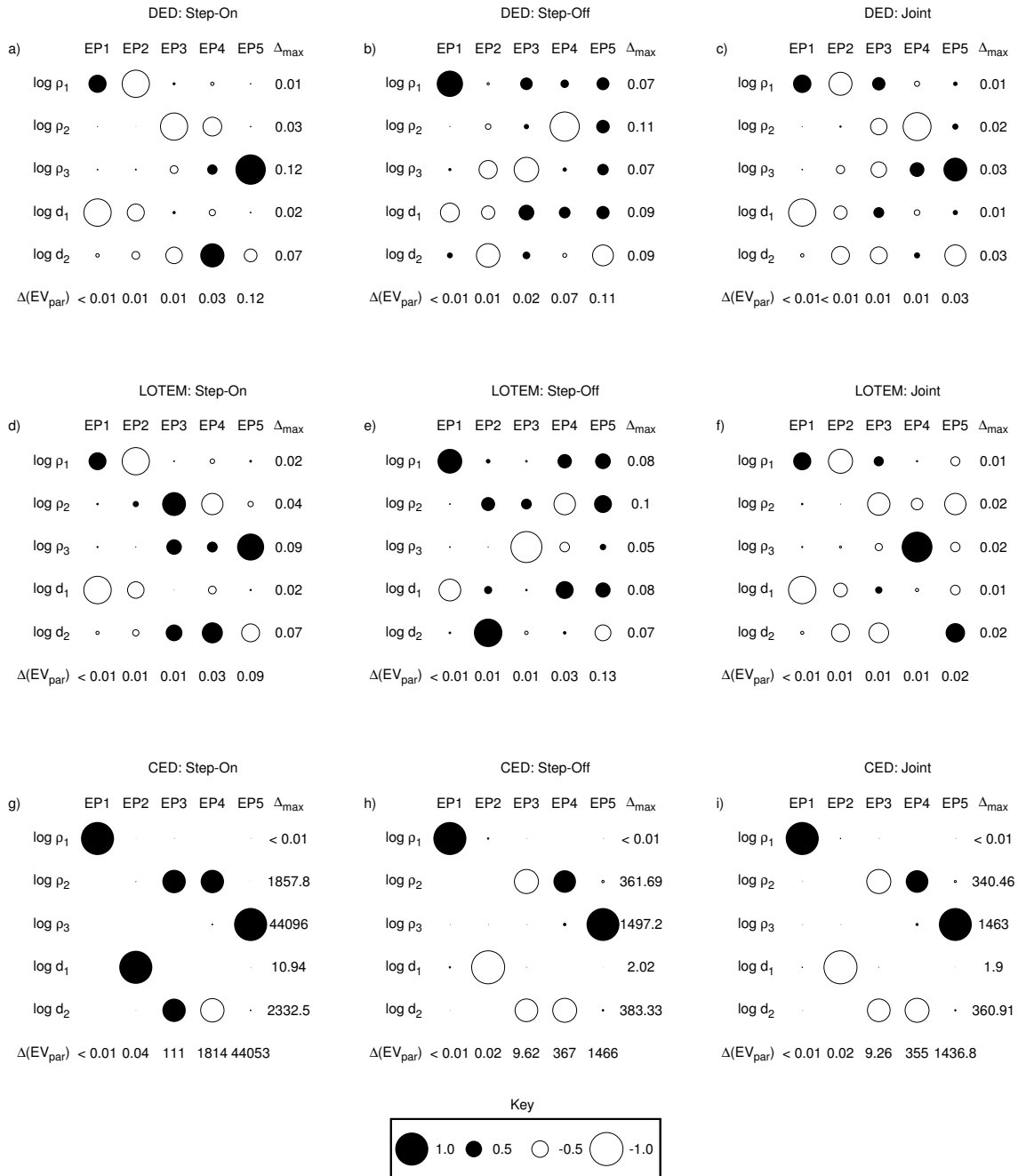


Figure 5.11: Eigenparameter analysis for LOTEM, DED and CED of Model D, displayed in Fig. 5.8. The radius of each circle is proportional to the coefficients of the \mathbf{V} -matrix from the SVD of the weighted Jacobian. EPs are sorted after the size of their corresponding eigenvalue, where EP1 is most, and EP5 is least important.

As EP1 is a linear combination of the weighted logarithmic model parameters, an EP composed of a black and a white circle of roughly equal size corresponds to the difference of the two log-parameters. Accordingly, a quotient of the original model parameters is resolved (*Swidinsky et al.*, 2012). Following this approach, EP1 of the DED-Step-On signal is interpreted as the ratio ρ_1/d_1 , with d_1 slightly dominant. Additionally, the parameters $\Delta(\text{EV}_{par})$ and Δ_{\max} are displayed corresponding to the standard error of the eigenparameter and the fractional errors of the logarithmic model parameters, respectively. The EP's are sorted according to the size of their associated eigenvalues, implying EP1 is most and EP5 least important.

Similar to the detectability study in the preceding section, the results of DED and CSEM are practically identical. Taking the derived hypothesis of the detectability study into account, the switch-on signal should be more sensitive towards the thickness of the overburden compared to the switch-off signal. The sensitivity study reveals a more complicated picture, as the signals are only consistent in EP1. Here, the ratio of ρ_1/d_1 is resolved, suggesting a consistent sensitivity between step-on/off. However, the remaining EP's differ for both LOTEM and DED. For instance, the resistivity thickness product of ρ_1 and d_1 is resolved in the step-on signal. Consequently, ρ_1 and d_1 could be resolved individually using the first two EP's of the step-on signal. In contrast, the step-off signal primarily contains contributions of d_2 in the 2nd and ρ_3 in the 3rd EP. Conversely, ρ_3 is the least important parameter in the step-on signal as it is only dominant in EP5. Thus, the SVD-analysis confirms the hypothesis that step-on and step-off signals are sensitive towards different model parameters. However, the parameters of the aquifer (ρ_2 and d_2) are evaluated as equal in both signals, as contributions appear in EP2 through EP4.

The detectability studies also suggest that the thickness of the resistive freshwater aquifer is delineated more clearly in the DED step-off signal compared to LOTEM. The SVD-analysis contradicts this assumption, presumably a result of the poor SNR of DED at late times. The values of Δ_{\max} are much smaller than unity for both DED and LOTEM, implying an equally good resolution of the model parameters in the extent of this study.

The joint interpretation of step-on and step-off signals is difficult to assess in terms of improved model parameter resolution. On the one hand, the values of Δ_{\max} and $\Delta(\text{EV}_{par})$ are smaller suggesting a higher resolution of the individual model parameters. On the other hand, the distribution and radii of the circles is similar to the individual SVD-analyses. The EP's are generally composed of a linear combination of two or more logarithmic model parameters. The exception is EP4 of LOTEM joint interpretation displayed in Fig. 5.11f, where ρ_3 is the lone resolved parameter.

Figure 5.11g through Fig. 5.11i illustrate the SVD-analysis of CED. The results indicate that CED is only capable of resolving the resistivity of the marine seafloor sediments ρ_1 . All other Δ_{\max} values exceed unity where the theoretical assumptions do not hold (*Edwards*, 1997). As a result, the parameters are not considered resolved. The main cause of the limited model parameter resolution for CED is attributed to the poor SNR. Based on these results, the feasibility of an actual CED application in Israel to resolve the sub-seafloor aquifer is majorly questioned. A successful CED application only seems feasible, if either current amplitudes are increased by multiple

order of magnitudes, and/or the error floor is greatly decreased. Both adjustments are technically not realisable in the extent of this project.

Discussion on SVD-analysis

The SVD-analysis visualises the resolution of CED, DED and LOTEM towards model parameters of a shallow marine aquifer model. Moreover, the study shows that step-on/off signals are sensitive towards different model parameters. A realistic noise approximation is included in the analysis causing a major reduction in the resolution for CED data. In contrast, due to the superior signal strength, both DED and LOTEM are capable of resolving the parameters of the aquifer. Furthermore, the SVD-analysis gives insights regarding the preliminary hypothesis stated at the beginning of the chapter.

- The model parameter resolution is indeed dependent on the current signal. The step-on signal is sensitive towards the model parameters of the overburden, whereas the step-off signal is more sensitive towards the resistivity of the lower half-space ρ_3 . With respects to the parameters of the resistive aquifer, both signals show comparable sensitivities.
- In the presented 1D sensitivity study, the DED step-off signals did not show a higher resolution compared to LOTEM. The advantages of a DED application, as indicated in the detectability studies, presumably vanish in the data errors. Consequently, the SNR is an important issue in comparing DED to LOTEM.
- The resolution of the model parameters seemed slightly improved for a joint interpretation. If this justifies the increased computational load in the data interpretation process remains questionable.

Based on the results of the SVD-analysis, a LOTEM application is sufficient to resolve the sub-seafloor aquifer. The results of *Lippert (2015)* have demonstrated this. However, the application of DED is not intended to compete with LOTEM in a 1D setting, but rather has advantages in detecting multi-dimensional resistivity structures (*Haroon et al., 2016*). Still, the 1D modelling studies have illustrated that the signal characteristics of DED justify an application. In contrast, CED does indeed exhibit the highest detectability contrast in the step-off signal. Yet, the poor signal amplitudes make a successful application doubtful.

5.2.4 Conclusions: Layered Aquifer

Modelling studies were conducted assuming a 1D resistivity model corresponding to a sub-seafloor freshwater aquifer embedded in saltwater saturated sediments of a shallow marine resistivity model. For this specific model, a water depth of 30 m was assumed.

First, studies were performed to investigate the most basic feature of an EM application called detectability. This feature indicates if the desired EM method can

distinguish between the signal of a target layer and the signal caused by the background environment. The study enabled some preliminary conclusions regarding the signals of CED and DED compared to LOTEM. First, CED has a high detectability in the step-off signal exceeding both DED and LOTEM. However, the SNR is poor at late times making an application in Israel rather unrealistic. Second, the detectability characteristics of DED and LOTEM are comparable. LOTEM has slight advantages due to the better SNR. The third and most important conclusion of the detectability study is that the signals of step-on and step-off are not necessarily consistent in terms of sensitivity towards certain model parameters. The modelling study suggests that different aquifer depths can only be detected using the step-on signal.

To further investigate the differences in step-on and step-off signals, the influence of the air-sea interface was investigated. Taking the derivative of the E_r field with respects to time, enabled the delineation of the time-window in which the aquifer footprint is measurable at the receiver. Moreover, the inferior amplitude compared to the DC level in combination with the early delay-times of the aquifer footprint imply, that the signal of the aquifer depth is masked by the DC level in the step-off signal.

An SVD-analysis was conducted for the three transmitters and two current types. The aim of the study was to further investigate the differences between step-on and step-off signals. Furthermore, the study is intended to investigate the model parameter resolution characteristics considering a realistic error estimation. In conclusion, the SVD-analysis confirmed the preliminary hypothesis of the detectability study. However, the advantages of DED compared to LOTEM for step-off signals proved false for this particular noise estimation. A joint interpretation tends to improve the resolution of model parameter combinations. To what extent this can be applied to measured data is difficult to assess using theoretically modelled data. Therefore, an attempt to interpret the measured data from Israel using both step-functions is realised in Chapter 8.

It should be mentioned that an interpretation of 1D inversion using synthetic 1D data is neglected at this point. The bathymetry in coastal regions will generally cause a multi-dimensional resistivity distribution. In the following chapter, 1D inversions of 2D data are conducted. All aspects of inverting the 2D data using 1D inversion are then investigated.

5.3 Geometrical Errors

The preceding modelling studies applied 1D resistivity models to study the detectability and resolution characteristics towards a sub-seafloor aquifer system using the CED, DED and in-line LOTEM methods. In the following section, the sub-seafloor resistivity model is considered secondary, as geometrical errors of CED and DED transmitters are systematically investigated. A background noise model is neglected in the following studies.

First, the transmitters are tilted within the water column similar to the effect that

a VED transmitter would experience. Note, the VED was not addressed in the detectability/resolution studies. Simply, the limited space within the water column prohibits a VED application in shallow sea environments. The resulting signal amplitudes are hardly measurable under realistic noise conditions. Nevertheless, the application of CED was considered as the equivalent of a VED, as the latter is known to suffer from an effect called non-verticality, shown for example by *Goldman et al.* (2015). The following non-verticality study will compare tilted CED/DED transmitters to VED for purpose of comparability.

Subsequently, the geometries of the CED and DED transmitters are distorted and the resulting transients are compared. For land-based CED measurements, the issue of electrical symmetry (equal current amplitudes) within the eight transmitter dipoles is known and has successfully been solved through the development of a transmitter unit (*Mogilatov and Balashov* (1996) and *Helwig et al.* (2010b)). By regulating the current amplitude in each dipole individually, inhomogeneous coupling conditions are circumvented and the resulting error is minimised. In marine applications, the stability of the current regulation in the eight dipoles is less severe due to the homogeneous coupling in seawater. However, in comparison to land-based measurements, the accurate geometrical symmetry of the transmitter is more difficult to handle. The study focuses on assessing the signal distortions caused by these geometrical inaccuracies.

In the extent of this study, an algorithm is developed which allows the applicant to manipulate the symmetry of CED, DED and even VED transmitters. Essentially, the complex geometries of the considered transmitters are simply calculated by superposition of horizontal electrical dipole sources. Accordingly, the geometries of each superimposed component is easily manipulated accounting for the symmetry errors that are studied in the following section. The algorithm was tested using comparative 3D modelling studies with `s1dmem3t`, in addition to comparisons to a further 1D algorithm that was developed contemporaneously².

5.3.1 Non-Verticality

The effect of non-verticality for VED sources and receivers is known and has been addressed in scientific literature, e.g. *Goldman et al.* (2015); *Haroon et al.* (2016). The following study investigates if CED/DED sources have the same vulnerability towards non-verticality. The study has been previously published by *Haroon et al.* (2016), but is repeated here for the shallow marine case with water depths of only 30 m. In contrast to the preceding modelling studies, the background resistivity model is considered of secondary importance. The main focus lies in investigating the errors caused by geometrical distortions of the transmitter antennas. Thus, the 1D model is fixed and consists of a 30 m thick seawater layer ($0.2 \Omega\text{m}$) and a half-space of $1 \Omega\text{m}$. It should be noted that a more resistive subsurface will magnify the errors caused by geometrical distortions. Accordingly, the demonstrated examples are considered the best-case scenario. Additionally, the dipole lengths of the DED are adapted to the intended dipole lengths of the CED for better comparability

²Personal communication with V. Mogilatov in August 2014.

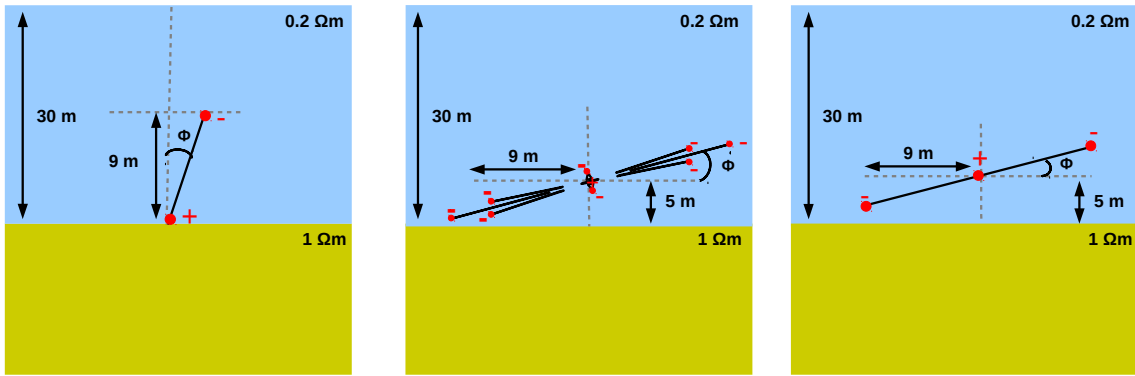


Figure 5.12: Schematic of non-verticality modelling for VED (left), CED (centre) and DED (right). The receiver of each transmitter is located on the seafloor at an offset of 50 m. Image modified after Haroon *et al.* (2016).

($dl = 9$ m). Subsequently, the errors are investigated as a function of dipole lengths.

In the following non-verticality study, the internal horizontal symmetry of the CED and DED transmitter is maintained, but the whole transmitter system is tilted (see Fig. 5.12). For CED, this means the eight HED components are at an angle of 45° . The horizontal disc of the transmitter antenna is tilted by a certain angle Φ . Likewise, VED and DED transmitters displayed in Fig. 5.12a and Fig. 5.12c are inclined by the same angle. In fact, the non-verticality description originates from an imperfect VED. In this case, Φ describes the angle of inclination, where $\Phi = 0$ represents an ideal, perfectly vertical transmitter. The transmitter dipoles have a length of 9 m and the E_r receivers are located on the seafloor at an offset of 50 m, corresponding to the short-offset CED setup. It should be noted that although the conventional VED applications, as applied by Helwig *et al.* (2013), generally utilise an E_z receiver, where the effect of non-verticality is less severe (Goldman *et al.*, 2015), only E_r transients are presented. Principally, this is due to comparability reasons. A comparison to the LOTEM method is neglected, as it is clear that an inclined HED source will produce only a small geometric error in form of a shift for small values of Φ . For the assessment of non-verticality of CED, DED and VED, a comparison to LOTEM is not relevant.

Transients are displayed at selected values of Φ for VED, CED, and DED are displayed in Fig. 5.13. The undistorted transients are displayed in black, the distorted transients in blue and green for selected angles of $\Phi = 2^\circ$ and $\Phi = 8^\circ$, respectively. The step-on transients are displayed in the top row, the step-off in the bottom row. The large deviations in the VED transient behaviour confirm that it is particularly susceptible towards non-verticality effects. For the investigated time range, the errors particularly affect the intermediate to late times of the transient. This is associated with the slower signal decay of the parasitic HED component that is produced in case of a tilted VED transmitter. In comparison, the signals of CED and DED are much less affected by non-verticality. For the selected values of Φ , differences in the transient behaviour are hardly noticeable throughout the entire time range. This can be explained by composition of the transmitter and the assumptions made in the extent of this modelling study. An imperfect VED will

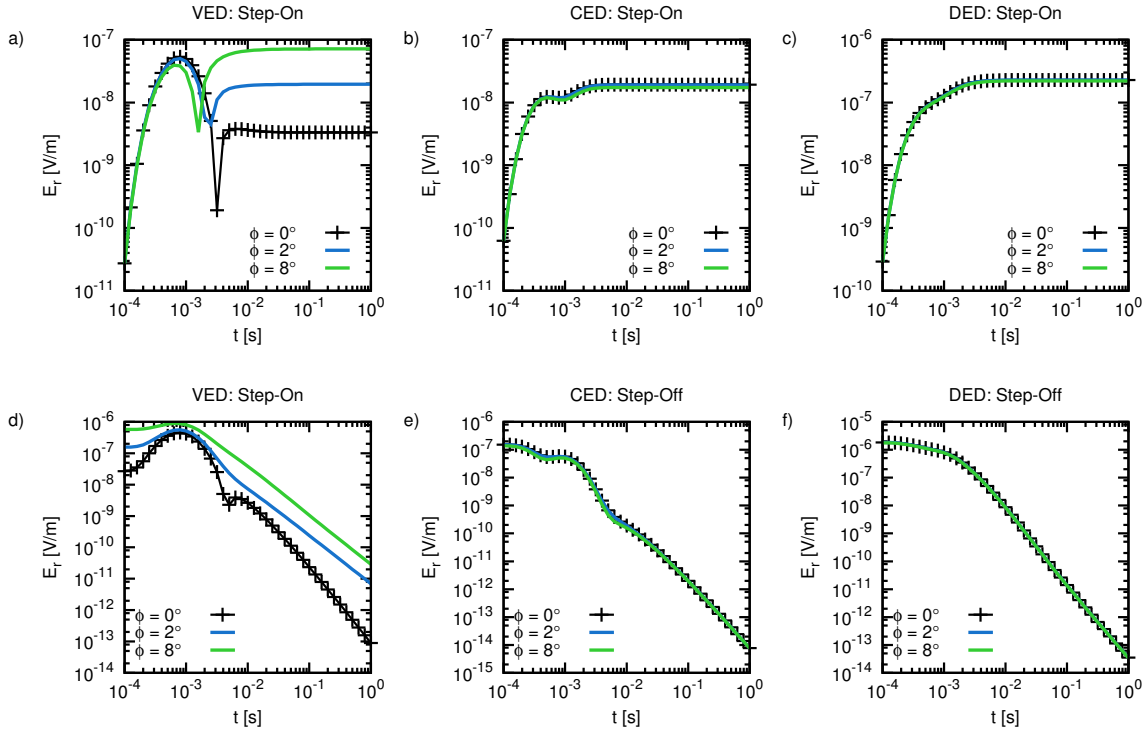


Figure 5.13: Non-verticality effect of VED (a and d), CED (b and e) and DED (c and f) for the configuration displayed in Fig. 5.12. Step-on signals are displayed on top, step-off on the bottom. Undistorted transients are plotted in black, distorted transients for selected angles of $\Phi = 2^\circ$ and $\Phi = 8^\circ$ are illustrated in blue and green, respectively.

generate a small, but relevant HED signal that is especially prominent at late times. In contrast, the CED is assumed as a disc, where the internal symmetry is maintained. Therefore, an inclination of the complete disc will solely produce a small additional vertical field component, which is considerably smaller in amplitude and decays faster. Consequently, the error is solely of geometric nature caused by the effective radius decrease due to the transmitter tilt. In principle, this also applies to the DED transmitter (Haroon *et al.*, 2016).

To further quantify the susceptibility of VED for the given resistivity model, tilt-angles that range from unrealistic values of $\Phi = 1e-3^\circ$ to realistic values of $\Phi = 10^\circ$ are investigated. A quantification of non-verticality effects for CED and DED are found in Haroon *et al.* (2016). The resulting relative errors for VED are presented as a function of time and tilt-angle for step-off and step-on signals in Fig. 5.14a and Fig. 5.14b, respectively. For a 9 m transmitter dipole, one would realistically expect Φ -values no smaller than $4^\circ - 5^\circ$ implying inaccuracies of 62 cm to 78 cm. For this case, the resulting errors exceed 500%. Sufficient data quality of a 9 m VED is reached for tilt-angles of $\Phi \leq 0.1^\circ$. Thus, positioning errors of only 1.5 cm are tolerated, which is hardly feasible in marine measurements.

Haroon *et al.* (2016) also mention that additional aspects might have an effect on the results of the presented modelling study. The effect of non-verticality may increase/decrease depending on the offset and/or position of the receiver. Also,

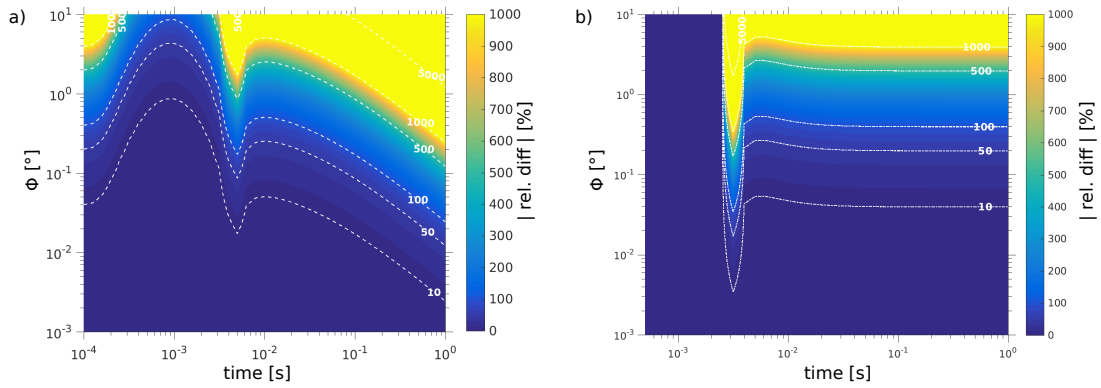


Figure 5.14: Relative errors displayed as a function of tilt-angle and time for a VED source as displayed in Fig. 5.12: (a) Step-off signal and (b) step-on signal. The white contour lines are displayed for better interpretation.

Goldman *et al.* (2015) show that an E_z receiver is less susceptible towards the effect of non-verticality. The position of the transmitter within the water column may also affect the absolute error values, but will generally not contradict the assertion of this study. If the internal symmetry of CED/DED is maintained, then a non-verticality effect is less prominent compared to VED.

5.3.2 Internal Transmitter Symmetry

The preceding non-verticality study assumes that the symmetry of the CED and DED transmitter antennas are maintained, meaning the angles in the horizontal plane between the each dipole is either 45° for CED or 180° for DED, respectively. Realistically, this assumption can rarely be held, as the complex transmitter geometries are prone to some physical distortions. These are expected to vary several decimal degrees during the transmitter construction. Additionally, ocean currents, winds, waves, etc. may have an effect on the transmitter symmetry by producing

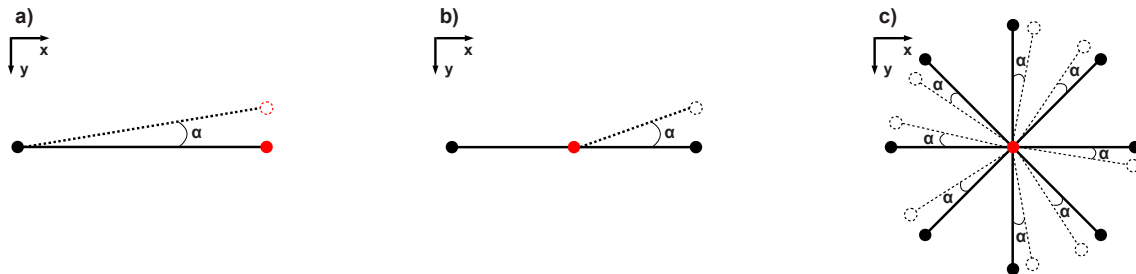


Figure 5.15: Geometrical error study investigating dipole movements of (a) LOTEM, (b) DED, and (c) CED. The black circles represent electrodes with one polarity, the red circles the electrodes with the opposite polarity. The solid lines represent the ideal transmitter, whereas the dashed lines represent the altered transmitter. α is the angle between ideal and altered transmitter (Haroon *et al.*, 2016).

small, but relevant arm movements. In the following modelling study, these errors are investigated using the 1D resistivity model displayed in Fig. 5.12. For this study, the transmitters are located on the seafloor. As non-verticality of VED will essentially have the same affect as the presented study, the comparison is confined to CED, DED, and LOTEM. The transmitter geometries are consistent with the preceding non-verticality study. A dipole length of 9 m is applied with an E_r receiver at an offset of 50 m. In an ensuing study, the geometrical errors are assessed as a function of dipole lengths.

As illustrated in Fig. 5.15, moving one or more transmitter electrodes away from its ideal position in the horizontal plane breaks the internal transmitter symmetry. The extent of alteration is described by the angle α . For DED, only one of the outer electrodes is altered, as a movement of both by the same angle would maintain the symmetry. In contrast, all outer electrodes of the CED transmitter are altered in opposite directions to simulate consistent geometrical distortions. If all outer electrode positions are altered in the same direction, the transmitter symmetry would also be maintained.

Transients and relative errors of LOTEM, CED, and DED for selected values of α are shown in Fig. 5.16. The step-on signals are displayed on top, step-off along the bottom. For angles of up to 10° , LOTEM is hardly affected by the transmitter asymmetry. The effect is negligible and typically lies in the error range of stacked data. This systematical error can be accounted for by declaring a minimum error on the data. Hence, the interpretation is not significantly affected. In comparison, the transients of CED/DED behave in a different manner. Also, differences are noticeable between the step-on and step-off response. For step-off displayed in Fig. 5.16e and Fig. 5.16f, the early times of the transients are shifted to a lower DC level depending on the value of α . For intermediate to late-times, the transient behaviour of the distorted data changes in comparison to the undistorted case. As a result, the errors explode at intermediate to late times. If α exceeds a certain value, sign-reversals appear in the step-off transient. In the case of CED, these sign-reversals are apparent for all distorted transients. In contrast, they appear in the DED signal only at $\alpha \geq 5^\circ$. Consequently, DED step-off transient tolerates small geometrical errors, whereas CED immediately punishes all geometrical inaccuracies.

The step-on signals, displayed in Fig. 5.16-top row, seem less susceptible towards geometrical errors. Deviations of several degrees are tolerated for a DED application. This is an improvement compared to the step-off signal and can make DED applications feasible, even for small dipole lengths. This assumption applies only if the SNR issue is addressed in a reasonable way. Geometrical errors are also less severe in the step-on response of the CED signal. However, no benefit arises from this attribute, as the modelling studies of a layered aquifer model show that the step-on response of short-offset CED is unappealing. It shows no detectability towards the resistive aquifer layer. Consequently, the increased stability of the CED step-on signal with respects to geometrical errors is useless.

Geometrical errors of CED and DED may either increase or decrease depending on the underlying resistivity model, transmitter-receiver offset, dipole length, acquisition window, etc. However, the behaviour is in general agreement with the study

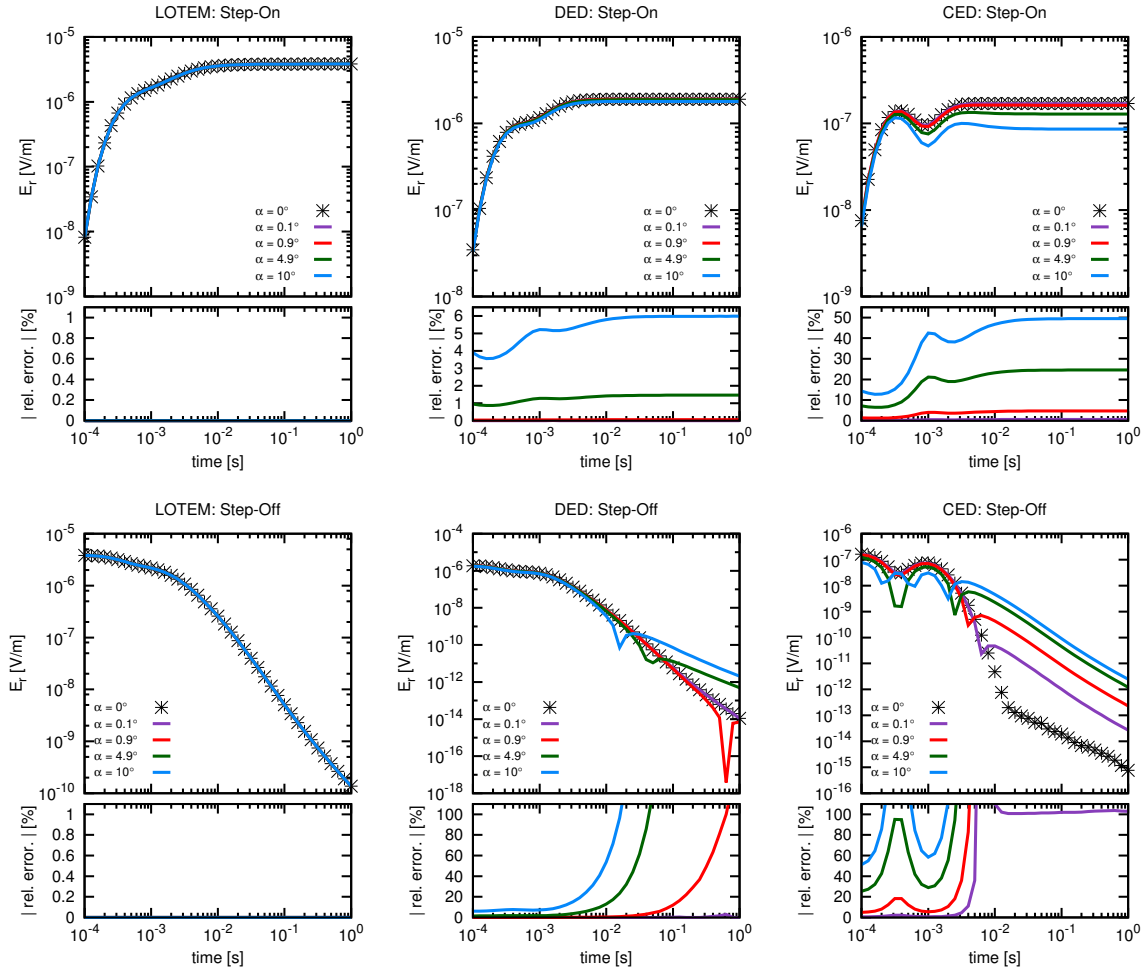


Figure 5.16: Transients and relative errors for selected values of α displayed as a function of time for LOTEM (left), DED (middle) and CED (right) for step-on (top) and step-off (bottom) signals. Distorted transients are displayed by coloured lines, undistorted transients by black markers.

shown in Fig. 5.16. To quantify the geometrical errors as a function of transmitter size (dipole length), further modelling studies are conducted. The RMS, expressed as the square root of the squared sum of relative differences is displayed as a function of α and dipole length in Fig. 5.17. The transmitter radius is varied between 10 m and 400 m. The offset of the receiver is constant at $r = 2.9 \cdot dl$. The odd scalar is chosen to take the developed DED system with the corresponding TX-RX offset into account ($dl = 200$ m, $r = 580$ m.). The background resistivity model stays consistent with the prior study. It should be mentioned that all α -values smaller than 1° are practically unrealistic for actual field measurements. They simply demonstrate the severity of the problem, especially for the CED step-off signal. The modelling study does not consider that under realistic conditions, each transmitter dipole will move by different α -values. Under these circumstances, the errors are increasingly unpredictable.

The errors of the step-off signal illustrated in Fig. 5.17c and Fig. 5.17d are significantly reduced if dipole lengths are increased. However, the errors of CED remain at

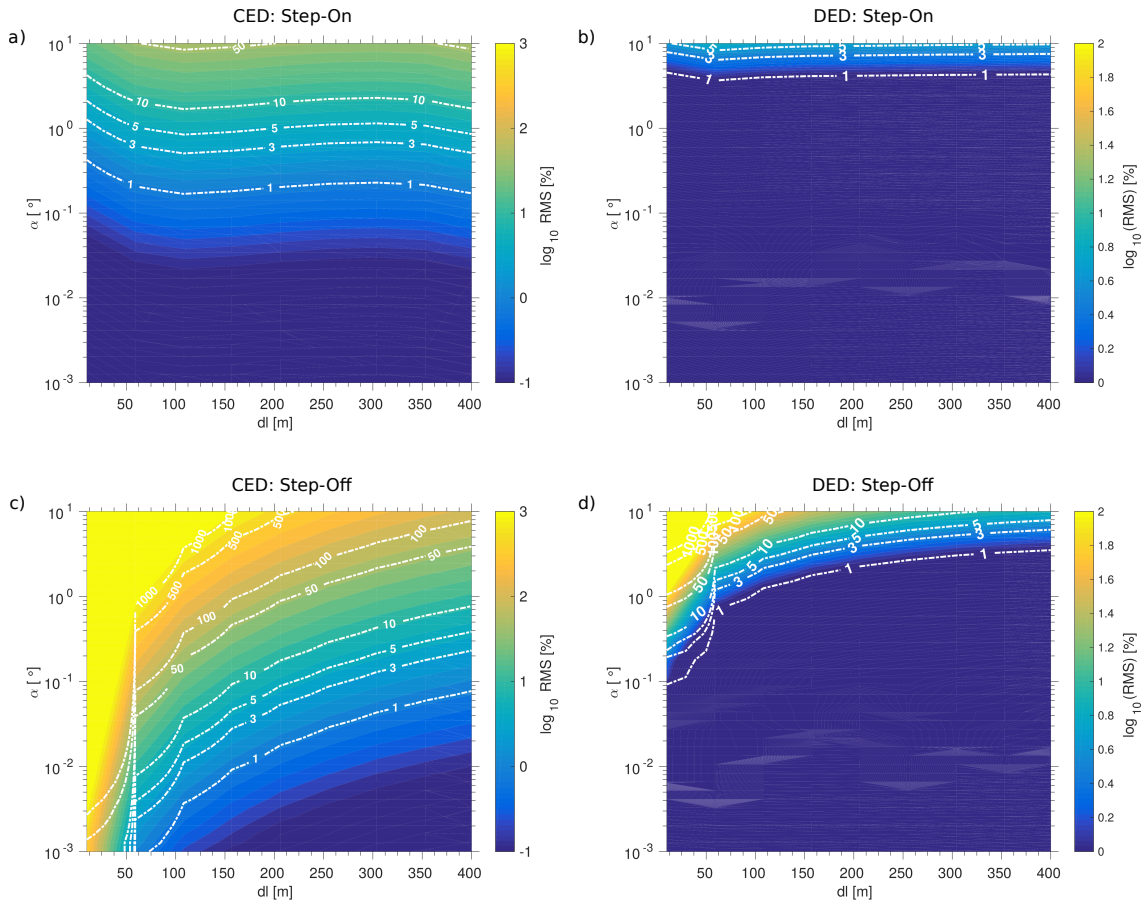


Figure 5.17: RMS errors displayed as a function of distortion angle α and dipole length: (a) CED step-on, (b) DED step-on, (c) CED step-off and (d) DED step-off. Signals are calculated for offsets of 2.9 times the dipole length. Contour lines are displayed for an easier assessment of the errors.

a considerably higher level compared to those of DED. For the latter, dipole lengths of 200 m show a sufficient decrease in RMS error to justify a practical application. In contrast, the RMS errors of the step-on signal are almost independent of the dipole length. This is explained by the different in DC voltages that are caused by the geometrical errors. In the case of step-on signals, these differences account for the majority of the RMS error (see Fig. 5.16).

The issue of errors caused by geometrical distortions makes an application of marine CED systems rather problematic as ocean currents may enforce small movements. The intended CED application using a small transmitter with a maximum radius of 9 m - 10 m and short-offset receivers is definitely unrealistic at the present time. Under these circumstances, a marine CED application in the extent of this thesis cannot be justified.

In contrast, a successful DED application is feasible, but requires a precise positioning of the transmitter system. Considering all the previous 1D modelling studies, a trade-off between transmitter radius, offset, detectability, resolution, and SNR needs to be considered before executing actual measurements. Additionally, further

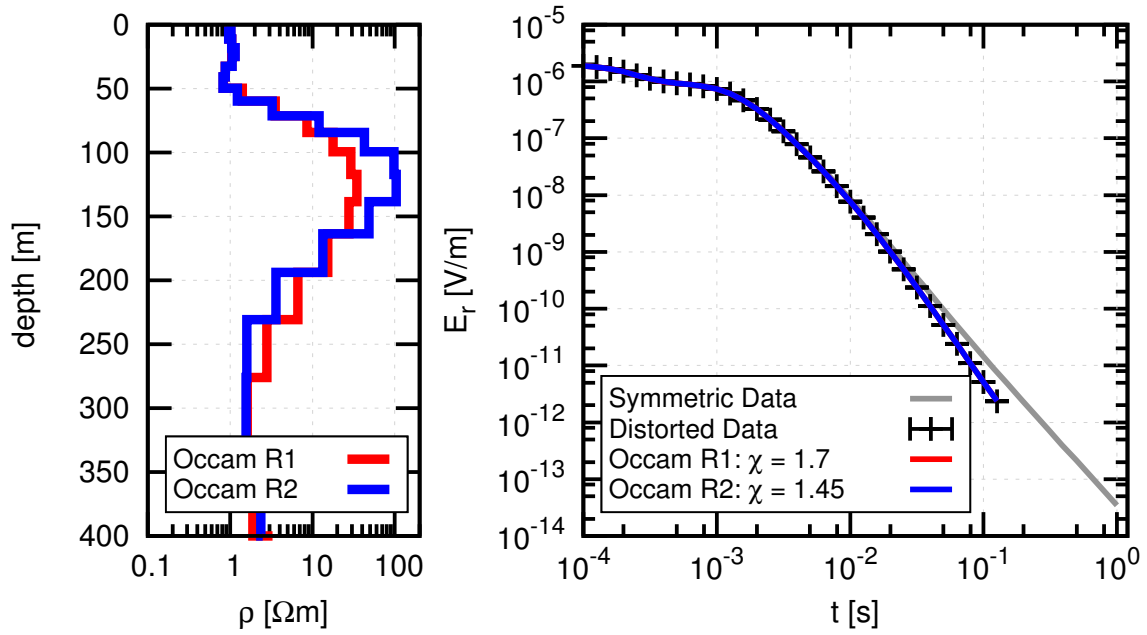


Figure 5.18: One-dimensional Occam inversion models of distorted step-off DED data. The geometrical distorting is assumed at an angle of $\alpha = 0.9^\circ$. The undistorted transient is displayed in grey.

multi-dimensional modelling studies will also play a relevant role in choosing the desired system configuration.

In conclusion, the geometrical error study expresses that a marine DED application is more feasible compared to a marine CED application for two main reasons: (1) the transmitter is less susceptible to geometric errors and (2) increasing the transmitter radius and offset of a DED system is much more practical in comparison to CED, as everything is in-line behind the ship. In this case, a towed DED system seems to be the most practical approach. In contrast, a marine CED transmitter is very costly to install, as the geometric requirements are very strict. A mobile measurement system is presently not imaginable. However, future marine CED applications may confine to reservoir monitoring using a large, permanently installed transmitter system with mobile receivers (*Haroon et al.*, 2016), or an arctic application using mobile ice floes as a basis for exploration purposes (*Mogilatov et al.*, 2016).

5.3.3 1D Inversion of Geometrically Distorted Data

The previous study quantified the errors as a function of geometrical distortion. However, the question remains of how an interpretation is falsified if geometrical distortions are ignored? The following study will focus on this topic. As practical CED applications are unrealistic at the present time and are not realised in the extent of this project, the following 1D inversion confines to DED data. The red transient displayed in Fig. 5.16 with a geometrical distortion of $\alpha = 0.9^\circ$ is interpreted. As a reminder, the resistivity model consists of a $1 \Omega\text{m}$ half-space underneath the transmitter. Ideally, the 1D inversion model should reproduce this structure.

The distorted DED step-off transient contains a sign-reversal at late-times. As this feature cannot be fitted using a 1D forward model, all data points trailing the sign-reversal are not considered. The edited step-off transient is displayed by black markers in Fig. 5.18. The step-on transient does not have to be edited as the errors are less severe in comparison.

The 1D inversion result of the distorted step-off transient is displayed in Fig. 5.18. The geometric distortion of the transmitter cause the transient to decay more quickly compared to the undistorted case. For an interpretation, this is quite problematic as the behaviour mimics a transient measured over a subsurface containing an intermediate resistive layer. Consequently, the 1D Occam inversion produces an imaginary resistive layer coincidentally in the expected depth range of the freshwater aquifer. Consequently, the resulting resistivity models of any measured DED step-off transient containing a resistive layer may be questioned, as it is difficult to precisely tow the system behind the ship.

The modelling studies presented in Fig. 5.17d indicate that errors are reduced for increased transmitter lengths. The inversion result is calculated for $dl = 9$ m. The applied DED system in Israel has dipole lengths of 200 m to account for these geometrical errors. However, a sign-reversal in the acquired step-off transients can always be associated with geometrical errors during the survey. The interpretation of the corresponding step-off transients should be conducted cautiously.

Modelling studies show that step-on transients are less affected by geometrical errors. In this context, the 1D Occam inversion models are also not affected. Compared to the results of the step-off transient, the inversion models displayed in Fig. 5.19

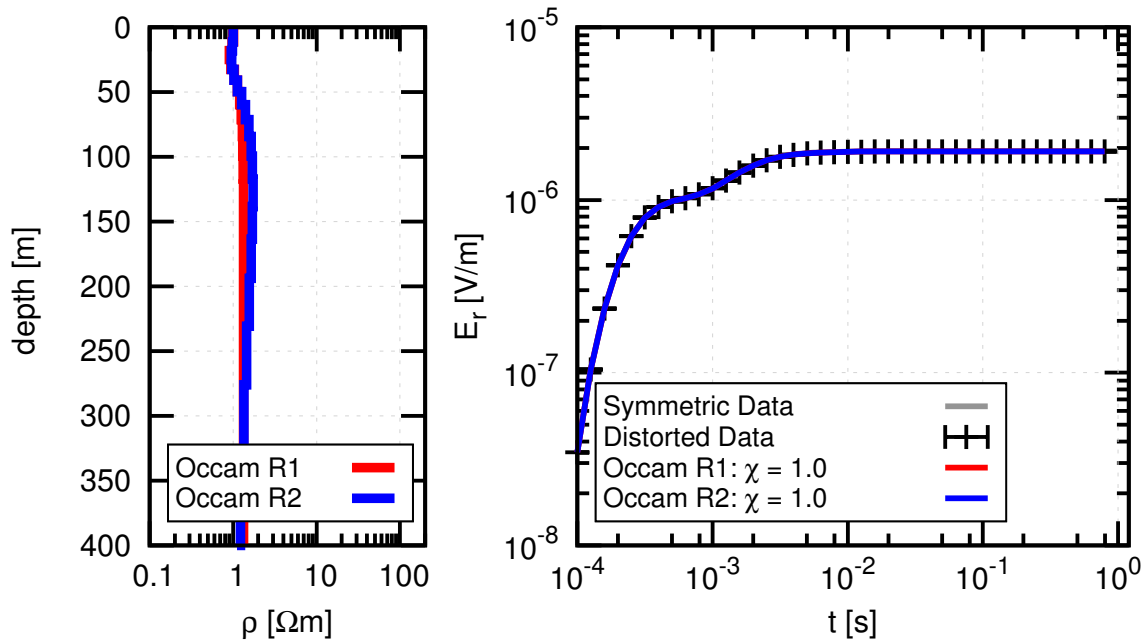


Figure 5.19: One-dimensional Occam inversion models of distorted step-on DED data. The geometrical distorting is assumed at an angle of $\alpha = 0.9^\circ$. The undistorted transient is displayed on the right in grey.

are nearly consistent with the original subsurface resistivity structure. A misinterpretation of geometrically distorted step-on data is not likely to occur for small geometrical inaccuracies.

5.4 Summary of 1D Modelling

Studying the signal characteristics using 1D resistivity models provided useful insights regarding the advantages and disadvantages of CED and DED in comparison to conventional EM sources. The results of the 1D modelling studies can be summarised as follows:

- Based on the detectability studies, a CED application in a short-offset configuration seems desirable as the step-off signal clearly exhibits the largest response towards a resistive sub-seafloor freshwater aquifer. However, a CED application is not reasonable under realistic noise conditions. First, the signal amplitude at late times is very poor indicating a massive SNR issue. Unfortunately, the aquifer response is only visible at these late-times in the CED step-off signal (see Fig. 5.3). Second, the CED step-off signal suffers from a severe susceptibility towards geometrical errors (see Fig. 5.16). In contrast, the step-on signal of CED is less susceptible towards these geometrical inaccuracies. However, the step-on transients show no detectability towards the resistive aquifer in the intended configuration (see Fig. 5.4). This problem may be solved by increasing the offset which, in turn, would magnify the SNR issue. As a consequence, the 1D modelling studies have underlined that the intended CED application is not realisable in the extent of this thesis.
- The detectability and resolution characteristics of DED are comparable to the standard in-line LOTEM application with the drawback of decreased signal amplitudes. Thus, for the detection of resistive 1D structures, a DED application instead of LOTEM is debatable. However, *Haroon et al. (2016)* show that clear advantages of DED over LOTEM are found for multi-dimensional resistivity structures. This is investigated in the following chapter.
- A DED application is also susceptible towards geometrical errors. The issue is less severe compared to CED. Geometrical distortions generally affect the step-off signals of DED and CED more severely. Sign-reversals in DED signals can be seen as an indication of a geometrical error. In this case, the interpretation of the step-off signal should be done cautiously, as an imaginary resistive layer may appear in the inversion model. This may be mistakenly interpreted as the resistive freshwater aquifer.
- For the given resistivity models, and particularly for the shallow water depths, the step-off and step-on responses are sensitive towards different model parameters. This applies to both, LOTEM and DED signals. The detectability study showed that the depth of the freshwater aquifer is more distinguishable in the step-on signal, whereas the step-off signal is more sensitive towards the lower

half-space. In terms of resolving the resistive aquifer, both signals are comparable. If these attributes can be applied in a joint interpretation remains unclear and will be tested on the measured DED data.

DED and also CED applications are intended to resolve multi-dimensional resistivity structures more clearly compared to LOTEM. Accordingly, the 1D modelling studies are important to study the signal characteristics, but are somewhat limited in their significance regarding the sub-seafloor freshwater aquifer in Israel. *Haroon et al.* (2016) show that CED and DED can clearly distinguish lateral resistivity discontinuities. This will be relevant to obtain information regarding the transition zone at the western aquifer boundary. The following chapter addresses multi-dimensional resistivity models and, specifically, the sub-seafloor aquifer model in Israel.

2D/3D Modelling of Resistive Formations

In the majority of cases, the resistivity structure of the subsurface is not composed of horizontal layers with infinite horizontal dimensions. Instead, the lateral extent of these structures is finite, or gradually changing in horizontal direction. Especially coastal regions are not sufficiently represented using a 1D resistivity model, due to the gradual increase of water depth from the coastline. Thus, multi-dimensional modelling studies are applied, as they more adequately describe the resistivity distribution of the subsurface. The following 2D/3D modelling studies are conducted with the `sldmem3t` algorithm (*Druskin and Knizhnerman, 1988, 1994*), which solves the three-dimensional Maxwell diffusion equations in the time domain.

The first section of this chapter describes the basic principles of the finite difference `sldmem3t` algorithm. It is described in numerous publications, e.g. *Hoerdt et al. (1992)*; *Druskin and Knizhnerman (1994)*; *Weidelt (2000)*; *Martin (2009)*, just to name a few. The following theoretical description is a summary of the above mentioned publications. In the extent of the presented thesis, the complex CED transmitter geometry is modelled for the first time using `sldmem3t`. Therefore, the emphasis lies on explaining the basics of the developed CED/DED grid generator. Subsequently, convergence and solution stability of `sldmem3t` is explained and analysed. A solution is compared to `MARTIN` for a 1D resistivity model. The numerical inaccuracy for a specific DED grid is derived and included in the error model of the 2D data interpretation shown in Chapter 9.

The signal characteristics of a DED transmitter for two-dimensional resistivity models are the main focus of this chapter. The models of interest are derived from *Lippert (2015)*, representing the expected resistivity distribution in the Palmahim region of Israel. First, the EM response for a realistic bathymetry model is explained and studied. As transmitter and receiver are generally located at different water depths due to the bathymetry, the effect of interpreting this modelled data using a 1D approach is investigated. A water depth is derived for specific transmitter-receiver configurations for which a reliable 1D inversion model are obtained. Subsequently, the two-dimensional resistive freshwater aquifer is introduced into the modelling study. Thereby, different structures of the saltwater/freshwater transition zone are analysed and evaluated. Finally, the reference error model presented in Section 5.1 is taken into account and the modelled 2D step-on data is interpreted using a 1D Occam inversion. Resistivity anomalies attributed to 2D effects in the 1D re-

sistivity models are analysed and discussed. The modelling studies show that the transmitter-receiver configuration with respect to the coast is crucial. Therefore, all relevant modelling studies simulate tow directions towards, and away from the coast.

Haroon et al. (2016) show modelling studies investigating a three-dimensional resistivity formation that represents a hydrocarbon reservoir embedded in marine sediments. They compare signals of CED, DED, LOTEM (TD-CSEM) and VED for short- and long-offset configurations. This study is included in Section 6.3 to demonstrate the 3D signal characteristics of CED and DED compared to other time-domain EM methods.

At the end of the chapter, the main results of the modelling studies are summarised. They are revisited in the interpretation of the measured data, as many similarities between the modelled and measured data are noticeable. They serve as the basis of the DED data acquisition and interpretation presented in Chapters 7 through 9.

6.1 3D Forward Operator

The `sldmem3t` code (*Druskin and Knizhnerman*, 1988, 1994) is used for solving the three-dimensional Maxwell diffusion equations in the time domain. The code has been applied at the IGM Cologne for many years, particularly due to its efficiency (*Weidelt*, 1986). Hence, many research articles/thesis from the IGM Cologne have published the theory of the algorithm, e.g. *Hoerdt et al.* (1992); *Martin* (2009); *Yogeshwar* (2014). The key aspects of the basic physics are presented here. For more detailed information regarding the theory of `sldmem3t`, refer to the above mentioned publications.

The theoretical description of `sldmem3t` is based on the non-stationary Maxwell equations in a quasi-static approach.

$$\nabla \times \mathbf{e} = -\partial_t \mathbf{b} \quad (6.1)$$

$$\nabla \times \mathbf{b} = \mu_0(\sigma \mathbf{e} + \mathbf{j}_e) \quad (6.2)$$

\mathbf{j}_e describes the current density of an external source. Following *Hoerdt et al.* (1992), the source current is switched on at $t = 0$ s so that \mathbf{j}_e is expressed as

$$\mathbf{j}_e = -\sigma \phi(x, y, z) \eta(t), \quad (6.3)$$

where the Heavyside function $\eta(t < 0) = 0$ and $\eta(t > 0) = 1$. Applying the *curl*-operator on Eq. (6.1) and substituting the Ampere's law at the designated location leads to the resulting diffusion equation

$$\nabla \times \frac{1}{\mu_0} \nabla \times \mathbf{e} + \sigma \partial_t \mathbf{e} = 0; \quad \text{for } t > 0, \quad \mathbf{e}|_{t=0} = \phi \quad (6.4)$$

This basic equation is solved using a finite difference discretisation scheme. The EM

fields are sampled on a staggered Yee-Lebedev grid (Yee, 1966). An exemplary Yee-cell is illustrated in Fig. 6.1. The electric field components are calculated along the cell edges. The time derivative of the magnetic field components are subsequently obtainable by applying Eq. (6.1). Accordingly, the associated magnetic field components are calculated on the plane-centres causing each component to be calculated at a different locations of the cell.

One feature of `sldmem3t` is the material averaging scheme that allows the calculated model to be independent of the discretising grid (Druskin and Knizhnerman, 1994). In this case, the physical parameters of the model are assembled within the field values. For an arbitrary 2D resistivity model, an exemplary description of the material averaging is displayed in Fig. 6.2. As the forward operator is three-dimensional, the resistivity values are considered constant in one lateral direction (in this case the x -direction) and vary only in the yz -plane. Note, for 3D models the averaging is extended in all directions. The field value at any node is weighted by the conductivity value of the adjacent cells and multiplied by the effective area (size of the shaded area in Fig. 6.2). Hence, the conductive medium is discretised spatially and the *curlcurl* operator is approximated using a finite difference approach (Hoerdt *et al.*, 1992). This leads to the following set of differential operations.

$$\mathbf{B}\hat{\mathbf{e}}(t) + \hat{\sigma}\partial_t\hat{\mathbf{e}}(t) = 0; \quad \text{for } t > 0, \quad \hat{\mathbf{e}}|_{t=0} = \phi \quad (6.5)$$

where \mathbf{B} is a symmetric, positive definite and high dimensional, but sparse $n \times n$ operator matrix and ‘ $\hat{\cdot}$ ’ represents the spatial discretisation. The value of n is approximately three times the number of grid points in x -, y - and z - direction. The ordinary differential equation system in Eq. (6.5) is transformed to normalised form (Hoerdt *et al.*, 1992) so that

$$\mathbf{A}\mathbf{u} + \partial_t\mathbf{u} = 0; \quad \text{for } t > 0, \quad \mathbf{u}|_{t=0} = \Phi \quad (6.6)$$

where

$$\mathbf{u} = \sqrt{\hat{\sigma}} \hat{\mathbf{e}}, \quad \Phi = \sqrt{\hat{\sigma}} \phi \quad \text{and} \quad \mathbf{A} = \frac{1}{\sqrt{\hat{\sigma}}} \mathbf{B} \frac{1}{\sqrt{\hat{\sigma}}}. \quad (6.7)$$

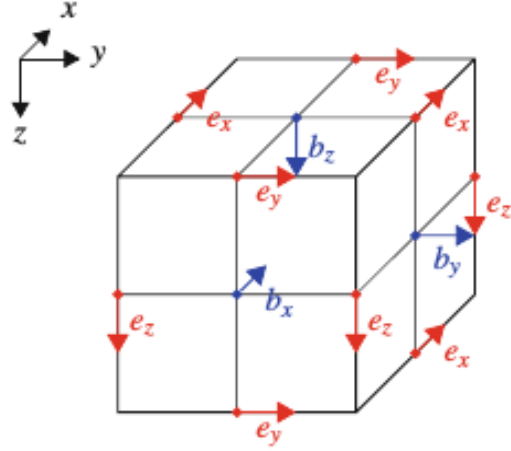


Figure 6.1: Example of a Yee-grid cell forming elementary loops where electric and magnetic field components are assumed to be edge-averaged and face-averaged, respectively (Börner, 2010).

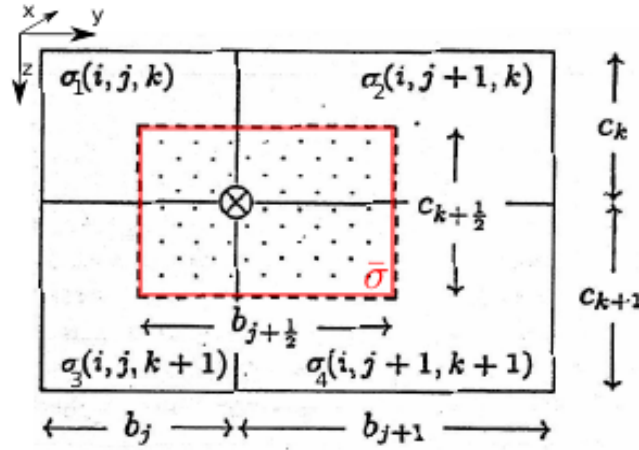


Figure 6.2: Geometry for averaging conductivities with current flow in x-direction. The averaging area is shaded. Image is taken from Yogeshwar (2014), with the original being from (Weidelt, 2000).

To solve the ordinary differential operator in Eq. (6.6), the spectral Lanczos decomposition method (SLDM) is applied. Following Hoerdt *et al.* (1992), an approximate solution of Eq. (6.6) is the Taylor expansion

$$\mathbf{u}_m = \sum_{k=0}^{m-1} \frac{t^k}{k!} \mathbf{A}^k \Phi \quad \text{or, alternatively} \quad \mathbf{u}_m = \sum_{k=1}^m (\mathbf{s}_k^T \Phi) \mathbf{s}_k \exp(-\lambda_k t) \quad (6.8)$$

where λ and \mathbf{s} are the eigenvalues and eigenvectors of system matrix \mathbf{A} , respectively. This approximate solution can be considered as an element of the Krylov subspace (Parlett, 1980; Hoerdt *et al.*, 1992).

$$\mathbf{K}_m(\mathbf{A}, \Phi) = \text{span}(\Phi, \mathbf{A}^1 \Phi, \mathbf{A}^2 \Phi, \dots, \mathbf{A}^{m-1} \Phi) \quad (6.9)$$

An appropriate basis of the Krylov subspace can be obtained using the Gram-Schmidt orthogonalisation. Following Börner (2010), the construction of a Krylov subspace basis consisting of m vectors \mathbf{q} can be achieved by the Lanczos process (Paige, 1980), which is based on the three-term recurrence

$$\mathbf{A} \mathbf{q}_i = \beta_{i-1} \mathbf{q}_{i-1} + \alpha_i \mathbf{q}_i + \beta_i \mathbf{q}_{i+1}, \quad i = 1, \dots, m-1. \quad (6.10)$$

where $\beta_0 \mathbf{q}_0 = 0$, $\beta_i > 0$ and $\mathbf{q}_1 = \Phi / \|\Phi\|$. The algorithm produces a series of m vectors $\mathbf{Q}_m = (\mathbf{q}_1, \dots, \mathbf{q}_m)$ and a tridiagonal matrix \mathbf{T}_m , where

$$\mathbf{T}_m = \begin{pmatrix} \alpha_1 & \beta_1 & & & & & \\ \beta_1 & \alpha_2 & \beta_2 & & & & \\ & & \ddots & \ddots & & & \\ & & & \beta_{M-2} & \alpha_{M-1} & \beta_{M-1} & \\ & & & & \beta_{M-1} & \alpha_M & \end{pmatrix}. \quad (6.11)$$

The Krylov subspace basis \mathbf{Q}_m satisfies

$$\mathbf{A}\mathbf{Q}_m = \mathbf{Q}_m\mathbf{T}_m + \underbrace{\beta_{m+1}\mathbf{q}_{m+1}I_m^T}_{\mathbf{R}\approx 0}. \quad (6.12)$$

I_m is the m^{th} column of the $m \times m$ identity matrix. By neglecting the residuum (second-term on the right) of Eq. (6.12) and rearranging, we obtain

$$\mathbf{A} \approx \mathbf{Q}_m\mathbf{T}_m\mathbf{Q}_m^T, \quad (6.13)$$

which is substituted into Eq. (6.6) so that we have to solve the equation

$$\mathbf{T}_m\tilde{\mathbf{u}} + \partial_t\tilde{\mathbf{u}} = 0; \quad \text{for } t > 0, \quad \tilde{\mathbf{u}}|_{t=0} = \|\Phi\|\mathbf{e}_1 \quad (6.14)$$

where $\tilde{\mathbf{u}} = \mathbf{Q}_m^T\mathbf{u}$ and $\mathbf{e}_1 = (1, 0, \dots, 0)$. The evaluation of Eq. (6.14) is more efficient since the matrix \mathbf{T}_m is much smaller compared to \mathbf{A} . If we denote λ and \mathbf{s} to be the respective eigenvalues and corresponding eigenvectors of \mathbf{T}_m and use the approximation in Eq. (6.8), the final solution is,

$$\mathbf{u}_m(t) = \|\Phi\| \sum_{i=1}^M \mathbf{q}_i \sum_{j=1}^M \mathbf{s}_{ij}\mathbf{s}_{1j}e^{-\lambda_j t}. \quad (6.15)$$

In this process, \mathbf{u}_m becomes a good approximation for \mathbf{u} . Compared to time-stepping algorithms, the asymptotic advantage of `sldmem3t` is proportional to \sqrt{t} , resulting in a significant computational time decrease for large t (*Hoerdt et al.*, 1992).

6.1.1 Grid Design

The main obstacles when applying `sldmem3t` is the necessity of a stable grid to find the correct solution. Stability and correctness for a specific grid are thereby tested against the 1D solution. A similar procedure is advisable when using more complex transmitter geometries. The existing grid generator `make_sldm_grid` by *Martin* (2009) is limited to standard loop or dipole sources. Generally, these standard transmitters are discretised by one or more current lines between two adjacent cells. The whole transmitter geometry is obtained by superposition of the individual current elements. Each current element is positioned at a specific grid node and assigned either a positive or negative current amplitude to compensate for the direction of current flow. These transmitter elements are seen as vectors with dipole lengths according to the spacing between neighbouring grid cells (*Martin*, 2009).

For a finite difference Yee grid, the common TEM/LOTEM transmitters are easy to discretise as the transmitter elements are commonly parallel to the horizontal grid lines. In the past, dipoles running diagonal to the grid lines have also been applied (*Hördt*, 1992; *Druskin and Knizhnerman*, 1994). This diagonal current element is obtained through superposition of two perpendicular current elements running

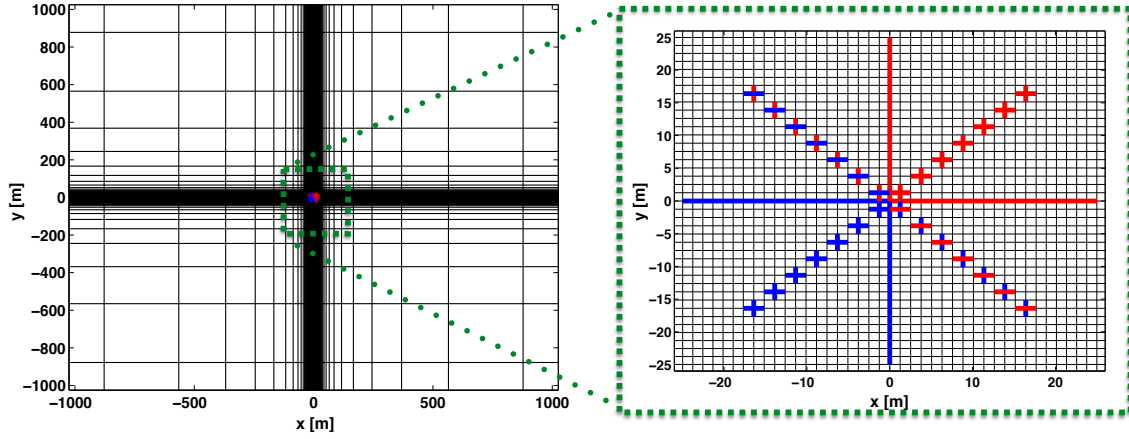


Figure 6.3: Finite difference grid for a Circular Electric Dipole transmitter. The blue and red lines in the right image represent dipole segments with negative and positive currents, respectively.

along the gridlines with common start or end points. The direction of current flow is accounted for by assigning a positive or negative current amplitude. The same approach is applied for the CED transmitter consisting of eight horizontal dipoles arranged in a star-shaped pattern with a central point. A new grid generator was developed for this purpose.

The most stable grid for multi-dimensional CED modelling studies consists of an inner and outer domain. The inner domain around the CED transmitter has linear grid spacing, whereas the outer domain uses logarithmically increasing grid spacing (see Fig. 6.3). The principles of the new grid generator remain consistent with the existing algorithm of *Martin* (2009). Depending on the conductivity structure of the investigated resistivity model and the time range that is being calculated, the grid will have a minimum (s_{min}) and maximum (s_{max}) spacing. Accordingly,

$$s_{min} = a \sqrt{\frac{t_{min}}{\pi \mu_0 \sigma_{max}}} \quad (6.16)$$

and

$$s_{max} = b \sqrt{\frac{t_{max}}{\pi \mu_0 \sigma_{min}}}, \quad (6.17)$$

where $t_{min/max}$ and $\sigma_{min/max}$ are the minimum and maximum values for time and conductivity, respectively. The factors a and b additionally increase the variability of the grid. *Hördt* (1992) proposes values of $a = b = 3$, whereas *Martin* (2009) chooses values of $a = 1$ and $3 \leq b \leq 9$. For small CED antenna of only several meters diameter, stable results are obtained for $a = b = 1/3$. In this case it was often necessary to reduce the value of s_{min} . For CED transmitters consisting of dipole lengths of several hundred meters, the values of $a = 1$ and $3 \leq b \leq 9$ are adequate.

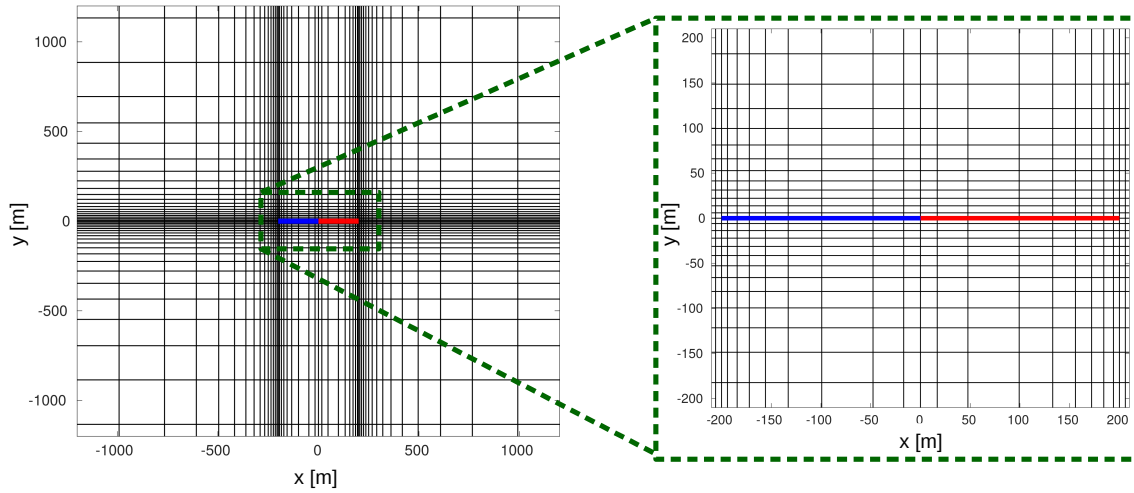


Figure 6.4: Finite difference grid of a Differential Electric Dipole transmitter. The blue and red lines in the left image represent dipole segments with negative and positive currents, respectively.

As the inner grid is used to discretise the transmitter, several requirements are necessary. First, the inner grid must be symmetrical in x - and y -direction to adhere to the symmetry of the transmitter components. Second, grid nodes are needed at $x = y = 0$ m for the transmitter components that run parallel to the grid and for the receivers. Third, horizontal grid nodes are needed at $\pm dl$ and $\pm \cos(45^\circ) \cdot dl$, to mark the lateral extent of the parallel and diagonal components, respectively. The largest gradient of the EM field is expected in the vicinity of the transmitter. Accordingly, the spacing between grid nodes in the outer domain begins with s_{min} in the vicinity of the transmitter and grows logarithmically with distance from the grid centre.

The discretisation in z -direction simply depends on the location of the transmitter. As a marine application is proposed in this study, the grid generator accounts for transmitter systems located on the seafloor, meaning conductive media (seawater) is located above the antenna. In this case, the vertical grid spacing is quite simple. Below the transmitter, the grid spacing starts with s_{min} and increases logarithmically with depth. Above the transmitter, the grid spacing also begins with s_{min} and increases logarithmically to $d_w/2$. After surpassing this point, the grid logarithmically decreases to the surface.

The grid of a DED source illustrated in Fig. 6.4 does not require a linear grid discretisation in the vicinity of the transmitter. Additionally, the x - and y -directions are not symmetrical as the transmitter only extends in the x -direction. Instead, the grid grows logarithmically in x -direction from the centre until half the dipole length is reached. Towards the outer ends of the transmitter, the grid spacing logarithmically decreases. The outer area of the grid is again characterised by a logarithmically increasing grid spacing. In comparison to CED, a DED discretisation causes less instability and is comparable to the efficiency of a standard HED transmitter.

Druskin and Knizhnerman (1994) state that the convergence estimation of Lanc-

zos decomposition method is dependent on the minimum (λ_0) and maximum (λ_n) eigenvalues. For an arbitrary model with constant coefficients these are calculated as,

$$\lambda_0 = \frac{\pi^2}{s_{max}^2 \sigma_{max} \mu_0} \quad (6.18)$$

and

$$\lambda_n = \frac{13}{s_{min}^2 \sigma_{min} \mu_0} \quad (6.19)$$

where s_{min} and s_{max} denote the smallest and largest dimensions of the discretisation. The number 13 describes the maximum number of non-zero elements in a row of the system matrix \mathbf{A} . The Lanczos process obtains an approximate solution of \mathbf{A} within the Krylov subspace. Therefore, *Druskin and Knizhnerman* (1994) present a threshold for the minimum dimension that the Krylov subspace should have. The value of M can be expressed in exact arithmetics as,

$$M = \frac{12}{s_{min}} \sqrt{\frac{t_{max}}{\mu_0 \sigma_{min}}} \geq \frac{1}{s_{min}} \sqrt{\frac{13 \cdot t_{max}}{\mu_0 \sigma_{min}}}, \quad (6.20)$$

where the term in the centre is implemented in the grid generator of *Martin* (2009) and the term on the right is suggested by *Druskin and Knizhnerman* (1994). However, for the intended modelling studies it was found that the value of M is still too small. *Martin* (2009) states that modelling studies in the marine environment generally require a larger Krylov subspace for convergence. Therefore, M is generally determined during the grid checks and subsequently kept fixed for the ensuing modelling studies. A premature truncation at convergence is neglected in the modelling studies.

6.1.2 Convergence of the Solution

The stability of a certain grid is generally verified through a comparative modelling study using a one-dimensional resistivity model prior to the multi-dimensional calculation. The solution of `sldmem3t` is compared to the transients of a 1D forward operator using the resistivity and thickness values used in the subsequent multi-dimensional modelling study. The relative residuals at each time point are used as a systematic error model for the 2D interpretation of field data. *Yogeshwar* (2014) applies these errors in a Gaussian error propagation. However, the errors of `sldmem3t` compared to a 1D forward operator are of systematic nature. Thus, the grid errors of `sldmem3t` are accounted for in the 2D data interpretation by simply adding a systematic error to each datum of the error estimate vector. In case the systematic error is smaller than the minimum assumed error of the measured data, the error remains unchanged. In the presented case, an systematic error $\Delta \mathbf{d}_{i,sldmem} = 2\%$ is added.

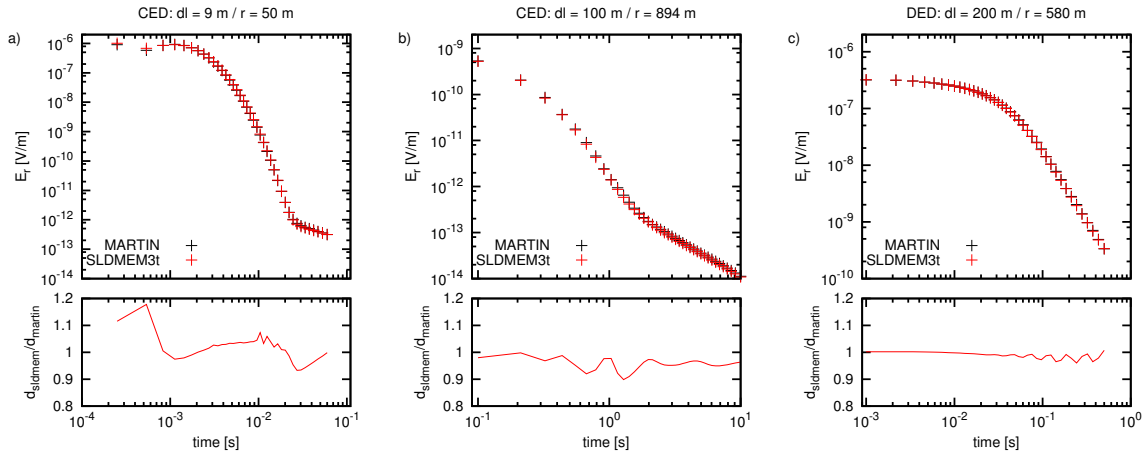


Figure 6.5: Grid checks using one-dimensional resistivity models: (a) small CED transmitter with $dl = 9$ m, (b) large CED transmitter with $dl = 100$ m and (c) DED transmitter $dl = 200$ m. The top images show the calculated transients of `slidemem3t` in red and `MARTIN` in black. The bottom images illustrate the ratios of both signals and is ideally equal to one.

Three output parameters are used to verify the convergence of the solution during the modelling study. Namely, these are RES, PROGN and EPS. As described by *Yogeshwar* (2014), the RES-parameter is the last time point of a specified control receiver, which is printed for a predefined step (generally for every 100 subspaces). Plotting RES against the iterations should show a converging behaviour towards a certain value. Since this parameter only represents one receiver, the one with the shortest offset to the transmitter is generally used, as it will have the largest dynamic range in the electric field. A stable solution in the nearest receiver indicates that receivers with larger offsets have also converged. In the reversed case, this cannot be generalised. PROGN describes the absolute difference of RES from the current iteration to a previous one. Hence, if the solution is converged, this value should ideally be zero, or in the majority of cases, close to zero. The EPS-parameter describes the rel. difference of RES from the current iteration to the previous one. This value is used in the Lanczos process to truncate the calculation if a predefined minimum threshold is surpassed. However, as the value of RES often oscillates at small iterations, the threshold may also be surpassed before the solution has actually converged. Therefore, the value is set to a $10^{-12}\%$ so that the calculation only truncates at the maximum number of subspaces M specified during the grid check.

To demonstrate the standard “Grid-Check” as applied, the following CED and DED models are used. We assume both transmitters to be seafloor based with a standard 1D resistivity model of $\rho_{1-3} = (1 \text{ } \Omega\text{m}, 100 \text{ } \Omega\text{m}, 1 \text{ } \Omega\text{m})$. The depth of the layers are dependent on the desired modelling study. For example, the studies of *Goldman et al.* (2015) and *Haroon et al.* (2016) required a CED with dipole lengths of 100 m. In this hydrocarbon modelling study, the resistive target formation is located at a depth of 1000 m beneath the seafloor. For the Israel model, the standard depths presented in the 1D modelling study are used. The DED transmitter has dipole

lengths of 200 m, whereas the CED transmitter ones of 9 m and 100 m. Three exemplary grid checks for a small CED, a large CED and a DED transmitter are displayed in Fig. 6.5a, Fig. 6.5b and Fig. 6.5c, respectively. The solution of `sldmem3t` is displayed in red, the one of `MARTIN` in black. The bottom images show the ratio of the signals and is ideally equal to one, in case the solutions are identical.

In general, the small CED with short-offsets shows the poorest result, especially at early times where relative errors exceed 10%. Also, the `sldmem3t` has minor errors in the range of largest curvature after $t = 10^{-2}$ s. In comparison to the grid checks shown by *Yogeshwar (2014)* and *Lippert (2015)*, the errors presented in Fig. 6.5a are larger. In part, the applied model has a larger resistivity contrast (three orders of magnitude) resulting in greater inaccuracies. Additionally, the small signal amplitudes and large dynamic range of the signal at short offsets may reduce the correctness of the solution. A large CED transmitter displayed in Fig. 6.5b, exhibits a greater consistency to the 1D solution. It is conspicuous that the greatest errors again occur in the time range of the largest curvature. However, the errors are much smaller compared to the small CED. The DED grid exhibits the lowest deviations to the 1D solution. Merely, the late times of the `sldmem3t` solution oscillate around values of the 1D solution. The signal ratios remain within the range of one, implying an adequate grid.

The `sldmem3t` output parameters RES, PROGN and EPS for the DED solution of Fig. 6.5c are displayed in Fig. 6.6a through Fig. 6.6c, respectively. The number of M iterations needed for convergence is significantly higher compared to modelling studies conducted with loop sources, e.g. *Yogeshwar (2014)*. In part, t_{max} is larger in the presented modelling studies, which directly influences the required subspace dimension M (refer to Eq. (6.20)). Moreover, *Martin (2009)* states that a larger value of M is required for calculating multi-dimensional models and for studies in the marine setting. Both cases apply to the presented modelling studies. The average applied value of M is between 35000 and 45000. As displayed in Fig. 6.6a, the RES parameter begins to converge at $M > 30000$. PROGN describes the absolute difference of RES for consecutive iterations. Hence, the smallest values are found where RES is small. At the stage where RES converges, a slight decreasing trend in PROGN is noticeable. However, the ideal value of zero is not reached. EPS tends to decrease as M increases with a final value of approximately $10^{-2}\%$. However, it is

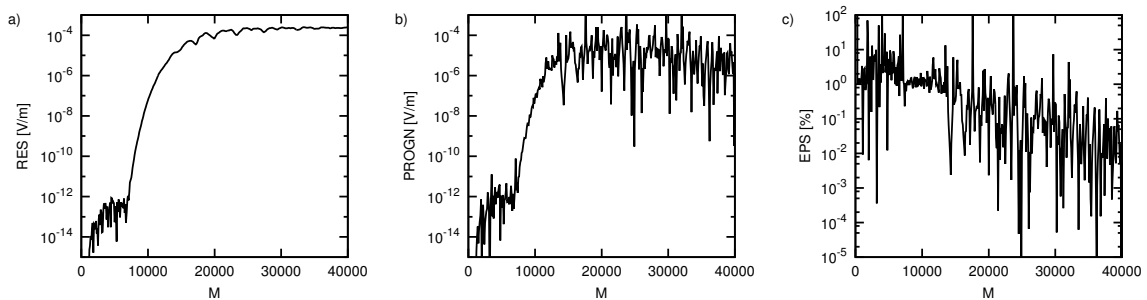


Figure 6.6: `sldmem3t` output parameters (a) RES, (b) PROGN and (c) EPS plotted against the number of Krylov subspaces for the `sldmem3t` solution shown in Fig. 6.5c.

not significant as none of the models were truncated before reaching the predefined number of M .

6.2 The 2D Aquifer Model

In the preceding chapter, the submarine freshwater aquifer was treated as a resistive layer with infinite lateral dimensions. However, in reality, this resistive body has lateral dimensions. Consequently, a 1D interpretation is not completely sufficient, especially in the vicinity of the aquifer edge. Additionally, the 1D models assume a constant bathymetry. As the measurements are conducted in the coastal region, this assumption does not hold. The following 2D modelling study will therefore address the following questions:

1. How does the bathymetry influence the data? Is it possible to interpret the data using 1D inversion, although transmitter and receiver are positioned at different water depths? What water depth should be used for the 1D inversion in order to minimise interpretation errors?
2. Does the 2D data show clear indications regarding the position of the transition zone?
3. Is the 2D data in the vicinity of the transition zone of the aquifer interpretable using 1D inversion? Are 2D effects noticeable in the 1D inversion models?
4. How do step-on/off signals react to both the bathymetry and the transition zone in comparison?

The first part of this section deals with constructing the marine aquifer model. The encountered challenges of combining the bathymetry, while maintaining an extended transmitter are elaborately discussed. Furthermore, the bathymetry may cause the transmitter and receiver to be located at different water depths. However, the 1D inversion approach does not account for this without considerably manipulating the resistivity model. To study the resulting effects, a 2D data set calculated in a region of large bathymetry is interpreted using 1D forward modelling and inversion. Thereby, the water depths are varied between values including the true water depth at transmitter and at the receiver. Modelling studies and inversion models are elaborately discussed to justify the ensuing procedure in interpreting measured DED data. Subsequently, the 2D-effect of the aquifer transition zone is investigated using profile plots. These curves are useful, as the calculated 2D data exhibits obvious behaviour that allows a clear detection of the aquifer edge along the profile. Finally, the generic 2D data is linked to the error model presented in Section 5.1 and interpreted using 1D Occam inversion. The latter is important as our primary tool for interpreting the measured data is 1D inversion. Apparent 2D effects in the 1D Occam inversion models are used to discuss the results of the measured data in Chapter 8.

6.2.1 Constructing the Bathymetry Model

Constructing the 2D model is complicated, as the seafloor bathymetry has to be taken into account. Prior to the measurements, bathymetry data was sparse and therefore, the following synthetic modelling study was conducted using an assumed bathymetry model taken from a nautical map and the model of *Lippert (2015)*. Compared to the true bathymetry model provided by the Israel Oceanographic and Limnological Research that was used to interpret the measured data, the applied model generally over-guesses the water depths by 0–3 m, depending on the distance to the coast.

One of the main difficulties of applying any CSEM method in coastal regions is the bathymetry in connection with the shallow water. The resistivity model of the subsurface is clearly not one-dimensional in this setting. Moreover, the bathymetry will also effect the alignment of the towed system as transmitter and receiver will not be parallel to the water surface, but rather follow the bathymetry. Hence, symmetrical errors (as investigated in Chapter 5.3) may also have to be considered if the bathymetry is too large. However, a more vital issue is how the real subsurface is discretised in either a multi-dimensional resistivity model using a finite-difference scheme or in a 1D resistivity model using the developed forward algorithm. Figure 6.7 shows sketches of the scenarios and illustrates how the bathymetry-issue is approached in terms of model discretisation. Note, the images in Fig. 6.7 are meant to exemplify and, therefore, exaggerate the problem. In truth, the bathymetry along the profile is not that extreme. As displayed in Fig. 6.7a, the transmitter and receiver align along the seafloor following the bathymetry. In this case, differences to a 1D interpretation (see Fig. 6.7c) are not only found in the different water depths at the transmitter and the receiver, but also to the inclination of the transmitter/receiver dipoles. The latter is previously discussed in Chapter 5.3. The following study will confine on investigating the influence of the water depth for a 1D interpretation. In 2D forward modelling using `sldmem3t`, the subsurface is discretised using a finite difference scheme. In this case, the main obstacle is to reproduce the correct bathymetry model using the finite-difference grid, while maintaining a stable solution for a given transmitter. The approach of *Lippert (2015)* was followed, where a horizontal plateau was created at each transmitter position to inevitably simplify

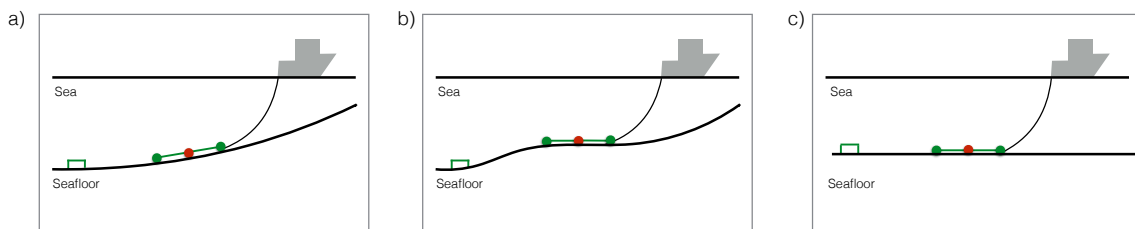


Figure 6.7: A sketch of the (a) true bathymetry model in the coastal region of Israel, (b) the adjusted bathymetry model applied for a 2D modelling study and (c) the 1D bathymetry model. Note, for (b), the bathymetry has to be altered to a plateau in the vicinity of the transmitter to minimise discretisation errors and maximise grid stability.

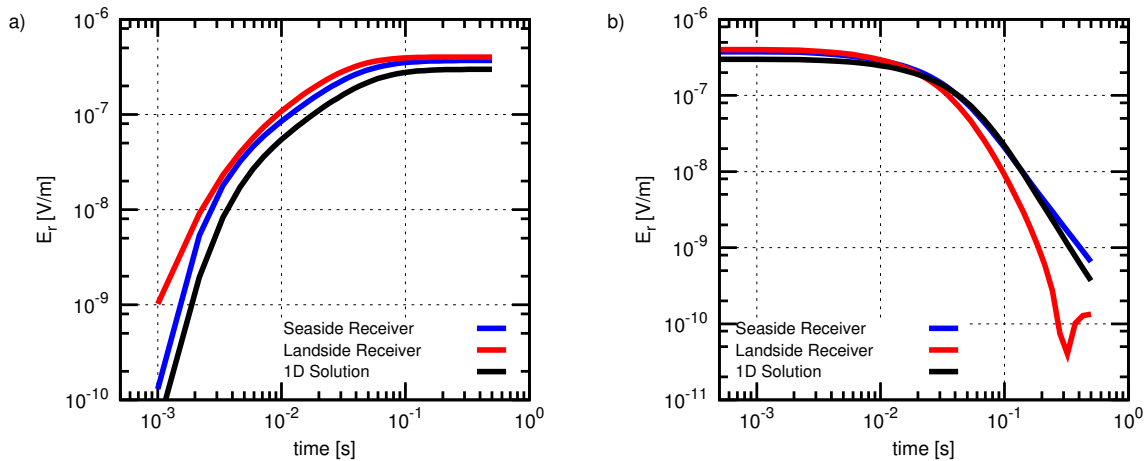


Figure 6.8: Synthetic transients of a 2D bathymetry model located at TX1 (see Fig. 6.9) for the sea-side receiver (red), land-side receiver (blue) and for a 1D case (black). The transmitter is located at a water depth of 26.6 m, whereas RxSea at 31.75 m and RxLand at 19.6 m. Both receivers are at offsets of 580 m. In (a) step-on signals and in (b) step-off signals.

the transmitter discretisation (see Fig. 6.7b). However, the majority of his modelling studies were conducted using a transmitter parallel to the coast, where no plateau is required.

The following modelling study and the 2D data interpretation of the measured data in Chapter 9 does not account for the true bathymetry as displayed in Fig. 6.7a. Instead, the 2D modelling studies confine to model types as displayed in Fig. 6.7b, whereas all 1D interpretations are restricted to the seafloor discretisation displayed in Fig. 6.7c.

The water depth ranges from 0 m at the coastline to approximately 37 m at a distance of 4800 m from the coastline. As mentioned, each transmitter position is altered to a plain of ca. 400 m to account for the elongated transmitter antenna. Thus, the models calculated at each transmitter differ slightly.

The bathymetry study will focus on two types of transmitter-receiver configurations. The first configuration simulates towing the system away from the coastline. Due to the design of the applied DED system (refer to Chapter 7), the receiver is located between the transmitter and the shoreline. This setup will be referred to as the land-side receiver or RxLand. The other arrangement is referred to as the seaside receiver or RxSea. Accordingly the system is towed towards the coastline and the receiver is located towards the sea. In both cases, signals are calculated for offsets of 580 m, coinciding with the far offset applied in the field measurements.

Different Water Depth at Transmitter & Receiver

Although the investigated subsurface resistivity model is multi-dimensional, 1D inversion serves as the primary interpretation tool of the measured DED data. The measurements are conducted in the coastal area and consequently, transmitter and

receiver are typically located at different depths. This especially applies to the stations located in the immediate vicinity of the coastline. The differences in water depths between transmitter and receiver reaches a maximum of 7 m at an offset of 580 m in this region. In a one dimensional forward model, bathymetry is not accounted for as the seawater is considered to be a horizontally layered block with a certain thickness. Is it possible to use one-dimensional models to correctly reconstruct the sub-seafloor resistivity structure in the presence of bathymetry? If so, what depth should be used? The depth at the transmitter, the depth at the receiver or a mean water depth? Does the chosen depth differ for RxLand and RxSea?

To illustrate the effect of a 2D bathymetry model on DED data, a selected transmitter location at 2000 m from coastline is chosen exemplarily. The calculated transients are displayed for step-on and step-off signals in Fig. 6.8a and Fig. 6.8b, respectively. Note, the applied subsurface resistivity model is illustrated in Fig. 6.9a. Clearly, the bathymetry and transmitter-receiver configuration respective the coastline have an obvious influence on the data. A similar effect has been published by *Goldman et al.* (2011), who studied the increase of target response for broadside magnetic field receivers located between transmitter and coast. The authors specifically mention that this is only valid in the short-offset range. The offsets applied here are greater compared to their study. Consequently, it remains unclear if the differences between RxSea and RxLand are explained by the coastal effect described by *Goldman et al.* (2011). An analysis of this issue could be of interest, but remains beyond the scope of this thesis. In the following, the focus lies on assessing if the transients are interpretable using 1D inversion.

The most apparent issue of the data shown in Fig. 6.8 concerns the step-off signal of the land-side receiver. It contains a sign-reversal at late times produced by the influence of the bathymetry. A 1D inversion of this transient is generally only possible if all data points following the sign-reversal are neglected. However, the interpretation remains misleading similar to the geometric error study in Section 5.3.2. The appearance of the sign-reversal will magnify the resistive aquifer as the decay is much steeper compared to the 1D solution. In case of a homogenous seafloor consisting of sediments, the sign-reversal will produce an imaginary resistive layer to appear in the inversion model leading to a misinterpretation of the data. Intriguingly, the step-off signal of the RxSea possesses no sign-reversal, allowing an interpretation using 1D inversion. Yet, problems may arise due to the moderate decay (compared to the 1D solution) of the transient. Ultimately, the response of the resistive aquifer is masked by the bathymetry. Accordingly, the step-off signal of RxSea is less effective in detecting the resistive aquifer using a 1D inversion approach. This agrees with modelling studies conducted by *Goldman et al.* (2011).

The step-on signals presented in Fig. 6.8a appear to be shifted by a quasi-static value due to the influence of the bathymetry. Thus, a 1D inversion of both step-on data sets is feasible. If a realistic resistivity model is retainable from the step-on signals will be investigated in the following. However, RxLand will again produce a magnifying effect towards a resistive layer due to the increased DC voltages and much larger amplitudes at early times.

For the following 2D bathymetry study, the resistivity values and depth/thickness

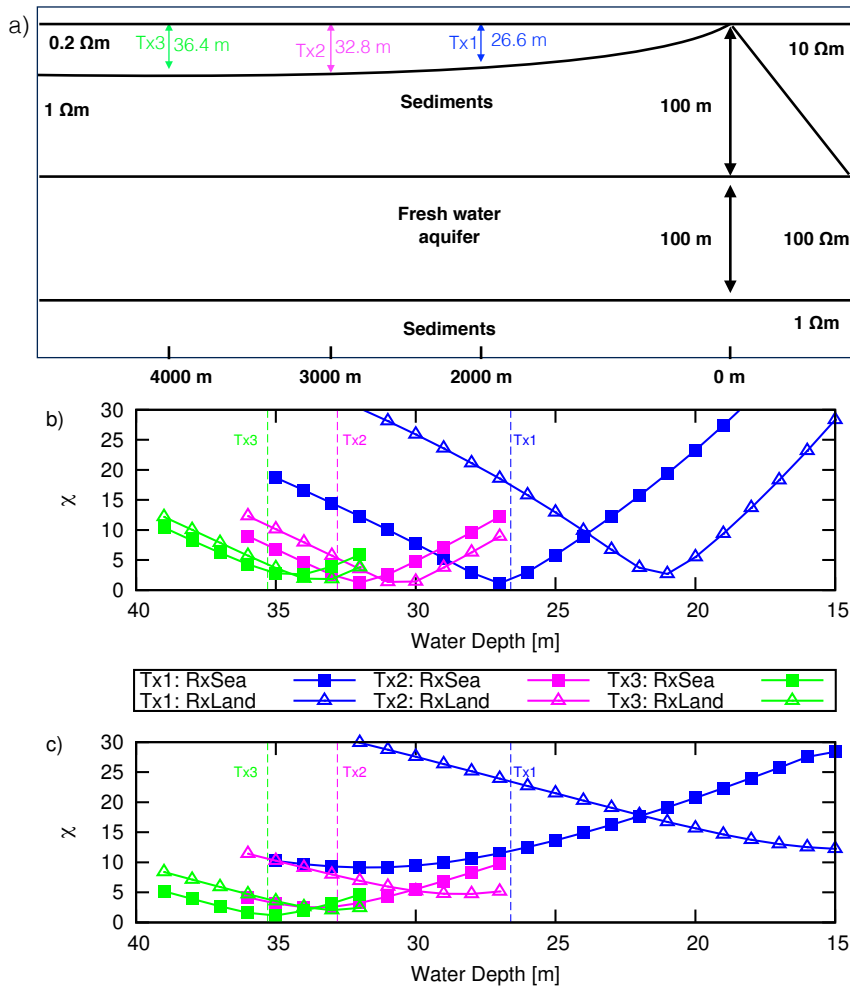


Figure 6.9: (a) Schematic of the 2D resistivity model used for the modelling studies. The data fit for different water depth of a 1D resistivity model are presented for (b) step-on and (c) step-off. Three exemplary transmitter locations are investigated displayed by blue, pink and green colours. Square and triangular markers are used for the sea-side (RxSea) and land-side (RxLand) receivers, respectively.

of the freshwater aquifer is known at every transmitter and receiver station of the generic 2D model. Therefore, the model parameters are convertible to a 1D resistivity model. For example, the 1D model underneath the transmitter located 2000 m from the coast at a depth of 26.6 m would have the following parameters: $\rho_{1-3} = [1 \text{ } \Omega\text{m}, 100 \text{ } \Omega\text{m}, 1 \text{ } \Omega\text{m}]$ and $d_{1-2} = [73.4 \text{ m}, 100 \text{ m}]$. A suitable 1D model is one, where the depth of the aquifer remains constant at 100 m below the sea-surface, but water-depth and sediment thickness variations achieve a minimum data fit χ or data fit of $\chi \leq 1$. As mentioned, only water depth and sediment thickness d_1 are adjusted accordingly, so that the aquifer remains fixed at 100 m beneath the sea-surface. The error model introduced in Section 5.1 is applied. A resulting error of $\chi \leq 1$ will imply that the 2D signal distortion caused by the bathymetry diminishes within the assumed error-bounds and is negligible. In this case, the 2D data can be fitted by the correct aquifer thickness, depth and resistivity values using a 1D approach. This modelling study is conducted for three exemplary transmitter

locations. The true water depth of each transmitter and the corresponding receivers are listed in Table 6.1.

The modelling study for the three exemplary transmitter locations is displayed in Fig. 6.9a. A receiver is located on either side of each transmitter position, referred to as RxSea and RxLand, respectively. The corresponding errors of RxSea are displayed by square markers, RxLand by triangular markers. Both are colour-coded with their corresponding transmitter. Tx1 is marked blue and RxSea and RxLand are located at a water depths of 31.75 m and 19.6 m, respectively. The resulting χ -errors are illustrated as a function of water depth in Fig. 6.9b and Fig. 6.9c for step-on and step-off excitations, respectively. For better reference, the true water depths of the transmitters are marked by vertical lines and labelled accordingly. The true water depth of either receiver is found in Table 6.1

Table 6.1: True water depths for the three exemplary transmitter positions.

	Transmitter	RxLand	RxSea
Tx ₁	26.6 m	19.6 m	31.75 m
Tx ₂	32.8 m	29.8 m	33.9 m
Tx ₃	35.3 m	34.1 m	36.4 m

The errors of the step-on signal displayed in Fig. 6.9b contradict the conclusions made by *Lippert* (2015). Based on similar modelling studies, he suggests to use the mean water depth between transmitter and receiver for a 1D interpretation. However, the presented results also indicate that the receiver position plays a relevant role. The lowest errors of RxSea are achieved at the transmitter water depth, whereas RxLand achieves a minimum error for water depths that are neither at the transmitter, receiver nor the mean value. The reasons for this contradiction to *Lippert* (2015) may be diverse. He conducted modelling studies for a HED transmitter that extends parallel to the coastline. Consequently, no imaginary plateau was needed in the bathymetry to discretise the transmitter. Moreover, the broadside LOTEM step-off signals will generally possess a sign-reversal for the investigated model and may therefore also behave differently compared to the DED step-on signals presented in Fig. 6.9b. Yet, the step-off signals presented in Fig. 6.9c are also not consistent. For shallow water, the best fit model tends to demand the water depth at the receiver. With increasing distance to the coast, RxSea achieves minimum errors for water depth at the transmitter, whereas RxLand requires the depth of the receiver (see curves of Tx3).

The most apparent characteristic of the error curves is the overall decrease of errors for larger water depths. This is in agreement with the LOTEM studies of *Lippert* (2015) that show the importance of the chosen water depths for transmitters/receivers located at depths between 15 m and 30 m. This region of the profile has the largest bathymetry effect and will influence the 1D interpretation most.

Up to now, the analysis is based on forward modelling studies, but has not been investigated for 1D inversion. The three exemplary transmitter positions displayed in Fig. 6.9a are interpreted using a 1D Marquardt inversion using different starting models with a fixed and predefined water depth. The results of the step-on signal are presented in Fig. 6.10. The top row shows the inversion models, the bottom

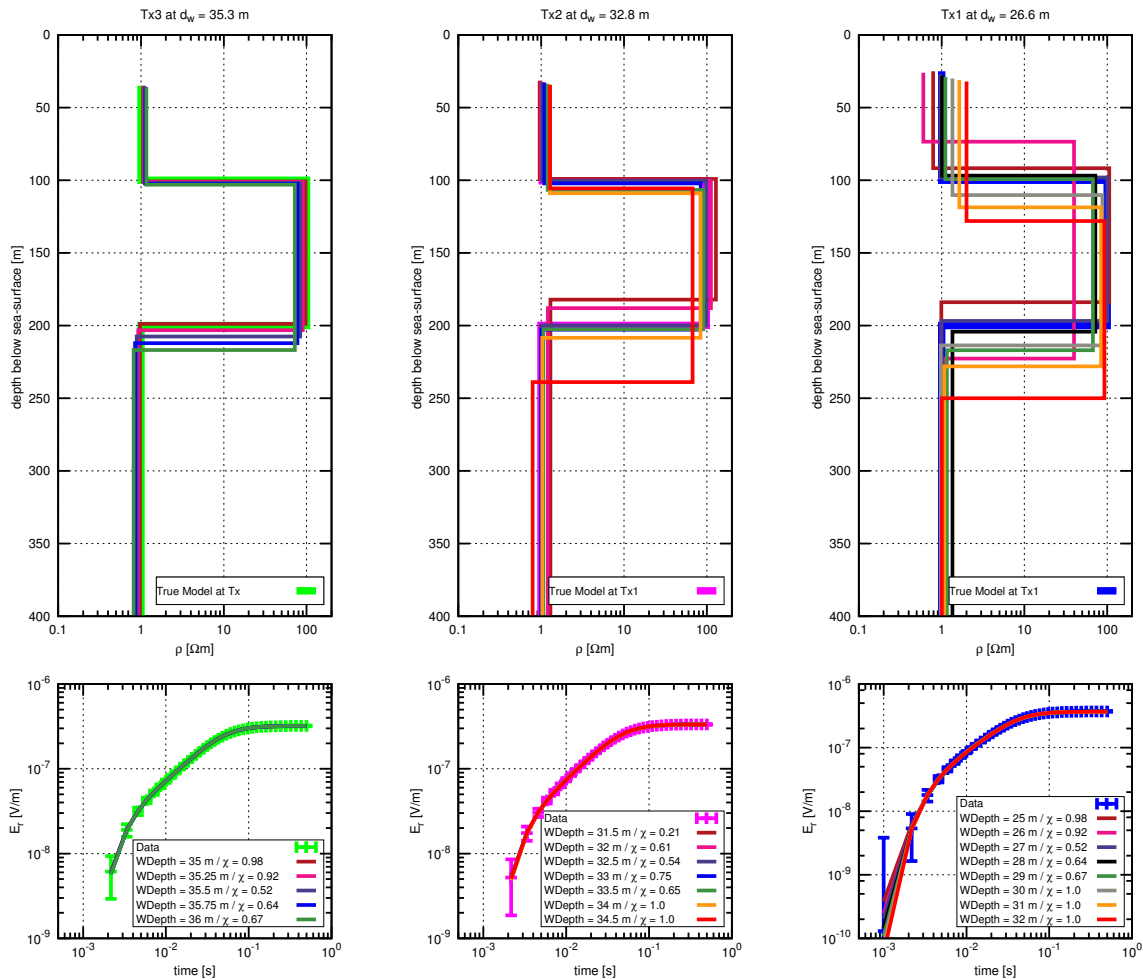


Figure 6.10: 1D Marquardt inversion of 2D-data for different predefined water depths. The transmitter Tx3, Tx2 and Tx1 are displayed in the left, centre and right images respectively. The top row illustrates the best-fit Marquardt inversion models, the bottom row the corresponding data fits.

row the corresponding transients. Note, the true-model and the 2D data is colour-coded with the respected transmitter position for better reference. As expected from the forward modelling study, the transmitter located in the region closest to the shoreline is most affected. The inversion models at Tx1 suggest that the water depth at the transmitter will lead to the most realistic solution. However, all models up to the mean water depth ($d_w \approx 29$ m) are consistent. The models with thicker water columns exaggerate the depth of the aquifer and the resistivity of the seafloor sediments. Although this effect is less prominent for Tx2, similar behaviour is noticeable. For transmitters located in regions of moderate bathymetry, a 1D interpretation becomes feasible. This is exemplified by Tx3, where only small differences in the inversion models are noticeable for different water depths. The inversion models of the step-off signals are not shown in the scope of this thesis as they are difficult to interpret without removing the sign-reversals prior to 1D inversion.

In conclusion, the bathymetry has a significant influence on the DED data. Espe-

cially RxLand has considerable distortions leading to sign-reversals of the step-off transient at late times. Adversely, the bathymetry effect will partly mask the aquifer response in the step-off transient of RxSea. Commonly, the step-on transients are less affected by the bathymetry as the minimum errors of the forward models approach $\chi = 1$. However for the specific model, the correct water depth for a 1D interpretation is difficult to choose, as mean depth values do not necessarily reconstruct the true sub-seafloor resistivity-depth structure.

Overall, a 1D interpretation of 2D data affected by bathymetry is technically possible, especially for step-on transients. For large distances to the coast, where the bathymetry is moderate, sufficient results are achieved using 1D inversion. In this setting, the chosen water depth has only limited effect on the resulting inversion model. Transmitters located closer to the coast have a significant 2D signal distortion. In this case, the chosen water depth has a strong influence on the inversion model. The choice of water depth is not only dependent on the type of current signal, but also on the specified Tx-Rx configuration.

For the following interpretation of synthetic DED data and the subsequent 1D inversion of measured DED data, the following conclusions are applied in terms of 1D inversion: For data acquired and/or modelled for a sea-side receiver, water depths at the transmitter are used for 1D inversion. For land-sided receivers, water depths of the mean value are used. If no convergence is reached for the latter, the water depth is successively decreased until the receiver water depth is reached.

6.2.2 The Aquifer Boundary

The position from the coastline and shape of the freshwater/seawater transition zone are the main targets of the marine DED experiment. The intention of applying a DED system instead of other conventional marine EM methods is the increased lateral resolution of DED (*Haroon et al.*, 2016). The question remains if DED is able to detect the position of the sub-seafloor aquifer edge and, additionally, distinguish between different mechanisms controlling the shape of the aquifer boundary. The following 2D modelling studies theoretically substantiate if DED is applicable to distinguish between a closed aquifer system or an open aquifer system, as presented by *Amir et al.* (2013). For the future exploitation of this freshwater body such information is vital to develop a rational water-management scheme. Additionally, long-term experiments may be installed to monitor the sequential changes of the aquifer.

Sketches of possible aquifer scenarios are illustrated in Fig. 6.11. The following resistivity models are assumed two-dimensional so that the resistivity in the third dimension is assumed constant. The first model is characterised by a vertical aquifer boundary (see Fig. 6.11a). In this case, the lower sub-aquifers thin out westwards passing into an aquicludal shale sequence that prohibits seawater to interact with the freshwater (*Kolton*, 1988; *Kafri and Goldman*, 2006; *Amir et al.*, 2013). The coastal observations of *Kafri and Goldman* (2006) and the marine LOTEM experiments of *Lippert* (2015) indicate that this possibility is conclusive as

resistive layers correlating to a freshwater aquifer are only found in the Palmahim region. The second model, displayed in Fig. 6.11b is characterised by a typical wedge-form representing a freshwater/seawater interface. This possible boundary shape was introduced by *Kafri and Goldman (2006)*, who based their illustrations on studies by *Kapuler and Bear (1970)*. In this case, seawater encroachment is occurring and the typical wedge-form of the freshwater-seawater interface is formed due to the density contrast of salt water and fresh water. The third model presented in Fig. 6.11c is based on *Amir et al. (2013)*, who presented numerical simulations of the same coastal aquifer. In their simulations, a brackish water zone is noticeable for the open aquifer scenario that is located to the west of the boundary. According to *Amir et al. (2013)*, this transition zone is likely characterised by a resistivity gradient, but is assumed to have a mean resistivity of $10 \Omega\text{m}$ for the sake of simplicity.

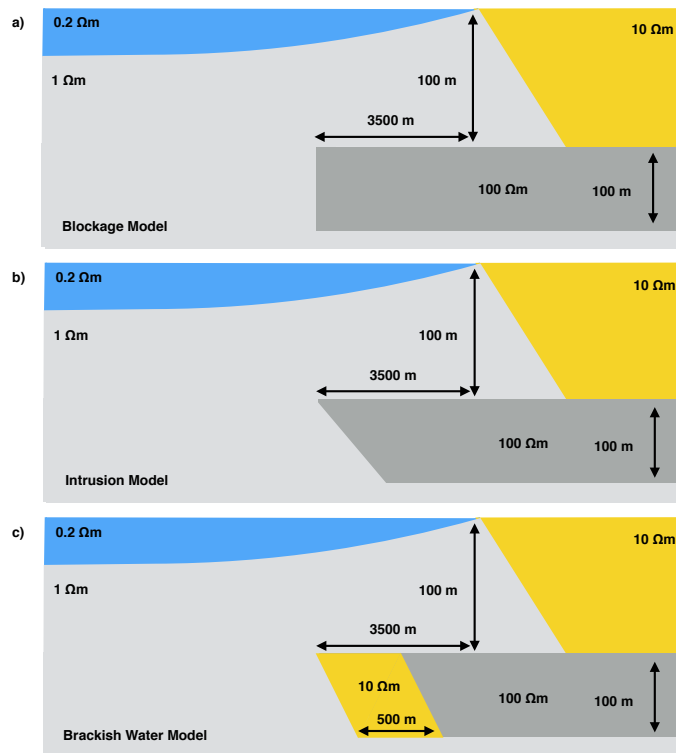


Figure 6.11: Schematic sketches of the 2D resistivity model used for modelling. In (a) the aquifer is blocked to the sea and no seawater encroachment occurs. In (b), seawater intrusion is occurring without a mixed-water zone ahead. In (c), a brackish water zone is located ahead of the freshwater body.

In the course of the following modelling study, the different aquifer boundary conditions are investigated in terms of variations in the transient response of marine DED data. For all aquifer models, the western edge is assumed to be located at profile meter 3500 m . The coastline is assigned profile meter zero. Furthermore, the aquifer is located at a depth of 100 m beneath the sea-surface. It is assumed that the depth of the aquifer does not change, only the thickness of the seafloor sediments is adjusted according to the bathymetry model.

The DED system is towed along a profile running perpendicular to the coastline and the aquifer boundary. The transmitter has a radius of 200 m with 1 A current amplitude. The receiver is towed along with the transmitter at a constant offset of 580 m . A transient is calculated every 100 m . The bathymetry study in the preceding section shows that the transient response is also dependent on the position of the receiver with respect to the transmitter and the coastline. Therefore, the following studies simulate towing the system towards and away from the coast, corresponding to a negative and positive profile direction. Again, the receivers are referred to as

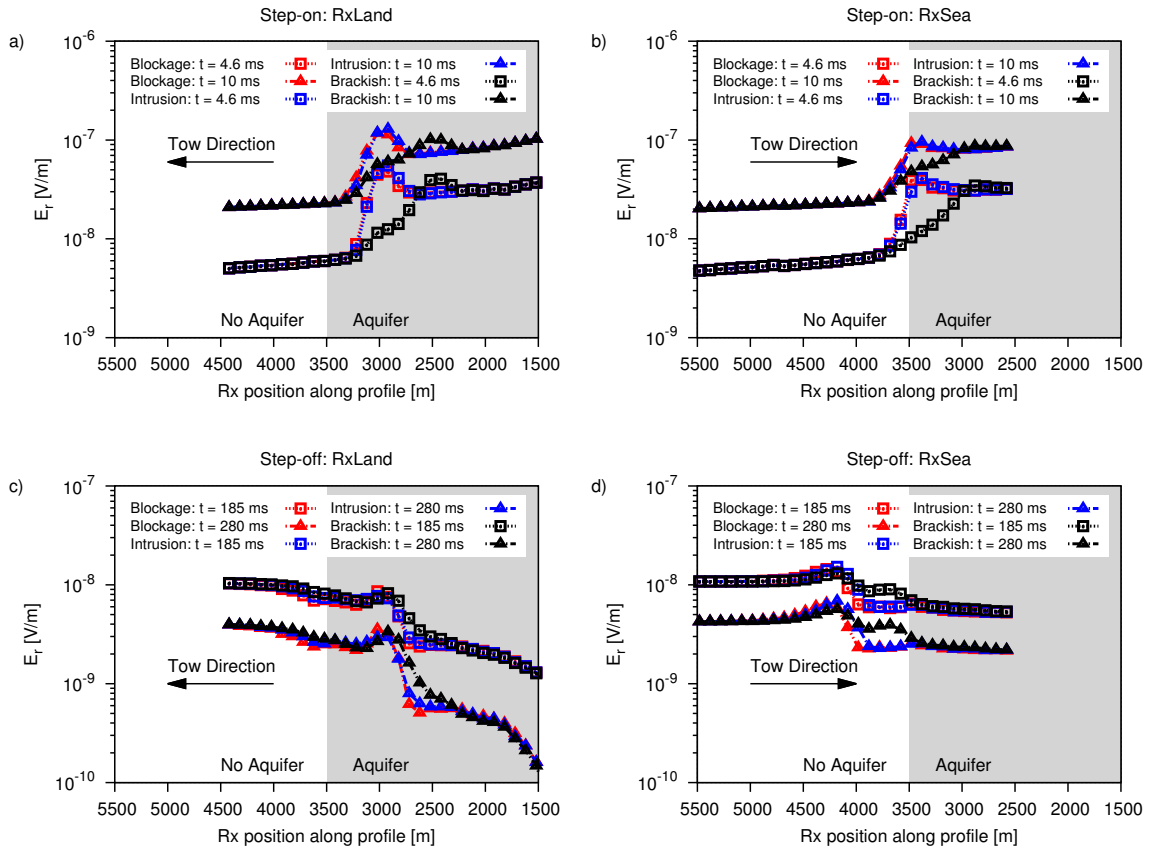


Figure 6.12: Profile plots for the three aquifer models displayed in Fig. 6.11 displayed by the red, blue and black lines, respectively. Two selected time delays are highlighted by square or triangular markers. The profile plots are displayed for RxLand (a and c) simulating a tow towards the sea, and for RxSea (b and d) simulating a tow towards the coast. The top row displays the step-on signals, the bottom row the step-off signals.

RxLand and RxSea, depending on their position with respect to the transmitter and Israeli coast.

Profile curves for selected delay times, chosen from the maximum normalised response of one-dimensional modelling studies are displayed in Fig. 6.12. Note, delay times of 500 ms for a step-off response are not considered due to the sign-reversal caused by the bathymetry. The signal amplitudes are plotted as a function of the receiver position along the profile. Accordingly, RxLand displayed in Fig. 6.12a and Fig. 6.12c are shifted more towards the coast, whereas RxSea in Fig. 6.12b and Fig. 6.12d is shifted towards the sea. The direction of tow is displayed for reference. However, an actual towing phase is not considered in the study. The position of the aquifer boundary is marked by the grey shaded background. Each figure contains six curves corresponding to the vertical, intrusion and brackish-water aquifer models displayed in Fig. 6.11a through Fig. 6.11c, respectively. In Fig. 6.12, these models are illustrated by red, blue and black curves, respectively. The two selected time delays are highlighted by square and triangular markers.

The step off signals, displayed in the bottom row of Fig. 6.12 are independent of

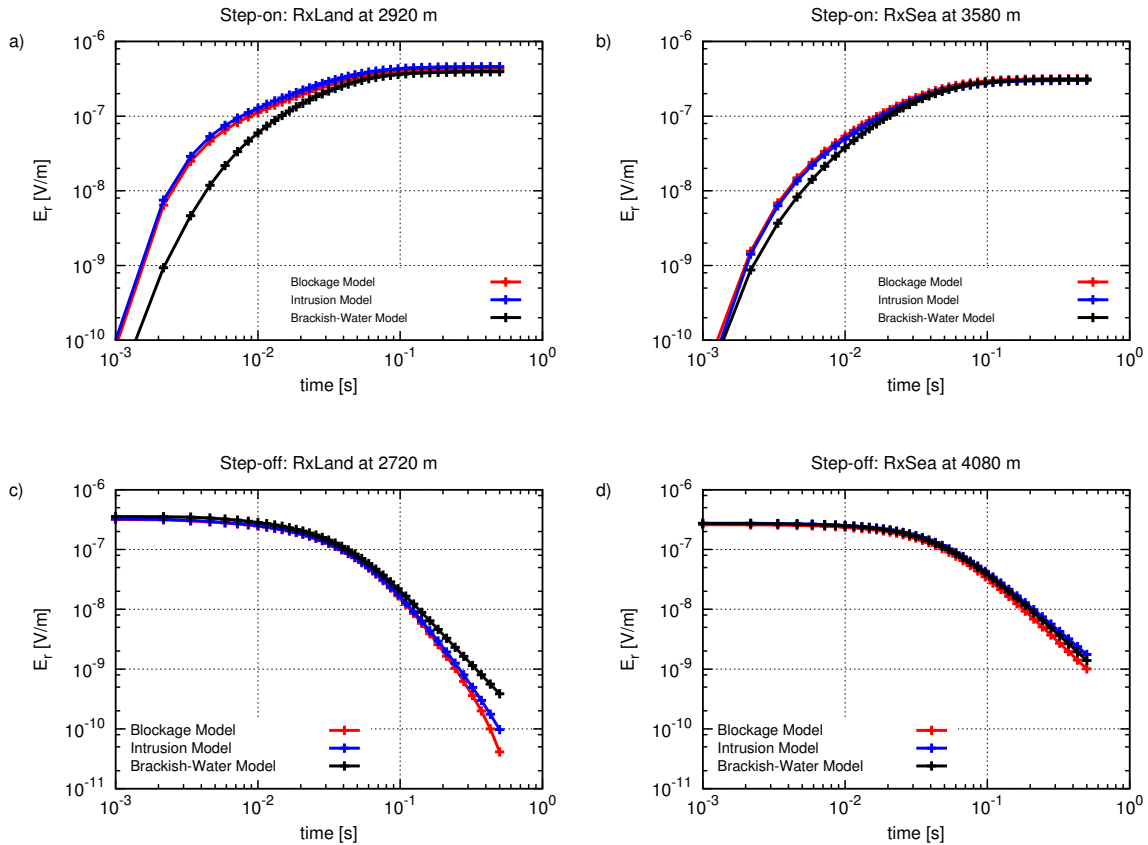


Figure 6.13: Transients corresponding to the three aquifer models shown in Fig. 6.11 are displayed by the red, blue and black lines respectively. The position of each transient is chosen at favourable locations determined by the profile plots in Fig. 6.12. Transients of RxLand are displayed in (a) and (c), RxSea in (b) and (d). The top row displays the step-on signals, the bottom row the step-off signals.

the tow direction. The aquifer boundary is detectable at either receiver as the transmitter crosses the resistivity discontinuity. Consequently, the lateral signal variation is either shifted towards the sea or towards the coast, depending on the direction of tow. The amplitudes acquired at RxLand are more than an order of magnitude lower compared to RxSea. This coincides with Fig. 6.8, where the signal amplitudes above the aquifer are clearly decreased for the land-side receiver. In contrast, the step-on signals displayed in the top row of Fig. 6.12 exhibit a greater dependency towards the tow direction. If RxSea is considered, the information regarding the position of the lateral resistivity discontinuity is registered as the receiver passes over the edge. Intriguingly, this does not apply to RxLand, where the 2D resistivity structure is acquired as the transmitter passes over the structure. This information is important when evaluating the measured data, as the position of the aquifer boundary may be misinterpreted, if the transmitter-receiver configuration is not taken into account.

Based on the profile curves alone, different hydrogeological scenarios at the western boundary are observable. A brackish water zone at the head of the aquifer is

distinguishable from the other scenarios. The slope of the profile curves is moderate compared to the other models due to the lower resistivity contrast between the background sediments and the brackish water. However, no obvious difference is noticeable between the curves of the Blockage and the Intrusion model. These may become apparent at other delay times, which is briefly investigated in Fig. 6.13.

Transients at favourable positions along the profile are presented in Fig. 6.13. Each signal and TxRx-configuration is represented. The transient colours are in unison with Fig. 6.12. Clearly, the step-off response of RxLand at 2720 m shows the greatest contrast in transient behaviour for different aquifer facies. Compared to the step-off response of RxSea, a contrast is apparent even between the Interface and Blockage model. The largest discrepancy is found at a time delay of 0.5 s, which may be problematic in terms of SNR or sign-reversals caused by bathymetry. The 1D modelling studies show that the step off response reaches the assumed noise level at approximately 200 ms for 3000 stacks. Accordingly, the SNR issue remains one of the limiting factors for interpreting the step-off transients. Additional technical considerations must be made prior to the measurements to allow sufficient data quality at 0.5 s.

The step-on transients displayed in the top row of Fig. 6.13 are inferior to the step-off signals in terms of detecting different aquifer boundary facies. An apparent difference in the transients of the Interface and Blockage model is not noticeable. An interpretation of the step-on signal may not adequately address the hydrogeological structure at the western aquifer boundary. However, the magnifying effect towards the sub-seafloor aquifer at RxLand, the distinguishable response of the Brackish water model and the possibility of interpreting the signal using 1D inversion makes its acquisition desirable.

In conclusion, the DED method is quite effective in locating the lateral extent of the sub-seafloor aquifer as profile curves exhibit a drastic increase and/or decrease of amplitude if transmitter or receiver cross the 2D resistivity structure. However, the transmitter-receiver configuration needs to be considered in this assessment considering the appearance of the 2D effect at different receiver locations for different tow directions. In the worst case scenario, the position of the aquifer boundary is misinterpreted by a distance equalling the corresponding offset. In terms of resolving different boundary mechanisms, the land-side step-off signal is the most promising. The differences in transient decay at late times for different aquifer facies are only apparent for this configuration. In comparison, the step-on signals can differentiate the Brackish-Water model, but cannot distinguish between the Blockage and Intrusion model.

Effect excluding Bathymetry - 2D Aquifer Model

As displayed in several preceding modelling studies, the bathymetry has a considerable effect on the acquired electric field data. The question may arise, if the EM signature of the 2D aquifer boundary is distorted by the bathymetry effect. Therefore, simplified 2D models excluding the coast and bathymetry are investigated. Again, both directions of tow are investigated.

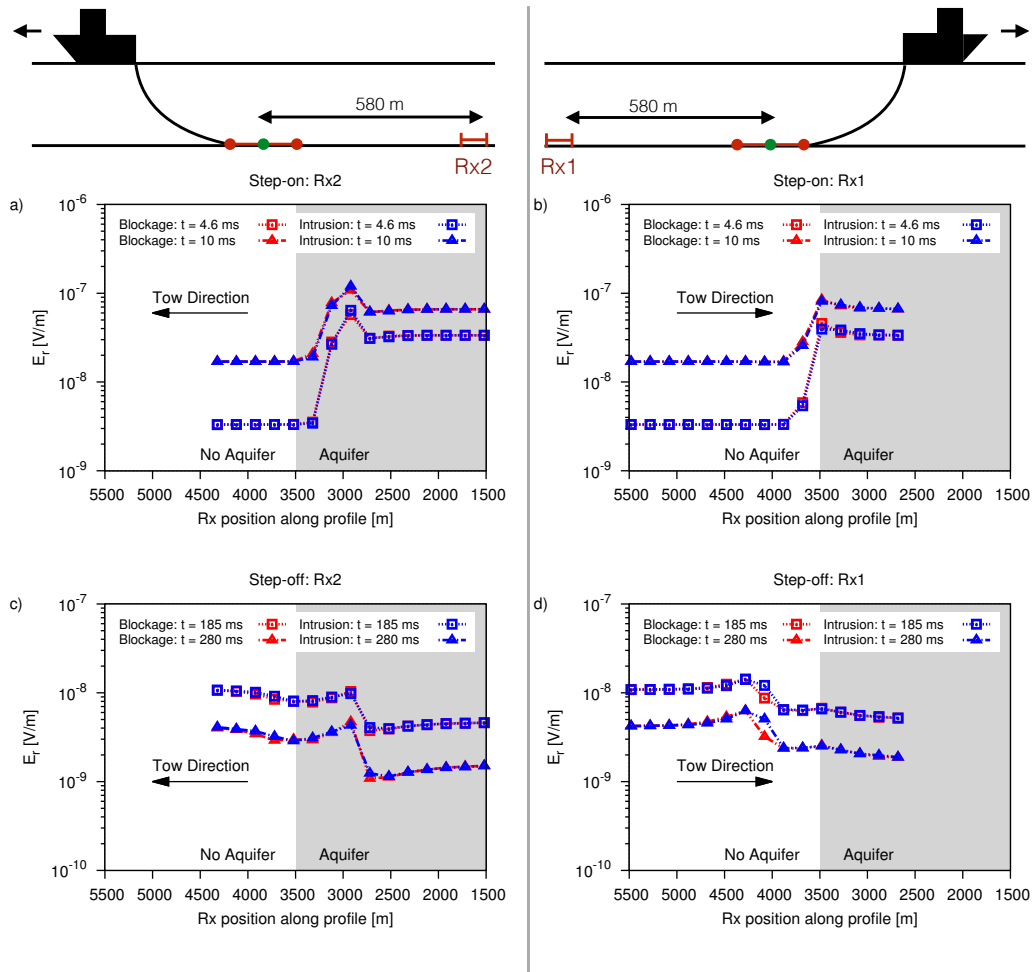


Figure 6.14: Profile plots for the Blockage and Intrusion model displayed by the red and blue, respectively. The land-block and bathymetry model are excluded from this study. Two selected time delays are highlighted by square or triangular markers. The profile plots are displayed for Rx2 in (a) and (c) and for Rx1 in (b) and (d), simulating different tow directions over the aquifer boundary. The top row displays the step-on signals, the bottom row the step-off signals.

The profile curves for this simplified 2D models illustrated in Fig. 6.14 have a high consistency to the previous plots that included the bathymetry (see Fig. 6.12). The effect of the lateral resistivity discontinuity appears to be more prominent if bathymetry is neglected. Yet, the dependency on the direction of tow remains.

One advantage of applying this simplified model, is the revision of solution stability. Regions located at large distances to the 2D structure should exhibit identical solutions due to the one-dimensional nature of the subsurface. The resulting profile curves in these regions are horizontal indicating a stable solution. In case of an unstable solution, due to an insufficient grid, the curves exhibit some curvature or even outliers. This is not the case for the calculated data in Fig. 6.14¹.

¹The identical grid was applied for the modelling studies including bathymetry.

6.2.3 1D Inversion of synthetic 2D data

In the preceding sections, modelling studies directly address issues of interpreting 2D data using a 1D inversion scheme. In the following, the calculated 2D data is evaluated using `MARTIN` for the three resistivity models presented in Fig. 6.11. In this context, the bathymetry issue is revisited, in addition to investigating the 2D effect of the aquifer boundary. To simulate a realistic setting, the error model as presented in Section 5.1 is applied. A 3000 m long transect is modelled running perpendicular to the coastline in East-West direction, 31 transients are calculated at equidistant points of 100 m. The conclusions of the seafloor bathymetry study are directly applied. For RxSea, the water depth at the transmitter is used. RxLand is interpreted using the mean water depth or a depth closer to the receiver in case no convergence is reached.

The 1D Occam inversion models of step-on signals with roughness-one regularisation are displayed in Fig. 6.15. The left column shows the inversion models of RxSea for the blockage, intrusion and brackish-water model displayed in c, e and g, respectively. The right column of Fig. 6.15 illustrates the identical order for RxLand. Note, the original 2D models are displayed by black lines. In total, six quasi-2D resistivity models are presented using a 1D stitched visualisation. Neighbouring stations have no relation to each other physically or mathematically. They are merely plotted together for a better representation of the 2D structure. All inversion are performed with starting models consisting of 20 layers increasing logarithmically in thickness. Note, although not specifically shown, all models achieve a fitting of $\chi = 1$, implying a data fit within the error bounds. Also, following the representation in the preceding studies, each coloured model is plotted at the location of the receiver.

The inversion models of RxSea (left column) reflect the conclusions made from the profile plots and transients displayed in the preceding section. The aquifer is detected in the signal as the receiver crosses the resistivity discontinuity. Consequently, the inversion models begin showing a resistive aquifer at this position. Additionally, the inversion results of the Blockage and Intrusion model shown in Fig. 6.15c and Fig. 6.15e are practically identical. Solely the Brackish-water model shows differences as the resistive part of the aquifer begins 500 m further towards the coast. An interesting feature is noticeable on between 3500 m and 4000 m. Apparently, the presence of the resistive aquifer causes a resistivity decrease in the depth range below 100 m, which is attributed to the 2D resistivity distribution. Between 1500 m and 2800 m, both transmitter and receiver are located above the resistive fresh water aquifer. Aside from the bathymetry, the sub-seafloor resistivity model is predominantly one-dimensional in this region of the profile consisting of a resistive layer embedded within conductive marine sediments. The depth of the aquifer is underestimated by approximately 20 – 30 m, which may be an effect of the bathymetry. Additionally, the resistivity values of the aquifer are underestimated, presumably due to the masking effect caused by the bathymetry on the response of RxSea. It should be mentioned that the inversion was conducted using a fixed CF equalling one, although the bathymetry causes a shift of the step-on signal. Inversion trials were attempted using a free CF, but resulted in inconsistent models. For RxSea, a CF of approximately 0.8 would account for the bathymetry effect. However, the

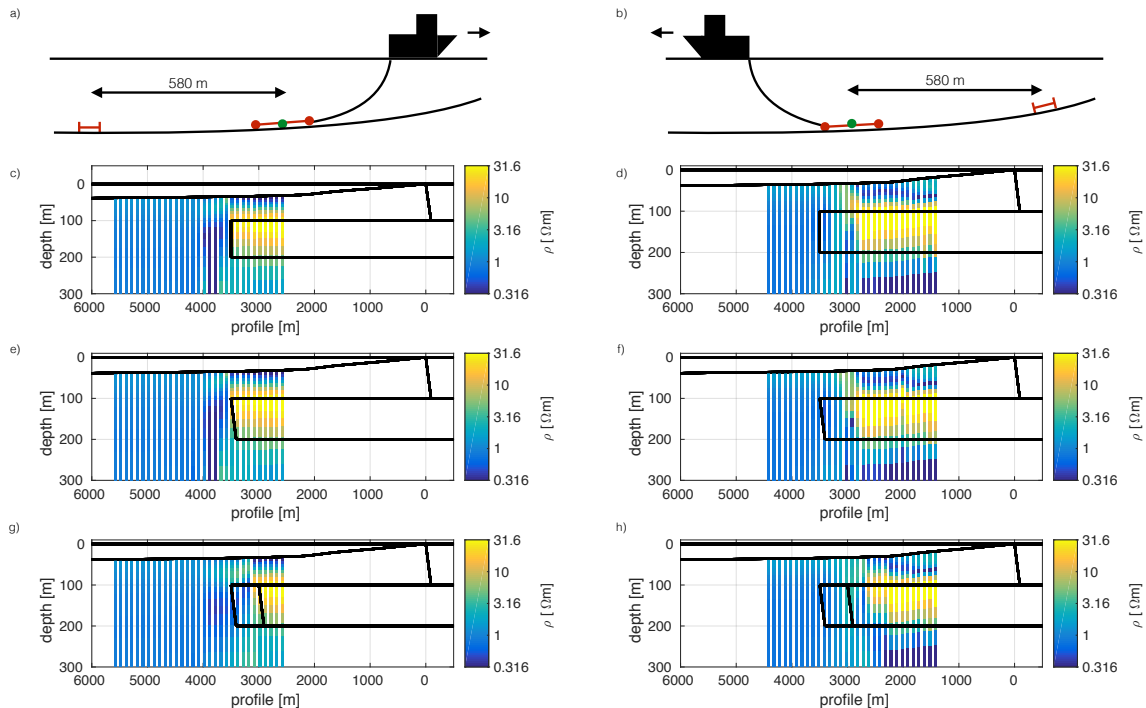


Figure 6.15: 1D Occam R1 inversion models of synthetic 2D data. The left column displays the scenario where the system is towed towards the coast and the receiver is located on the sea-side of the transmitter. The right column displays the scenario of towing the system towards the sea. The receiver is located on the land-side of the transmitter. In (c) and (d), the aquifer is blocked to seawater intrusion, in (e) and (f) characterised by a seawater/freshwater interface and in (g) and (h) has a brackish water zone to its West. All inversion models are plotted at the location of the receiver.

shift masks the complete response of the freshwater aquifer. Consequently, all 1D inversion models using both measured and modelled 2D data are conducted with a fixed CF.

In comparison to RxSea, the inversion models of RxLand are different, but remain consistent with the results of the profile plots in Fig. 6.12. The resistive aquifer is detectable at the receiver provided the transmitter is still located above the aquifer. As the transmitter passes over the lateral boundary, no aquifer signal is registered at the receiver. As a result, the resistive layer is only visible at stations, where these conditions are held. This coincides with the results of the profile curves. Also, the resistivity values of the resistive layer in the 1D inversion models is generally higher compared to RxSea. This is an attribute of the RxLand configuration that possesses a magnifying effect for the resistor due to the steeper decay of the transient.

6.2.4 Conclusions: 2D Aquifer Model

The preceding modelling and inversion studies underlined the complexity of DED measurements in the coastal regions of Israel. The bathymetry is quite dominant,

but is not incorporated in 1D inversion. Consequently, modelling studies were conducted to investigate the bathymetry effect on the acquired data. The results revealed the following conclusions:

- The land-side receiver is more susceptible to the bathymetry. For step-off signals, this may result in a sign-reversal at late-times. The bathymetry results in a shift of the step-on signal, which could become an issue if a free CF is allowed in 1D inversion as the aquifer footprint will be masked. Furthermore, RxSea is also affected by the bathymetry. In part, the step-off signal of the resistive aquifer is masked due to the slower decay of the signal.
- For a 1D inversion, a fixed water depth is generally needed to interpret 2D data. Modelling studies show that there are dependencies on configuration and type of current signal. Minimum errors are achieved for RxSea if water depths at the transmitter are chosen. In contrast, RxLand is best interpreted using the mean water depth or a water depth close to the receiver.
- In regions of slight bathymetry, the correct resistivity model of the sub-seafloor can be reconstructed using 1D inversion. In regions of stronger bathymetry, the chosen water depth has a large influence on the resulting 1D resistivity model.

The main aim of the DED application is to detect the position of the western aquifer boundary and to distinguish between different mechanisms that may control the shape of this boundary. The former is investigated using profile plots, the latter using transients. Three possible two-dimensional resistivity models are derived from preceding LOTEM studies and literature concepts, referred to as the Blockage, Intrusion and Brackish-water models. The theoretical assessment of the modelled data leads to the following conclusions:

- The position of the lateral resistivity boundary is accurately detectable using profile plots. However, due to the complexity of the signal, bathymetry, transmitter-receiver configuration (tow direction) and applied current signal need to be considered to avoid a misinterpretation.
- In general, the step-off signal exhibits a higher distinguishability of the aquifer position and shape compared to the step-on signal. This favourable quality of the DED step-off signal is further investigated for 3D targets in the subsequent section.

Finally, the feasibility of a 1D inversion of 2D data was studied. A realistic noise model was considered for the modelled 2D data. The general results show that a 1D inversion of step-on data is indeed possible, maybe even sufficient for a preliminary interpretation. Yet, the 1D inversion models do not reflect the correct resistivity model for RxLand due to a lateral shift of the 2D aquifer response along the profile. A subsequent 2D interpretation is advisable to obtain the correct information regarding the position and shape of the western aquifer boundary.

6.3 Signal-Variations of resistive 3D Targets

Studying the freshwater aquifer using a two-dimensional resistivity model revealed that the DED step-off response exhibits the highest sensitivity towards lateral resistivity contrasts. But how do DED signals compare to those of other EM methods? A three-dimensional modelling study is conducted to clarify this question. Specifically, the response of CED, DED, TD-CSEM, and VED are investigated for a finite resistive slab of $100 \Omega\text{m}$ and a thickness of 100 m embedded in marine sediments at a depth of 1000 m beneath the seafloor. Such model adequately represents a hydrocarbon saturated reservoir. As displayed in Fig. 6.16, the lateral extent of the slab is, thereby, either $900 \text{ m} \times 900 \text{ m}$ or $4500 \text{ m} \times 4500 \text{ m}$ shown by red and blue lines, respectively. The former representing a resistive body with dimensions smaller than the depth of burial and the latter one that is much larger. No bathymetry is considered meaning that the model consists of a lateral seafloor at a depth of 100 m below the surface. Profile curves at time-delays of $t = 10 \text{ s}$ are calculated for CED, DED, VED and TD-CSEM and plotted against the transmitter position (in km) along a profile crossing directly above the resistive body in Fig. 6.17. Note, the signals are plotted for the transmitter positions as the previous studied revealed that step-off signals will follow the shape of the resistive structure as the transmitter passes over the lateral resistivity variations. All data points at sufficiently late times show a comparable behaviour and time-delays of $t = 10 \text{ s}$ are chosen arbitrarily. The centre of the resistive body is located at 0 m. Both short and long offset configurations are investigated with receivers Rx1 and Rx2, respectively. Note, this exact study is published in *Haroon et al. (2016)*, but is repeated here to highlight the exceptional lateral detectability of DED under noise-free conditions. Hence, the study may seem biased towards CED, DED and even VED. If noise were considered, CSEM is superior to all other methods due to SNR considerations. Therefore, the following study does not aim at questioning the effectiveness of CSEM, but rather, uses CSEM as a comparison.

Goldman et al. (2015) presents a similar 3D modelling study focussing on the lateral resolution of CED and VED in a short offset configuration for water depths of 100 m and 1000 m. They argue that both VED and CED have exceptional lateral resolution capabilities in comparison to the FD-CSEM method, even in deep-sea environments. CED and VED show a considerable response towards small resistive bodies with lateral dimensions smaller than the depth of burial. In the short-offset configuration, the signals of CED and VED remarkably follow the shape of the resistive body. Furthermore, they state that shallow marine applications are more effective using CED, since the depth of the water column does not limit the application and a signal-to-noise issue is less likely. However, the effects caused by geometrical distortions are not considered in their study.

Goldman et al. (2015) use a VED- E_z receiver configuration as it is applied commercially, e.g. *Helwig et al. (2013)*. The presented modelling study confines to E_r -receivers for reasons of comparability. Compared to *Goldman et al. (2015)*, the offsets between Tx and Rx1 are of a factor two to four times larger depending on the applied method. Nonetheless, the general results of *Goldman et al. (2015)* for short offsets are reproducible. The signal follows the shape of the resistive body

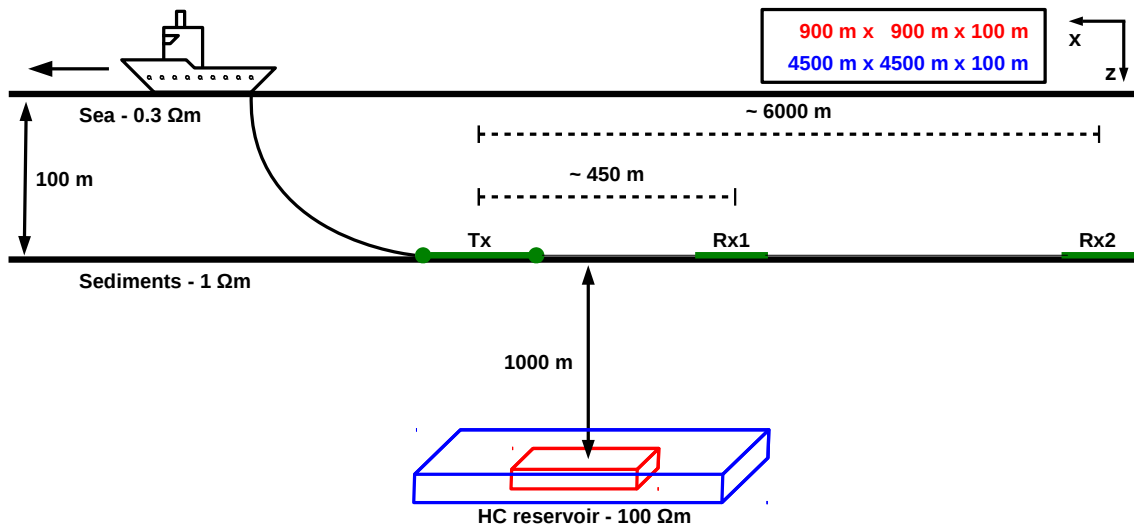


Figure 6.16: Three-dimensional modelling study. A HC saturated body with a resistivity of $100 \Omega\text{m}$ and a thickness of 100 m is embedded in marine sediments. The lateral dimensions of the resistive body are finite and are either $900 \text{ m} \times 900 \text{ m}$ or $4500 \text{ m} \times 4500 \text{ m}$. The four EM systems are towed over the centre of the body with receiver offsets of approximately 450 m and 6000 m representing the short and long offset acquisition (Haroon et al., 2016).

with amplitude maxima directly over the edge of the body. Furthermore, the signals of CED and VED are practically identical, although amplitudes differ by a half order of magnitude. If signal-to-noise is neglected in the theoretical assessment, the study shows that CED and/or VED may easily detect resistive bodies with small lateral dimensions and thicknesses of 100 m or more assuming a conductive homogeneous host medium. Moreover, the lateral boundaries of the resistive body are easily located using both methods as the signal amplitudes are at a maximum.

The signal amplitudes of TD-CSEM are approximately three orders of magnitude larger compared to the other methods (see Fig. 6.17a). However, the signals show no significant response toward the resistive 3D bodies. Therefore, an application of CSEM is not advisable for this geological setting in the short offset configuration. In contrast, the profile curves of DED shown in Fig. 6.17e are very similar to those of CED and VED. This contradicts the 1D modelling results where the detectability of DED was comparable to TD-CSEM (LOTEM). The signal follows the shape of the resistive body and is, therefore, in unison with the signals of CED and VED. Depending on the drag-direction, the signal may reach either maximum or minimum amplitude above the edges. This may be considered a disadvantage as signal-to-noise may become a relevant issue when applying DED to detect resistive 3D bodies. However, the 1D background signal of DED exceeds those of CED and VED by almost one order of magnitude and is, therefore, more suitable.

The situation slightly changes in a long-offset configuration (cf. Fig. 6.17-right column). The most obvious change is that the signal dynamics of all methods are limited in comparison to the short offset configuration. The amplitude of TD-CSEM now exceeds the other methods by one to two orders of magnitude. All methods are

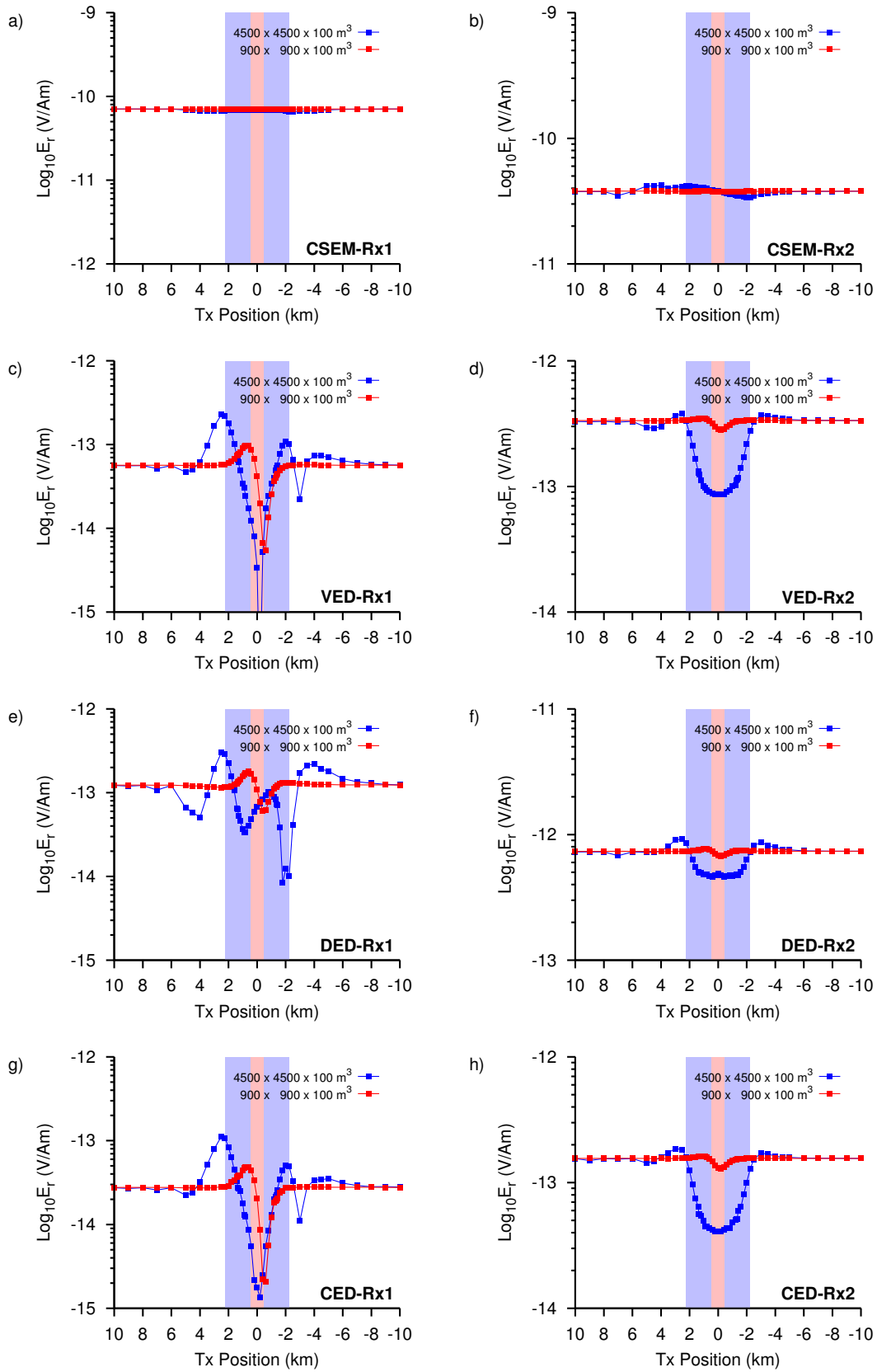


Figure 6.17: Profile plots of CSEM, VED, DED and CED at time-delays of $t = 10$ s. The left column represents the short-offset ($r \approx 450$ m) configuration and the right column the long-offset ($r \approx 6000$ m) configuration. The red line illustrates the response of the 900 m x 900 m body, the blue line the 4500 m x 4500 m body. The background colours represent the lateral dimensions of the resistive bodies (Haroon et al., 2016).

less sensitive towards the small resistive body. However CED and VED signals still show a significant response. The DED signal displayed by the red line in Fig. 6.17f exhibits a response, but may generally be indistinguishable from the background signal.

In comparison, the large resistive body is detected by all methods. However, TD-CSEM shows a limited response. In comparison, CED, VED and DED all have a significantly larger response. Again, the signal of the latter three follows the shape of the resistive body, although not as accurate as in the short offset case. Also, the amplitudes of all methods are minimal above the centre of the body. This may result in a signal-to-noise problem.

The clear advantage of TD-CSEM compared to the other methods is the signal amplitude; both in the short and long offset setting. However, the step-off response of TD-CSEM shows practically no response towards a resistive block with finite dimensions. In comparison, CED, VED and DED are clearly superior in this aspect. However, the issue of signal-to-noise needs to be examined closely, as all three methods have a clear disadvantage in signal strength compared to TD-CSEM. The enhanced lateral detectability of CED, VED and DED may still justify future application attempts.

As DED has considerable advantages over CSEM (LOTEM) for short-offset applications, an application for hydrocarbon exploration may be justified. The limiting factor is the SNR, which is also common for VED applications. Yet, the enhanced lateral detection of a three-dimensional resistive body clearly distinguishes the DED system from a conventional inline CSEM (LOTEM) system.

6.4 Summary of 2D/3D Modelling

Multi-dimensional modelling studies are conducted as they describe the subsurface resistivity structure more adequately. To study the signal of DED in a 3D setting, a new `sldmem3t` grid generator was introduced that enables an easy discretisation of more complex transmitter geometries. Generally, these grids may be optimised for future applications due to the time-consuming nature of finding a stable solution. The latter especially concerns the CED grid, which can be problematic in a short-offset configuration. Future developments may consider choosing logarithmic grid spacing even for the inner domain of the grid.

The DED application as intended in Israel was subsequently thoroughly investigated for a 2D-Aquifer model. The results show the influences of bathymetry and tow direction on the data. Especially step-off data is affected more severely and is difficult to interpret using 1D inversion due to sign-reversal, rapid transient decay, etc. This may influence the data acquisition of DED measurements, as step-on signals provide a sufficient 1D inversion result. Generally, the step-on signals are less sensitive towards the 2D effects caused by the bathymetry and the aquifer boundary. The future application may foresee a preliminary 1D interpretation using the step-on signals in conjunction with a final multi-dimensional assessment of step-off data. Obviously, a multi-dimensional assessment may also be conducted using both signals.

In terms of resolving the hydrogeological structure at the western aquifer boundary, the step-off signals are clearly superior.

One clear advantage of applying the DED method in a fixed-offset configuration are so-called profile curves. At selected time samples where the aquifer response is expected, lateral amplitude variations in the acquired signal are clearly visible. These allow to precisely located the lateral resistivity discontinuity, provided the transmitter-receiver configuration is taken into account. Furthermore, preliminary assertions can be made based on the profile curves as a behaviour is noticeable if a brackish water zone is located at the head of the aquifer.

As shown by *Haroon et al.* (2016), the DED step-off signal is comparable to the high-resolution methods VED and CED. However, under realistic noise conditions, the SNR issue still prohibits an interpretation of the step-off data. Future DED applications need to consider this issue and find solutions in order to obtain adequate measurement results.

Field Survey & Data Processing

The first marine DED field survey was conducted in Israel, April 2016. In the following chapter, the DED system, data acquisition procedure and data processing are described. The first section will describe the new marine DED system and the field procedure during the survey. As the systems was applied for the first time, a detailed explanation of the different components is given. Furthermore, the main issues that arose prior to, and during the measurements are explained. Suggestions are made for necessary developments in future DED applications. Subsequently, impressions of the field survey are presented along with a detailed overview of the acquired data.

The second section of this chapter deals with the measured data sets. A new time-domain EM processing software is introduced, associated with the data format of the KMS-820 acquisition unit. Explanations are given using data examples to visualise the processing steps in a comprehensive manner. A background noise evaluation is applied together with the processed data to assess data quality and validate the derived error estimates. Finally, all acquired data sets are presented along the profile and preliminary predictions regarding the sub-seafloor resistivity structure are made based on their transient behaviour.

One issue that has to be pointed out beforehand, is the data gap at the centre of the profile in a so-called No-Anchor-Zone. The existence of this zone was known prior to the measurement, but never treated as an obstacle by the partners from the IOLR. However, due to technical difficulties, their research vessel was not ready four weeks before the measurements and, as a result, cancelled their participation. Fortunately, the organisation EcoOcean stepped in and provided their vessel including crew for these measurements. Due to the short notice, they had concerns about towing over the No-Anchor-Zone. Consequently, no data is acquired in this area of the profile.

7.1 Field Survey

In April 2016, the first marine DED survey was carried out on the profile of *Lippert* (2015) near the Mediterranean coastline of Bat Yam, Israel. The four-day survey was carried out with the Mediterranean Explorer from EcoOcean. In total, 11 transmitter locations with two receiver stations each were measured along a transect of approximately 4 km in length.

The general survey design is based on the marine LOTEM results of *Lippert (2015)*, which indicate a resistive layer extending from the coastline to approximately 3.5 km offshore. This resistive layer was found to be a lower sub-aquifer of the Mediterranean aquifer of Israel (*Kafri and Goldman, 2006; Goldman et al., 2011; Lippert, 2015*). However, due to the limited lateral resolution of the marine LOTEM measurements and sparse data density along the profile, the location of the lateral transition between this resistive zone and the conductive marine sediments can only be assumed between two electrical field receivers located 400 m apart.

The primary aim of applying the marine DED system is to investigate the seaward extent of the resistive freshwater aquifer including its western boundary. The obtained data will enable a more sophisticated interpretation of the transition zone between the conductive sediments and the resistive freshwater aquifer. Ideally, the acquired DED data set will enable an adequate assessment of the western boundary structure and predict if the aquifer is open to the sea or blocked from seawater encroachment. Furthermore, the profile is extended towards the coastline to validate the results of marine LOTEM and prove the feasibility of the novel marine DED system.

7.1.1 The DED System

The designed DED system is a seafloor-based transmitter/receiver array consisting of a DED transmitter antenna and two in-line electrical field receivers. The latter are located at offsets of 370 m (Rx1) and 580 m (Rx2). This had numerous practical and theoretical reasons. Theoretically, the target formation is located at a rather shallow depth of 60 m - 100 m beneath the seafloor. Therefore, larger offsets are generally not necessary to resolve the target formation. Furthermore, the marine DED application intends to investigate the freshwater/seawater transition zone. Smaller offsets are beneficiary as the measured signal integrates over less volume of earth, increasing the lateral resolution. Moreover, the obstacle of the No-Anchor-Zone (cf. Section 7.1.2) posed a practical problem since it was not allowed to drop the system in this region. Thus, deployment had to start either east or west of this zone. The chosen offsets minimised the area where no data was acquired.

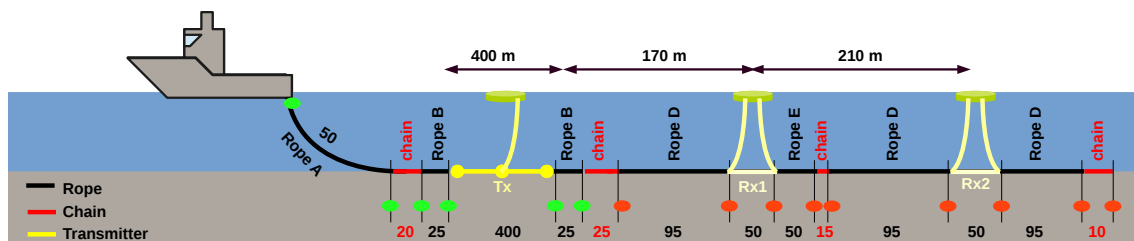


Figure 7.1: Sketch of the applied DED-transmitter/receiver system. Note, the image is not to scale. The complete system is made of ropes (black), chains (red) and the transmitter antenna (yellow). Each rope segment has a different length, depending on its tag.

The No-Anchor-Zone is a pronounced feature in the profile. All stations located east of this zone are referred to as the land-side stations. Accordingly, all stations located west are referred to as the sea-side stations. It was attempted to place the receivers as close as possible to the boundaries of the No-Anchor-Zone. This was achieved on the land-side, but not on the sea-side of the No-Anchor-Zone. To avoid missing the freshwater/seawater transition zone, consecutive stations are at distances of several hundred meters or less.

As displayed in Fig. 7.1, the seafloor towed system consists of ropes, chains and the double-dipole transmitter antenna. The system includes both transmitter (Tx) and electrical receivers labelled Rx1 and Rx2, corresponding to the near and far receiver, respectively. In comparison to the previous marine LOTEM system, where the transmitters and receivers were autonomously positioned, this type of fixed-offset system has two main advantages. (1) The offset is more precisely known and cannot deviate considerably from the reference value. (2) The data interpretation is simplified, as profile plots are applicable to determine lateral resistivity discontinuities. The use of a calibration factor in the inversion/modelling scheme is minimised due to the constrained offset variations.

Drifting lines during the measurement phase were counteracted by including segments of 10 mm anchor chains at different positions along the system. In this way, the mobility of the system was reduced.

The tail of the measurement system, referred to as the ropes, chains and receivers behind the transmitter antenna, is constructed with several segments of predefined lengths. These are illustrated in Fig. 7.1. At each joint, a shekel was used to connect the segments and, additionally, attach either receiver electrode or placement buoy. The loose ends of the receiver electrodes are attached to buoys that are later connected to a floating receiver stations. At each measurement point, the data loggers are manually reconfigured.

7.1.2 Measurement Procedure

The complete system was deployed each morning and gathered each evening to avoid issues with the fishing industry. Field impressions are given in Fig. 7.2. During deployment, the ship slowly moved along the profile at constant speed, while releasing the system starting with the tail. A further motorised ship was attached to the tail of the system to maintain the positioning during the deployment. Receiver electrodes were hooked into the line and the connector was thrown into the water with a buoy. The second boat gathered each connector and fastened them to the receiver platforms. After deployment, the leading transmitter ship towed the line several hundred meters to straighten the system.

At each measurement station, the transmitter ship released the front of the system and relocated to the transmitter centre to connect to the vertical power source cable leading to the central electrode on the seafloor. Upon connection, the measurement phase began and took approximately 45 - 60 minutes. Subsequently, the ship disconnected from the power source cable, gathered the front of the system and towed to the next position. Meanwhile, the data loggers and anchors were retrieved by the

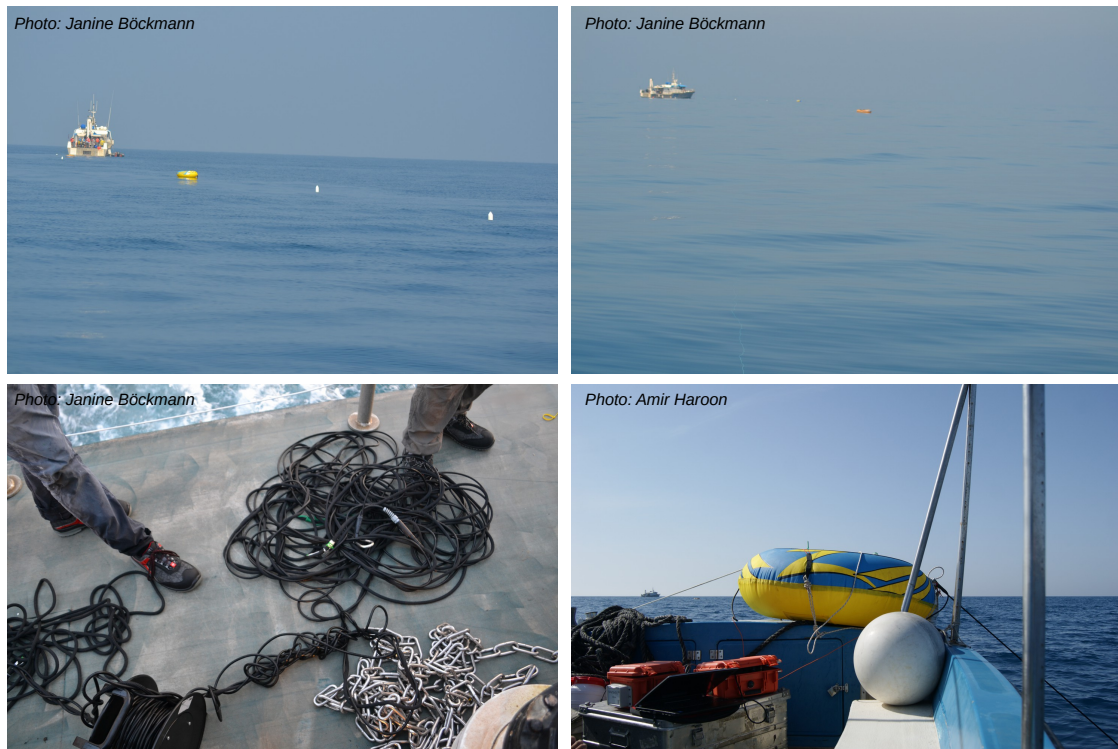


Figure 7.2: Impressions of the field survey. On the top-left, the transmitter system is being deployed at quiet sea conditions. The top-right displays the setup during the measurement from the receiver platform Rx2. The Mediterranean Explorer is located at the transmitter donut. The bottom-left image shows tangled cables during the clean-up. The bottom-right image shows impressions from the receiver boat during the measurement.

second boat.

During the clean-up procedure, the large ship was set to slow reverse while the cables and lines were spooled onto drums. The receiver electrodes were disconnected and spooled onto separate drums. In some cases, this procedure was quite difficult, as lines and ropes got tangled (see Fig. 7.2).

7.1.3 Field Setup

During the four survey days, 11 transmitter locations were measured along a ca. 4 km profile. The profile runs perpendicular to the coastline directly crossing the assumed saltwater/freshwater transition zone assumed at 3.25 km - 3.65 km from the coastline. The acquired receiver stations are displayed in Fig. 7.3 by black triangles. They are named p01FR through p17NR. The number describes the location along the profile, 01 being closest to the shoreline and the tags NR or FR describe if the station was measured by the near (Rx1) or far (Rx2) receiver, respectively.

The profile is interrupted between p06FR and p07FR due to a No-Anchor-Zone displayed in Fig. 7.3. Unfortunately, the transition zone lies either close to, or

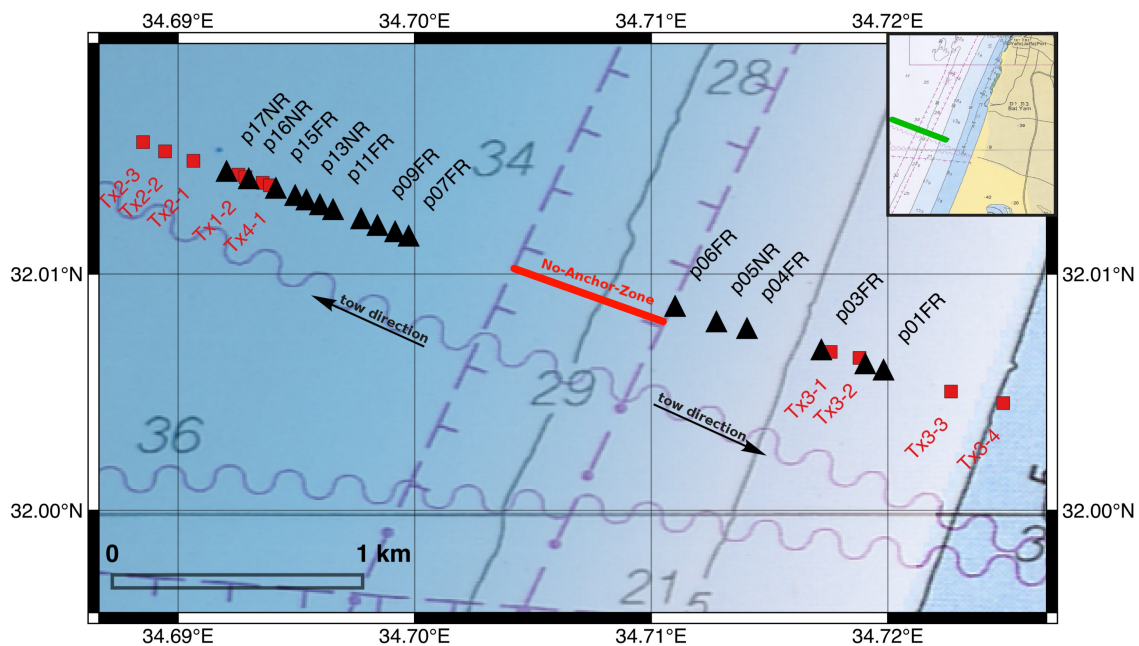


Figure 7.3: Map of the survey area near the coastline of Bat Yam, Israel. The black triangles describe the location of each receiver and the red squares of each transmitter location. The receivers are labelled according to their position along the profile, 01 being closest to the shore. The transmitters are labelled in chronological order.

directly underneath this region. As previously mentioned, the system is always deployed so that the receivers are located closest to the No-Anchor-Zone. Therefore, the transmitter is located on the sea-side of the receivers to the West and on the land-side of the receivers towards the east of the No-Anchor-Zone. In Fig. 7.3, the tags of the transmitter stations are marked by red squares and labelled according to the measurement day in chronological order, e.g. Tx2-1: Day two, station 1. According to the 2D modelling studies, the following attributes are to be kept in mind.

- In case the aquifer is present to the east of the No-Anchor-Zone, the received signals are partly masked to its signature due to the effects of the bathymetry. This especially applies to the step-off signals.
- Provided the western edge of the aquifer is detectable, a signal at the sea-side receivers is expected as the transmitter crosses the lateral resistivity discontinuity. This needs to be considered when interpreting the data and the derived profile curves.

One of the main differences in comparison to land-based EM measurements is the positioning of the measurement system. The positions shown in Fig. 7.3 are the central positions of the transmitter and receiver dipoles measured using a hand-held GPS device at the surface. In order to maintain the position along the profile, the Captain of the Mediterranean Explorer was given GPS data with equidistant stations

located 100 m apart. The ship was towed along the profile stopping at specific stations. The position of the transmitter and receiver platforms were acquired using hand-held GPS after each platform was secured with anchors. The exact position of the system on the seafloor remains unknown. The receiver offsets are assumed fixed at 370 m and 580 m due to the tension on the line during the tow. To prevent the platforms from drifting during the measurement, each platform was secured using anchors in order to account for winds, currents and/or tidal effects.

7.1.4 Issues during Data Acquisition

Several issues arose during the measurement, some of which are relevant for future DED applications. The measurement procedure applied surface-based data loggers with seafloor-based electrodes. This approach needs to be reconsidered prior to future applications. Substantial problems arose with all lines/cables going to the surface. First, it was difficult and dangerous to attach the receiver electrodes to the line during deployment. Second, the seafloor-based system developed a torque during the tow phase, which resulted in tangled ropes/cables (see Fig. 7.2). The clean-up was extremely complicated, as all components had to be untangled upon arriving on the main ship. One approach to prevent this in the future DED applications is to use swivels instead of shekels at the joints. These will compensate for the torque in the rope/chains during the tow. Additionally, it should be considered to place everything in water-proof casing on the seafloor, including the transmitter and the receiver equipment to prevent issues with tangled ropes/cables.

The measurement procedure needs to be optimised in the future. Relocating the transmitter ship at every station costs time, which is a financial factor when applying marine DED. A hardware development of the DED antenna is recommended. The current should flow through a coaxial tow cable from the transmitter ship to the leading electrode. This would save time as the transmitter ship would not need to relocate from the front of the transmitter to the centre at each station. A further benefit would be the reduced EM noise as transmitter and receivers are located on the seafloor. However, this development could complicate a clean differential dipole signal. Therefore, this needs to be carefully thought about.

Some issues also arose with the KMS-820 acquisition unit. As one receiver was autonomous, a scheduler was used to start the measurements. At two stations, this scheduler did not work for unknown reasons. If this is a systematic error, needs to be investigated in future field work.

7.2 Data Processing

Measured time-domain EM data is generally superimposed by different noise sources. As a consequence, a single recorded signal of a specific current step-function suffers from poor SNR. The noise sources are generally categorised into either periodic or sporadic noise. The main periodic contribution is the 50 Hz (and uneven harmonics) from the local power network. In most cases, the sporadic forms of noise appear in

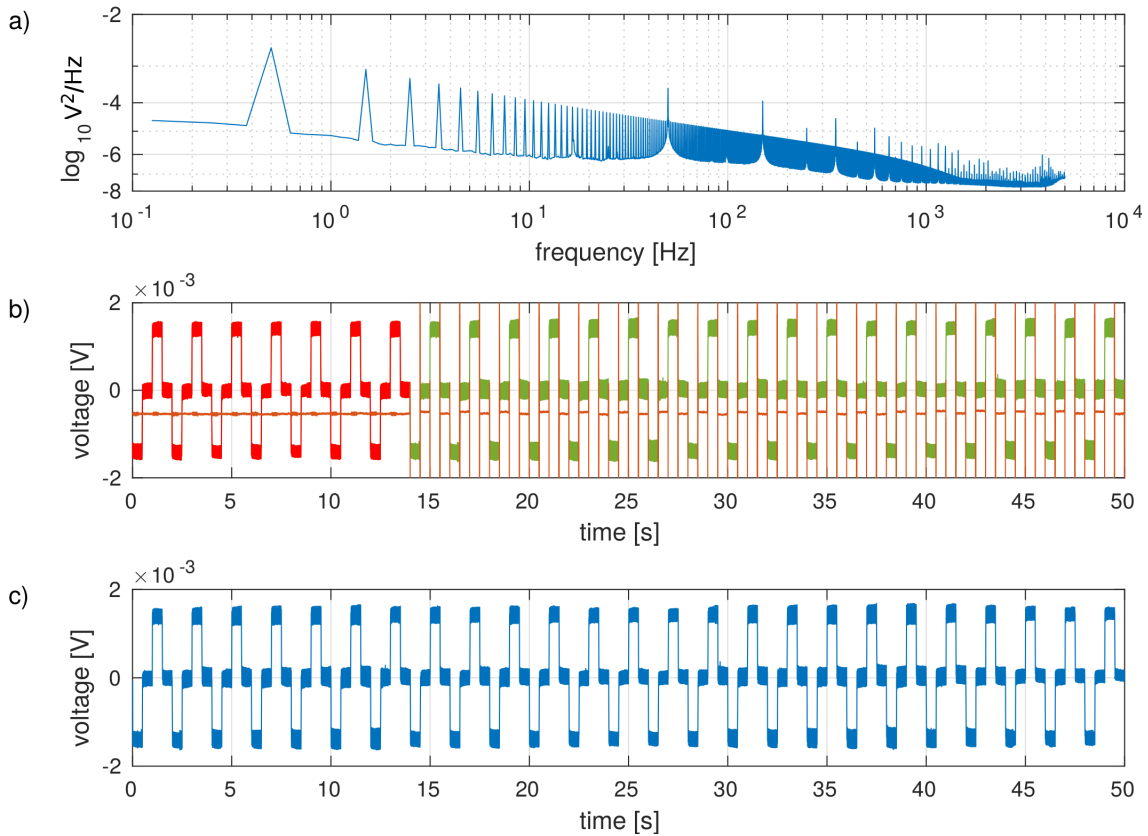


Figure 7.4: In-line DED electric field data measured during the test measurements in Cuxhaven, Germany. The power spectra of the recorded time series is displayed in (a). All recorded channels are displayed in (b) and the shifted time-series is displayed in (c).

the measured time series as voltage spikes, drifts, steps or white noise. In any case, the superimposing EM noise needs to be removed from the time series prior to the interpretation. For LOTEM and DED, the data processing is a crucial step, as an improper processing scheme will falsify or even prohibit an interpretation.

A standardised LOTEM processing scheme is presented by Scholl (2001) using `segy_pro` and applied in many thesis from the IGM Cologne, e.g. Kalscheuer (2004); Haroon (2012); Lippert (2015). In the following, a new data processing scheme will be presented and illustrated using a selected data set from the acquired marine DED data. In comparison to the standard LOTEM processing, only few changes have been made to compensate for the new data format and acquisition characteristics of the KMS-820 data logger.

The application of `segy_pro` is specifically designed for processing data acquired using either SUMMIT or TEAMEX units. Prior to the Israel measurement, KMS-820 data was reformatted to `seg_y`-format and processed using `segy_pro`, e.g. Haroon *et al.* (2015). This approach is quite cumbersome and, additionally, limits the benefits of the new KMS-820 data logger. The following section will be a comprehensive description of the processing scheme for time-domain data acquired using the KMS-820.

In general, the processing scheme is not altered significantly. However, one major difference is determining the starting point of the first current step-function. In comparison to the SUMMIT-receivers, which were triggered using a synchronised clock, the KMS-820 records one continuous times series. Thus, the starting point of the first current transmission is not directly known and has to be defined using the output signal of a synchronised GPS clock. One synchronised clock is located at the transmitter and is responsible for triggering the current signal. The second clock is located at the receiver and its output signal is recorded on an open channel of the KMS-820. The starting point of the first current excitation recorded at the receiver is later determined using this signal. Additionally, an onset range consisting of a certain number of data samples before the first current transmission is considered. All points recorded previous to the onset range are neglected. Note, due to previous processing convention, the onset is included in the time series. These points are declared with negative time values and are generally not displayed in the following figures. For land-based LOTEM, a 100% duty cycle current signal is commonly applied. In this case, the onset is used to level the transients, simulating a step-on current excitation with twofold amplitude.

In Fig. 7.4, exemplary DED data measured in Cuxhaven, Germany is displayed. In the top image, the power spectra is shown to analyse the periodic signal and noise contribution. Figure 7.4b shows the first 50 s of the measured time series on both channels. The orange lines displays the clock signal that starts triggering at approximately 14 s. Generally, the clock triggers from the beginning of the recording. In this specific case it was attached to the data logger at a later time to emphasise this processing step. The data located to the left of the first trigger (displayed in red) is neglected after determining the point of the first current transmission. The data displayed in green, is considered and shifted accordingly so that the first desired step-function is located $t = 0$ s. Figure 7.4c displays the shifted data ensuing this process. At this stage, the recorded data is also analysed for correctness. Although unlikely, the most obvious errors are discrepancies between the recorded data and the current cycle. Possible errors are mistakes in the input data, or false information of the recording sheet. In comparison to processing with `seqy_pro`, the sampling rate is obtained directly from file header of the measured input data.

After determining the starting point of the time series, the further processing steps are similar to the standard LOTEM procedure. These are summarised into the following five processing steps.

1. digital filtering
2. cutting the time series into half/full period segments
3. levelling
4. cluster analysis to remove clearly distorted data
5. log-gating and gate-stacking or stacking and smoothing

In the following, these steps will be described and illustrated using selected data from Israel. To prevent confusion, the following terminology is used for the pro-

cessing. The original data is considered to be the measured time series containing all recorded current step signals. After this time series has been cut into full/half-period lengths (Step 2), the data is referred to as time segments. An array of N number of time segments exists after cutting. The stacked data (Step 5) is referred to as the transient.

7.2.1 Digital Filtering

Measured EM data is often superimposed by a periodic anthropogenic contribution that originates from the local power network and/or the railway. For the majority of marine EM measurements, this periodic noise does not play a relevant role, as measurements occur far away from civilisation. Additionally, the conductive seawater shields the received signal from unwanted anthropogenic influences. However, in this specific case, the measurements are performed in the coastal area of Bat Yam. Consequently, the data contains the 50 Hz signal and its uneven harmonics. To remove this undesired noise contribution from the time series, digital filters are applied. In the past, different variations of Lock-in-filters were used. Although these were quite effective in LOTEM data processing, the data sets acquired in Israel are processed using a different filter called “three-point filter”. Primarily, this is due to the fact that the 50 Hz signal does not dominate the measured time series and can be removed without distorting the data in the extent of a Lock-in-Filter.

Three-point Filter

The digital three-point filter applied in the processing scheme was provided by Tilman Hanstein. The following explanations are for sake of completeness and are not self-developed¹.

The three-point filter uses recurrence of the transmitting signal in full and half periods. As the step-function is reoccurring several thousand times within the extent of the time series, the filter incorporates the value of one data point with a further one at half-period distance. The filter begins from $t = 0$ s and simply moves from sample to sample, calculating an average value between the designated point and the one at a half-period distance. Moving positive in time, the signal is filtered according to,

$$\bar{d}_i = \frac{1}{2}(d_i - d_{i+T/2}), \quad i = 1, 2, \dots, M - T/2 \quad (7.1)$$

where \bar{d}_i is the time series filtered in one direction, M the total number of data points and $T/2$ refers to a half-period length in data points. Note, the subtraction compensates the negative polarity of the signal at half-period distance. Subsequently, the filter starts at the last data point and moves in negative time direction, again filtering the time series according to

¹Personal communication with Tilman Hanstein who provided the filtering software as a contribution to the KMS-820 acquisition unit.

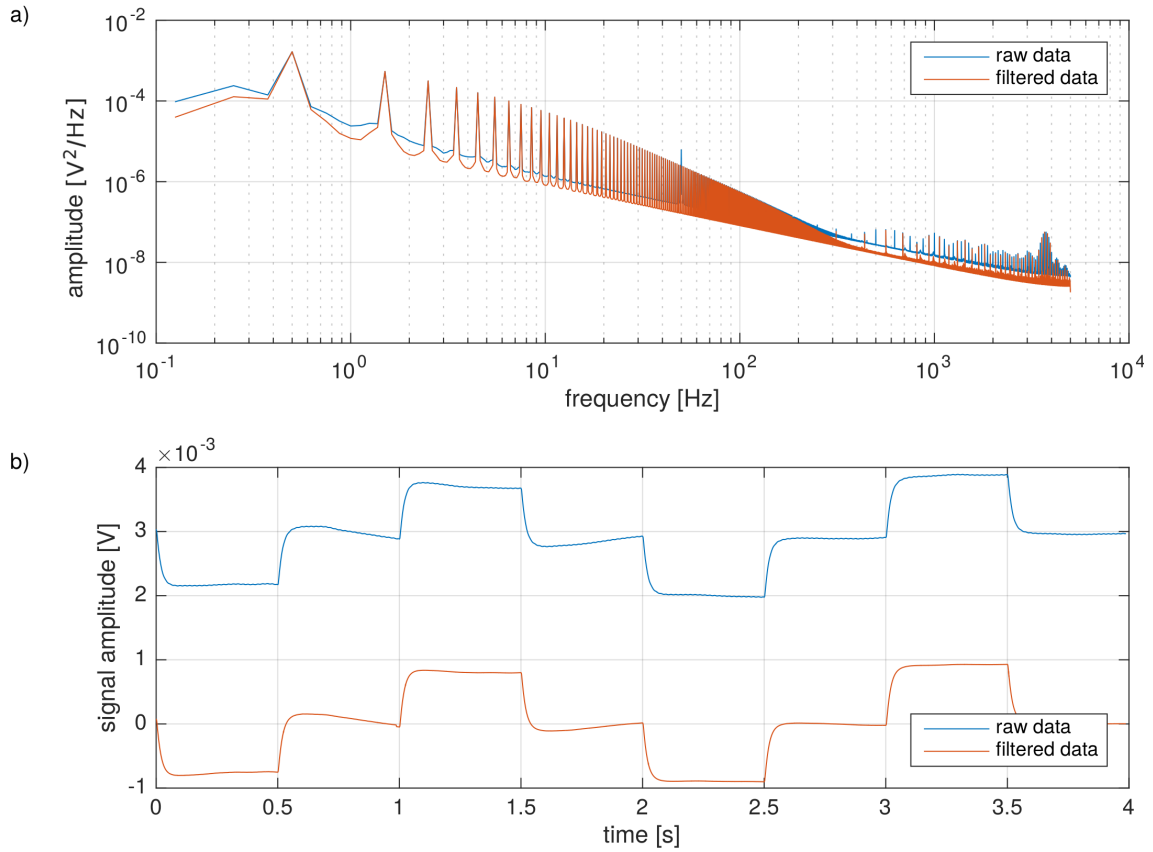


Figure 7.5: (a) Power spectra and (b) time series segment of electrical field data measured at station p16NR. In blue, the raw data is displayed, in orange the filtered data.

$$\hat{d}_j = \frac{1}{2}(\bar{d}_j - \bar{d}_{j-T/2}), \quad j = M, M - 1, \dots, T/2 \quad (7.2)$$

where \hat{d}_j is the filtered time series.

Figure 7.5 shows an exemplary data set measured at station p16NR. The original data is displayed in blue, the filtered data in orange. As the station is located 3970 m from the coastline, the 50 Hz contribution is diminutive and hardly noticeable in the time series segment. However, the power spectra shows a 50 Hz peak in the raw data that is removed by the filter. Additionally, since positive and negative polarisations are added, the filter shifts the time series so that its mean value should equal zero. This can be seen as a preliminary levelling process.

Low-frequency Noise

The three-point filter may also be applied to remove long-periodic noise or quasi-periodic voltage drifts. The filter is applied successive times starting with large period lengths that are an uneven harmonic of the actual current cycle. Incrementally, the period lengths are decreased until the actual transmitting period length is

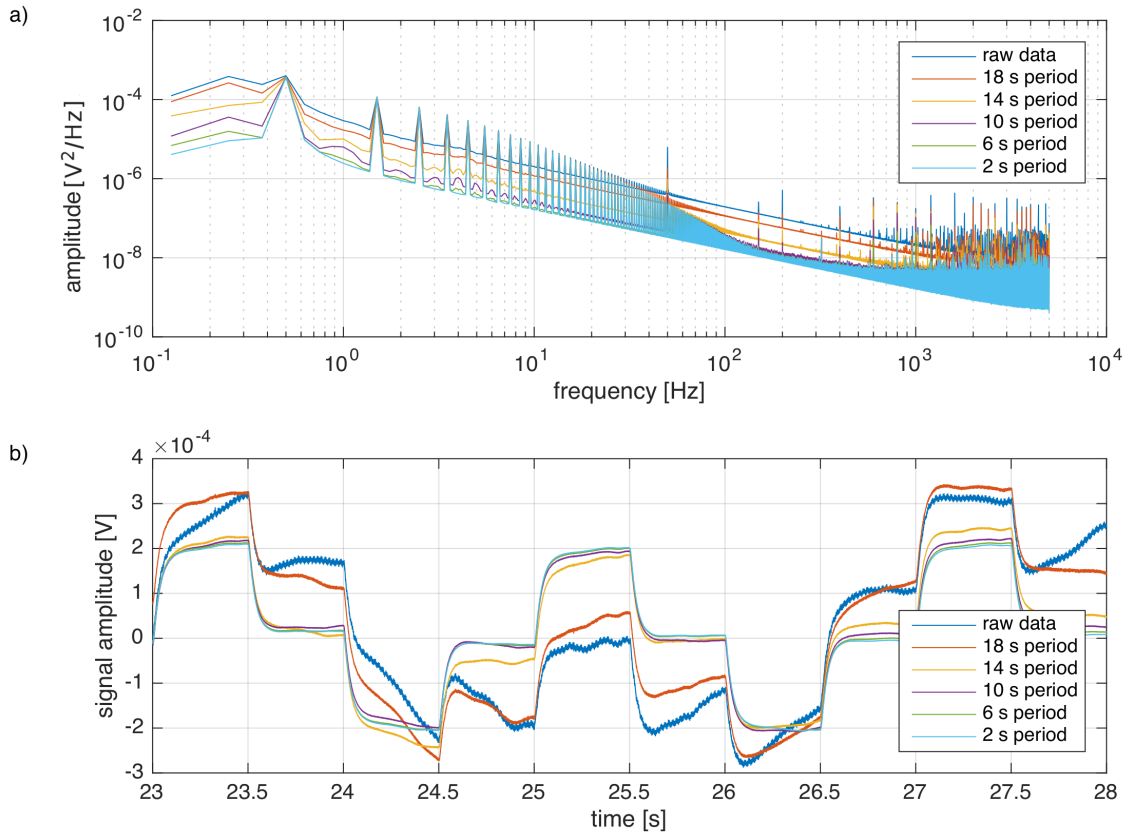


Figure 7.6: (a) Power spectra and (b) time series segments of electrical field data measured at station p11FR. The data was filtered multiple times using the three-point filter starting from period lengths of 18 s (orange) and incrementally decreasing to period lengths of 2 s (light blue). This approach is used to minimise the long-periodic noise.

reached.

Displayed in Fig. 7.6 are the power spectra and exemplary time series at $23 < t < 28$ s for the raw data and the five filtering steps. During the first step, where a period length of 18 s is dictated, only small changes between the raw (dark blue) and filtered (orange) time series are visible. The power spectra shows a small decrease in the amplitude of the 50 Hz frequency. While further reducing the period lengths, a long-periodic smoothing of the time series is visible (between yellow and orange line). The additional steps of 10 s (purple), 6 s (green) and 2 s (light blue) have only limited filter updates, but also contribute to removing the low-frequency noise. In addition to removing the voltage drifts after the final filter iteration, the 50 Hz frequency including uneven harmonics are also removed. The remaining high-frequency noise is insignificant in terms of data quality. At least for the considered DED data set.

For the majority of the measured stations, this process was not necessary. However, this technique substantially improved the data quality at the respected stations, where these low-frequency noise sources occurred.

7.2.2 Cutting & Levelling

The measured time series contains multiple current excitations (> 1000) that are used to improve the SNR by stacking the data. To do so, the original time series is first cut into segments of full periods. Each time series segment may still contain a certain DC-contribution due to device specifications or self-potentials in the subsurface. The levelling process removes these time independent signal contributions from the time series. First, the mean value of each time segment is calculated according to,

$$U_{DC} = \frac{1}{i_b - i_a + 1} \sum_{j=i_a}^{i_b} d_j \quad (7.3)$$

where i_a and i_b generally define the start and end point of each full-periodic time segment, respectively. If no DC-contribution is contained, Eq. (7.3) will be equal to 0. In all other cases, U_{DC} is subtracted from each data point of the time segment. Subsequently, each time segment is cut into lengths of half-periods. Every second half-periodic time segment is mirrored at the x -axis and shifted in time so that the current excitation begins at $t = 0$ s. Thereby, the total number of acquired signals increases by a factor of 2.

If necessary, the half-periodic time series may also be levelled, provided the time segment is several data points longer than a half period (*Scholl*, 2001). In this case, U_{DC} can be calculated according to

$$U_{DC} = \frac{1}{2(i_b - i_a + 1)} \sum_{j=i_a}^{i_b} (d_j - d_{j+T/2}), \quad (7.4)$$

where $T/2$ describes the length of a half-period in data points.

7.2.3 Cluster Analysis

After cutting the original time series into half-periodic segments, an analysis of the individual time segments is difficult and time consuming. However, the data may still contain time segments that are clearly distorted and/or do not contain transmitting signals, as measurements are usually continued after the transmitter is disconnected. These are removed from the data set to prevent an influence in the stacking process.

An analysis of each time segment is quite ineffective, especially if several thousand need to be analysed. A cluster analysis is used to sort each time segment into predefined groups depending on its behaviour. The standard LOTEM processing uses a *Sift-and-Shift* algorithm. A similar intrinsic MATLAB function called *kmeans* is applied to cluster the data.

In Fig. 7.7, the data acquired at station p16NR is clustered into two groups. Cluster 1 contains 2454 members that resemble and electrical field for an active transmitter.

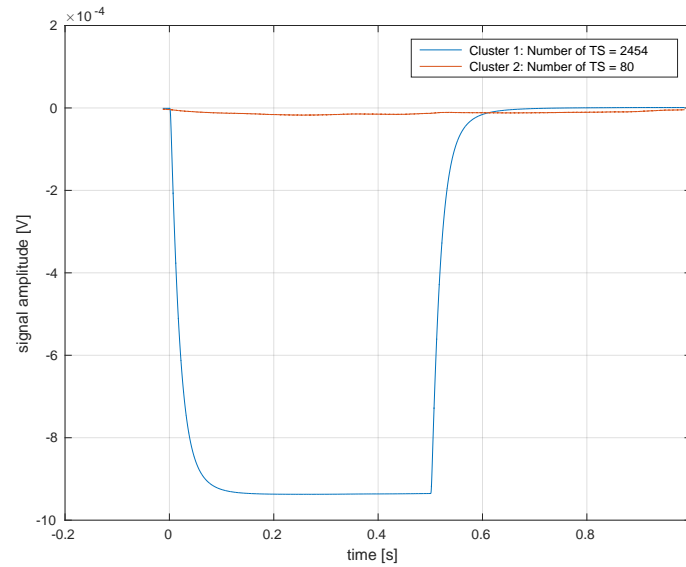


Figure 7.7: Mean values of two Clusters for the half-periodic time segments. The blue line shows the first cluster with 2454 members, the red line the second cluster with 80 members. The members of Cluster 2 are removed from all subsequent processing steps as they were measured when the transmitter was inactive.

Cluster 2 contains only 80 members and has no resemblance with a transmitting current signal. Presumably, this data was recorded as the transmitter was inactive. For further processing, the members of Cluster 2 are removed from the data set and are not considered.

Normal probability plots are used to investigate the data distribution of the measured data. The figures indicate if the data sample is normally distributed or not. The sorted voltages at an arbitrary time sample, or an averaged interval, are plotted against the probability. If the sorted samples are normally distributed, they will be linear, or close to linear. All other distributions will cause the sorted samples to have curvature.

The raw data set, the data set excluding Cluster 2, and the final data set prior to stacking are illustrated as normal probability plots in Fig. 7.8. The green markers represent the sorted amplitudes. The solid blue line between 0.25 and 0.75 coincides with robust linear fit of the first and third quantile. The dashed blue line is an extrapolation of the solid blue in order to evaluate the linearity of the data. The probability values describe the percentage of how many data points are less than or equal to the desired sorted voltage. The value at a probability of 0.5 would in turn be the median value of the sorted data set.

Figure 7.8a shows a normal probability plot of the full data set including the members of Cluster 2. The data set includes time segments measured with an active and inactive transmitter, and is therefore non-linear. Hence, the ensemble of time segments are not normally distributed. Moreover, a gap in the sorted amplitudes is visible that divides the data into two transmitter states (active and inactive). Figure 7.8b illustrates the normal probability plot of the data set excluding the

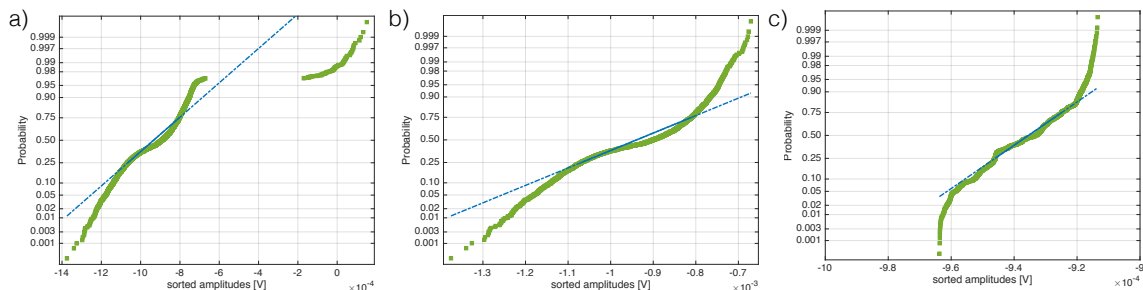


Figure 7.8: Normal probability plots at a selected intermediate time of $t = 0.2512$ s for (a) the complete data set, (b) the data set without members of Cluster 2, and (c) the data set after levelling and log-gating prior to stacking. The sorted data is plotted in green and a robust linear fit between the first and third quantile in blue.

members of Cluster 2. Compared to Fig. 7.8a, the sorted amplitudes of the latter show no gap as the largest measured voltages are removed. The data set is approaching a normal distribution. However, the sorted data still contains curvature, especially at the upper and lower ends of the sorted data vector. This is typical for TDEM data and can also be found in LOTEM data sets, e.g. *Scholl* (2005). Prior to log-gating the data, this effect can be further reduced by levelling the data to the onset (see Fig. 7.8c). Note, the absolute values of the levelled data in Fig. 7.8c have a higher consistency in comparison to the other plots. Interpreting the linearity of the plotted data shown in Fig. 7.8c, we find that a 10% - 25% threshold is adequate for the stacking process. In this case, neglecting the highest and lowest voltages would enforce a quasi-normal distributed data set. Further explanations regarding the stacking algorithm and error estimations are described in the following section.

7.2.4 Log-Gating and Gate-Stacking

The log-gating/gate-stacking algorithm following *Munkholm and Auken* (1996) is implemented in the new processing software. However, the present smoothing scheme using a time-variable Hanning-Window of *Hanstein* (1996) remains implemented as a further option. The standard LOTEM processing steps using `segyp` contains a robust stacking method including error estimation with a subsequent smoothing scheme. Thereby, the data points of the post-stacked transient are averaged over a successively increasing interval and weighted by a Hanning-Window (*Scholl*, 2005). No normal error propagation is considered in the smoothing scheme as the errors tend to get too small at late times, due to the large averaging-window. In contrast to the standard LOTEM processing steps, *Munkholm and Auken* (1996) introduce an algorithm where the data is log-gated and subsequently gate-stacked to obtain a more sophisticated noise model for TEM data. Additionally, the errors are estimated in the final step of processing and no further error propagation estimation is needed. In the following, the log-gating/gate-stacking scheme is explained and compared to the standard LOTEM processing using a Hanning-Window. Finally, the marine DED data is processed according to the approach of *Munkholm and Auken* (1996), as the noise considerations seem more intuitive.

The data is measured using a specific sampling rate, resulting in a linear time vector with time-steps equalling the sampling rate. The process of log-gating refers to an integration of the measured voltages over time intervals that increase logarithmically (*Munkholm and Auken, 1996*). The early time-gates contain only few linear time samples, whereas the later time-gates contain many. Therefore, the effect of log-gating will decrease the error estimations with some proportion to time. In the case of white noise, the relation is $1/\sqrt{t}$ (*Munkholm and Auken, 1996*).

The process of log-gating is exemplified in Fig. 7.9. The measured time segments (black) and stacked transient (blue) are displayed for linear and logarithmic time in Fig. 7.9a and Fig. 7.9b, respectively. The boundaries of the logarithmic gates are displayed by red dots, the time points of the final transient by red crosses. More intuitively displayed in Fig. 7.9a, the gates increase logarithmically in time. The early time gates may contain only one or two data points and are therefore, practically identical to the measured data. The log-gated time points at late times are averaged using a larger number of measured time samples that are fitted using polynomial curve. Sporadic noise contributions in form of voltage spikes at intermediate to late times are smoothed rigorously prior to gate stacking resulting in smoother data that contain less outliers compared to the linear time segments. This stabilises the stacking result. Subsequently, each log-gated time point is stacked to improve the SNR of a single measurement. In this sense, the SNR of a single measurement (s_0/n_0) is improved by,

$$\frac{s_0}{n_0} = \sqrt{N} \frac{s}{n} \quad (7.5)$$

where s/n refers to the SNR of the stacked transient and N the number of stacked

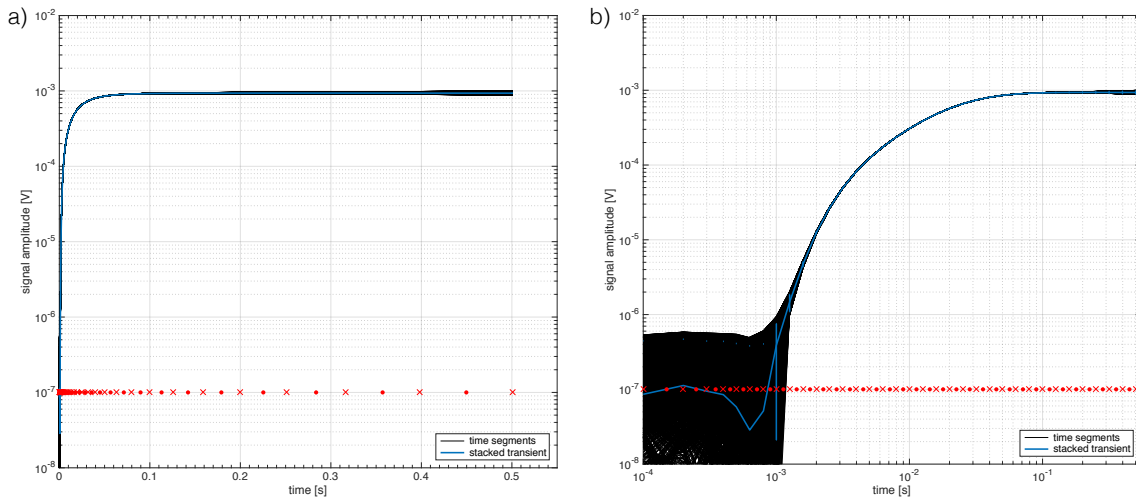


Figure 7.9: Exemplary illustration of how data is log-gated using the data acquired at Station p16NR. All measured time segments are displayed in black. The stacked transient in blue. The red dots symbolise the logarithmically increasing gate boundaries for (a) linear time and (b) logarithmic time. The red crosses represent the time points of the final transient.

times segments.

A selective, sometimes also called robust stacking scheme is applied to ensure that the final transient is less influenced by voltage drifts and other forms of sporadic noise. First, time segments are levelled and the voltages at each time gate are sorted in descending order. A normal probability plot will determine the threshold of the selective stacking scheme. Subsequently, the percentage of data determined by the chosen threshold is removed from the upper and lower portions of the sorted data vector. The mean value of the remaining data is then calculated according to

$$\bar{d}_i = \frac{1}{k_{max} - k_{min} + 1} \sum_{j=k_{min}}^{k_{max}} d_{ij}, \quad (7.6)$$

where k_{min} and k_{max} are the minimum and maximum indexes corresponding to the threshold of the sorted vector, respectively. As mentioned, all values with indexes larger than k_{max} and smaller than k_{min} are not considered.

The error is estimated during the stacking process. For normally distributed data, the standard deviation of the data seems to be a reasonable error estimate (*Scholl, 2005*). If N measurement values are distributed normally around the mean value \bar{d}_i , the standard deviation is

$$\sigma_i = \sqrt{\frac{1}{N-1} \sum_{j=1}^N (\bar{d}_i - d_{ij})^2}. \quad (7.7)$$

It accounts for 68.27% of the data set and can often be considered a reasonable error estimate. Yet, field data is rarely normally distributed around a mean value (*Scholl, 2005; Helwig, 2000; Scholl, 2001*), but enforced using the selectively stacking scheme. In that case, the standard deviation calculated with Eq. (7.7) is inconsistent with the measured data and the resulting errors will be too small for EM data. Following *Scholl (2005)*, it is more reasonable to calculate the data errors according to

$$\tilde{\sigma}_i = \frac{q_{3i} - q_{1i}}{1.35}, \quad (7.8)$$

where q_{3i} and q_{1i} are the values of the 75% and 25% thresholds of the sorted data vector, respectively. The denominator of Eq. (7.8) will cause $\tilde{\sigma}_i \approx \sigma_i$ for normally distributed data (*Scholl, 2005*).

Errors calculated according to Eq. (7.8) may still be improper, as they do not account for systematic errors, low frequency noise sources, and errors due to the system response. Therefore, each datum is assigned a minimum percentage error to account for these systematic errors. For DED data in Israel, a minimum error of 1% is declared corresponding to the marine EM studies of *Hölz et al. (2015)*.

The log-gating and gate stacking process is applied instead of the time-variable Hanning-Window. Therefore, a qualitative comparison is undertaken. Exemplary data is displayed in Fig. 7.10. Note, the transients were not interpolated to equal

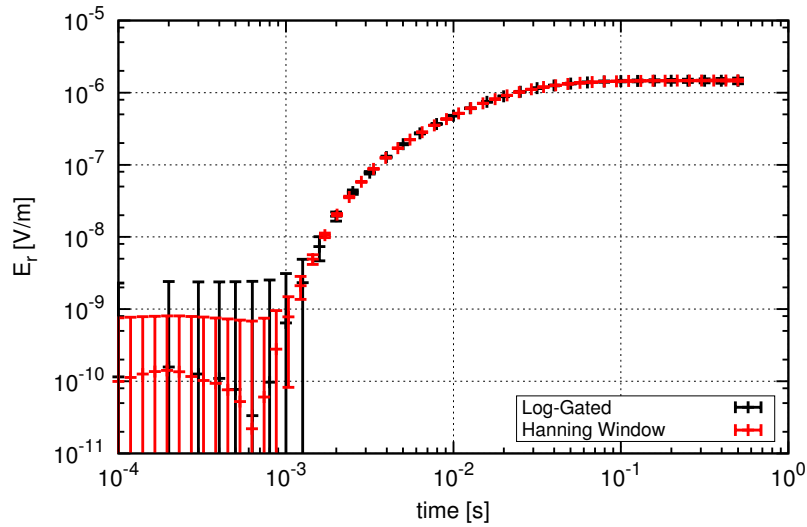


Figure 7.10: Comparison between log-gated/gate-stacked data in black and stacked and smoothed data in red.

time points. The log-gated data is displayed in black, the stacked and smoothed data in red. Overall, the data values are nearly identical aside from the very early times ($t < 1e^{-3}$ s), where the data has a poor SNR. For intermediate to late times, the data errors are comparable. The early time errors are larger for the log-gated data due to the moving average scheme. The errors are determined after the measured voltages are integrated over a time window. Accordingly, the values close to the noise floor will be influenced more severely. In contrast, the errors for the Hanning-Window scheme are calculated prior to smoothing. Therefore, the errors only depend on the stacking error at one linear time stamp and do not take neighbouring data points into account. As a result, the errors are smaller for data points in the vicinity of the noise floor if a Hanning-Window is applied. However, this does not mean that the smaller error estimates reflect the true uncertainty of the measured data. Thus, the log-gating/gate-stacking scheme was inevitably chosen to process the measured data, as the errors seem to be more reasonable.

7.3 Background Noise Measurements

During the survey, noise measurements were conducted at selected stations. The EM background noise is determined by measuring without a transmitting signal. In the following, these measurements are assessed and compared to the error estimates of the measured data. Specifically, the large error at early times for step-on and at late times for step-off are analysed under consideration of the background noise model.

According to *Munkholm and Auken (1996)*, the log-gated noise should have a time-dependent decay proportional to $1/\sqrt{t}$ for Gaussian noise with a zero mean. In the case of the noise measurements displayed in Fig. 7.11, this only corresponds to the late times of $t > 0.1$ s, illustrated by the red line. For early times, the noise

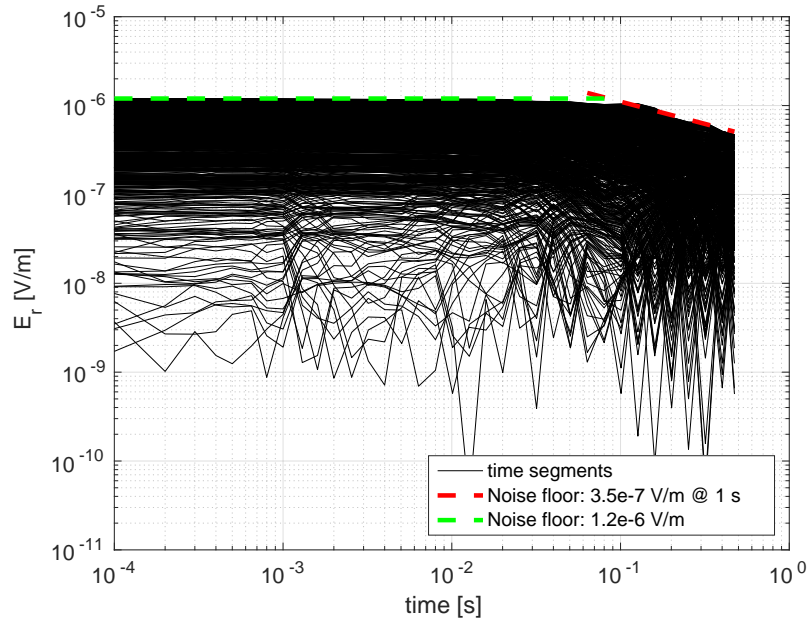


Figure 7.11: Background EM noise measurements from station p12NR. Displayed are the individual time segments in black, a constant noise floor of $1.2e^{-6}$ V/m in green and a time dependent noise level of $3.5e^{-7} \cdot t^{-0.5}$ V/m in red.

measurements appear to be constant in time (green line). Although this seems contradictory to the work of *Munkholm and Auken (1996)*, it is logical considering the different acquisition parameters. The TEM transients of *Munkholm and Auken (1996)* were acquired with a much higher sampling rate compared to the data in Israel. The log-gating scheme in the time ranges considered by *Munkholm and Auken (1996)* average over a higher number of data points in comparison to the early time range of the DED data. Therefore, a $1/\sqrt{t}$ dependency is not necessarily expected at early times of the DED data. The time-dependent noise decay becomes apparent at late times, where a decay of the noise floor resembles $1/\sqrt{t}$.

For the step-on signals, the EM noise at early times is most relevant, as the registered signal increases with time. For step-off, the late-time noise is important, as they decay below the noise level at certain delay times. In the following, the noise model for step-on/off are discussed together with the background noise model. The maximum errors, derived from the noise models of each day (displayed for Day 1 in Fig. 7.11 by green and red lines), are normalised by \sqrt{N} and the current amplitude of the corresponding transmitter station. This normalised noise level is generally referred to as the noise floor. It differs at each station due to the dependency on the number of utilised stacks and threshold chosen before stacking.

In Fig. 7.12, the processed transients measured at station p03FR are displayed. In general, the derived noise floor shows a high consistency to the error estimates of the measured data, illustrated by the error bars. The early time points of the step-on signal ($t < 1e^{-3}$ s) are beneath the noise floor. Consequently, the associated error estimations are large. As the signal increases and surpasses the noise floor, the errors decrease reaching the declared minimum error of 1%.

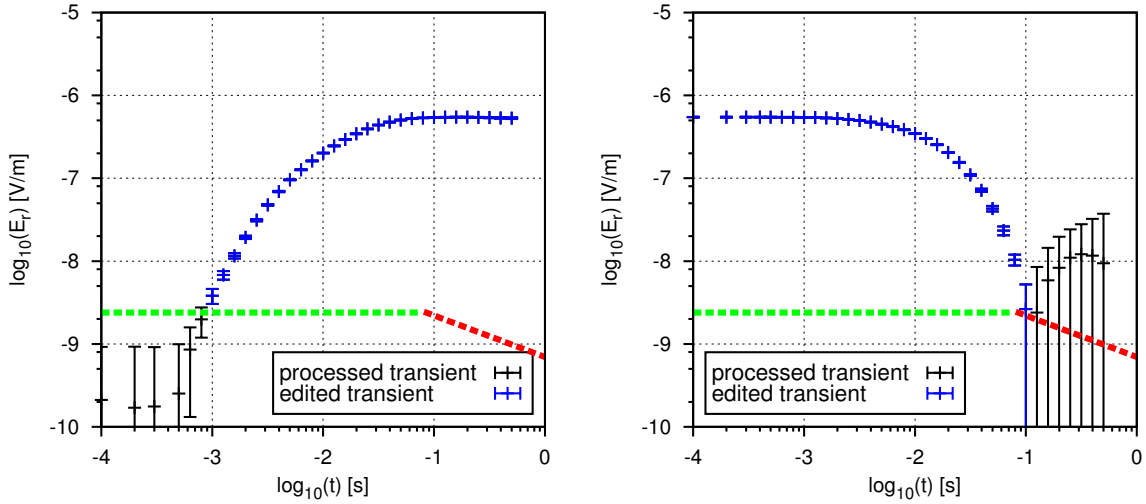


Figure 7.12: Processed transients at station p03FR. The step-on transient (left) is influenced by the noise model at $t < 1e^{-3}$ s, whereas the step-off transient (right) is influenced at $t > 8e^{-2}$ s. The normalised noise level is displayed by the dashed coloured lines.

The step-off transient is displayed in the right image of Fig. 7.12. The transient is especially susceptible towards a poor SNR at late times, as the transmitted current signal reaches zero. Accordingly, the transient signal will decay into the noise floor at late times. The majority of the step-off signals acquired in Israel possess a sign-reversal. However, this does not coincide with the step-on signal. These may appear in step-off transients as a result of bathymetry and/or geometrical inaccuracies (refer to Chapter 6 and Chapter 7). However, it is difficult to determine if these appear due to bathymetry effects or due to the poor SNR at late times. In any case, sign-reversal cannot be assessed using 1D inversion. For the following inversion and modelling scheme, the step-off transients are cut before the sign reversal and all following time points are neglected. In the following, these will be named edited step-off transients.

7.4 Field Data

Each data set is processed and edited according to the processing steps presented in the preceding section. In total, 17 stations were recorded along the profile: 6 from the near-receiver and 11 from the far-receiver. The stations on the land-side of the No-Anchor-Zone (p01 - p06) are expected to be above the freshwater aquifer. The remaining stations, located on the sea-side (p07 - p17) are either above the aquifer transition zone or above a half-space consisting of seafloor sediments. Note, the station names corresponding to the position along the profile are listed in Appendix A. In the following, the processed and edited transients are displayed and preliminary assertions are made based on the transient decay and derived profile plots for step-on and step-off signals. Note, separate plots display the near and far receivers, as the amplitudes and dynamic ranges differ by approximately one order of magnitude. The transients of each receiver are therefore only compared to themselves.

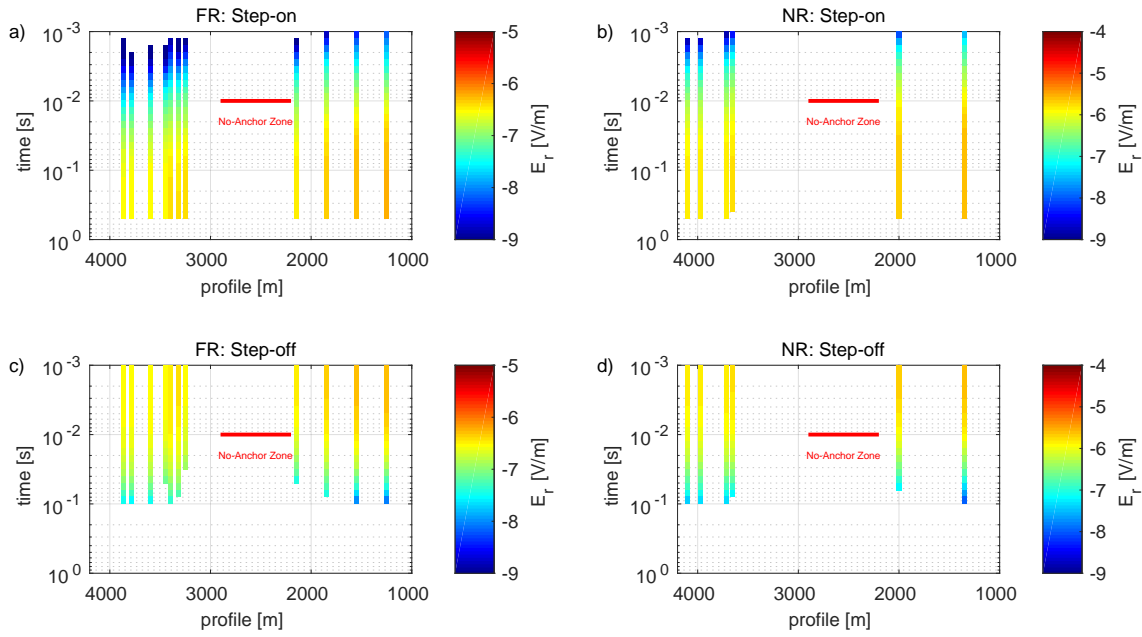


Figure 7.13: Processed and edited transients Rx2 (a and c) and Rx1 (b and d) plotted against the position along the profile. The step-on signals are displayed on top, the step-off on the bottom. The signal amplitude at specific times is illustrated by the colour bar.

Figure 7.13 shows the acquired transients plotted against the position along the profile. The y -axis is time in s and is not to be mistaken for depth. The colour bar refers to the associated signal amplitude. In the left column, the data of the far-receiver are displayed. The right column shows the data of the near-receiver. Due to the technical difficulties during the measurement, five stations are missing from the near-receiver (refer to Section 7.1.4). The top figures display the step-on signals from $t = 1e^{-3} - 0.5$ s. The bottom the step-off transients in the same time range. Note, the colour scales for far- and near-receiver differ due to the differences in signal amplitude and dynamic range.

The increased signal amplitudes at late times for stations located between 1000 m and 2300 m is one prominent feature in the step-on data (see Fig. 7.13a). These increased DC voltages imply the presence of a more resistive subsurface compared to the remaining sea-side stations. This is a preliminary indication that the resistive freshwater aquifer is detected. Moreover, these increased DC voltages are apparent in all stations up to station p09FR. The remaining sea-side stations exhibit much lower DC voltages, suggesting a more conductive subsurface. A preliminary interpretation of the data suggests that the freshwater aquifer extends seawards up to station p09FR or to approximately 3400 m from the shore. This effect is also apparent in the early times of the step-off data. Consequently, the measured DC voltages of both data sets convey a consistent image of the subsurface resistivity structure.

Aside from the DC voltages, very little information can be extracted from the transient behaviour. The step-on data of the sea-side stations exhibit decreased electrical fields at early times, which may be a further indication of a more conductive sub-

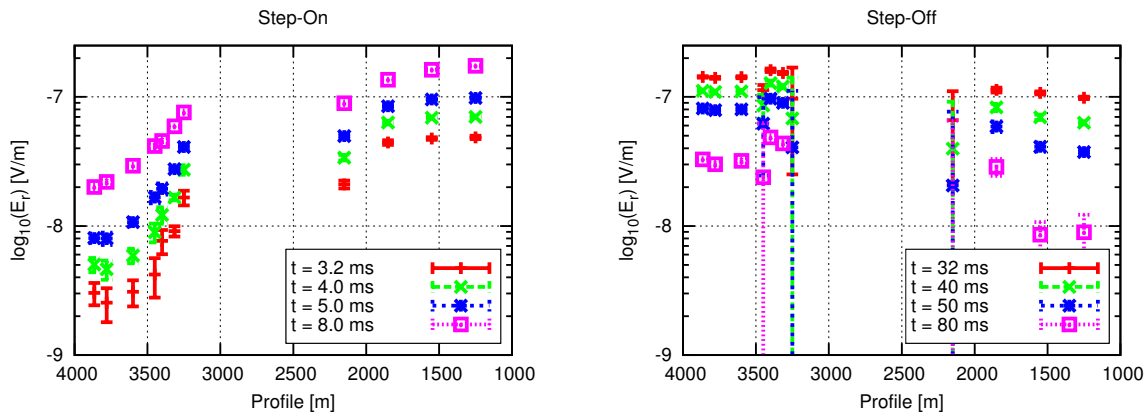


Figure 7.14: Profile plots of measured data at the far receiver for selected time points. The step-on signals are displayed on the left, the step-off on the right. The coloured markers display radial electric field amplitudes at selected time points plotted along the profile.

surface. Unfortunately, the step-off data cannot be assessed in an adequate manner, as they do not reach the time range where an aquifer signature is noticeable (see Chapter 5).

To identify if a lateral resistivity discontinuity is apparent in the measured data, profile plots are utilised. These are presented in Fig. 7.14 at selected time points for step-on and step-off data. Unfortunately, the step-off data does not show a significant result, as time samples are shown that are less relevant in identifying the freshwater aquifer. Of course, this is due to the poor SNR of the late-time data that is below the noise floor. In contrast, the step-on data clearly indicates a 2D resistivity structure and resemble the profile plots of the synthetic modelling study (see Fig. 6.12). According to the latter, the aquifer boundary is located at a distance from the peak corresponding to the offset. Unfortunately, the peak cannot be identified due to data gap in the No-Anchor-Zone. However, if we assume the peak to be located somewhere near 3000 m, then the aquifer boundary should be located at around 3600 m from the shore.

7.5 Summary of the Field Survey and Data Processing

The first marine DED measurement was conducted off the Mediterranean coastline of Israel to study a sub-seafloor groundwater body. In total, 11 transmitter stations were measured during the four-day survey. Due to technical difficulties with their research vessel, the original project partners from IOLR were unable to participate. Fortunately, EcoOcean offered to conduct the survey. However, the original plan of towing the system over the No-Anchor-Zone was denied by the new Captain and as a result, a data gap exists in the profile centre. However, data was obtained on both sides of the pipeline and therefore, a delineation of the sub-seafloor resistive

freshwater aquifer is still possible. Additional technical difficulties and poor weather conditions during some survey days prohibited sufficient data quality at five stations. These data sets are neglected in the following interpretation.

A 50% duty cycle transmitting signal was utilised to enable a joint evaluation using both step-off and step-on transients at each station. Unfortunately, the step-off signals suffer from a poor SNR at late times, and as a result, only the early to intermediate times are interpretable. If this is a bathymetry effect, a geometrical distortion or solely a noise issue remains unanswered. However, it is unfortunate as the synthetic 2D modelling studies show that the late times of the step-off transients are important to derive the hydrogeological structure of the western aquifer boundary. In contrast, the step-on transients are of much higher data quality in the relevant time range. Solely the very early times ($t < 1e^{-3}$ s) are below the noise floor, but are disregarded in the interpretation. Fortunately, the aquifer response is expected to be at several ms and is unaffected by the poor SNR earlier than 1 ms.

The acquired data shows very similar features compared to the synthetic data calculated in the 2D modelling studies. Especially the profile plots of the step-on data indicate a lateral resistivity contrast located at approximately 3600 m. A resistive body is expected to the East and a conductive body to the West. The following inversion and modelling studies will show that further information regarding the sub-seafloor resistivity structure can be derived from the measured DED data. Based on the measured step-on data, an assessment of the hydrogeological structure at the western aquifer boundary is feasible.

1D Inversion of Field Data

One-dimensional interpretation of the acquired DED data is the focus of this chapter. Often, 1D inversion is considered first due to the small computational load compared to a full multi-dimensional inversion or modelling study. Furthermore, the preceding 2D modelling studies show that an adequate estimation of the true sub-seafloor resistivity structure is possible using the step-on signals in a 1D inversion. In the following, the earth is assumed as a stratified medium consisting of homogeneous, isotropic layers with certain thickness and resistivity values. In 1D inversion, these model parameters are varied in order to fit the measured data.

Commonly, two inversion approaches are applied to minimise the chance of a misinterpretation. These are generally referred to as Occam and Marquardt inversion. The Marquardt inversion scheme is more dependent on *a-priori* information of the interpreter compared to Occam inversion. For example, judging the correct number of layers, resistivity values and thicknesses of the starting model is difficult beforehand. This may lead to misinterpretation of the data if falsely chosen. Thus, it is advisable to conduct the Occam inversion first, using both regularisations. Based on the resulting resistivity models, a starting model for the Marquardt inversion is derived with estimations for number of layers, resistivity and thickness values. Subsequently, different analyses are performed using the best fit Marquardt inversion model to investigate model parameter resolution. These include the calculation of equivalent models, an SVD analysis of the weighted Jacobian and further 1D modelling studies.

The Occam inversion models consist of a fixed number of layers with logarithmically increasing thicknesses and variable resistivity values. In the inversion scheme, only resistivity values are varied to fit the measured data while keeping the thicknesses of each defined layer constant. All displayed Occam inversion models consist of 20 layers with a minimum thickness of 5 m. Trials were made with models of 25 and 30 layers, but showed no noticeable differences to the 20 layer model. To limit the computational load, a 20-layer model is chosen for the following data interpretation.

The measurements were conducted using a 50% duty cycle signal. The original plan aimed at interpreting both step-on and step-off signals jointly in order to obtain an improved resistivity-depth model. The 1D modelling studies indicate that either current signal is sensitive towards different model parameters. The step-on signal provides more information regarding the depth of the resistive aquifer, whereas the step-off signal exhibits an increased sensitivity towards the resistivity of the lower conductive half-space. Accordingly, a joint interpretation may increase the resolu-

tion of all parameters, provided a sufficient data quality is reached. Unfortunately, this is not the case for the measured step-off transients. As a result, no significant improvement is noticeable. This is demonstrated for one exemplary station located above the resistive aquifer. The interpretation of all other stations confines to step-on signals.

The $CF = 1$ is fixed during the 1D inversion process. However, a comparison of a fixed and free CF is conducted at the end of this chapter to motivate the application of a CF in the 2D interpretation shown in Chapter 9.

The resistivity-depth models displayed in this chapter refer to the depths below the seafloor. For each station, the correct water depth is acquired from multi-beam data and fixed for the process of inversion. The water resistivity was derived from in-situ measurements presented by *Lippert* (2015) and remains constant at a value of $0.2 \Omega\text{m}$. The inversion software *MARTIN* offers the possibility of also inverting for seawater thickness and resistivity. However, the provided bathymetry data of the Israel Oceanographic and Limnological Research allows a precise representation of the true bathymetry. The applied water depths are derived from these measurements and remain constant in the inversion process. Note, different water depths are applied depending on the transmitter-receiver configuration along the profile. For more information regarding this topic refer to Section 6.2.1.

8.1 Evaluation of the Current Signals

The application of a 50% duty cycle signal did not achieve the desired results, as the poor data quality of the step-off signals prohibit a complete joint interpretation. Consequently, this approach is abandoned in the extent of this thesis. Yet, a joint evaluation at one selected station does seem useful, as the approach may become relevant for future shallow marine DED applications. In the following, station p03FR is chosen exemplarily, as it is located above the resistive aquifer. The inversion results are compared to the 1D modelling studies presented in Section 5.2.

First, each transient acquired at station p03FR is interpreted individually using the inversion schemes of Occam and Marquardt. Subsequently, the transients are jointly inverted and resolution studies are conducted. Finally, the value of jointly interpreting both signals is analysed and compared to the 1D modelling results. An outlook is given for future applications.

8.1.1 Comparison of Current Signals

For the comparison of the acquired transients, a common figure scheme is used to display the results. The left subfigure displays the inversion models for Occam R1, Occam R2, Marquardt and the equivalent models in orange, red, blue and grey, respectively. In the top right subfigure, the measured data including error estimates are displayed by black markers. The calculated data of each inversion model is plotted in the respective colour. The bottom right subfigure displays the residual error ϵ_i of the measured and calculated data at each time sample. Highlighted in

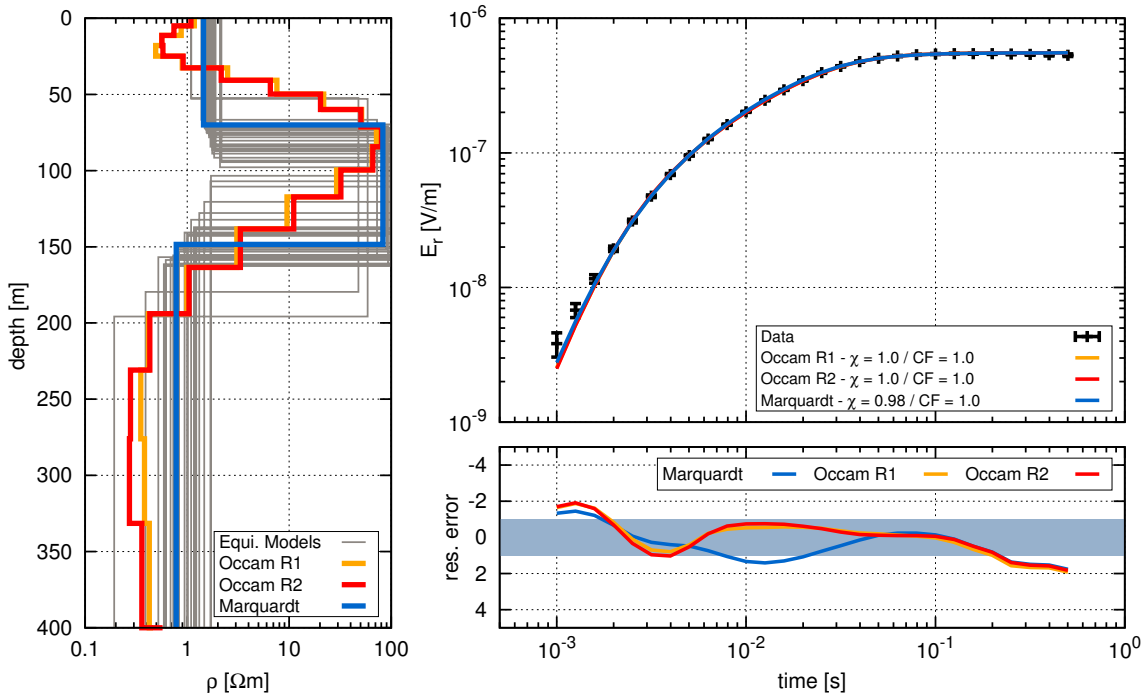


Figure 8.1: Inversion models obtained from the step-on transient at station p03FR. The left image shows the inversion models for Occam-R1/R2, Marquardt and equivalent models in orange, red, blue and grey, respectively. The image on the top right displays the measured and calculated data. The bottom right image shows the residual error as a function of time. The blue box describes the range in which the calculated transients are within the error bounds.

blue is the range where $-1 \leq \epsilon_i \leq 1$, indicating a data-fit within the error bounds at each time sample.

The inversion results of the step-on transient at station p03FR are displayed in Fig. 8.1. The data fit of all inversion models is $\chi \leq 1$, denoting a resistivity-depth structure that adequately explains the measured data within the error estimates. However, the residuals plotted for each time stamp indicate that the majority of intermediate time points are over-fitted, whereas the very early and very late times are outside of the error bounds. As all three inversion models exhibit this characteristic, the following scenarios are debatable. (1) The 1D inversion cannot fit all data points within the error estimates as the resistivity-depth model may be incorrect. The two-dimensional effect of the bathymetry may prohibit and adequate data fit using 1D inversion (see Section 5.2). (2) The water depth is over-estimated causing the calculated data at early times to be smaller than necessary. (3) The error estimates for the first two and last three time points are too small. (4) Errors in the system response may decrease the data fitting at early times.

Generally, all of the above stated scenarios may apply. Especially the 1D interpretation of 2D data needs to be considered. However, the residual errors at each time sample do not exceed a value of two and an average fit of $\chi \leq 1$ is reached. The resistivity-depth model describes the data in a sufficient manner, which is under-

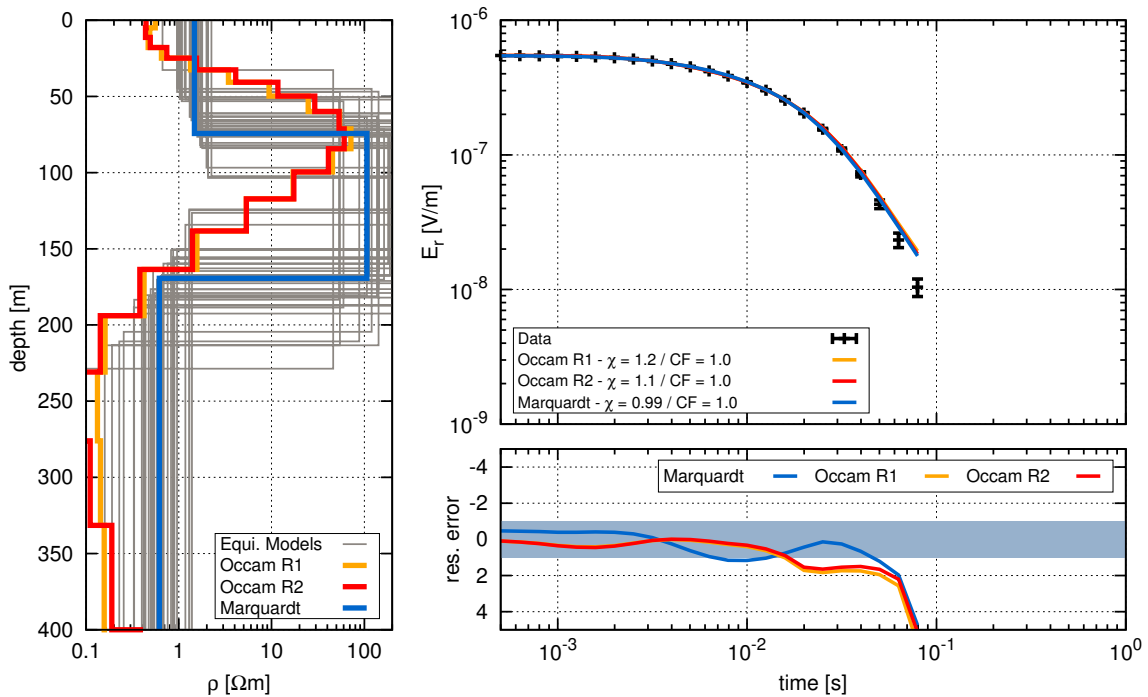


Figure 8.2: Inversion models obtained from the step-off transient at station p03FR. The left image shows the inversion models for Occam-R1/R2, Marquardt and equivalent models in orange, red, blue and grey, respectively. The image on the top right displays the measured and calculated data. The bottom right image shows the residual error as a function of time. The blue box describes the range in which the calculated transients are within the error bounds.

lined by the 1D inversion of synthetic 2D data. Furthermore, the derived resistivity model is consistent with the marine LOTEM results of *Lippert* (2015).

The resistivity models show a three-layer subsurface with a resistive layer enclosed by conductive layers above and below. The resistivity values from the top to bottom are approximately $\rho_{1-3} = (1.4 \Omega\text{m}, 100 \Omega\text{m}, 0.7 \Omega\text{m})$. The resistive layer is located at a depth of approximately 50 m - 70 m beneath the seafloor, which coincides with the expected depth of the freshwater aquifer. However, absolute values of the resistivity, depth and thickness may differ due to the variability in the equivalent models. Several combinations of the corresponding model parameters achieve equal data fits. Despite the variability of absolute values, all equivalent models are consistent showing an intermediate resistive layer embedded between two conductive layers.

The 1D inversion models obtained from the step-off transients at station p03FR are illustrated in Fig. 8.2. Note, due to the poor data quality at late times, the transient is cut at approximately 90 ms. In general, the inversion models exhibit a high consistency with the models obtained from the step-on inversion. The resistive layer has comparable resistivity and depth values, but a larger thickness. It is debatable if this is a result of the poor data fit at late times (see Fig. 8.2), or due to the limited sensitivity of the step-off signal towards the aquifer thickness (see Fig. 5.3). The transient is edited by removing all data points following the

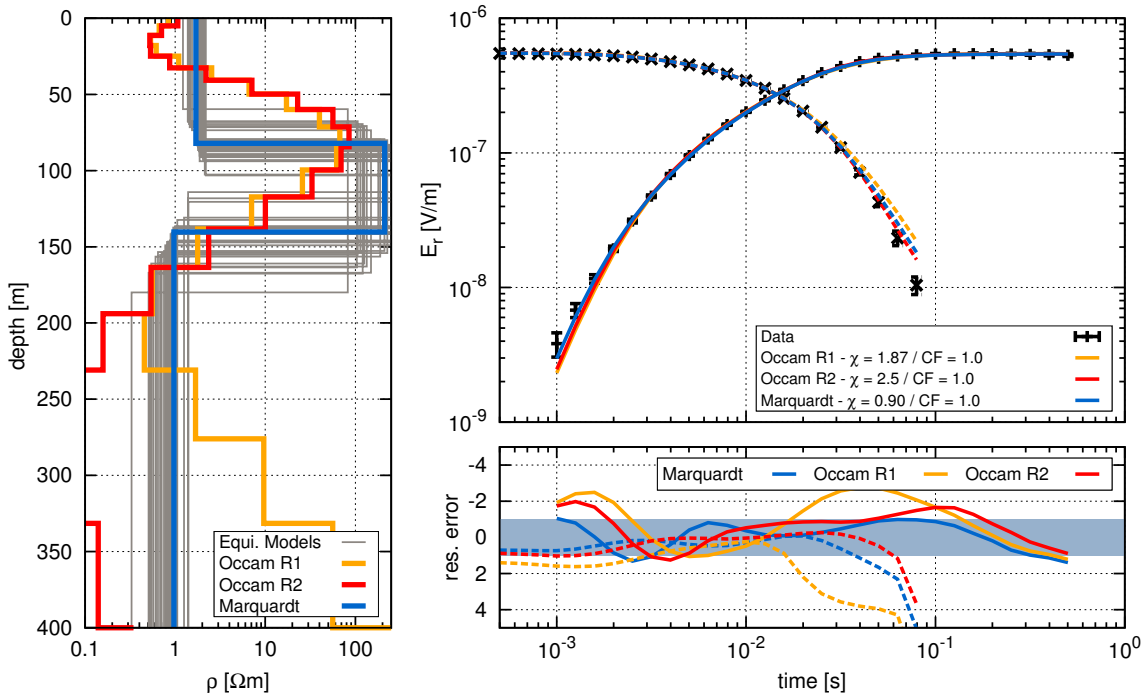


Figure 8.3: Models obtained from the joint inversion at station p03FR. The left image shows the inversion models for Occam-R1/R2, Marquardt and equivalent models in orange, red, blue and grey, respectively. The image on the top right displays the measured and calculated data. The dashed lines represent the calculated response for step-off, the solid step-on. The bottom right image shows the residual error as a function of time. The blue box describes the range in which the calculated transients are within the error bounds.

sign-reversal. However, the step decrease of the transient indicates that preceding data points may also be influenced by the sign-reversal. This effect is similar to the data distortions studied in Section 5.3.3. The appearance of the intermediate resistive layer may result solely from the steeper decay caused by sign-reversal and not from the geological structure of the subsurface. This is problematic, especially since the main aquifer response is expected at the late times that are removed from the transient. Consequently, it is difficult to judge if the higher variability of the equivalent models results from an data artefact or from the missing data points at late times.

Both step-on and step-off current signals achieve similar results in the individual assessment. It seems natural to use both in the interpretation, as the synthetic modelling studies indicate that each transient is sensitive towards different model parameters. Additionally, the joint inversion should limit the number of equivalent models and consequently reduce the ambiguity of the inversion problem (*Jupp and Vozoff, 1975b*). The corresponding joint-inversion results are illustrated in Fig. 8.3. Since step-on and step-off signals obtained similar solutions in the individual interpretation, it is not surprising that the joint inversion models are also similar. However, the two Occam inversion models clearly separate at a depth of 200 m below the seafloor. A first assumption could be a decreased resolution below this

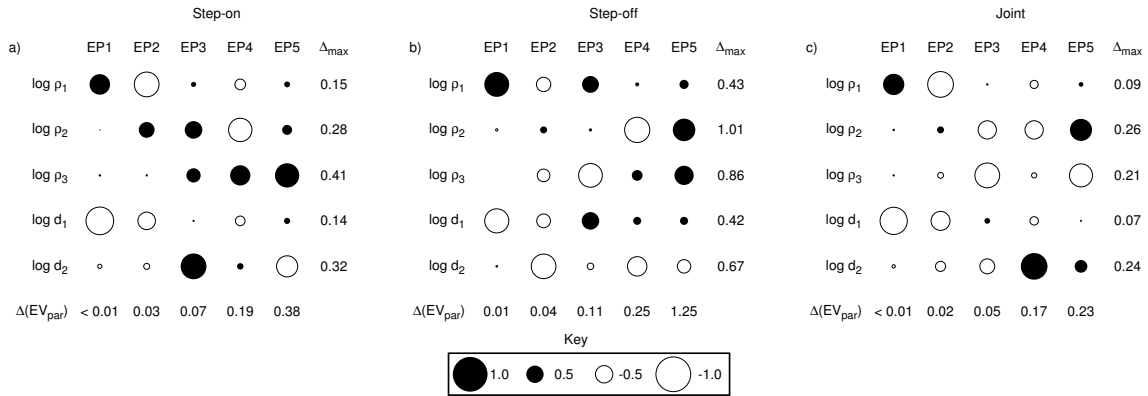


Figure 8.4: Graphical SVD-analysis of the weighted Jacobian. The radius of each circle is proportional to the coefficients in the matrix \mathbf{V} . The analysis for (a) Step-on, (b) Step-off and (c) joint inversion are shown.

depth. However, the residual errors also reveal that the calculated data of both Occam models are quite different, which may also account for the separation. In the range above 200 m, both Occam inversion models are consistent showing an intermediate resistive layer embedded by conductive layers above and below.

The resistivity value of the resistive layer is of a factor two larger in the Marquardt joint inversion model compared to the individual inversion. A decline in the aquifer thickness is also noticeable. The decreased variability of the equivalent models indicates a more conclusive picture of the resistivity-depth model compared to the single inversion, primarily in the regions of low resistivity above and below the resistive layer. If this attribute favours the application of a joint inversion is difficult to assess based solely on equivalent models. The following SVD analysis and importances study will help clarify if benefits of a joint inversion compared to a single inversion exist.

Based on the results of the inversion models alone, a conclusive evaluation of favouring inversion of either step-on, step-off, or joint is hardly feasible. A clear distinction may only arise in terms of consistency with previous measurements, data quality, SNR and computation time. In this sense, the step-on transient has clear advantages for 1D inversion due to the superior data quality. The poor data quality of the step-off signal is unfortunate as modelling showed that multi-dimensional effects are easier to distinguish using step-off signals. A fair comparison is not feasible with the acquired data set. However, SVD-analysis of the weighted Jacobian is conducted to further investigate the resolution characteristics of each transient.

To investigate the model parameter resolution of the three interpretation possibilities, a SVD analysis of the weighted Jacobian is carried out. The visual representation of the SVD analysis is presented for step-on, step-off and joint interpretation in Fig. 8.4a, Fig. 8.4b and Fig. 8.4c, respectively. The values $\Delta(EV_{par})$ and Δ_{max} are derived from the eigenparameters and eigenvalues following *Edwards (1997)*. A detailed explanation is found in Section 4.3.1. The EPs are sorted according to the size of their corresponding eigenvalue from left to right. Hence, EP1 is most relevant and EP5 least relevant. The radius of the circles are proportional to the coefficients

in the matrix \mathbf{V} , where the black and white colours highlight positive or negative coefficients, respectively.

All columns of Fig. 8.4a have more than one dominant entry, each associated to a log-scaled model parameter. For example, the first column (EP1) of Fig. 8.4a is interpreted as the linear combination

$$EP1 \approx V_{11} \cdot \log_{10}(\rho_1) - V_{41} \cdot \log_{10}(d_1). \quad (8.1)$$

In terms of the physical parameters, the first column is considered as,

$$\rho_1^{V_{11}}/d_1^{V_{41}}. \quad (8.2)$$

As the sign of the coefficient V_{41} is negative, this relation is seen as the resistivity-thickness quotient of ρ_1 and d_1 . Following this concept, the second column of Fig. 8.4a is the reciprocal resistivity-thickness product of the same parameters, with additional influences of ρ_2 . Thus, ρ_1 and d_1 can be resolved individually by EP1 and EP2, as the corresponding errors Δ_{max} are much smaller than unity. EP3 through EP5 share various combinations of the remaining model parameters d_2 , ρ_2 and ρ_3 . Where ρ_3 is least resolved, as its main contribution is in EP5. The values of Δ_{max} are much smaller than unity in Fig. 8.4a, indicating that all parameters are assumed resolved. The SVD analysis of the measured step-on data is practically identical to that of the synthetic modelling studies (see Fig. 5.11).

In Fig. 8.4b, the arrangement of the circles is different, indicating sensitivities towards other model parameters. Similar to Fig. 8.4a, EP1 is interpreted as the resistivity-thickness quotient of the first layer. However, the largest coefficient of EP2 comes from d_2 with considerable contributions from d_1 , ρ_3 and ρ_1 . The relatively large value of Δ_{max} suggests that d_2 is only moderately resolved. In that manner, ρ_2 is considered poorly resolved and ρ_3 moderately to poorly resolved. Hence, due to the poor SNR, the step-off signal can really only resolve ρ_1 and d_1 in a sufficient manner. The poor SNR of the step-off signal is unfortunate, as ρ_3 is theoretically better resolved compared to the step-on signal (see Fig. 5.11).

The SVD analysis of the joint inversion presented in Fig. 8.4c indicates improved resolution towards all model parameters compared to the individual SVD-analysis displayed in Fig. 8.4a and Fig. 8.4b. The arrangement of the circles and values of $\Delta(EV_{par})$ are very similar to the step-on signals. Differences can be found in the values of Δ_{max} , where the joint inversion has slight advantages. Clear differences are seen for ρ_3 , where an

Table 8.1: Importances of model parameters from the Marquardt inversion: 0 - 0.5 poorly resolved (-). 0.51 - 0.7 (o) moderately resolved. 0.71 - 1.0: well resolved (+). The CF is kept fixed at 1 for all inversion models.

	Step-on	Step-off	Joint
ρ_1	+	+	+
ρ_2	+	-	+
ρ_3	+	+	-
d_1	+	+	+
d_2	+	+	+
CF	1	1	1

improvement of resolution is observable for the joint inversion. In comparison to the step-off signal, the joint inversion exhibits much better resolution. Of course, this cannot be generalised, but is rather a result of the poor data quality in the step-off signal.

The importances of the corresponding Marquardt inversion models of Fig. 8.1 through Fig. 8.3 are listed in Table 8.1. The importances are discretised into groups labelled (-), (o) and (+), according to their respective values. Following *Lippert (2015)*, an importance of 0 - 0.5 denotes a poor parameter resolution (-). Values between 0.51 - 0.7 imply a moderate parameter resolution (o). Well-resolved parameters have an importance of 0.71 - 1 (+). The importances are generally consistent with the interpretation based on the SVD-analysis. However, the resolution of the single inversion tends to be better than expected. Surprisingly, based on the importances, ρ_3 of the joint inversion seems poorly resolved, although the SVD analysis proposed an enhanced resolution compared to step-on. This seems somewhat contradictory. All other model parameters are generally consistent between a joint inversion and a single inversion of step-on.

The sensitivity study using \mathbf{V} -matrix analysis and importances does not allow a clear evaluation of a resolution enhancement using joint inversion. The main conclusion of the sensitivity analysis is the poor result of the step-off signal due to the SNR issues. The step-on and joint interpretation are similar, where adequate results are obtained by inverting only step-on with less computational effort. For the acquired DED data, this approach is followed. Yet, future marine DED applications may still favour joint interpretation if step-off data of decent quality is obtained.

8.1.2 Significance of the resistive Aquifer

All inversion models shown in Fig. 8.1 through Fig. 8.3 suggest a resistive layer embedded in conductive marine sediments. Due to the previous marine LOTEM results of *Lippert (2015)* and TEM results of *Kafri and Goldman (2006)*, this resistive layer is interpreted as the sub-seafloor freshwater aquifer. The significance of this resistive aquifer is examined using a 1D modelling study. The parameters concerning the resistive aquifer, in this case depth (d_1), thickness (d_2) and resistivity (ρ_2) are varied, while keeping the resistivity values of the marine sediments (ρ_1 and ρ_3) constant at the result of the best fit Marquardt inversion model. The parameters concerning the aquifer are varied between the values: $d_1 = 10$ m - 200 m, $d_2 = 10$ m - 200 m and $\rho_2 = 0.1$ Ω m - 1000 Ω m. The modelling study also includes the case of no aquifer and even a conductive aquifer. It should be mentioned that although the resistivity of the conductive background sediments are kept constant, they have an elementary role on the modelling studies as a variation will broaden the equivalence domain. Yet, resistivity values of saltwater saturated sediments are expected to be at around 1.4 ± 0.5 Ω m. Consequently, strong variations in these parameters are not expected.

Figure 8.5 shows the results of the above-described modelling study in form of heat maps that represent the equivalence domain of the corresponding model parameter variation. Dark shading represents areas of good data fit, whereas light areas

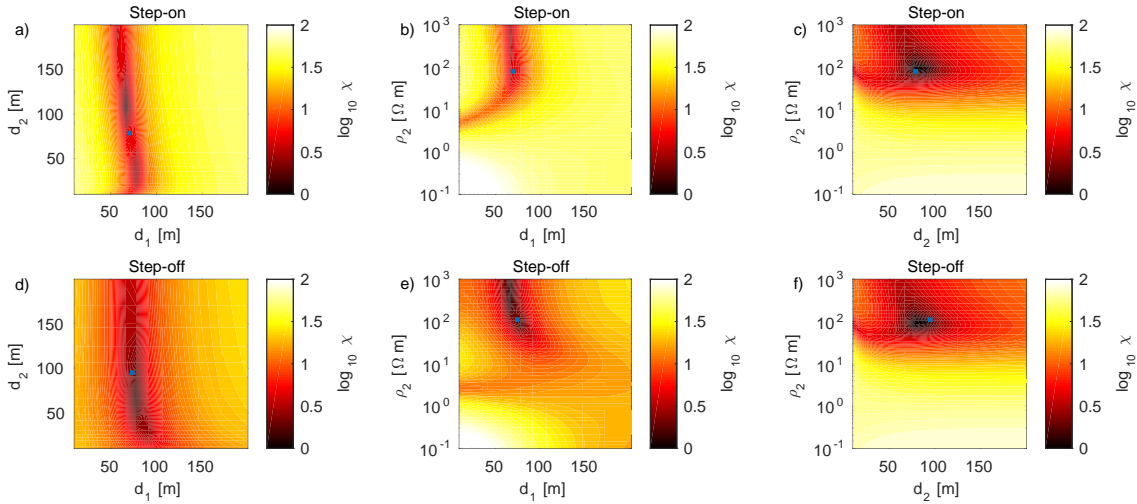


Figure 8.5: Modelling studies investigating the significance of the resistive aquifer layer. Illustrated are the logarithmic χ -values as colours for different variations of the aquifer parameters depth (d_1), thickness (d_2) and resistivity (ρ_2). The step-on signals are displayed in the images a) through c), the step-off in d) through f). The blue marker displays the values acquired by the Marquardt inversion.

describe regions of poor data fit. In images (a) through (c) step-on data fits are presented. In (d) through (f) step-off data fits. The errors are plotted as a function of model parameter variation for the three combinations, d_1 - d_2 , ρ_2 - d_1 , and ρ_2 - d_2 , respectively. The missing parameter in each combination is taken from the best fit Marquardt model. The blue marker in each plot symbolises the parameter combination of the best fit Marquardt inversion model.

The equivalence domain of the step-on signal is narrower compared to the step-off signal for all parameter variations. The exception is the variation of aquifer thickness and resistivity displayed in Fig. 8.5c and Fig. 8.5f. Here, the equivalence domain of both signals is nearly identical, suggesting a resistivity increase of the second layer with values exceeding 50 Ω m and corresponding thicknesses of 50 m - 100 m. In Fig. 8.5b and Fig. 8.5e, the variation of aquifer resistivity and aquifer depth is displayed for step-on and step-off, respectively. The equivalence domain suggests that the depth of the resistive layer is mapped more precisely using the step-on signal, as small alterations of this parameter will cause inferior fitting. This coincides with the detectability and resolution studies using synthetic data (see Chapter 5). Moreover, the results of Fig. 8.5b imply that a resistive aquifer is needed to fit the measured data. All models located within the dark regions of the equivalent domain have a higher resistivity than the seafloor sediments (1.4 Ω m). In Fig. 8.5a and Fig. 8.5c, the thickness-depth ratio of the aquifer is varied. Again, the equivalence domain is similar in both images, but the step-on signal is more precise. The depth of the aquifer is more restricted compared to its thickness. The latter may vary throughout the investigated model parameter space without considerably influencing the data fit. For step-on signals, variations of d_2 are again more restricted compared to step-off.

8.1.3 Summary of Current Signal Comparison

Evaluating the similarities of step-on and step-off signals at station p03FR leads to the following conclusions.

- The 1D inversion models of either signal are similar, although the step-off transient is clearly disadvantage due to the insufficient SNR at late times.
- Due to the poor data quality of the step-off transient and the limited transient length, the step-on signal has a superior resolution compared to step-off.
- The joint-inversion does not necessarily improve the result of the step-on inversion. SVD analysis indicates an improvement of resolution, which is contradicted by the model parameter importances. A clear indication of a resolution improvement is not observable.
- The equivalence domain studies indicate that the intermediate resistive aquifer is needed to sufficiently explain the measured data. This applies to both step-on and step-off.

In the extent of the thesis, 1D inversion models are calculated for step-on, step-off and joint inversion at all stations. The following interpretation will confine to the step-on signals. Joint inversion models at each station are shown in Appendix B.

8.2 1D Inversion of all Stations

In the following, 1D inversion results are displayed as a cross-section to convey a quasi-2D impression of the subsurface resistivity structure. The general procedure of the 1D inversion is identical to the previous section. First, the Occam models are calculated to derive a starting model for the Marquardt inversion at each station. Subsequently, resolution studies are realised using importances and SVD analysis. The latter is partly found in Appendix B as a resolution study at exemplary stations is sufficient for the interpretation.

For all following images containing cross-sections of the 1D inversion models, the following information should be considered. The shoreline is located at 0 m of the profile (extended towards the Southeast). The stations are labelled from right to left, station p01FR through p17NR. For a description of the station name, refer to Section 7.1.3 or Appendix A.

The Occam inversion models displayed in Fig. 8.6 are consistent with the marine LOTEM data of *Lippert* (2015). The exception is station p02NR, where the resistive aquifer is not detected. However, all other stations located east of the No-Anchor-Zone show a consistent image with an intermediate resistive layer. A depth interval of increased resistivity (30 Ωm - 60 Ωm), with a thickness of 70 m - 90 m, begins at a depth of 70 m beneath the seafloor. Above and below, zones of lower resistivity, interpreted as seafloor sediments are found. All stations have a data fit of $\chi \approx 1$.

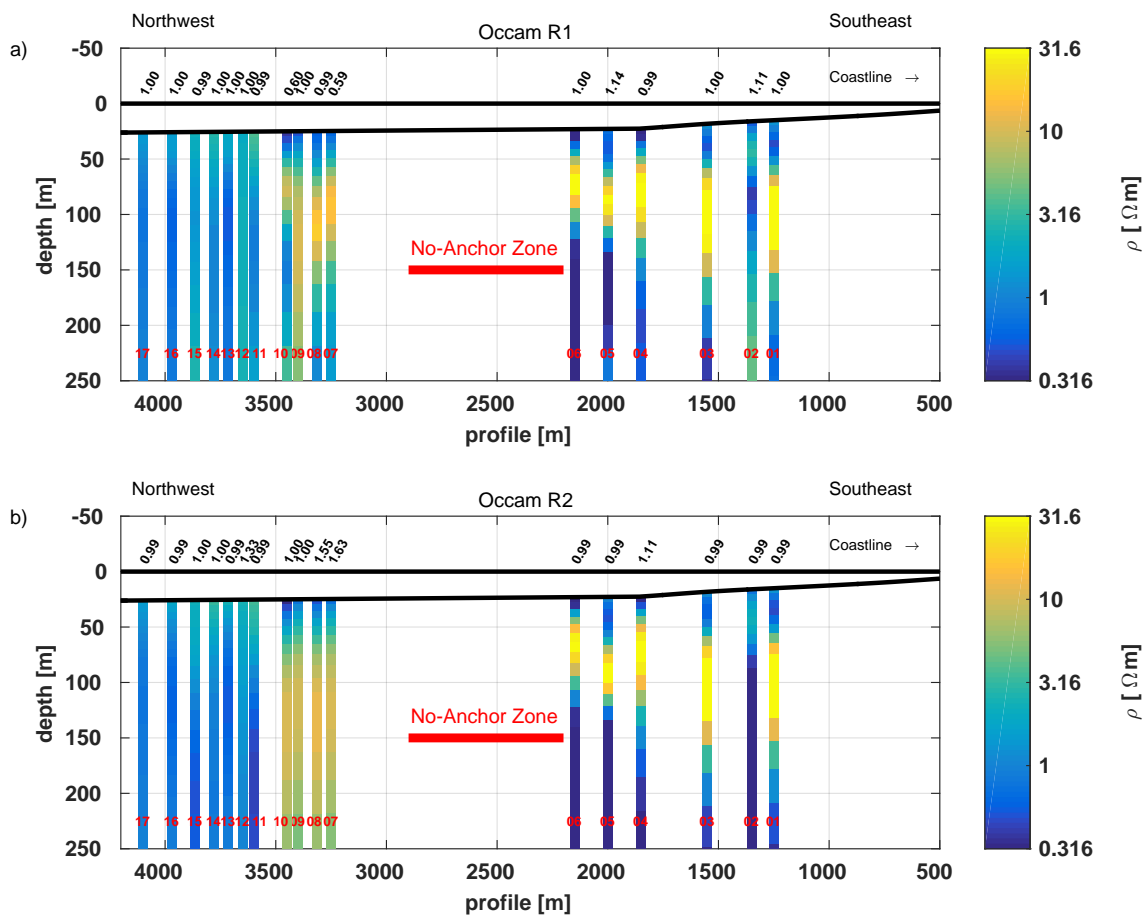


Figure 8.6: Occam Inversion models for Step-On signals of roughness 1 (top) and 2 (bottom) plotted against the receiver positions along the profile. The bathymetry is plotted using black lines and is derived from multi-beam data made available by IOLR. The data fit in form of χ is displayed above each model. The station numbers are displayed in red.

On the sea-side of the No-Anchor-Zone, a lateral resistivity variation is noticeable. The stations located close to the No-Anchor-Zone show a resistivity increase in the depth range of the assumed aquifer. However, the resistivity values do not reach the ones obtained at the land-side stations. This may suggest, that the freshwater/seawater transition zone is composed of a brackish water region, where the resistivity is clearly decreased compared to regions of freshwater. This would indicate an open aquifer scenario suggest by *Kapuler and Bear (1970)*. However, the considered Brackish-Water model in the preceding 2D modelling study (Section 6.2.2) also accounted for a brackish water zone. A region of moderate resistivity is not apparent in the 1D inversion models of the synthetic 2D data. Instead, the models are unable to map the brackish water zone completely. A possible alternative interpretation may be that the brackish water zone extends for either more or less than the assumed 500 m considered in the modelling studies.

Indications of a lateral resistivity contrast located to the west of the No-Anchor-Zone are visible in the 1D inversion models. Similar to the 1D inversion of synthetic 2D

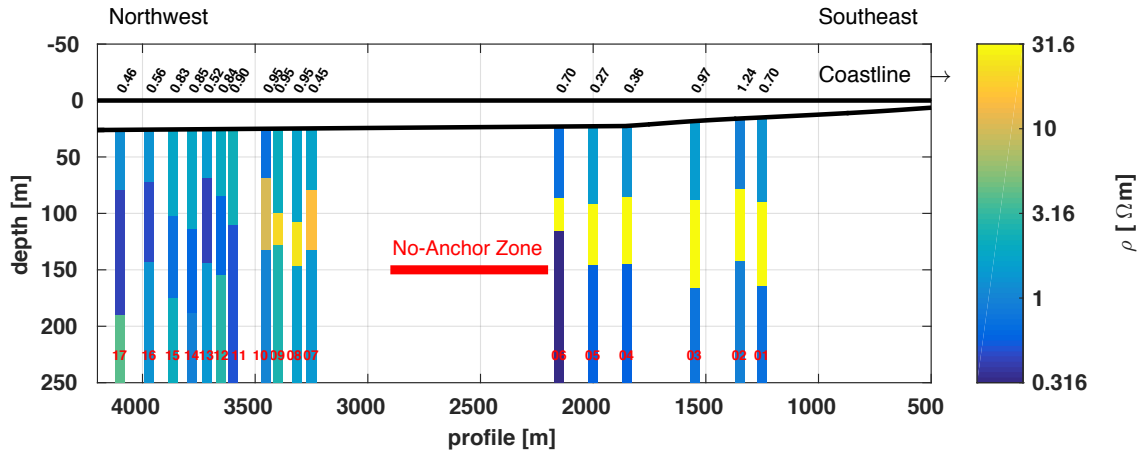


Figure 8.7: Marquardt inversion models for Step-On signals plotted against the receiver positions along the profile. The bathymetry is plotted using black lines and is derived from multi-beam data made available by IOLR. The data fit in form of χ is displayed above each model.

data presented in Section 6.2.2, conductive areas are located west of the transition zone are visible in the inversion models between 3500 m and 4000 m. Due to the colouring of the models, these effects are not well defined in the Occam models, but are especially prominent in the Marquardt inversion models displayed in Fig. 8.7. This is in general agreement to the modelling studies presented in Fig. 6.15. Unfortunately, the resistivity decrease is less prominent in the inversion models of the measured data. In part, this may be due to the general systematic errors, e.g. errors in offset, water depth, current amplitude, processing, etc. that do not affect modelled data. Additionally, the tow direction plays a dominant role. Nevertheless, a general tendency of similar behaviour is noticeable between the 1D inversion models of the measured and synthetic data.

One advantage of the acquired DED data set is that inversion models are obtained

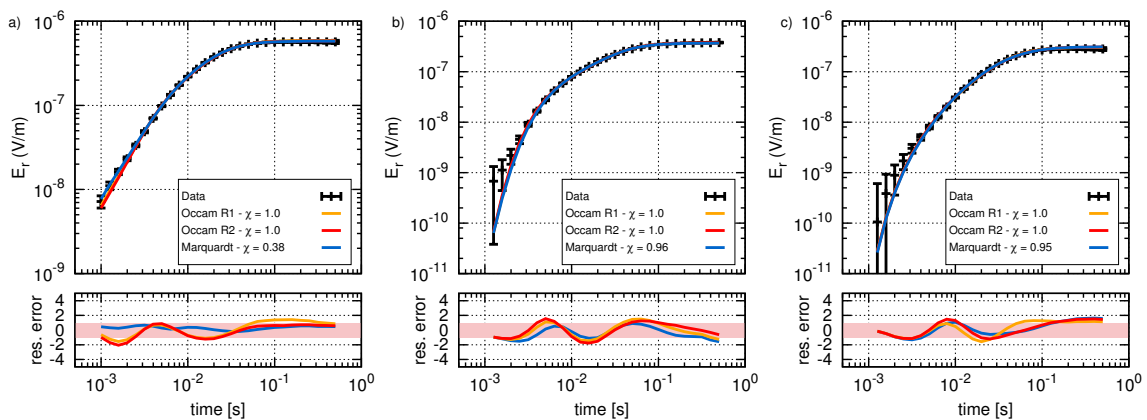


Figure 8.8: Data fit for the inversion models displayed in Fig. 8.6 and Fig. 8.7 for stations $p01FR$ (a), $p08FR$ (b) and $p15FR$ (c), respectively. The top images show the transients, the bottom the residual errors.

with a fixed $CF = 1$. Largely, this is due to the coupled transmitter-receiver measurement system that prohibits large offset errors. For the acquired LOTEM data set, this was not the case. The bathymetric effect causes a shift in the data, but can be ignored to obtain a good estimation of the sub-seafloor resistivity structure (see Section 6.2.2). Studies are performed for inversion models using a free $CF \neq 1$. Selected examples are presented in Fig. 8.11. These motivate a variable CF between 0.9 and 1.1 in the 2D modelling study presented in Chapter 9.

The data fit at selected stations for the Occam and Marquardt models are displayed in Fig. 8.8. The measured and calculated transients at stations p01FR, p08FR and p15FR are displayed in Fig. 8.8a, Fig. 8.8b and Fig. 8.8c, respectively. These stations are chosen as they are located above the aquifer, above the transition zone and towards the sea. The data fit of the remaining stations is given in Appendix B. The displayed data sets are fitted with $\chi \leq 1$, implying a data fit within the error bounds. No general tendency is observable in the residual errors as the calculated transients oscillate within the error estimates. One feature that is apparent are the superior data fits of the Marquardt inversion models. This general tendency is related to the truncation procedure of the Occam inversion and does not reflect the superiority of a Marquardt inversion model.

8.2.1 Importances and Resolution Analysis

Similar to the previous section, the model parameter resolution is investigated using importances and SVD analysis. Equivalent models are neglected, but can be viewed for the individual stations in Appendix B.

Figure 8.9 shows the SVD analysis for the selected stations p01FR (a), p08FR (b) and p15FR (c). The SVD-analysis of station p01FR presented in Fig. 8.9a, is practically identical to the step-on SVD analysis in Fig. 8.4a. At station p08FR, shown in Fig. 8.9b located above the assumed transition zone, the sensitivities are slightly different. EP1 and EP2 are sensitive towards the original model parameters ρ_1 and d_1 . The differences compared to Fig. 8.9a are the coefficients of EP3 through

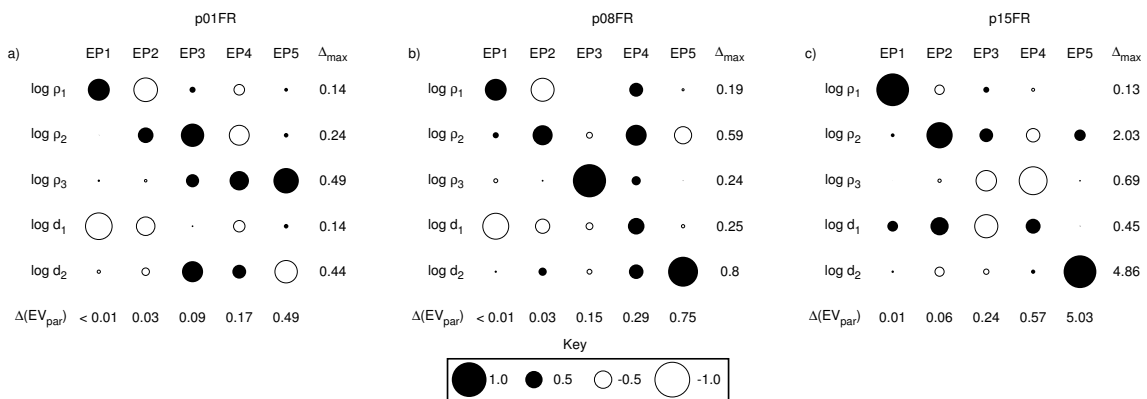


Figure 8.9: SVD analyses for the Marquardt inversion models displayed in Fig. 8.7 for stations p01FR (a), p08FR (b) and p15FR (c), respectively.

Table 8.2: Importances of model parameters from the Marquardt inversion: 0 - 0.5 poorly resolved (-). 0.51 - 0.7 (o) moderately resolved. 0.71 - 1.0: well resolved (+).

	p01FR	p02NR	p03FR	p04FR	p05NR	p06FR	p07FR	p08FR	p09FR	p10FR	p11FR	p12NR	p13NR	p14FR	p15FR	p16NR	p17NR
ρ_1	+	+	+	+	+	+	+	+	+	+	+	+	+	+	+	+	+
ρ_2	+	-	+	+	+	+	+	+	o	+	+	-	+	+	+	o	+
ρ_3	+	-	+	+	+	o	+	+	-	-	-	-	-	-	-	-	+
d_1	+	o	+	+	+	+	+	+	+	+	+	o	+	+	+	+	+
d_2	+	-	+	+	+	o	-	-	-	-	+	-	-	-	-	-	+
CF	1	1	1	1	1	1	1	1	1	1	1	1	1	1	1	1	1

EP5. The main contribution of EP3 comes solely from ρ_3 , denoting a resolved model parameter. $\Delta_{max}(\rho_3) = 0.24$ suggests that the original parameter is resolved better than $\pm 24\%$ meaning $\rho_3 = 1.59 \pm 0.38 \Omega\text{m}$. In contrast, ρ_2 and d_2 are only moderately to poorly resolved at p08FR. In Fig. 8.9c, EP1 and EP5 each have one dominant entry, associated to the model parameters ρ_1 and d_2 , respectively. Yet, Δ_{max} indicates that only ρ_1 and d_1 are well resolved, whereas ρ_3 is moderately resolved. The fractional errors $\Delta_{max}(\rho_1) = 0.13$ states that the original parameter should be resolved better than $\pm 13\%$ meaning $\rho_1 = 1.79 \pm 0.23 \Omega\text{m}$ of the original parameter. Note, a three-layer Marquardt inversion was conducted, although the Occam results indicated a two-layer or even homogeneous sub-seafloor setting. The SVD-analysis confirms that only model parameters are resolved that certify this prediction and the results of the Occam inversion models. A resistive intermediate layer is not needed to fit the data at station p15FR.

The SVD analysis of the step-on signal at the presented stations is consistent with the corresponding importances displayed in Table 8.2. Therefore, an examination of the importances is sufficient to obtain information regarding the resolution of specific model parameters for all stations along the profile. Note, all stations are inverted for a three-layer model although stations p11FR through p17NR only require a two-layer model for an adequate data fit. It should be mentioned that the importances refer to the values of the Marquardt model and are not to be confused with the presence of a resistive layer. Remember, stations p11FR through p17NR generally indicate a conductive second layer due to the 2D effect of the aquifer boundary. The calibration factor is listed in the final row of the table.

The model parameter importances at all stations clearly show that the resistivity and thickness of the seafloor sediments is best resolved. The values generally suggest a good resolution with exception of station p02NR and p12NR, where d_1 is moderately resolved. The importances calculated for the land-side stations (p01FR through p06FR, excluding p02NR) indicate a well-resolved resistive freshwater aquifer. In contrast, the stations p07FR through p10FR show high importances for the resistivity of the aquifer, but low ones for the thickness. For the remaining sea-side stations, a homogeneous sub-seafloor structure is assumed, although the data is fitted using a three-layer model. This assumption is validated in the ensuing 1D modelling studies.

8.2.2 Validating the Results

The 1D inversion models generally show a consistent image. However, two main issues remain. First, the inversion models at station p02NR do not agree with those of the neighbouring stations. Second, the resolution of the model parameters in the transition zone are not always well-resolved at all receiver stations. The significance of the resistive freshwater layer is examined using modelling studies at selected stations along the profile. These are p01FR, p02NR, p08FR and p16NR. The results of the modelling study are presented in Fig. 8.10 as coloured heat maps, representing the equivalence domain for the respective model parameter variations.

The top row of Fig. 8.10 displays the result of the modelling study for Station p01FR. The images are practically identical to the step-on results at station p03FR-Step-on presented in Fig. 8.5. The equivalence domain displayed in Fig. 8.10b validates

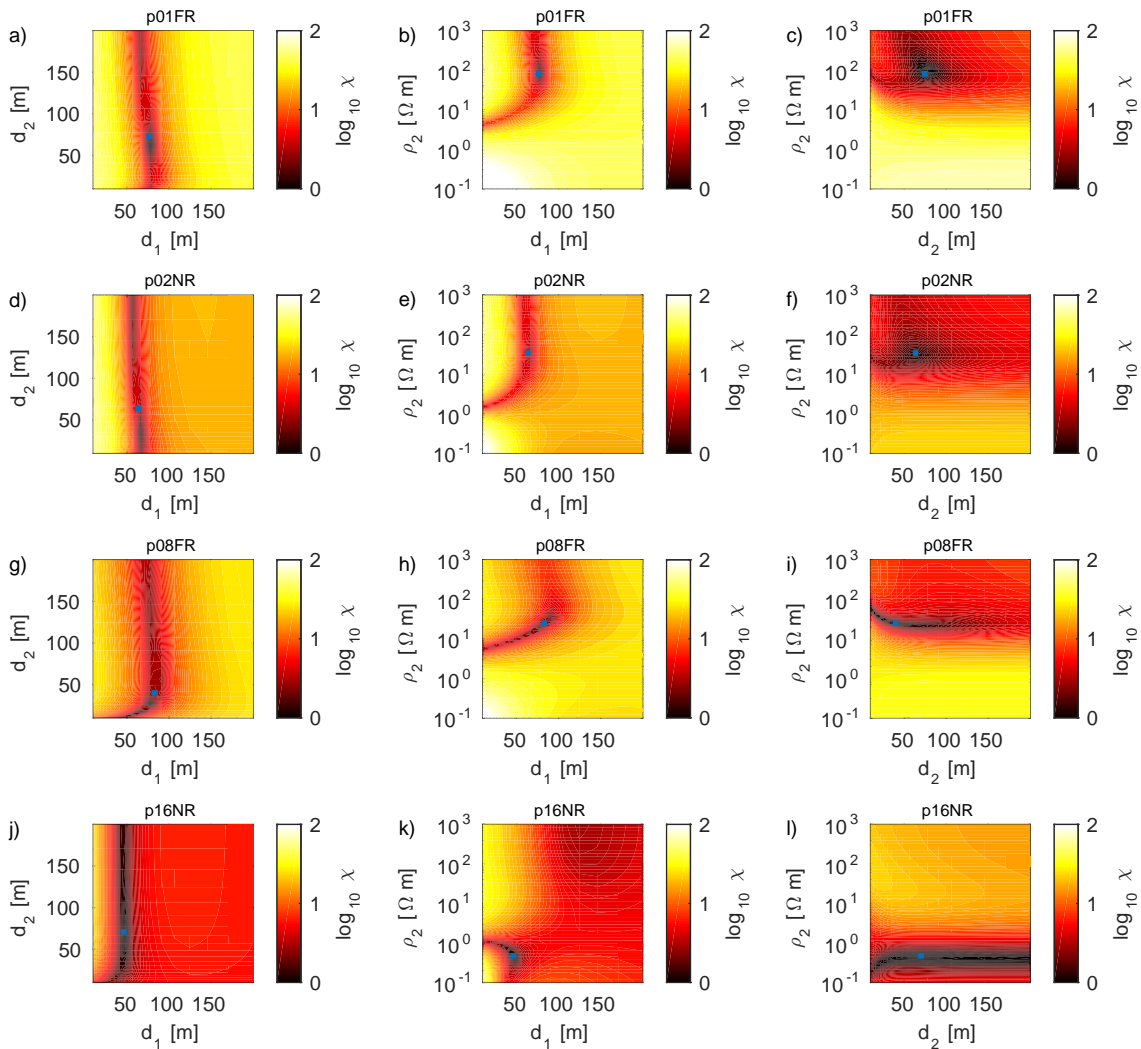


Figure 8.10: Modelling studies investigating the significance of the resistive aquifer layer. Illustrated are the logarithmic χ -values as colours for different variations of aquifer parameters, i.e. depth (d_1), thickness (d_2) and resistivity (ρ_2) for station p01FR (a -c), p02NR (d-f), p08FR (g-i) and p16NR (j-l).

the presence of the resistive freshwater layer. Resistivity values equal or below the background sediments are punished by a high error, sometimes exceeding $\chi > 100$. Accordingly, minimum errors at station p01FR are achieved for aquifer resistivity values of $30 \leq \rho_2 \leq 300 \Omega\text{m}$. This is confirmed by the equivalence domain presented in Fig. 8.10c, which portrays similar ρ_2 values. The lowest errors are achieved for an aquifer thickness between 50 m and 100 m.

The Occam inversion models at station p02NR suggest a different sub-seafloor resistivity structure compared to stations p01FR and p03FR. However, the model parameter study (second row of Fig. 8.10) exhibits a general consistency to p01FR, implying that the measured data is sensitive towards the same model parameters. A similar sub-seafloor resistivity structure is likely. However, the equivalence domain is darker, suggesting a poorer resolution of the model parameters as a wider range of parameter combinations achieve equally low data fits. This applies particularly to the resistivity-thickness variation of the aquifer illustrated in Fig. 8.10f.

The third row of Fig. 8.10 shows model parameter variations for station p08FR, located directly above the assumed transition zone. The validation study suggests that the resistive second layer is not necessarily important to fit the data (cf. Fig. 8.10h). Minimum errors are achieved for values of $6 \leq \rho_2 \leq 90 \Omega\text{m}$. In contrast to the land-side stations, this is a clear decrease. Moreover, the resistivity-depth product shown in Fig. 8.10i suggests different dependencies. In this case, the thickness of the aquifer is not bounded between 50 m and 100 m. Instead, a broader range of acceptable values are tolerated, provided the resistivity of ρ_2 is approximately 20 Ωm . This suggests that d_2 is rather irrelevant to achieve an equal data fit, which coincides perfectly with the importances and SVD-analysis displayed in Table 8.2 and Fig. 8.9, respectively.

The bottom row of Fig. 8.10 presents the equivalence domain of the model parameter variation at station p16NR. At this station, no resistive freshwater layer is present in the inversion models. The most prominent features in the bottom row are variations involving ρ_2 . Compared to the other stations, p16NR distinctly indicates that the resistive aquifer is not present. A minimum error is only reached if $\rho_2 \leq 1 \Omega\text{m}$, which is approximately the value of the background sediments. The data evidently indicates that the westward extent of the freshwater aquifer ends before station p16NR, confirming the marine LOTEM study of *Lippert (2015)*.

8.3 Calibration Factor

The use of a CF is popular in 1D EM inversion in order to fit the data. A constant shift in the data may be caused by near-surface inhomogeneities and/or poor coupling of the transmitter electrodes (*Strack, 1992; Hördt and Scholl, 2004*). *Lippert (2015)* uses the CF to account for positioning errors of the receivers. Furthermore, the 2D bathymetry effect shifts the acquired data, which may be accounted for in 1D inversion using a CF . A fixed CF equalling one was chosen for 1D inversion for the following reasons:

- Positioning errors of the receivers are limited, as they are connected to the

transmitter with ropes.

- According to the Israeli-Crew and scientists, the seafloor in the survey area is very homogenous and not affected by outcrops. Additionally, the electrodes of the transmitter are coupled to the subsurface by seawater. Local inhomogeneities near the transmitter are rather unlikely.
- 1D inversion of synthetic 2D data proved that a $CF \neq 1$ is not necessary to obtain an adequate resistivity model with a reasonable data fit.

Moreover, the acquired data does not show reasoning for the use of a CF . In Fig. 7.14, selected data points of each acquired transient are plotted against the profile position. In case of distorted data superimposed by a time-independent shift, the profile curves would be more rugged. This is not the case. Neighbouring stations at large distances to the expected aquifer boundary are nearly identical and the curve in the vicinity of the 2D structure is smooth. Consequently, a large variation of the CF is not justified.

A CF may still be necessary in the following 2D modelling study to adequately fit the data. This is necessary as lateral resistivity variations are not considered within the seafloor sediments and within the resistive freshwater aquifer. Solely the boundary of the aquifer is accounted for, similar to the 2D modelling studies in Chapter 6. Hence, fitting all data sets with one model may be challenging, as the resistivity and thickness values of the 1D inversion models at different stations are

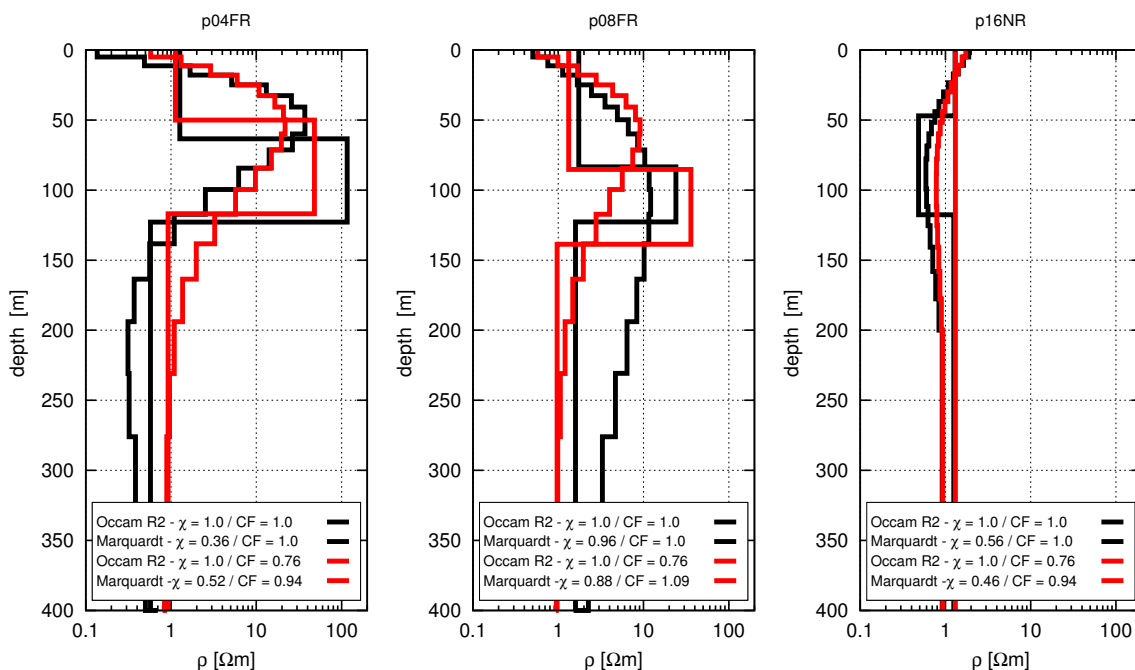


Figure 8.11: Occam R2 and Marquardt inversion models obtained for free (red lines) and fixed (black lines) calibration factors at Stations p04FR, p08FR and p16NR displayed in a, b and c, respectively. The data fit and CF of each inversion model are listed in the legend of each plot.

not exactly equal. In case of a simplified 2D model, where large regions of constant resistivity are dictated, a problem may arise in fitting the data. A CF can account for these variations. To analyse to what extent the use of CF influences the DED data, 1D inversion is performed at selected stations with a free CF . The comparison is shown in Fig. 8.11.

Displayed in Fig. 8.11 are the Marquardt and Occam R2 resistivity-depth models for a fixed (black) and free (red) CF at stations p04FR, p08FR and p16NR in a, b, and c, respectively. The errors and final CF values are given in the legend of each plot. For stations located above the freshwater aquifer or above the transition zone, the CF has a limited influence. Of course, the resistivity and/or thickness values do not match exactly, but the results are generally consistent. For station p16NR, the CF actually allows a fitting of the data with a homogeneous subsurface of $1.4 \Omega\text{m}$, which confirms the prior interpretation of the 1D inversion models.

In summary, the use of a CF does not considerably alter the 1D inversion results. Additionally, since the bathymetry is accounted for in the 2D modelling study, large shifts of the data are not expected. Therefore, CF values confining to $0.9 \leq CF \leq 1.1$ are allowed for the following 2D modelling study to fit all acquired data using a mean 2D resistivity model.

8.4 Summary of 1D Inversion

The acquired data is interpreted using the 1D inversion schemes of Occam and Marquardt. The attempt to apply both step-on and step-off signals to improve the inversion result offers only limited benefit, as the step-off data is of poor quality due to the mentioned SNR issues. If higher data quality is achieved in future measurements, a more qualified evaluation regarding the benefit of using both signals can be made. In the presented case, no clear improvement to the results of the step-on signals is recognisable. Appropriately, only step-on signals are applied to interpret the measured data at all stations.

The inversion models along the profile are generally consistent with the derived models of *Lippert* (2015). The stations located on the land-side of the No-Anchor-Zone show a resistive freshwater aquifer in a depth range of 70 m to 150 m. On the sea-side of the No-Anchor-Zone, the sub-seafloor resistivity model is multi-dimensional. Accordingly, the stations located nearest to the No-Anchor-Zone exhibit a resistive layer in the depth range of the expected freshwater aquifer, whereas stations located further west include no resistive layer. However, the resistivity values of the detected aquifer west of the No-Anchor-Zone are typically lower compared to the land-side stations. If this indicates a brackish water zone remains unanswered, but will be addressed in the following 2D modelling study. This resistive layer disappears for the sea-side stations located furthest away from the No-Anchor-Zone. Instead, the Marquardt inversion models indicate a conductive layer at a depth of approximately 100 m, which is also a prominent feature in the 1D inversion of synthetic 2D data. Consequently, this is interpreted as a 2D effect, which is also clearly identifiable in the profile plots of the acquired data (see Fig. 7.14).

Finally, the different combinations of the aquifer parameters are varied at selected stations to validate both the inversion models and the following resolution study. For stations located above the resistive aquifer or the transition zone, a clear indication of its occurrence is given. A resistive second layer is needed to adequately fit the data. This validates the detection of the freshwater body up to a distance of approximately 3500 m from the coastline. In the following 2D modelling study, the location of the aquifer boundary is determined more precisely.

2D Modelling of Measured Data

The 1D interpretation of the measured marine DED data indicates the presence of a resistive layer located between the coastline and the No-Anchor-Zone. It is apparent in the 1D inversion models of stations p01FR through p06FR and extends to approximately 3500 m from the coast. This structure is interpreted as the freshwater aquifer and is still noticeable in the first receiver stations located west of the No-Anchor-Zone (stations p07FR through p10FR). It disappears in the continuation of the profile and is not detectable at stations p11FR through p17NR. This indicates a multi-dimensional sub-seafloor resistivity structure, which is supported by the shape of the measured profile curves. These exhibit a clear decrease of the radial electric field amplitude towards the sea. However, due to the data gap of the No-Anchor-Zone, a clear distinction of the lateral aquifer boundary is difficult to derive from the measured data and 1D inversion models alone. Further interpretation is needed.

The following 2D modelling study has two main objectives. The first objective is to locate the western aquifer boundary along the profile. The second objective is to derive a 2D resistivity-depth structure that identifies if an open or closed aquifer scenario is more likely. The latter objective is difficult to achieve without a proper 2D inversion code. Yet, the standard interpretation of marine TDEM applications

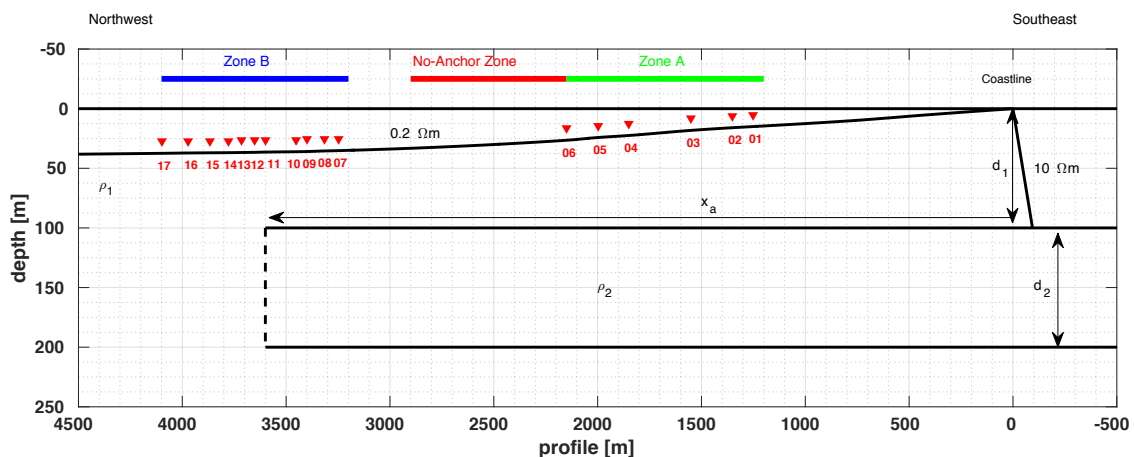


Figure 9.1: The 2D model consisting of the five variable model parameters ρ_1 , ρ_2 , d_1 , d_2 and x_a . The obtained transients are divided into two zones called Zone A and Zone B, corresponding to the stations located to the East and to the West of the No-Anchor-Zone.

and especially marine DED still lacks 2D inversion. Frequency-domain EM data is commonly interpreted in two dimensions. This is largely due to the software package **MARE2DEM** (Key, 2012b) that is freely available to the scientific community. Such algorithm is still not available for marine TDEM data, but will be emphasised in future DED developments (cf. Chapter 10). *Yogeshwar* (2014) recently applied a 2D inversion on land-based TEM data using the 2D time-domain inversion package **SINV** (Martin, 2009). Yet, the inversion algorithm has not been applied for buried sources or sources located within the marine environment. The possibility for interpreting a DED source is currently not implemented in **SINV**.

Instead, the standard interpretation approach for measured marine TDEM data, and specifically marine DED data, is a 1D inversion followed by a 2D/3D brute-force and/or trial-and-error modelling study. In the presented case, the former 2D approach is applied to find an ensemble of resistivity models that best describe the measured data. In some cases the proposed modelling procedure, described in the following, is referred to as a Hedgehog Inversion scheme.

As displayed in Fig. 9.1, the model parameter space consists of five parameters ρ_1 , ρ_2 , d_1 , d_2 and x_a . The latter describes the lateral boundary position of the aquifer with respects to the coastline. These model parameters are subdivided into sampled intervals between minimum and maximum values listed in Table 9.1. The minimum and maximum resistivity and thickness values are chosen from the 1D inversion results. The position of the lateral aquifer boundary is varied between expected values derived from the measured profile curves. Subsequently all parameter combinations are tested.

To decrease the computational load, the receiver stations are divided into two zones called Zone A and Zone B. The stations of Zone A are located above the resistive aquifer, but far away from the expected boundary. Thus, the aquifer boundary was kept constant at 2800 m for the stations of Zone A, thereby decreasing the potential models for each transmitter station of Zone A from 58 240 to 4480. The closest receiver of Zone A is located at a distance of approximately 700 m to the boundary at $x_a = 2800$ m. The stations of Zone B are tested for all possible model parameter combinations, including different positions of the aquifer boundary. The modelling study is conducted using the forward modelling algorithm `sldmem3t`¹.

In the first part of this chapter, the 2D interpretation procedure is described. Several steps are necessary to compare the calculated transient to the measured data. Subsequently, best fit models for each zone are presented. A resistivity depth structure is derived and analysed for the receivers located in Zone A. Afterwards, the stations in Zone B are used to detect the position of the aquifer boundary. The models containing the most likely boundary positions are subsequently used to derive a resistivity depth model for the stations in Zone B. Model parameter dependencies are studied and compared to the derived models of Zone A. Finally, a mean resistivity model of Zone B is derived to investigate different hydrogeological structures at the western aquifer boundary. A brackish water zone is introduced into the model to investigate

¹In total, 425 600 forward calculations are realised on the HP-Cluster of the University of Cologne. Each forward calculation has an approximate duration of 45 minutes. A single node computer would need approximately 319 200 hours or 36.4 years to conduct this study.

Table 9.1: Model parameters tested in the 2D modelling study to fit the measured DED data. For the stations of Zone B, all combinations of five parameters are tested. Stations of Zone A are only tested for the resistivity and thickness parameters.

Parameter	Value	Dimension	# of Models
ρ_1	0.5:0.1:2.0	Ωm	16
ρ_2	30:10:100	Ωm	8
d_1	60:10:100	m	5
d_2	40:10:100	m	7
x_a	2800:100:4000	m	13

if equal data fits are reached. An improved data fit would indicate that an open aquifer scenario is more likely. In contrast, inferior data fits would imply a closed aquifer scenario. Note, the ideal approach would be a complete parameter variation for different hydrogeological boundary conditions. However, the computational load was not realisable in a justifiable time frame. Future developments towards a 2D inversion scheme for marine DED data is needed to optimise the interpretation procedure in the future.

A summary, based on the derived insights of the 2D modelling study is given in the final section of this chapter. The benefits and drawbacks of this marine DED application are explained in connection with the likely seawater intrusion scenarios.

9.1 2D Interpretation Procedure

The sub-seafloor resistivity model displayed in Fig. 9.1 is discretised into five model parameters. The shape of the 2D aquifer boundary is assumed to be vertical. Additionally, the resistivity values for land and seawater are assumed constant at values of 10 Ωm and 0.2 Ωm , respectively. The bathymetry model is derived from multi-beam data provided by the IOLR and remains constant throughout the modelling study. The resistivity of the background sediments ρ_1 , the aquifer resistivity ρ_2 , the aquifer depth beneath the sea-surface d_1 , the aquifer thickness d_2 , and the lateral position of the aquifer boundary x_a are varied². The receivers of Zone A are tested for parameter combinations of ρ_1 , ρ_2 , d_1 and d_2 . For four transmitter locations, 17920 forward calculations are realised. The five parameters listed in Table 9.1 are tested for the receivers in Zone B, resulting in 407680 forward calculations. Subsequently, the following procedure is applied to process and analyse the calculated transients.

- A comparison between the calculated transients and the measured data is only feasible if the system response is taken into account. Accordingly, a convolution between the calculated transients and the system response is conducted using MAXPROC.

²For the 2D modelling study, d_1 describes the depth beneath the sea surface. The 1D inversion models display the depth beneath the seafloor.

- Subsequently, the calculated data is interpolated to the time samples of the measured data.
- A χ -error is calculated according to Eq. (4.14) using linear data vectors. The error estimates of the data is adjusted by adding the systematic numerical error of `sldmem3t`. Thereby, the new error estimation is $\Delta\hat{d}_i = \Delta d_i + \Delta d_{i,sldmem}$, where $d_{i,sldmem} = 2\%$. Additionally, a line search for a CF between 0.9 and 1.1 is conducted to achieve the optimal data fit for each model. The resulting models are treated as equals, independent of the corresponding CF. For the stations of Zone B, the distribution of the CF for each station is shown in Appendix C.
- The profile is sub-divided into two domains called Zone A and Zone B. Zone A includes stations p01FR through p06FR, located east of the No-Anchor-Zone. The remaining stations belong to Zone B and are used to quantify the location of the western aquifer boundary. Finally, an ensemble of best fit models is derived including all models that lie within 20% of the best fit model. The model parameters are presented for each zone and compared.
- The hydrogeological shape of the western boundary is investigated last. The synthetic 2D modelling studies show that the DED signals of a vertical boundary and an interface boundary are practically identical. Therefore, the main focus will lie in analysing if a brackish water zone exists at the head of the freshwater aquifer. A limited modelling study is conducted varying only, the lateral extent and the resistivity of the brackish water zone. All remaining model parameters are derived from the preceding 2D interpretation of the stations in Zone B and kept constant.

9.2 Best Fit Models

Lateral resistivity variations of the seafloor sediments ρ_1 and the freshwater aquifer ρ_2 are not considered in these simplistic models. Additionally, it is also assumed that the aquifer has no lateral thickness variations d_2 and remains at a constant depth d_1 beneath the sea-surface throughout the profile. To find one specific resistivity model explaining all stations is therefore difficult, as many parameter combinations may achieve a similar data fit. This is especially the case for the variation of the boundary position x_a . Therefore, an ensemble of model parameter combinations that best explain the measured data or excerpts of the measured data are presented. This ensemble consists of so-called equivalent models that fit the measured data within a 20% margin of the best model.

9.2.1 Aquifer Depth, Resistivity and Boundary Position

The primary goal of the DED application in Israel is to obtain information regarding the position and shape of the western aquifer boundary. The distance from the lateral resistivity discontinuity of stations p01FR through p06FR, is too large to be

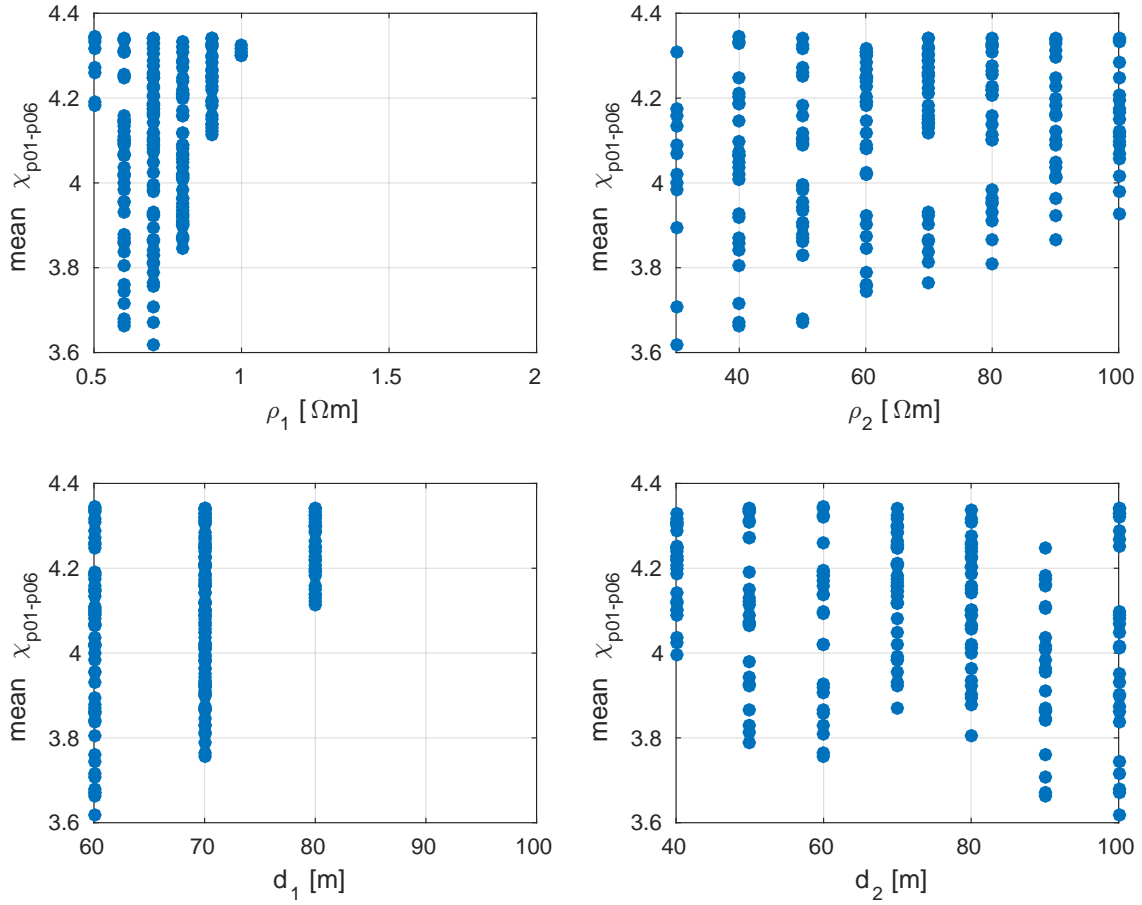


Figure 9.2: Scatter plots of the 200 best fit models for the parameters ρ_1 (top left), ρ_2 (top right), d_1 (bottom left) and d_2 (bottom right) vs. the χ . The x-axis of each subfigure displays the entire investigated model parameter space.

affected by variations. Hence, equivalent data fits are achieved for a resistivity-depth structure that is independent of the western aquifer boundary, which is assumed at the shortest possible distance of $x_a = 2800$ m. The mean χ of the best fit models, calculated for all six receiver stations, is displayed for the corresponding model parameters using scatter plots in Fig. 9.2. In total, 200 models are within the 20% margin of the best fit model and are considered equivalent. The mean χ errors for stations of Zone A range from 3.62 to 4.35, implying a moderate, but acceptable data fit.

The top-left subfigure of Fig. 9.2 shows the distribution of ρ_1 versus the χ for all equivalent models. Accordingly, ρ_2 , d_1 , and d_2 are displayed in the other subfigures. The model parameter distribution indicates certain attributes of the equivalent models. For example, the range of the investigated values for ρ_1 and d_1 is limited, but spread across the entire investigated model parameter space for ρ_2 and d_2 . This feature confirms the resolution analysis of the 1D inversion studies, that indicates an enhanced resolution towards the depth of the aquifer and the resistivity of the seafloor sediments. Also, general trends are apparent in the distribution of each specific model parameter. For example, $\rho_1 = 0.7 \Omega\text{m}$ achieves the best fit, while the

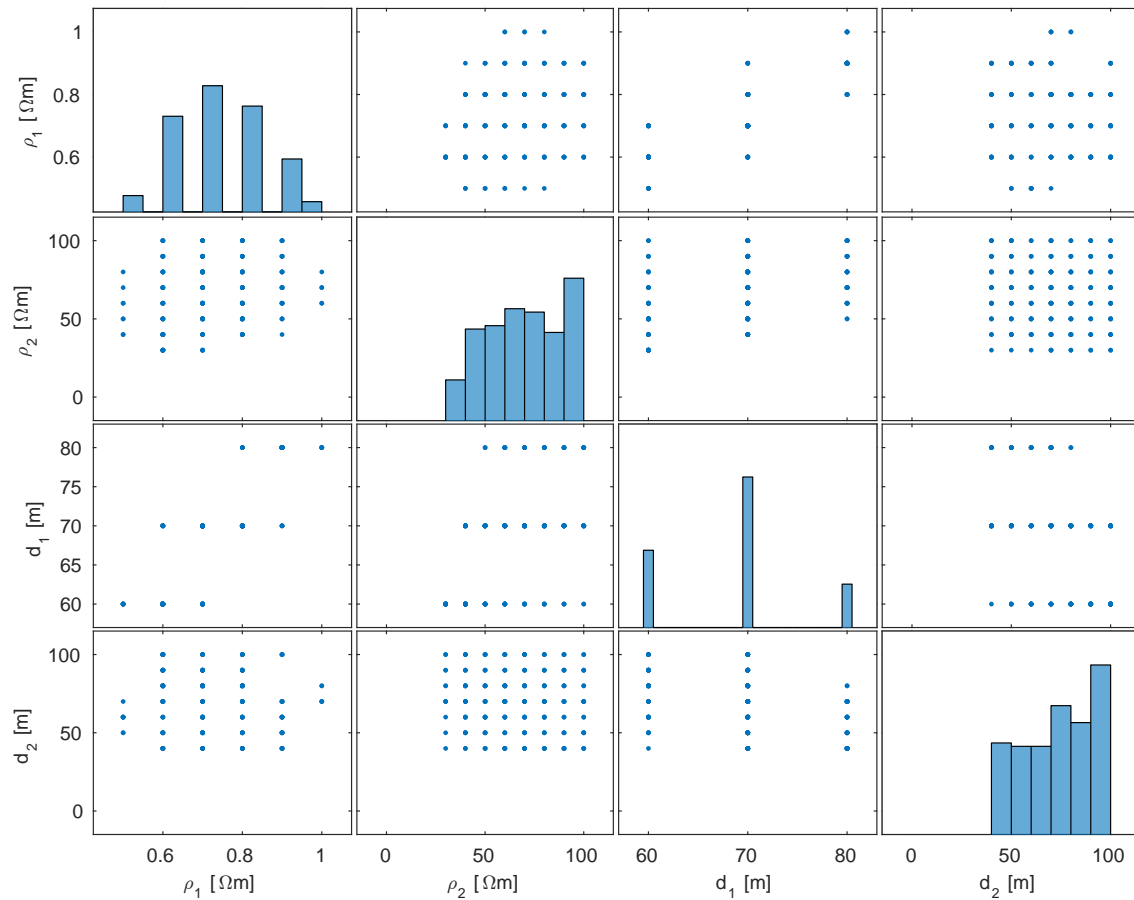


Figure 9.3: Distribution of model parameter combinations for the 2D model acquired for transients of Zone A. The subfigures display the distribution of equivalent models for certain parameter combinations. The histograms along the main diagonal show the distribution of each specific model parameter with itself.

errors increase for smaller or larger values. A resistivity of $\rho_1 > 1 \text{ } \Omega\text{m}$ is not included within the equivalent models. A similar trend is distinguishable for d_1 , where values of $d_1 > 80 \text{ m}$ are not considered. The minimum data fit is achieved for $d_1 = 60 \text{ m}$.

The values obtained for d_2 and ρ_2 are spread throughout the entire modelling domain. The best data fit is achieved for an aquifer with a resistivity of $30 \text{ } \Omega\text{m}$ and a thickness of 100 m . This may indicate a reciprocal ratio of the two parameters that is inevitably resolved. If values of $d_1 < 60 \text{ m}$ or $\rho_2 > 100 \text{ } \Omega\text{m}$ achieve equivalent fits remains undetermined in this study, due to the limited range of the investigated model parameter space.

Analysing Fig. 9.2 alone may be misleading, as it is difficult to distinguish model parameter combinations and quantify the number of specific model parameters contained within the 200 accepted equivalent models. This information is extracted from the equivalent models using Fig. 9.3. Each subfigure of Fig. 9.3 shows combinations of two specific model parameters. Along the main diagonal, histograms are shown to visualise the contributions of one specific model parameter. For example, the top left corner of Fig. 9.3 shows a histogram for ρ_1 . The majority of equivalent

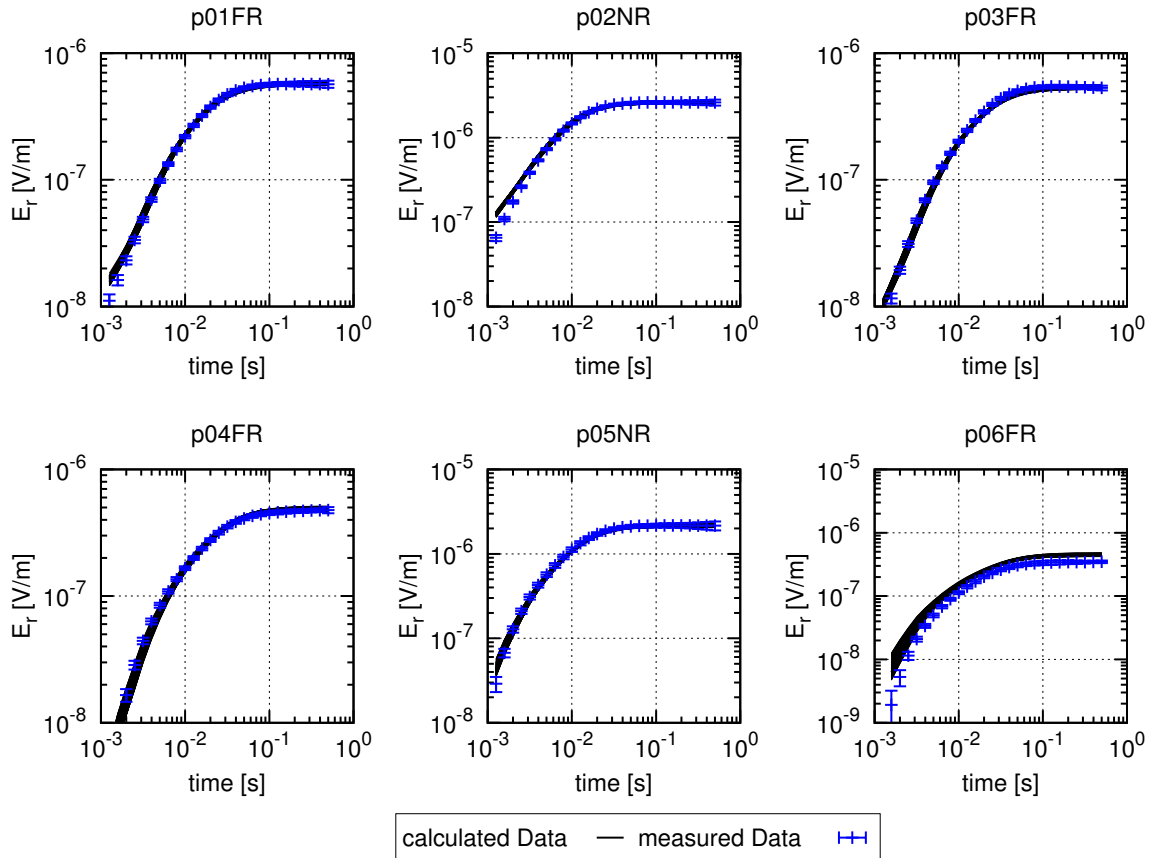


Figure 9.4: Transients of stations of Zone A (station p01FR through station p06FR). The measured step-on data is displayed in blue, the calculated transients of all equivalent models in black.

models have value of $\rho_1 = 0.7 \Omega\text{m}$. In this specific case it seems that the values are normally distributed. A similar behaviour is found for d_1 , but does not apply to ρ_2 and d_2 . The latter seem to be uniformly distributed across the investigated model parameter space. Solely the amount of models with values of $d_2 = 100 \text{ m}$ and $\rho_2 = 100 \Omega\text{m}$ are slightly overrepresented.

Analysing the distribution of certain parameter combinations indicates that ρ_1 and d_1 are interrelated. If d_1 increases, ρ_1 will also increase meaning that the conductivity will decrease. Although, the preliminary interpretation of Fig. 9.2 indicated that this also applies to ρ_2 and d_2 , the results of Fig. 9.3 prove that this relation does not necessarily apply. For a certain value of ρ_2 , all investigated aquifer thicknesses are found within the equivalent models.

The data fit at stations p01FR through p06FR for the considered equivalent models is qualitatively displayed in Fig. 9.4. A quantification of the data fit at each station is found in Appendix C. Although an acceptable mean χ of 3.62 to 4.35 is achieved, it is quite apparent that stations p02NR and p06FR exhibit an inferior data fit. The early times of p02NR are not fitted, whereas the entire time range of p06FR is poorly fitted. At p02NR, the 1D inversion models are not consistent to the adjacent receivers, which may imply a signal distortion that masks the effect of the resistive

aquifer. Station p06FR is located directly on the boundary to the No-Anchor-Zone and may also be affected by the gas pipeline. A certain signal distortion is imaginable, but is not apparent in the 1D interpretation. However, the profile plots do indicate a slight decrease in the measured electric field amplitude compared to the adjacent FR-receiver (p04FR). A more complicated subsurface resistivity structure may also be the cause of this effect. Therefore, a conclusive interpretation regarding the large deviations between the measured and calculated transients at p06FR is difficult.

Data of Zone B

The location of the western aquifer edge is expected west of the No-Anchor-Zone. To analyse the 2D structure of this resistivity discontinuity, only stations of Zone B (stations p07FR through p17NR) are considered. The main explanation of limiting this interpretation to these specific stations is the computational expense. In total, 215040 additional forward calculations would have been necessary without achieving a more conclusive result, as the stations of Zone A are not sensitive towards the location of the 2D aquifer boundary.

Forward calculations of all possible model parameter combinations listed in Table 9.1 are calculated for each station. Thereby, 4480 different resistivity/depth combinations are tested for each possible boundary position (x_a) between 2800 m and 4000 m from the coastline. The resistivity/depth combinations repeat themselves for each boundary position. Therefore, the accumulation of models achieving a $\chi \leq 1$ at each receiver station will demonstrate which boundary position best describes the measured data of Zone B. The most likely boundary position is one, where the accumulation is greatest. The results are displayed as cumulative bar graphs for each

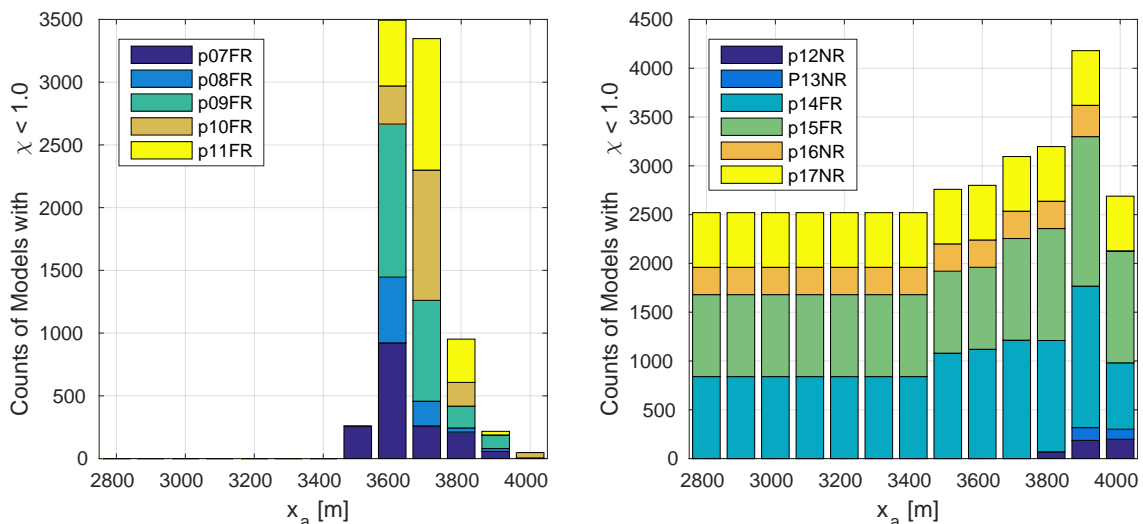


Figure 9.5: Images displaying the accumulation of models reaching a $\chi \leq 1$ vs. the position of the western aquifer boundary. The results of each receiver are displayed by cumulative bar plots. The left subfigure shows p07FR through p11FR, the right p12NR through p17NR. Each receiver is represented by different colours.

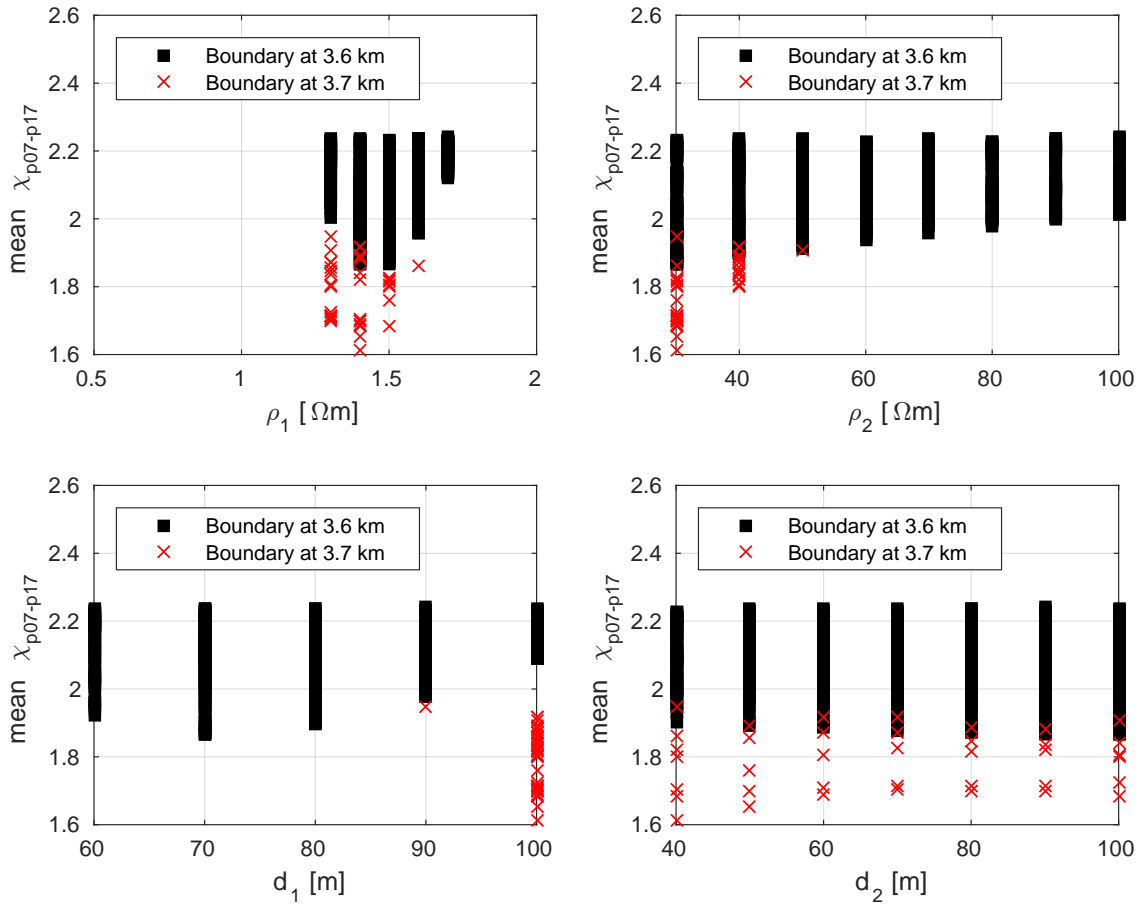


Figure 9.6: Scatter plots of the best fit models for the parameters ρ_1 (top left), ρ_2 (top right), d_1 (bottom left) and d_2 (bottom right) vs. the χ . The x-axis of each subfigure displays the entire investigated model parameter space. The black and red markers represent a boundary position of 3600 m and 3700 m, respectively.

station in Fig. 9.5. Based on the profile curves in Fig. 7.14, stations p07FR through p11FR are expected above the aquifer boundary. Stations p12NR through p17NR are located further west and will have a decreased sensitivity towards the aquifer boundary.

The results displayed in Fig. 9.5 are quite conclusive in terms of mapping the western aquifer boundary. A distinct increase of models with a $\chi \leq 1$ is visible for stations p07FR through p11FR for a boundary position at 3600 m or 3700 m, slightly favouring the former. Receivers p07FR to p09FR favour a boundary at 3600 m, whereas receivers p10FR and p11FR support an aquifer edge at 3700 m from the coastline. At stations p12NR through p17NR, models with $\chi \leq 1$ are found for all possible boundary positions. This indicates that the signals are indifferent to the aquifer boundary and sufficient data fit is reached depending on the value of ρ_1 . Specifically, this applies to p14FR through p17NR.

The western edge of the freshwater aquifer is likely located at 3600 m or 3700 m from the coastline. These are the investigated positions that are particularly prominent in Fig. 9.5. Thus, the following investigation of the sub-seafloor resistivity values

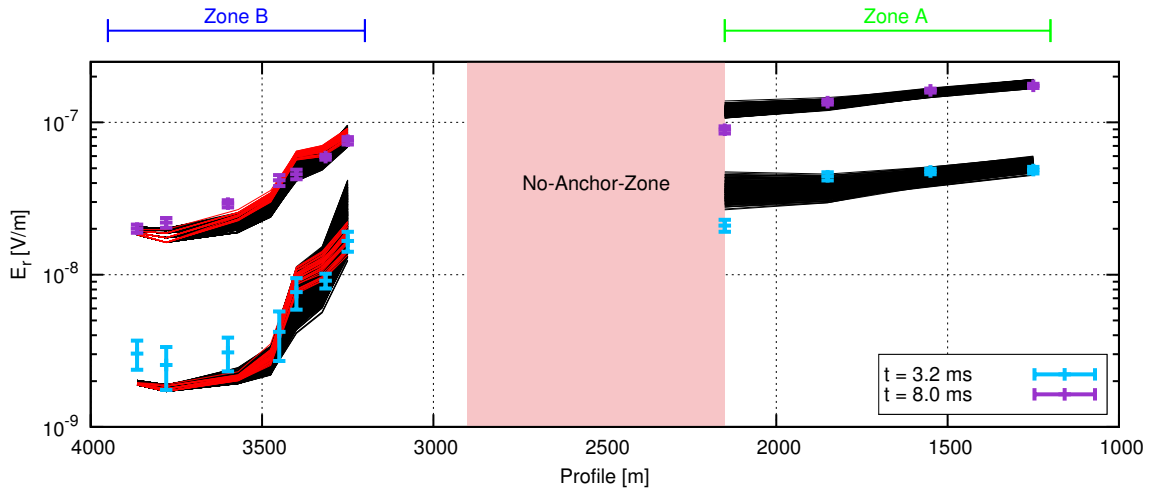


Figure 9.7: Profile curves of measured and calculated data for selected delay-times of 3.2 ms and 8.0 ms. The calculated profile curves in Zone A are independent of the aquifer boundary and are displayed in black. The calculated curves in Zone B are displayed for $x_a = 3600$ m and $x_a = 3700$ m by black and red lines representing the calculated data of the equivalent models, respectively.

(ρ_1 and ρ_2) and thickness values (d_1 and d_2) is conducted only for these two possible boundary positions. A mean χ is calculated for all stations of Zone B. All models that have a χ within 20% of the best fit model for each boundary are considered to be equivalent. The distribution of ρ_1 , ρ_2 , d_1 and d_2 for all equivalent models are displayed in Fig. 9.6 using scatter plots. The black markers represent the models with a boundary at 3600 m, the red markers the models with a boundary at 3700 m.

The distribution of resistivity and thickness values for the two considered boundary positions are consistent. The resulting data fits lie between $1.6 \leq \chi \leq 2.2$ for all equivalent models denoting a decent fit of the measured data. The models containing the aquifer boundary at 3700 m achieve a superior data fit. Yet, the models of $x_a = 3700$ m are more restricted in terms of model parameter variations. Furthermore, the number of equivalent models is considerably smaller in comparison. In general, the parameters for both model types can be concluded as follows. The sediment resistivity ρ_1 varies between values of $1.2 \Omega\text{m}$ and $1.7 \Omega\text{m}$. The best fit model is found at $\rho_1 = 1.4 \Omega\text{m}$ for both boundary locations. These values do not coincide with the sediment resistivity values obtained in the evaluation of Zone A, which permitted only $\rho_1 \leq 1 \Omega\text{m}$. Possible explanations for this discrepancy may be lateral resistivity variations in the seafloor sediments and/or an incorrect representation of the bathymetry that directly influences the resistivity of the sub-seafloor sediments (see Section 6.2). Fortunately, the variation is rather insignificant so that $\rho_1 = 0.6 - 1.6 \Omega\text{m}$.

Although minimal, further inconsistencies between the evaluation of Zone A and Zone B are found in the depth of the resistive freshwater aquifer. In Zone A, the equivalent models indicate the aquifer at a depth of $d_1 \leq 80$ m, whereas Zone B allows the aquifer to be located at depths of up to $d_1 = 100$ m. For a boundary at 3700 m, an aquifer depth of 100 m is even most likely, as all equivalent models

(except one) map the aquifer at this depth. For a boundary position at 3600 m, the entire investigated model parameter space of d_1 is possible, although the best fit model is found for $d_1 = 70$ m. This may indicate that the aquifer does not progress parallel to the surface. Consistencies between the station of Zone A and Zone B are found in the resistivity and thickness of the resistive aquifer (ρ_2 and d_2). The best fit model is found for an aquifer resistivity of $\rho_2 = 30 \text{ } \Omega\text{m}$ and thickness of $d_2 = 100$ m. Both parameters are rather poorly resolved for $x_a = 3600$ m, indicated by the large variation across the entire investigated parameter space. For models where $x_a = 3700$ m, this variation is more restricted.

The measured and calculated data in form of profile curves are displayed for two selected delay-times in Fig. 9.7. The measured data in Zone A is fitted for forward models that are independent of the aquifer boundary and are displayed by black lines. Measured data of Zone B is fitted for an aquifer boundary at 3600 m in black and a boundary at 3700 m in red. Note, the χ errors at each station are displayed in Appendix C. In general, the profile curves at time-delays of 3.2 ms and 8 ms are well represented by the calculated data. Qualitatively, the models with $x_a = 3700$ m achieve a superior fitting compared to models with $x_a = 3600$ m. Additionally, the variation of the equivalent models for the former is less pronounced due to the restricted variations of model parameters. Yet, both models achieve a reasonable fit of the measured data and may be considered as equivalent.

The equivalence domain for different parameter combinations is displayed in Fig. 9.8 for $x_a = 3600$ m (a and b) and for $x_a = 3700$ m (c and d). The left figures show the equivalence domain in dependence of ρ_1 - d_1 - ρ_2 , the right figures show the dependency of d_2 - d_1 - ρ_2 . All combinations of parameters within this body are considered equivalent as they achieve data fits within 20% of the best fit model. For $x_a = 3600$ m, the resistivity of the seafloor sediments (ρ_1) is well confined to values of approximately $\rho_1 = 1.4 \pm 0.2 \text{ } \Omega\text{m}$. In contrast, ρ_2 and d_1 are less confined and are interrelated. If ρ_2 increases, d_1 also increases. Consequently, if the aquifer possesses a higher resistivity, it will also be located at a greater depth. The equivalence domain for $x_a = 3600$ m illustrated in Fig. 9.8b is less conclusive, but also indicates the same dependency between depth and resistivity of the freshwater aquifer. If the aquifer is found at a depth of over 90 m beneath the sea-surface, the resistivity will need to surpass $50 \text{ } \Omega\text{m}$ in order to be considered an equivalent model. In contrast, an aquifer found at shallower depths will also have a lower resistivity value. d_2 is least resolved, as the entire investigated model parameter space is represented. Moreover, no clear dependencies to other model parameters are observable.

The equivalence domain for $x_a = 3700$ m is displayed in Fig. 9.8c and Fig. 9.8d. Compared to the subfigures in Fig. 9.8a and Fig. 9.8b, the equivalence domain is more confined. Consistencies are found in the derived resistivity value of ρ_1 , which is equal to $1.4 \text{ } \Omega\text{m}$. Inconsistencies are noticeable in the dependency of d_1 and ρ_2 . In case of $x_a = 3700$ m, the aquifer parameters are confined to a depth of 100 m beneath the sea-surface and a resistivity of $30 \text{ } \Omega\text{m}$. This does not necessarily contradict the results for $x_a = 3600$ m, as values of x_a seem to be equivalent in combination with other model parameters. Consequently, the model parameters of the aquifer (d_1, d_2 and ρ_2) may also be interrelated to the lateral position of the aquifer boundary.

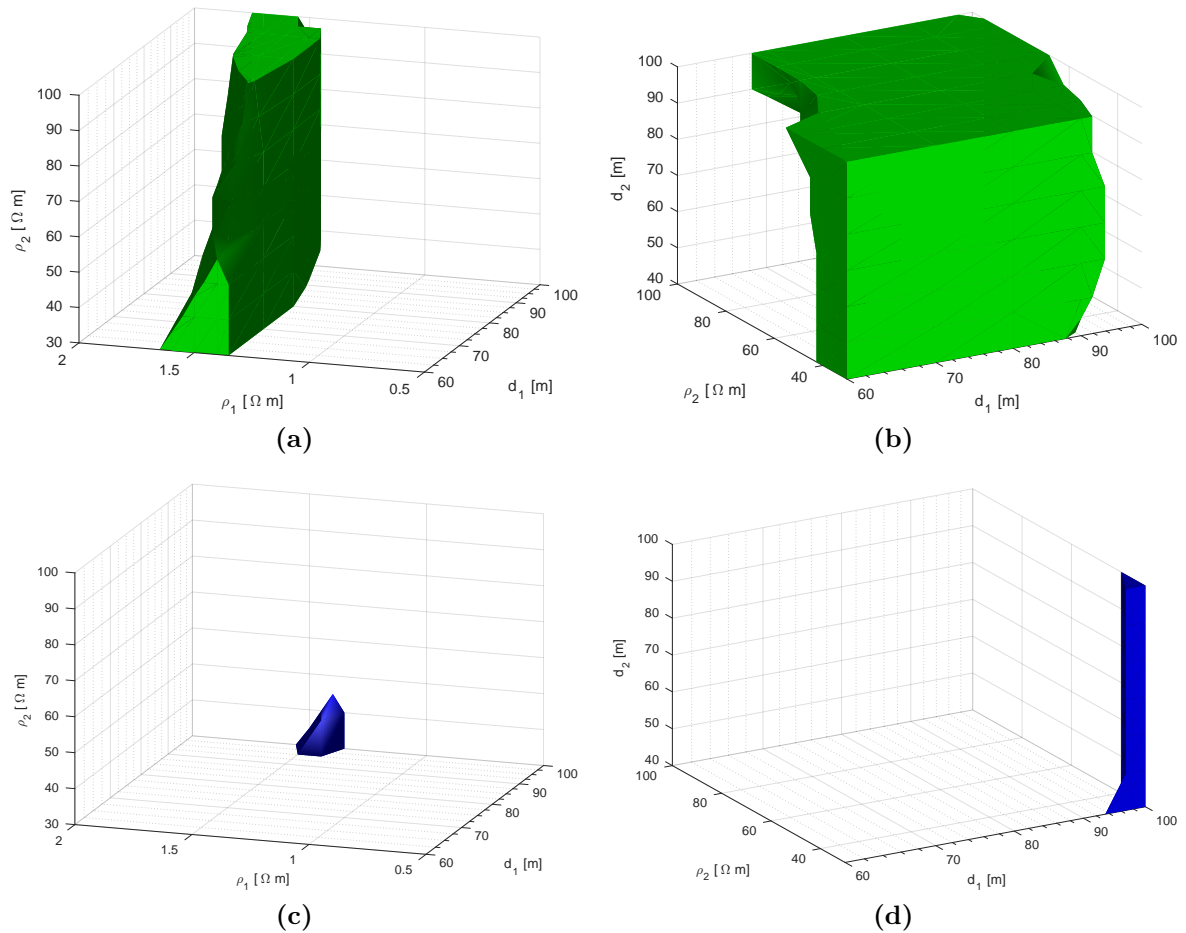


Figure 9.8: Bodies representing the equivalence domain in a three dimensional model parameter space for $x_a = 3600$ m (top) and $x_a = 3700$ m (bottom). Subfigures (a) and (c) span the model space ρ_1 , d_1 , ρ_2 , whereas subfigures (b) and (d) span the space d_2 , d_1 , ρ_2 . Considered are all models within a 20% threshold of the best fit model.

Illustrated in Fig. 9.9 are measured step-on transients at each station of Zone B with blue markers and the equivalent transients for $x_a = 3600$ m and $x_a = 3700$ m by black and red lines, respectively. Qualitatively, the calculated transients represent the measured data quite accurately. Exceptions are the early times at stations p09FR, p16NR and p17NR along with the intermediate times at p12NR, where discrepancies are visible. A quantitative data fit at each station for all equivalent models is displayed in Appendix C.

A superior data fit is achieved at stations p07FR through p11FR with the aquifer boundary at 3700 m. This is observable at station p07FR, where the variations between the black lines at early times is prominent, even for the visual interpreter. However, the results displayed in Fig. 9.5 indicated that the boundary is best interpreted using stations p07FR through p11FR. Thereby, a boundary at $x_a = 3700$ m seems most likely for these selected stations. Other stations, e.g. p15FR exhibit no apparent difference between the models of possible boundary positions indicating that this parameter is less relevant for the data fit at these stations.

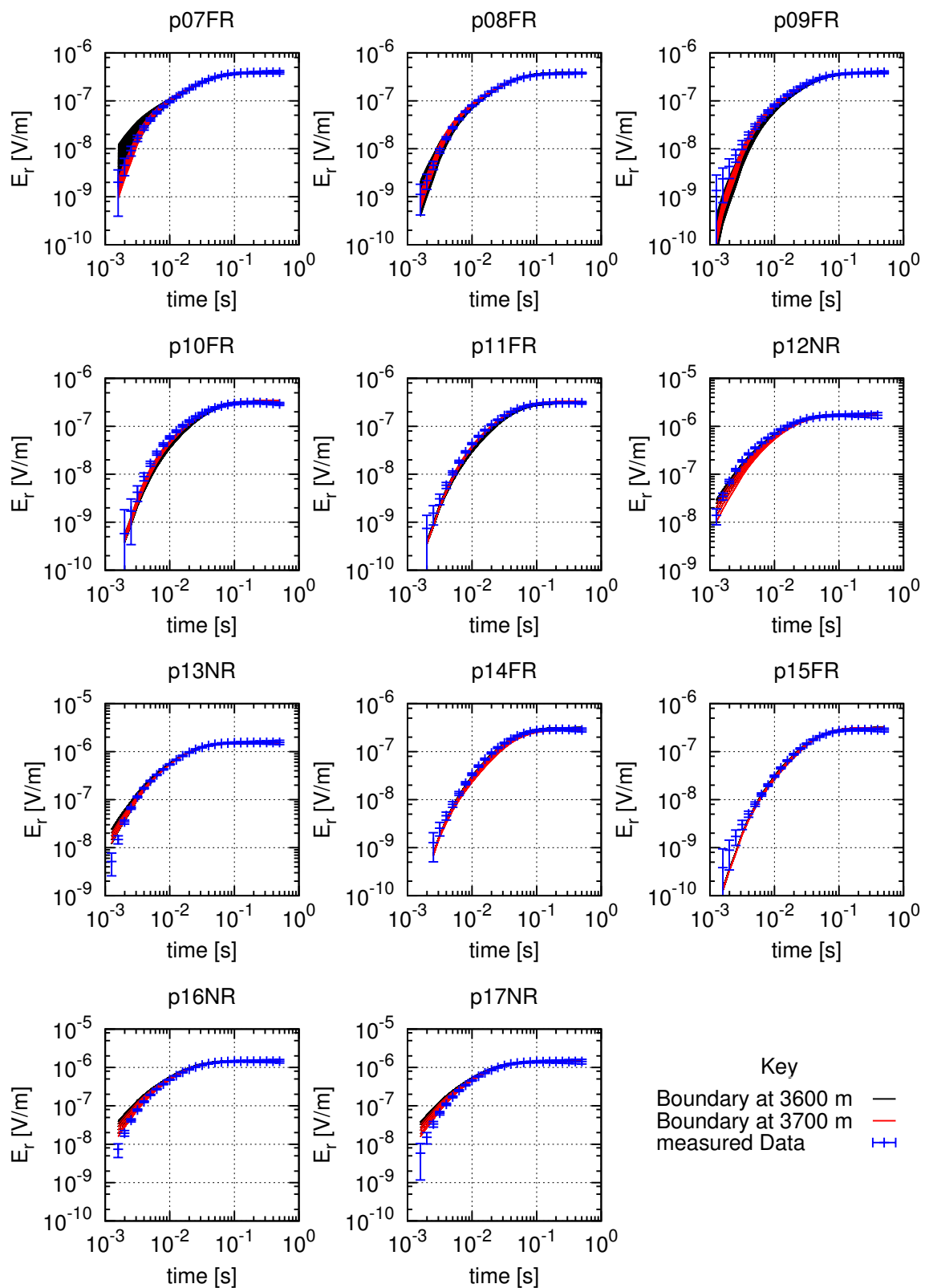


Figure 9.9: Transients for stations of Zone B (station p07FR through station p17NR). The measured step-on data is displayed in blue, the calculated transients of all equivalent models in red and black, corresponding to values of $x_a = 3700$ m and $x_a = 3600$ m, respectively.

9.2.2 Boundary Shape

The second main objective of the DED application in Israel is to determine if the sub-seafloor aquifer is open or closed to seawater intrusion. The synthetic 2D modelling study shows that DED is theoretically capable of distinguishing between a gradual or sudden resistivity discontinuity at the western edge of the sub-seafloor aquifer. Provided the open aquifer scenario is characterised by a zone of brackish water at its head, DED data can be applied to determine if such body exists. To investigate the measured data from Israel, a mean resistivity model is derived with the fixed model parameters $\rho_1 = 1.4 \Omega\text{m}$, $\rho_2 = 30 \Omega\text{m}$, $d_1 = 100 \text{ m}$, $d_2 = 100 \text{ m}$ and $x_a = 3700 \text{ m}$, corresponding to the best fit models of Zone B. Additionally, a further body is introduced at the head of the western aquifer boundary, representing a brackish water zone. As illustrated in Fig. 9.10, this zone has a lateral extent of dx_b and a resistivity of ρ_b . The latter parameters are varied between values of $dx_b = [100, 300, 500, 700, 900] \text{ m}$ and $\rho_b = [0.7, 1.4, 3, 5, 10] \Omega\text{m}$. Data fits are calculated at each station of Zone B to investigate if an improvement is reached for a specific combination of dx_b and ρ_b . For clarification, the value $\rho_b = 1.4 \Omega\text{m}$ simulates a closed aquifer scenario. $\rho_b = 0.7 \Omega\text{m}$ is a conductive body, whereas $\rho_b = [3, 5, 10] \Omega\text{m}$ represent a brackish water body within the specified values of *Kafri and Goldman* (2006). The variations of dx_b will detect how far this zone extends towards the sea.

The data fit in form of a χ -error is computed for each station along the profile in Zone B. The corresponding errors are shown as a function of station position along the profile in Fig. 9.11. The subfigures are sorted for values of dx_b in descending order. Each figure contains five coloured lines representing one specific resistivity value of the brackish water body. The light blue line represents a conductive body and the red line a closed aquifer scenario. The remaining grey, olive and purple lines

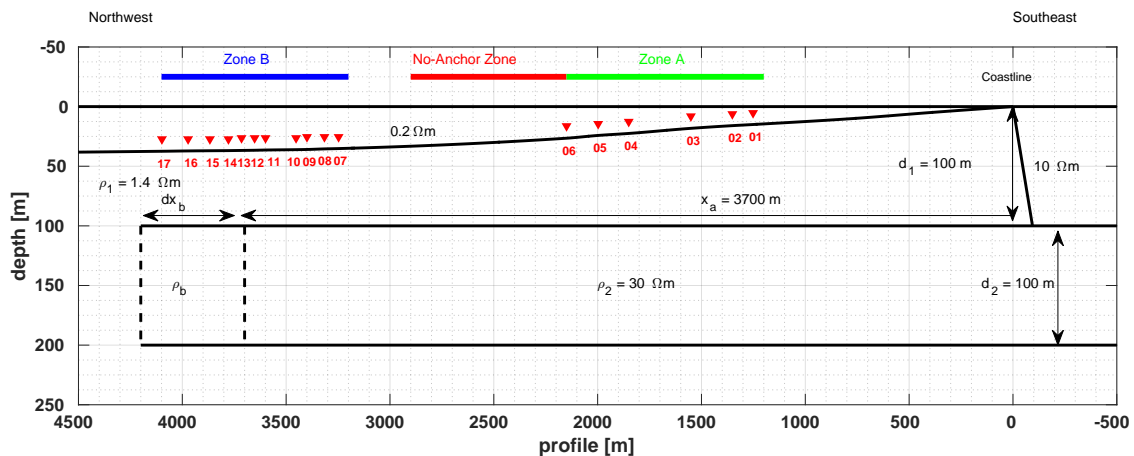


Figure 9.10: The 2D model consisting of the five fixed model parameters $\rho_1 = 1.4 \Omega\text{m}$, $\rho_2 = 30 \Omega\text{m}$, $d_1 = 100 \text{ m}$, $d_2 = 100 \text{ m}$ and $x_a = 3700 \text{ m}$ and two variable model parameters dx_b and ρ_b .

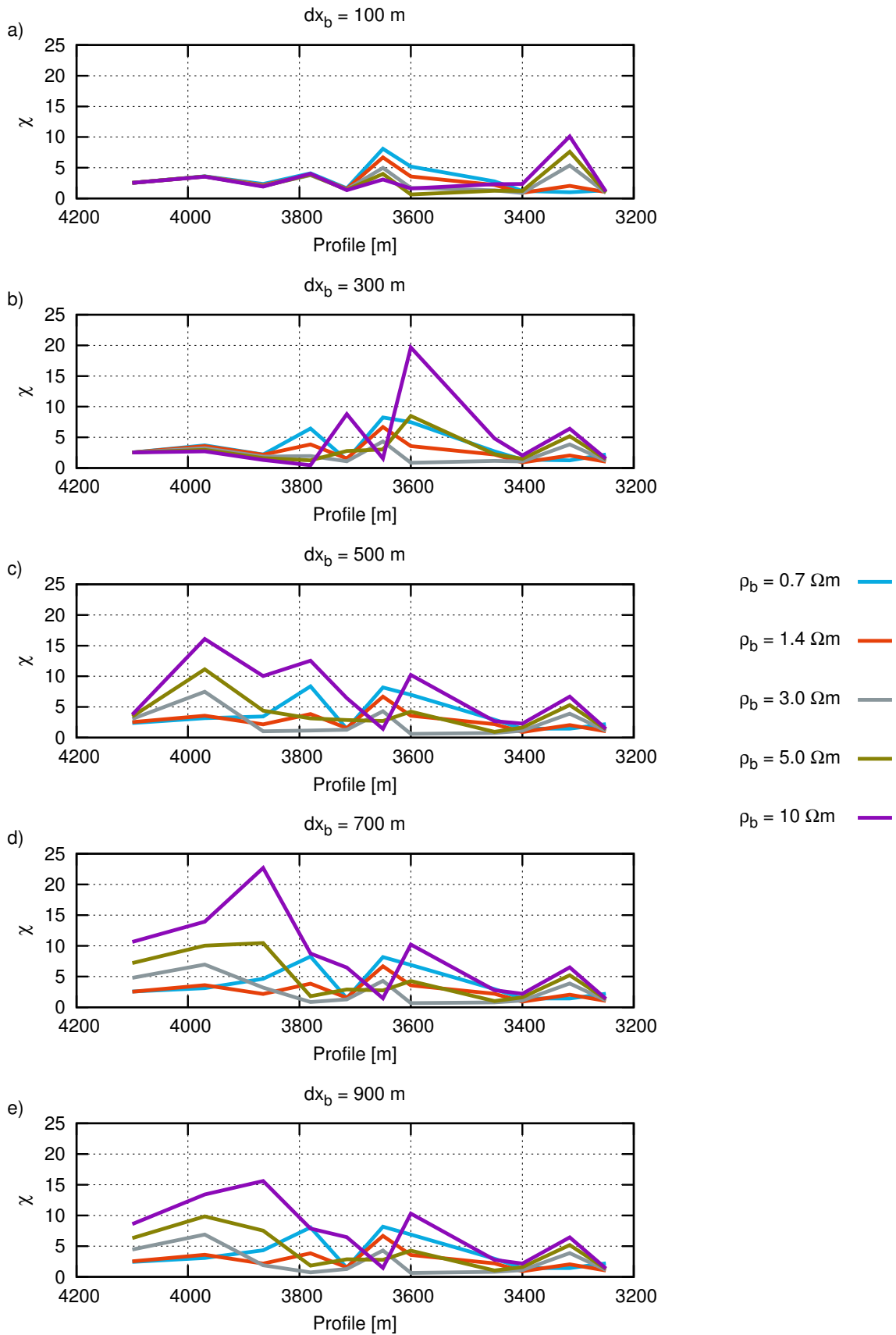


Figure 9.11: Data fits of data from Zone B for possible western aquifer boundary conditions. The models are sorted according to the lateral extent of a mixed-water zone of (a) 100 m length, (b) 300 m length, (c) 500 m length, (d) 700 m length and (e) 900 m length. The coloured lines represent a specific ρ_b value listed in the key.

represent an open aquifer scenario with a brackish water zone of 3.0 Ωm , 5.0 Ωm and 10 Ωm , respectively. The station names to the corresponding profile positions of Fig. 9.10 are listed in Appendix A.

The data fits for all models are practically identical at stations located 3900 m or more from the coastline, if the lateral extent of the additional body is limited to $dx_b \leq 300$ m. Bodies with greater lateral dimensions influence the data fit at all measured stations. The resulting χ -errors show that a 2D body with a resistivity of $\rho_b = 10$ Ωm or $\rho_b = 0.7$ Ωm are the least likely scenarios. Depending on dx_b , all data fits increase at every station with the exception of p12NR located at 3650 m. At this station, a minimum χ is reached for $\rho_b = 10$ Ωm . Resistivity values of $\rho_b = 3$ Ωm or $\rho_b = 5$ Ωm improve the data fit. Especially $\rho_b = 3$ Ωm tends to improve the overall data fit for stations located between 3400 m and 3900 m. At the beginning and end of the profile, the data fit is less ideal for this specific model.

Astonishingly, the closed aquifer scenario $\rho_b = 1.4$ Ωm behaves exactly opposite. In the range of 3400 m to 3900 m, the data fit is slightly inferior compared to the model with $\rho_b = 3$ Ωm . However, at the beginning and end of the profile, the errors are superior to the latter. A brackish water zone is therefore not likely to extend for more than 300 m from the western aquifer boundary. Instead, a minimum error model is obtained for a zone with lateral dimensions of $dx_b \leq 300$ m with a resistivity $\rho_b = 3 - 5$ Ωm . An open aquifer scenario is interpreted as the most likely hydrogeological setting.

Based on this modelling study, the most realistic hydrogeological boundary is indeed an open aquifer scenario, as the errors are at a minimum for the case that $dx_b \leq 300$ m. This applies to the majority of stations along the profile. Only station p08FR at 3315 m contradicts this scenario. The overall trend indicates a gradual boundary with limited lateral extent between the freshwater aquifer and the seafloor sediments at 3700 m before the coastline. Note, the closed aquifer scenario achieves only slightly inferior data fits. As a consequence, the possibility of a closed aquifer scenario cannot be denied.

In conclusion, the 2D modelling studies indicate that the measured DED data favours a sub-seafloor resistivity model with a gradual boundary between the resistive freshwater aquifer and the conductive surrounding sediments. Yet, this can only be seen as an indication favouring one possible scenario. Final certainty can only be achieved by in-situ measurements, such as borehole data. In this case, the DED data is useful as the position of the western aquifer boundary is determined at 3600 m or 3700 m. Drilling projects in the immediate vicinity of the boundary will clarify if the aquifer is inevitably open or closed to seawater encroachment.

9.2.3 Summary of 2D Modelling

A 2D modelling study using `sldmem3t` is conducted with the aim of acquiring an ensemble of 2D resistivity models that sufficiently explain the measured step-on DED transients. This large-scale modelling study includes over 425 600 forward calculations that were run on the HPC at the University of Cologne. The results are binned into receivers located in two separate zones, called Zone A and Zone

Table 9.2: Model parameter variation for the 2D modelling study to fit the measured data.

Parameter	Zone A	Zone B: 3600 m	Zone B: 3700 m
ρ_1	0.5 Ωm - 1.0 Ωm	1.2 Ωm - 1.7 Ωm	1.2 Ωm - 1.6 Ωm
ρ_2	30 Ωm - 100 Ωm	30 Ωm - 100 Ωm	30 Ωm - 40 Ωm
d_1	60 m - 80 m	60 m - 100 m	100 m
d_2	60 m - 100 m	40 m - 100 m	40 m - 100 m
x_a	-	3600 m	3700 m

B. Zone A includes all stations located east of the No-Anchor-Zone, far away from the assumed aquifer edge. Consequently, these six stations were utilised to derive the likely parameters of the sub-seafloor aquifer, but not to determine the lateral position of the western aquifer edge. The remaining stations, located west of the No-Anchor-Zone belong to Zone B. The two primary objectives of the 2D modelling study in Zone B are to locate the western aquifer boundary and to determine if an open or closed aquifer scenario is more likely. The aim of locating the lateral extent of the freshwater aquifer is clearly achieved. The modelling study indicates that the western aquifer edge is located at either 3600 m or 3700 m from the coastline. All other boundaries contradict the DED data in the scope of this modelling study.

The results regarding the hydrogeological structure of the western aquifer boundary are less clear. A mean resistivity model was derived from the brute-force approach for the stations of Zone B. Additionally, a further body was included in the model at the head of the freshwater aquifer. The lateral extent and resistivity of this body was varied. The results indicate that an increased resistivity of 3 Ωm to 5 Ωm improve the data fit for most stations located in Zone B. This implies an open aquifer scenario in this region. Yet, a clear certification can only be validated by in-situ measurements. In this case, the application of DED was still valuable, as the position of the aquifer edge is detected.

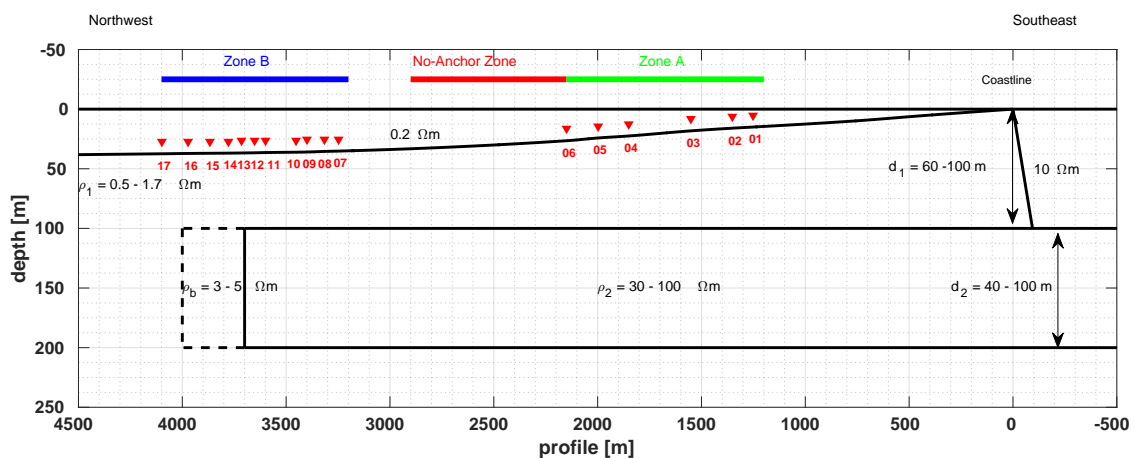


Figure 9.12: Final 2D resistivity model for offshore Bat Yam, Israel. The model parameters incorporate the results of all equivalent models of Zone A and Zone B.

The summarised results of the 2D modelling study are listed for stations in Zone A and Zone B in Table 9.2. A pictographic model of the subsurface resistivity structure is illustrated in Fig. 9.12. Aside from the resistivity and thickness of the seafloor sediments that show discrepancies between the models obtained in Zone A and Zone B, common values exist between the transients in both zones. The dashed line in Fig. 9.12 illustrates the potential brackish water body at the head of the freshwater aquifer. The values of the sub-seafloor sediments are confined to values between $0.5 \Omega\text{m}$ and $1.7 \Omega\text{m}$, although it should be kept in mind that the stations of Zone A achieve a better fit using lower values of ρ_1 , whereas the receivers of Zone B require higher values. The aquifer is located at a depth of 60 m to 100 m with a resistivity between $30 \Omega\text{m}$ and $100 \Omega\text{m}$ and a poorly resolved thickness of 40 m to 100 m.

Summary & Conclusion

Previous marine LOTEM measurements were effective in detecting a sub-seafloor aquifer in the Palmahim region of Israel, but lacked the necessary lateral resolution to determine the mechanism controlling its occurrence. Therefore, EM methods with a higher lateral resolution were needed to fundamentally predict if this sub-seafloor freshwater body is exposed to seawater intrusion.

Two novel marine EM methods called Circular Electric Dipole (CED) and Differential Electric Dipole (DED) were proposed to derive the hydrogeological mechanism at the western aquifer boundary. The aim of the presented thesis was to theoretically substantiate both methods for an intended application in Bat Yam, Israel.

Prior to the first application, several 1D modelling studies were conducted studying the signal characteristics of novel the DED and CED methods in comparison to the conventional LOTEM method. In the extent of these 1D modelling studies, it was realised that the electric fields acquired at the receiver behaved differently depending on the current step-function. Is the current switched-on, the DED and LOTEM signals become sensitive towards depth variations of a sub-seafloor resistive layer. The CED is thereby completely insensitive towards the resistive layer in the short-offset configuration. In contrast, the switch-off signals of DED and LOTEM exhibit a far lower response towards these depth variations. CED on the other hand exhibits a detectability exceeding the other methods by orders of magnitude. These preliminary results were subsequently confirmed by resolution studies using an SVD-analysis of the Jacobian.

Taking a realistic EM noise consideration into account, the 1D modelling studies indicated that the CED application has insufficient signal amplitudes to delineate the resistive aquifer. Moreover, the application is extremely susceptible towards geometrical errors of the transmitter antenna. Distortions of only several millimetres cause significant parasitic effects in the acquired signal that made a successful application of CED in Israel doubtful. As a result, the intended CED application was not realised in the extent of this thesis.

The DED method exhibits less susceptibility towards these geometrical errors. Therefore, a new fixed-offset, seafloor-based DED transmitter/receiver system was built. In this fixed-offset configuration, the radial electric field is sensitive towards 2D resistivity structures. Profile curves can be used to locate lateral resistivity discontinuities. This applies to mapping both 2D structures expected in Israel and 3D structures representing a hydrocarbon saturated body. However, DED is also sensi-

tive towards 2D effects caused by the bathymetry. This 2D effect is more pronounced in the step-off signal, as sign-reversals may appear. Due to the characteristics of the excited EM field, a 1D interpretation of such data is not feasible. The step-on signals experience a quasi-static shift, but may still be interpreted using a 1D inversion approach. In this case, the declared 1D seawater depth has to be chosen cautiously. The resulting inversion models strongly depend on the transmitter/receiver configuration with respects to the coast. If the correct water depth is considered for a 2D bathymetry model, an adequate representation of the sub-seafloor resistivity structure can be realised using 1D inversion models of the step-on data.

Further 2D modelling studies focussed on the hydrogeological structure at the western aquifer edge. Based on the hydrogeological groundwater flow simulations of *Amir et al.* (2013), a gradual salinity gradient is formed at the head of the freshwater region for an open aquifer scenario. *Kafri and Goldman* (2006) and *Lippert* (2015) see a closed aquifer scenario as a sharp lateral resistivity contrast between freshwater aquifer and surrounding sediments. Simplified resistivity models for the above-mentioned seawater encroachment scenarios were theoretically investigated using 2D modelling studies. Profile-curves at selected time samples showed that the lateral resistivity discontinuity is locatable using the DED system. However, tow directions need to be considered for a correct interpretation. Furthermore, the DED method is capable of differentiating between the closed and open aquifer scenarios, provided that a gradual resistivity gradient exists for the latter case. Different shapes of the aquifer boundary (vertical or wedge-shaped) induce (practically) identical step-on signals, but may become apparent at the late times of the step-off signal.

First DED measurements were carried out in Israel, April 2016. During the four-day campaign, 11 transmitter positions with 17 interpretable receiver stations were measured on the profile of *Lippert* (2015). New data processing scripts were utilised for the first time. The resulting transients are similar to the synthetic 2D data that was derived from the LOTEM results of *Lippert* (2015). Profile curves of the measured data show a clear indication of a lateral resistivity discontinuity between a conductive media interpreted as seawater saturated sediments in the West and a resistive body interpreted as the freshwater aquifer in the East. This prediction is supported by the measured DC voltages that clearly show a more resistive subsurface towards the coast.

The measured data was interpreted using 1D inversion. Due to the poor data quality of the acquired step-off signals, a full interpretation using both current step-functions was not feasible. Still, a preliminary comparison was conducted at a selected station. The intended joint inversion approach did not show superior resolution compared to the single inversion of the step-on signals. Consequently, the remaining interpretation presented in this thesis is based on the measured DED step-on data.

The obtained 1D inversion models exhibit a high consistency to the inversion models of marine LOTEM measurements. The resolution analysis proved that a resistive layer in the depth range of the expected freshwater body is needed to obtain a sufficient data fit for all stations located east of the No-Anchor-Zone. In turn, the stations located west of the No-Anchor-Zone did not require a resistive layer in the

subsurface to achieve an adequate data fit.

A 2D modelling study using `s1dmem3t` was realised to fit the measured marine DED data. In total, over 425 600 forward calculations were executed for 11 transmitter positions. An ensemble of best fit models was determined to derive the parameters of the aquifer. The results for the receivers located to the West of the No-Anchor-Zone detect the aquifer boundary at 3600 m or 3700 m before the Israeli coast. An interpretation of the hydrogeological setting at the aquifer boundary was realised. The best data fit is achieved if the model contains a further block of moderate resistivity between 3 Ωm to 5 Ωm and a lateral extent of smaller 300 m at the head of the aquifer. These resistivity values coincide with the resistivity values of brackish water in the coastal aquifers of Israel presented by *Kafri and Goldman (2006)*. However, this hypothesis should be treated cautiously, as a closed aquifer scenario achieved only slightly inferior data fits. In-situ measurements are necessary to further conclude this hypothesis. In this sense, the DED application was still justified as the aquifer boundary is now confined to a lateral extent of ± 100 m.

Coming back to the objectives of this thesis stated in Section 2.3. A novel marine DED system was developed, tested and applied in field measurements for the first time. The results of the step-on data are consistent with *Lippert (2015)* and validate the applicability of the system. Moreover, the aquifer edge is located to the West of the No-Anchor-Zone and is now defined at 3600 m - 3700 m from the Israeli coastline. Predictions regarding the hydrogeological structure at the western aquifer boundary were also possible using the step-on data. An open aquifer scenario seems to be the likely hydrogeological setting. However, the latter predictions should be examined cautiously, as they can only be verified using in-situ measurements, e.g. borehole data.

Overall, the development and application of the novel DED system has to be classified as a success. Yet, DED is presently not at par with the existing TD-CSEM applications due to the complicated measurement procedure. However, the enhanced lateral resolution for 2D structures justifies further developments. Some of these were already mentioned in Section 7.1.4. The main emphasis for the practical development should lie on optimising the measurement procedure so that more data can be acquired. A relocation of the ship at each station should be avoided in future applications. Applying seafloor-based receiver units will be a further simplification of the measurement procedures.

The most obvious theoretical development is the necessity of a multi-dimensional DED inversion software. The method is designed to locate lateral resistivity variations more precisely. However, the data interpretation until now is based on 1D inversion with subsequent 2D modelling. This is quite time-consuming and computationally expensive. A more sophisticated 2D interpretation approach is needed. Plans to realise this in the near future are currently being examined. Furthermore, a 1D Markov-Chain Monte-Carlo inversion exists for DED applications, but was not presented in the context of this thesis. This should be implemented in the standard 1D interpretation scheme in the future.

Aside from practical and theoretical developments, marine DED needs further applications to analyse the strength and weaknesses of the method. At the present

time, it seems advisable to restrict DED applications to investigating resistive layers that are located no more than 200 m below the seafloor. Especially the analysis of both current step-functions seems beneficiary in future shallow sea experiments.

Bibliography

- Abramowitz, M., and I. A. Stegun (1972), *Handbook of mathematical functions with formulas, graphs and mathematical tables: National Bureau of Standards*, 10 ed., Dover Publications Inc.
- Amir, N., U. Kafri, B. Herut, and E. Shalev (2013), Numerical Simulations of Submarine Groundwater Flow in the Coastal Aquifer at the Palmahim Area, the Mediterranean Coast of Israel, *Water Resources Management*, 27, 4005–4020, doi:10.1007/s11269-013-0392-2.
- Archie, G. E. (1942), The Electrical Resistivity Log as an Aid in Determining Some Reservoir Characteristics, *Trans. Am. Inst. Min. Metal. and Petr. Eng.*, 146, doi:10.2118/942054-G.
- Asten, M. W. (1987), Full transmitter waveform transient electromagnetic modeling and inversion for soundings over coal measures, *Geophysics*, 52(3), 279–288, doi:10.1190/1.1442302.
- Börner, R. U. (2010), Numerical Modelling in Geo-Electromagnetics: Advances and Challenges, *Surveys in Geophysics*, 31, 225–245, doi:10.1007/s10712-009-9087-x.
- Bubnov, V. P., V. Goldansky, A. S. Kashik, M. M. Mandelbaum, N. Rykhlini, and V. V. Chemyak (1984), Spatial differentiation in electric survey [in Russian], *Russian Geology and Geophysics*, 6, 106–111.
- Cagniard, L. (1953), Basic theory of the magnetotelluric method of geophysical prospecting, *Geophysics*, 18(3), 605–635, doi:10.1190/1.1437915.
- Chave, A. D. (1984), The Frechet Derivatives of electromagnetic induction, *Journal of Geophysical Research*, 89(B5), 3373–3380, doi:10.1029/JB089iB05p03373.
- Chave, A. D., and A. G. Jones (Eds.) (2012), *The Magnetotelluric Method: Theory and Practice*, Cambridge University Press.
- Chen, J., and D. L. Alumbaugh (2011), Three methods for mitigating airwaves in shallow water marine controlled-source electromagnetic data, *Geophysics*, 76(2), F89–F99, doi:10.1190/1.3536641.
- Christensen, N. B. (1990), Optimized Fast Hankel Transform Filters, *Geophys. Prospect.*, 38(5), 545–568, doi:10.1111/j.1365-2478.1990.tb01861.x.

- Connell, D., and K. Key (2013), A numerical comparison of time and frequency-domain marine electromagnetic methods for hydrocarbon exploration in shallow water, *Geophys. Prospect.*, *61*(1), 187–199, doi:10.1111/j.1365-2478.2012.01037.x.
- Constable, S. (2010), Ten years of marine CSEM for hydrocarbon exploration, *Geophysics*, *75*(5), A67–A81, doi:10.1190/1.3483451.
- Constable, S. C., and C. S. Cox (1996), Marine controlled-source electromagnetic sounding 2. The PEGASUS experiment, *Journal of Geophysical Research*, *101*(B3), 5519–5530, doi:10.1029/95JB03738.
- Constable, S. C., R. L. Parker, and C. G. Constable (1987), Occam's Inversion: A practical algorithm for generating smooth models from electromagnetic sounding data, *Geophysics*, *52*(3), 289–300, doi:10.1190/1.1442303.
- Cox, C. S., S. C. Constable, A. D. Chave, and S. C. Webb (1986), Controlled source electromagnetic sounding of the oceanic lithosphere, *Nature*, *320*, 52–54, doi:10.1038/320052a0.
- Darnet, M., P. V. D. Sman, R. E. Plessix, J. L. Johnson, and M. Rosaenquist (2010), Exploring with Controlled Source Electromagnetic (CSEM) methods: from 2D profiling to 2D multi-azimuthal surveying, in *EGM 2010 International Workshop, Adding new value to Electromagnetic, Gravity and Magnetic Methods for Exploration*.
- Davydycheva, S., and N. Rykhliniski (2009), Focused Source EM Survey - New Solution for Both Shallow and Deep Water, in *71st EAGE Conference and Exhibition incorporating SPE EUROPEC 2009*, X018, doi:10.3997/2214-4609.201400503.
- Davydycheva, S., and N. Rykhliniski (2011), Focused-source electromagnetic survey versus standard CSEM: 3D modeling in complex geometries, *Geophysics*, *76*(1), F27–F41, doi:10.1190/1.3511353.
- Davydycheva, S., N. Rykhliniski, and P. Y. Legeydo (2006), Electrical-prospecting method for hydrocarbon search using the induced-polarization effect, *Geophysics*, *71*(4), G179–G189, doi:10.1190/1.2217367.
- Druskin, V. L., and L. A. Knizhnerman (1988), Spectral differential-difference method for the numeric solution of three-dimensional nonstationary problems of electric prospecting, *Izvestiya: Earth Physics*, *24*(8), 641–648.
- Druskin, V. L., and L. A. Knizhnerman (1994), Spectral approach to solving three-dimensional Maxwell's diffusion equations in the time and frequency domains, *Radio Science*, *29*(4), 937–953, doi:10.1029/94RS00747.
- Edwards, N. L. (2005), Marine Controlled Source Electromagnetics: Principles, Methodologies, Future Commercial Applications, *Surveys in Geophysics*, *26*(6), 675–700, doi:10.1007/s10712-005-1830-3.
- Edwards, R. N. (1997), On the resource evaluation of marine gas hydrate deposits using seafloor transient electric dipole-dipole methods, *Geophysics*, *62*(1), 63–74, doi:10.1190/1.1444146.

- Edwards, R. N., and A. D. Chave (1986), A transient electric dipole-dipole method for mapping the conductivity of the sea floor, *Geophysics*, *51*(4), 984–987, doi:10.1190/1.1442156.
- Eidesmo, T., S. Ellingsrud, L. M. MacGregor, S. Constable, S. A. Sinha, S. Johansen, F. N. Kong, and H. Westerdahl (2002), Sea Bed Logging (SBL), a new method for remote and direct identification of hydrocarbon filled layers in deepwater areas, *First Break*, *20*(3), 144–152, doi:10.1046/j.1365-2397.2002.00264.x.
- Ellingsrud, S., T. Eidesmo, S. Johansen, M. C. Sinah, L. M. MacGregor, and S. Constable (2002), Remote sensing of hydrocarbon layers by seabed logging (SBL): Results from a cruise offshore Angola, *The Leading Edge*, *21*(10), 972–982, doi:10.1190/1.1518433.
- Farquharson, C. G., and D. W. Oldenburg (2004), A comparison of automatic techniques for estimating the regularization parameter in non-linear inverse problems, *Geophysical J. Int.*, *156*(3), 411–425, doi:10.1111/j.1365-246X.2004.02190.x.
- Ferguson, I. J., and R. N. Edwards (1994), Electromagnetic Mode Conversion By Surface-Conductivity Anomalies: Applications For Conductivity Soundings, *Geophysical J. Int.*, *117*(1), 48–68, doi:10.1111/j.1365-246X.1994.tb03303.
- Filloux, J. H. (1967), An ocean bottom, D component magnetometer, *Geophysics*, *32*(6), 978–987, doi:10.1190/1.1439910.
- Gehrmann, R. (2014), Non-linear Bayesian inversion of controlled source electromagnetic data offshore Vancouver Island, Canada, and in the German North Sea, Ph.D. thesis, University of Victoria.
- Gehrmann, R. A. S., J. Dettmer, K. Schwalenberg, M. Engles, S. E. Dosso, and A. Özmaral (2015), Trans-dimensional Bayesian inversion of controlled-source electromagnetic data in the German North Sea, *Geophys. Prospect.*, *63*(6), 1314–1333, doi:10.1111/1365-2478.12308.
- Ghosh, D. (1971), The application of linear filter theory to the direct interpretation of geoelectrical resistivity sounding measurements, *Geophys. Prospect.*, *19*(2), 192–217, doi:10.1111/j.1365-2478.1971.tb00593.x.
- Goldman, M., A. Arad, U. Kafri, D. Gilad, and A. Melloul (1988), Detection of fresh-water/sea-water interface by the time domain electromagnetic (TDEM) method in Israel, in *Proc. 10th SWIM, Ghent*, edited by W. de Breuck & L. Walschot.
- Goldman, M., B. Rabinovich, M. Rabinovich, D. Gilad, I. Gev, and M. Schirov (1994), Application of the intergrated NMR-TDEM method in groundwater exploration in Israel, *Journal of Applied Geophysics*, *31*(1-4), 27–52, doi:10.1016/0926-9851(94)90045-0.
- Goldman, M., E. Levi, B. Tezkan, and P. Yogeshwar (2011), The 2D coastal effect on marine time domain electromagnetic measurements using broadside dBz/dt of an electrical transmitter dipole, *Geophysics*, *76*(2), F101–F109, doi:10.1190/1.3525276.

- Goldman, M., V. Mogilatov, A. Haroon, E. Levi, and B. Tezkan (2015), Signal detectability of marine electromagnetic methods in the exploration of resistive targets, *Geophys. Prospect.*, *63*(1), 192–210, doi:10.1111/1365-2478.12151.
- Guptasarma, D., and B. Singh (1997), New digital linear filters for Hankel J0 and J1 transforms, *Geophys. Prospect.*, *45*(5), 745–762, doi:10.1046/j.1365-2478.1997.500292.x.
- Haland, E., E. G. Flekøy, and K. J. Måløy (2012), Vertical and horizontal components of the electric background field at the sea bottom, *Geophysics*, *77*(1), E1–E8, doi:10.1190/GEO2011-0039.1.
- Hanstein, T. (1992), Iterative und parametrisierte Dekonvolution für LOTEM Daten, in *Protokoll über das 14. Kolloquium Elektromagnetische Tiefenforschung*, pp. 163–172, Dt. Geophys. Gesellschaft.
- Hanstein, T. (1996), Digitale Optimalfilter für LOTEM Daten, in *Protokoll über das 16. Kolloquium Elektromagnetische Tiefenforschung*, edited by K. Baur and A. Junge, Deutsche Geophysikalische Gesellschaft.
- Haroon, A. (2012), The application of the Long Offset Transient Electromagnetic Method in Perekishkul, Azerbaijan, Master's thesis, University of Cologne.
- Haroon, A., M. Goldman, and B. Tezkan (2013), Marine Circular Electric Dipole (MCED): A new innovative electromagnetic technique for delineating resistive submarine targets, in *MARELEC, Hamburg*.
- Haroon, A., J. Adrian, R. Bergers, M. Gurk, B. Tezkan, A. L. Mammadov, and A. G. Novruzov (2015), Joint inversion of long-offset and central-loop transient electromagnetic data: Application to a mud volcano exploration in Perekishkul, Azerbaijan, *Geophys. Prospect.*, *63*(2), 478–494, doi:10.1111/1365-2478.12157.
- Haroon, A., V. Mogilatov, M. Goldman, R. Bergers, and B. Tezkan (2016), Exploration of resistive targets within shallow marine environments using the Circular Electrical Dipole and the Differential Electrical Dipole methods: A time-domain modelling study, *Geophysical J. Int.*, *205*(2), 1032–1048, doi:10.1093/gji/ggw051.
- Helwig, S. L. (2000), Vibrotem, Ph.D. thesis, University of Cologne.
- Helwig, S. L., V. Mogilatov, and B. Balashov (2010a), Enhanced sensitivity in land EM by using an unconventional source, in *EGM 2010 International Workshop*.
- Helwig, S. L., V. Mogilatov, and B. Balashov (2010b), The use of a circular electrical dipole source in hydrocarbon exploration, in *SEG Annual Meeting*.
- Helwig, S. L., A. W. E. Kaffas, T. Holten, Ø. Frafjord, and K. Eide (2013), Vertical dipole CSEM: Technology advances and results from the Snøhvit field, *First Break*, *31*(4), 63–68.

- Hoerdt, A., V. L. Druskin, L. A. Knizhnerman, and K. M. Strack (1992), Interpretation of 3-D effects in long-offset transient electromagnetic (LOTEM) soundings in the Muensterland area/Germany, *Geophysics*, *57*(9), 1127–1137, doi:10.1190/1.1443327.
- Holten, T., E. Flekkøy, K. Måløy, and B. S. Singer (2009), Vertical source and receiver CSEM method in time-domain, in *79th Annual Meeting, Expanded Abstracts*, pp. 749–752, SEG.
- Hölz, S., A. Swidinsky, M. Sommer, M. Jegen, and J. Bialas (2015), The use of rotational invariants for the interpretation of marine CSEM data with a case study from the North Alex mud volcano, West Nile Delta, *Geophysical J. Int.*, *201*, 224–245, doi:10.1093/gji/ggv015.
- Hördt, A. (1989), Ein Verfahren zur 'Joint Inversion' angewandt auf Long Offset Transient Electromagnetics and Magnetotellurik, Master's thesis, University of Cologne.
- Hördt, A. (1992), Interpretation transient elektromagnetischer Tiefensondierung für anisotrop horizontal geschichtete und für dreidimensionale Leitfähigkeitsstrukturen, Ph.D. thesis, University of Cologne.
- Hördt, A., and C. Scholl (2004), The effect of local distortions on time-domain electromagnetic measurements, *Geophysics*, *69*(1), 87–96, doi:10.1190/1.1649378.
- Hunziker, J., E. Slob, and W. Mulder (2011), Effects of the airwave in time-domain marine controlled-source electromagnetics, *Geophysics*, *76*(4), F251–F261, doi:10.1190/1.3587222.
- Johansen, H., and K. Sørensen (1979), Fast Hankel transforms, *Geophys. Prospect.*, *27*(4), 876–901, doi:10.1111/j.1365-2478.1979.tb01005.x.
- Jupp, D. L. B., and K. Vozoff (1975a), Stable Iterative Methods for the Inversion of Geophysical Data, *Geophys. J. R.*, *42*(3), 957–976, doi:10.1111/j.1365-246X.1975.tb06461.x.
- Jupp, D. L. B., and K. Vozoff (1975b), Joint Inversion of Geophysical Data, *Geophys. J. R.*, *42*(3), 977–991, doi:10.1111/j.1365-246X.1975.tb06462.
- Kafri, U., and M. Goldman (2005), The use of the time domain electromagnetic method to delineate saline groundwater in granular and carbonate aquifers and to evaluate their porosity, *Journal of Applied Geophysics*, *57*(3), 167–178, doi:10.1016/j.jappgeo.2004.09.001.
- Kafri, U., and M. Goldman (2006), Are the lower subaquifers of the Mediterranean coastal aquifer of Israel blocked to seawater intrusion? Results of TDEM (time domain electromagnetic study), *Israel Journal of Earth and Science*, *55*(2), 55–68, doi:10.1560/Q567-832K-0420-067V.
- Kalscheuer, T. (2004), Die Auswertung der LOTEM-Daten vom Suedhang des Merapi, Master's thesis, University of Cologne.

- Kapuler, Y., and J. Bear (1970), Numerical solutions to the movement of the interface in a multi-layered coastal aquifer, *Tahal, Water Planning for Israel. Rep. 01/74/70 (in Hebrew)*.
- Key, K. (2012a), Is the fast Hankel transform faster than quadrature?, *Geophysics*, 77(3), F21–F30, doi:10.1190/geo2011-0237.1.
- Key, K. (2012b), Marine EM inversion using unstructured grids: a 2D parallel adaptive finite element algorithm, in *SEG Technical Program Expanded Abstracts*, pp. 1–5, doi:10.1190/segam2012-1294.1.
- Kolton, Y. (1988), Examination of the connection between seawater in the Pleistocene aquifer in the Mediterranean shelf of central Israel., *Tahal, Water Planning for Israel. Rep. 01/88/31 (in Hebrew)*.
- Lanczos, C. (1964), *Applied Analysis*, Prentice-Hall.
- Legeydo, P. Y., M. M. Mandelbaum, and N. Rykhliniski (1990), Application of differentially adjusted electric exploration of the Nepa Dome [in Russian], *Soviet Geology and Geophysics*, 31(86-91).
- Legeydo, P. Y., M. M. Mandelbaum, and N. Rykhliniski (1997), Results of a differential-normalized electrical prospecting in the Central part of the Nepa arch on the Siberian platform [in Russian], *Russian Geology and Geophysics*, 38, 1707–1713.
- Levenberg, K. (1944), A method for the solution of certain nonlinear problems in least squares, *Quarterly of Applied Mathematics*, 2(2), 164–168.
- Lines, L. R., and S. Treitel (1984), A review of least-squares inversion and its application to geophysical problems, *Geophys. Prospect.*, 32(2), 159–186, doi: 10.1111/j.1365-2478.1984.tb00726.x.
- Lippert, K. (2015), Detektion eines submarinen Aquifers vor der Küste Israels mittels mariner Long Offset Transient-elektromagnetischer Messung, Ph.D. thesis, University of Cologne.
- Lippert, K., B. Tezkan, R. Bergers, and M. Goldman (2012), Erkundung eines Aquifers unter dem Mittelmeer vor der israelischen Küste mit Long Offset Transient Elektromagnetik, in *72. Jahrestagung der Deutschen Geophysikalischen Gesellschaft*.
- Mandelbaum, M. M., E. B. Ageenkov, P. Y. Legeydo, P. Y. Perserev, and N. Rykhliniski (2002), Normalized-differential electrical measurements in hydrocarbon exploration: the state of the art and prospects for future, *Russian Geology and Geophysics*, 43, 1085–1143.
- Marquardt, D. W. (1963), An Algorithm for Least-Squares Estimation of Nonlinear Parameters, *Journal of the Society for Industrial and Applied Mathematics*, 11(2), 431–441, doi:10.1137/0111030.

- Martin, R. (2009), Development and application of 2D and 3D transient electromagnetic inverse solutions based on adjoint Green functions: A feasibility study for the spatial reconstruction of conductivity distributions by means of sensitivities, Ph.D. thesis, University of Cologne.
- Meju, M. A. (1994), *Geophysical Data Analysis: Understanding Inverse Problems in Theory and Practice*, Society of Exploration Geophysicists.
- Menke, W. (1984), *Geophysical Data Analysis: Discrete Inverse Theory*, Academic Press, Inc.
- Moghadas, D., M. Engels, and K. Schwalenberg (2015), 1D joint multi-offset inversion of time-domain marine controlled source electromagnetic data, *Geophys. Prospect.*, *63*(6), 1334–1354, doi:10.1111/1365-2478.12281.
- Mogilatov, V. (1992), A circular electrical dipole as a new source in electric surveys., *Izvestiya: Physics of the solid Earth*, *6*, 97–105.
- Mogilatov, V. (1996), Excitation of a Half-space by a Radial Current Sheet Source, *PAGEOPH*, *147*(4), 763–775.
- Mogilatov, V., and B. Balashov (1996), A new method of geoelectrical prospecting by vertical electric current soundings, *Journal of Applied Geophysics*, *36*, 31–41.
- Mogilatov, V., and A. V. Zlobinsky (2008), Software for the Inductive Impulse Electrical Prospecting, *Journal of Applied and Industrial Mathematics*, *2*(1), 100–112, doi:10.1134/S1990478908010110.
- Mogilatov, V., and A. V. Zlobinsky (2014), A circular electrical dipole: a transmitter for TEM surveys, *Russian Geology and Geophysics*, *55*(11), 1340–1346, doi:10.1016/j.rgg.2014.10.009.
- Mogilatov, V., M. Goldman, M. Persova, Y. Soloveichik, Y. Koshkina, O. Trubacheva, and A. Zlobinskiy (2016), Application of the marine circular electric dipole method in high latitude Arctic regions using drifting ice floes, *Journal of Applied Geophysics*, *135*, 17–31, doi:10.1016/j.jappgeo.2016.08.007.
- Munkholm, M., and E. Auken (1996), Electromagnetic Noise Contamination on Transient Electromagnetic Soundings in Culturally Distrubed Environments, *Journal of Environmental Engineering Geophysics*, *1*(2), 119–127, doi:10.4133/JEEG1.2.119.
- Newman, G. A. (1989), Deep transient electromagnetic soundings with a grounded source over near-surface conductors, *Geophysical Journal*, *98*(3), 587–601, doi:10.1111/j.1365-246X.1989.tb02292.
- Paige, C. C. (1980), Accuracy and effectiveness of the Lanczos Algorithm for the Symmetric Eigenproblem, *Linear Algebra and its Applications*, *34*, 235–258, doi:10.1016/0024-3795(80)90167-6.
- Parlett, F. B. (1980), *The Symmetric Eigenvalue Problem*, Prentice-Hall.

- Petry, H. (1987), Transient Elektromagnetische Tiefensondierung - Modellrechnungen und Inversion, Master's thesis, University of Cologne.
- Scholl, C. (2001), Die Periodizität von Sendesignalen bei Long-Offset Transient Electromagnetics, Master's thesis, University of Cologne.
- Scholl, C. (2005), The influence of multidimensional structures on the interpretation of LOTEM data with one-dimensional models and the application to data from Israel, Ph.D. thesis, University of Cologne.
- Scholl, C., and R. N. Edwards (2007), Marine downhole to seafloor dipole-dipole electromagnetic methods and the resolution of resistive targets, *Geophysics*, 72(2), WA39–WA49, doi:10.1190/1.2434775.
- Schwalenberg, K., and M. Engels (2011), Marine Controlled Source Electromagnetic Methods for Gas Hydrate Assessment: New Instrumentation and First Results from the Black Sea Test Cruise, in *24. Kolloquium Elektromagnetischer Tiefenforschung, Neustadt*.
- Schwalenberg, K., M. Haeckel, J. Poort, and M. Jegen (2010), Evaluation of gas hydrate deposits in an active seep area using marine controlled source electromagnetics: Results from Opouawe Bank, Hikurangi Margin, New Zealand, *Marine Geology*, 272(1-4), 79–88, doi:10.1016/j.margeo.2009.07.006.
- Singer, B. S., and S. Atramonova (2013), Vertical electric source in transient marine CSEM: Effect of 3D inhomogeneities on the late time response, *Geophysics*, 78(4), E173–E188, doi:10.1190/geo2012-0316.1.
- Sorensen, K., and N. Christensen (1994), The fields from a finite electrical dipole - A new computational approach, *Geophysics*, 59, 864–880, doi:10.1190/1.1443646.
- Spangenberg, E. (2001), Modeling of the influence of gas hydrate content on the electrical properties of porous rock, *Journal of Geophysical Research*, 106(B4), 6535–6548, doi:10.1029/2000JB900434.
- Spies, B. (1989), Depth of investigation in electromagnetic sounding methods, *Geophysics*, 54(7), 872–888, doi:10.1190/1.1442716.
- Spies, B. R., and F. C. Frischknecht (1991), *Electromagnetic Sounding, Electromagnetic Methods in Applied Geophysics*, vol. 2, chap. 5, Society of Exploration Geophysicists, doi:10.1007/BF01452955.
- Strack, K. M. (1992), *Exploration with Deep Transient Electromagnetics*, Elsevier.
- Swidinsky, A., S. Hölz, and M. Jegen (2012), On mapping seafloor mineral deposits with central loop transient electromagnetics, *Geophysics*, 77(3), E171–E184, doi:10.1190/geo2011-0242.1.
- Telford, W. M., L. P. Geldart, R. E. Sheriff, and D. A. Keys (1976), *Applied Geophysics*, Cambridge University Press.

- Veeken, P. C. H., P. Y. Legeydo, Y. A. Davidenko, E. O. Kudryavceva, S. A. Ivanovm, and A. Chuvaev (2009), Benefits of the induced polarization geoelectric method to hydrocarbon exploration, *Geophysics*, *74*(2), B47–B59, doi:10.1190/1.3076607.
- Ward, S., and D. L. B. Hohmann (1988), *Electromagnetic Theory for Geophysical Applications*, vol. 1, chap. 1, Electromagnetic Methods in Applied Geophysics, Society of Exploration Geophysics, doi:10.1190/1.9781560802631.
- Weidelt, P. (1986), Einfuehrung in die elektromagnetische Tiefensondierung, Lecture Notes.
- Weidelt, P. (2000), Elektromagnetische Tiefensondierung, in *18. Kolloquium*.
- Weidelt, P. (2007), Guided Waves in marine CSEM, *Geophysical J. Int.*, *171*(1), 153–176, doi:j.1365-246X.2007.03527.x.
- Weiss, C. J. (2007), The fallacy of the "shallow-water problem" in marine CSEM exploration, *Geophysics*, *72*(6), A93–A97, doi:10.1190/1.2786868.
- Winsauer, W. O., H. M. Shearin, P. H. Masson, and M. Williams (1952), Resistivity of Brine-Saturated Sands in Relation to Pore Geometry, *AAPG Bulletin*, *36*(2), 253–277.
- Yee, K. S. (1966), Numerical solution of initial boundary problems involving Maxwell's equations in isotropic media, *IEEE Trans. Antenn. Propagat.*, *14*, 302–309.
- Yogeshwar, P. (2014), A resistivity-depthmodel of the central Azraq basin area, Jordan: 2D forward and inverse modeling of time domain electromagnetic data, Ph.D. thesis, University of Cologne.
- Ziolkowski, A., and D. Wright (2007), Removal of the airwave in shallow-marine transient EM data, in *77th Annual International Meeting*, Expanded Abstracts, pp. 534–538, SEG, doi:10.1190/1.2792478.

Setup and Nomenclature

The following Chapter shows the information regarding the DED measurements in Israel. A detailed sketch of the measurements setup is displayed along with the information to the receiver stations.

Table A.1: Information to receiver positions from the measurements.

Station	Position [m]	Offset [m]	kS/s	Period [s]	Current [A]	Stacks	Water Depth at Rx [m]	Water Depth at Tx [m]
p01FR	1250	580	10	2	25.4	1099	15.0	9.0
p02NR	1350	370	10	2	25.4	1661	15.95	11.0
p03FR	1550	580	10	2	25.4	1595	18.2	11.0
p04FR	1850	580	10	2	25.1	1245	22.5	16.0
p05NR	2000	370	10	2	25.4	1332	24.2	18.0
p06FR	2150	580	10	2	25.4	1119	26.5	18.0
p07FR	3250	580	10	2	25.4	1139	35.2	37.0
p08FR	3315	580	10	2	25.6	1849	35.45	37.0
p09FR	3400	580	10	2	25.4	1063	35.95	37.2
p10FR	3450	580	10	2	25.6	1367	36.1	37.3
p11FR	3600	580	10	2	25.7	2243	36.4	37.5
p12NR	3650	370	10	2	25.6	2837	36.6	37.3
p13NR	3715	370	10	2	25.7	2031	36.75	37.5
p14FR	3780	580	10	2	25.6	1993	36.9	37.7
p15FR	3865	580	10	2	25.5	2077	37.0	38.1
p16NR	3970	370	10	2	25.6	1483	37.15	37.7
p17NR	4100	370	10	2	25.5	2129	37.45	38.1

1D Inversion - Extended

In the following section, the 1D inversion results are shown for Step-On, and joint inversion. The SVD-analysis of the step-on Marquardt inversion is also given.

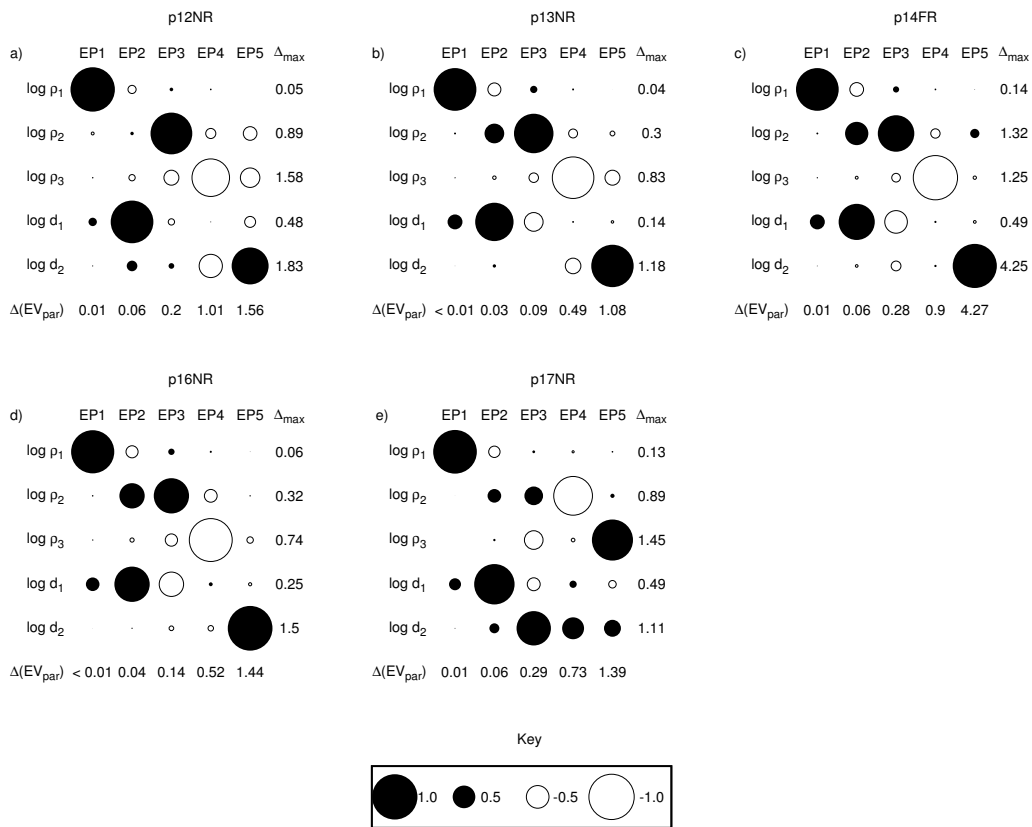


Figure B.1: SVD analysis for several stations along the profile.

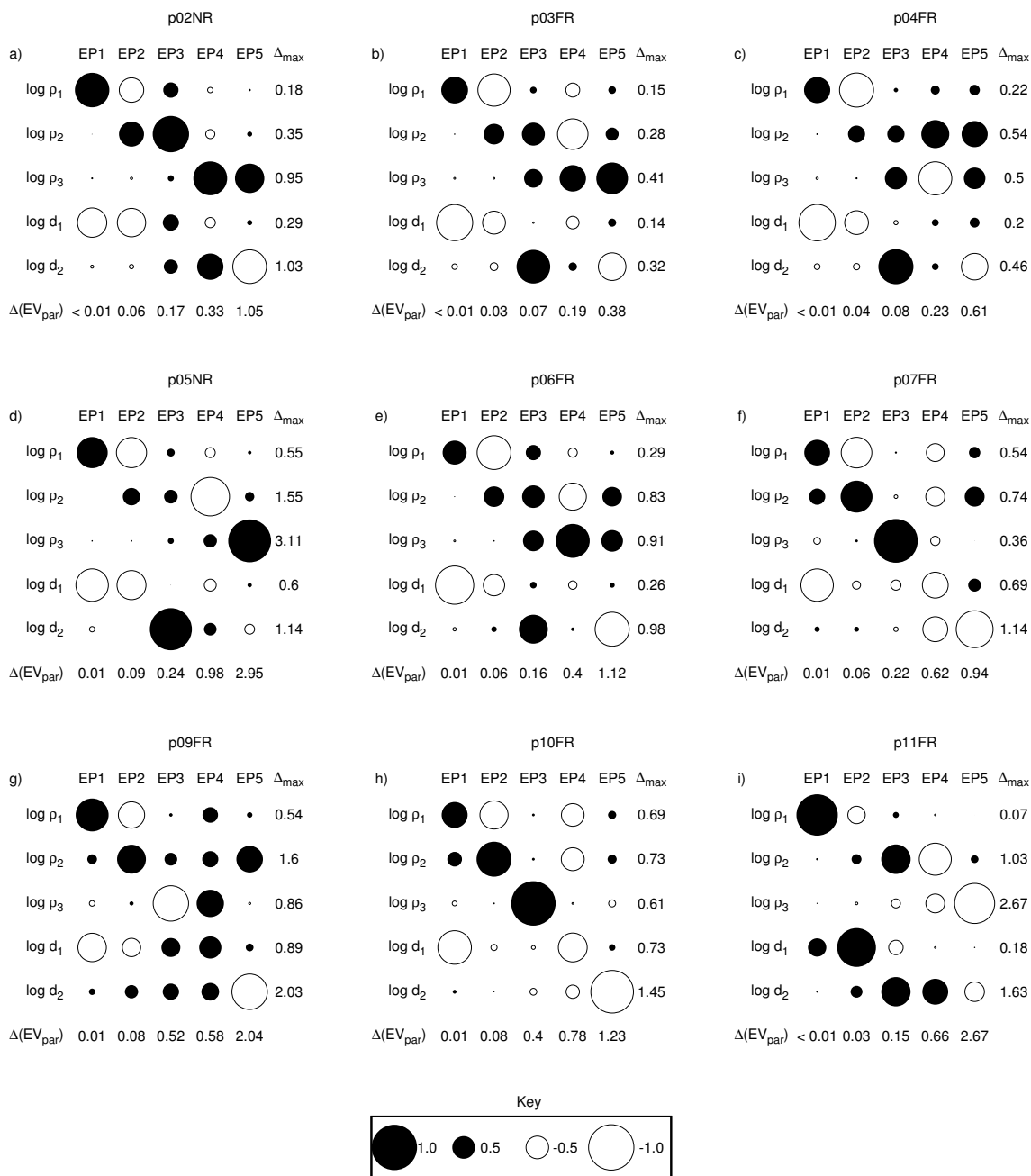


Figure B.2: SVD analysis for several stations along the profile.

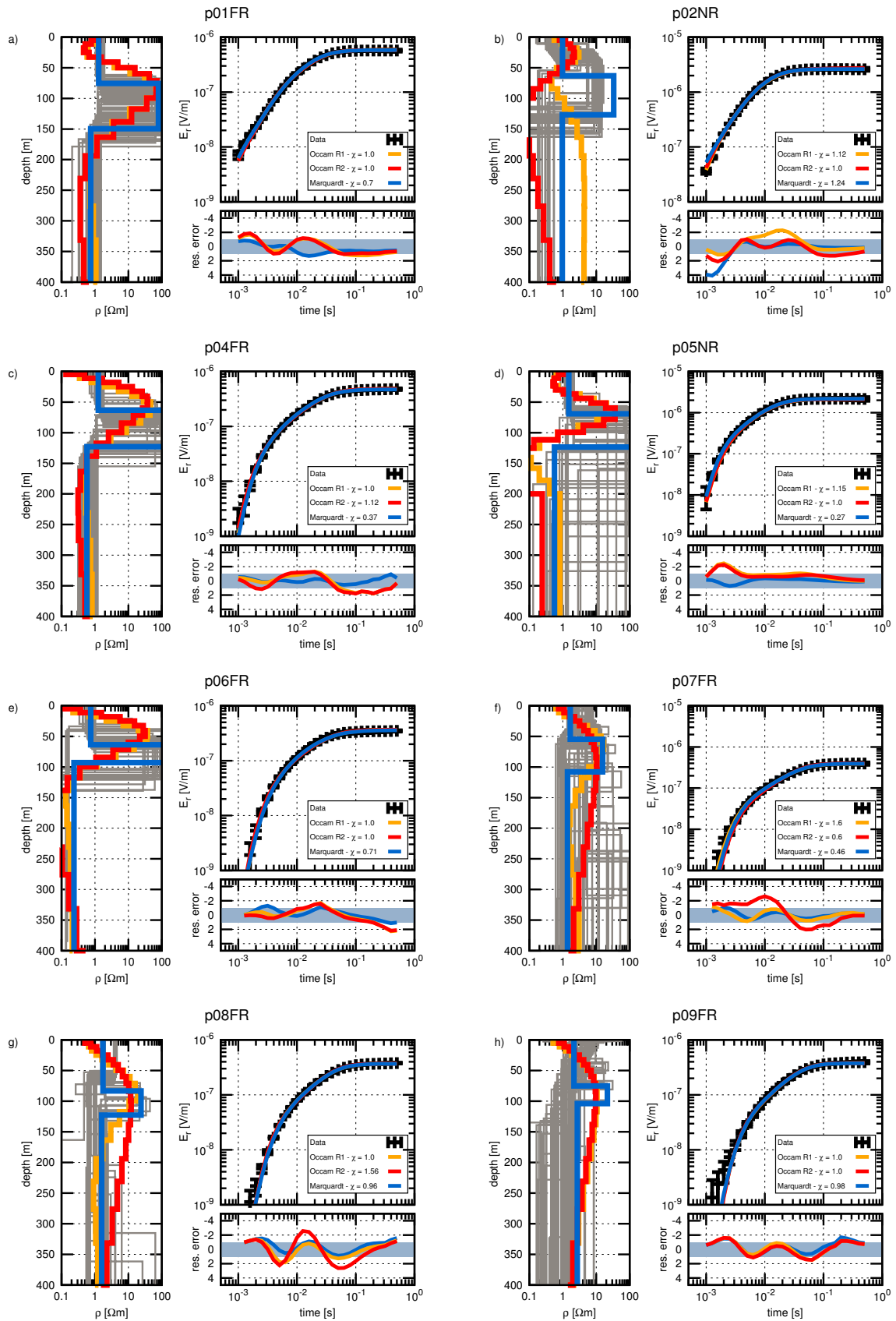


Figure B.3: Inversion models of step-on signals for stations p01FR through p09FR in (a) through (h), respectively.

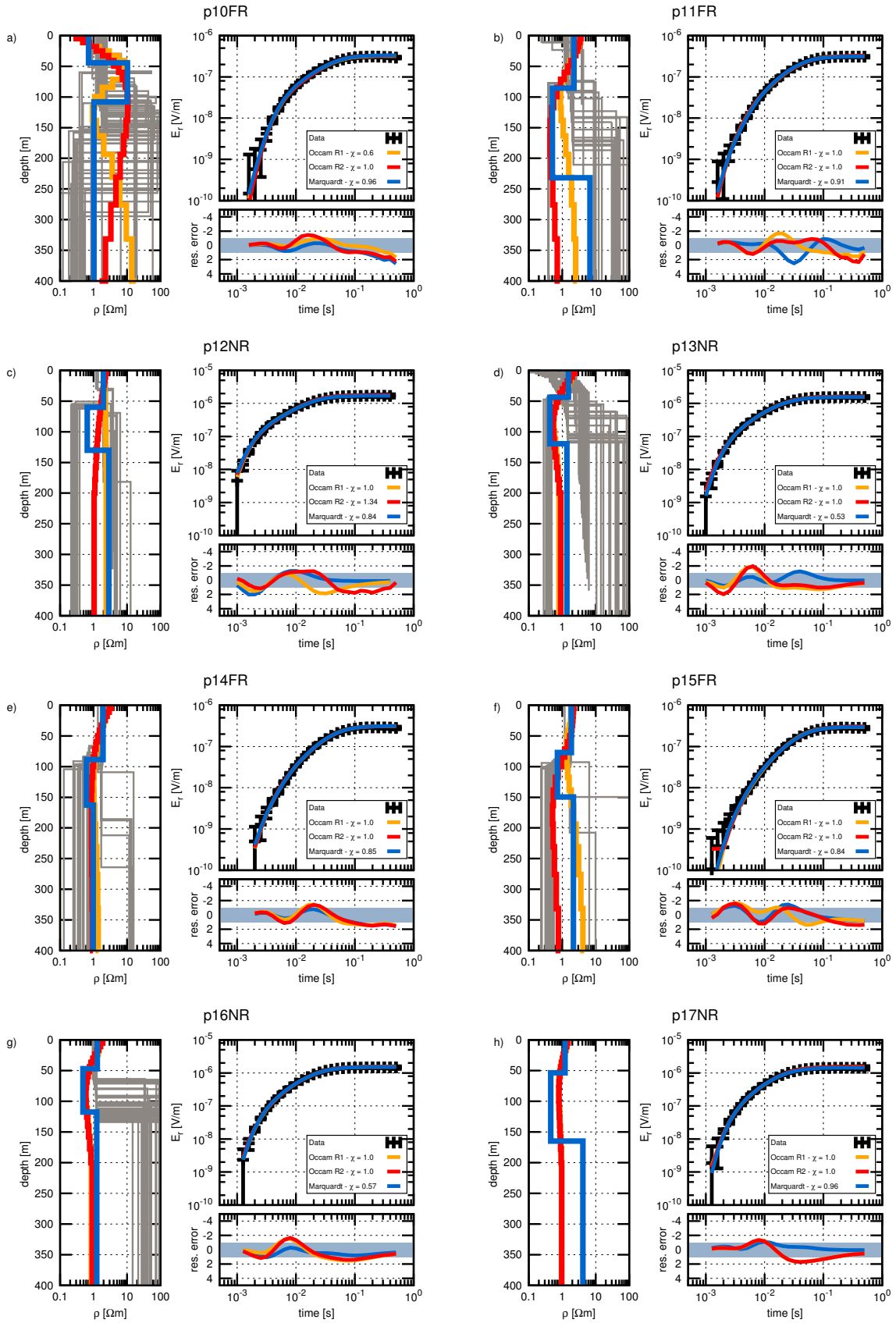


Figure B.4: Inversion models of step-on signals for stations p10FR through p17NR in (a) through (h), respectively.

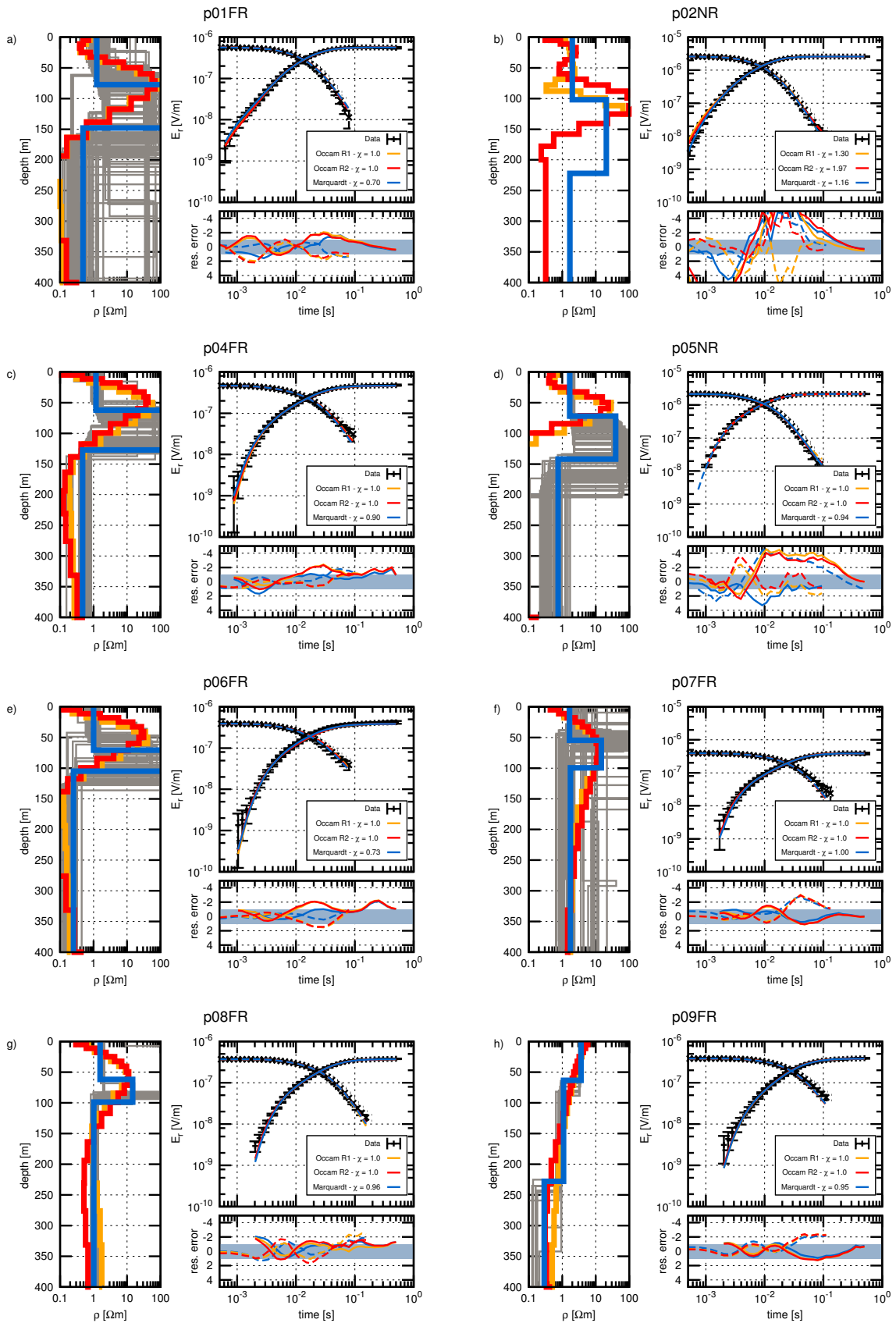


Figure B.5: Joint-Inversion models of step-on/off signals for stations p01FR through p09FR in (a) through (h), respectively.

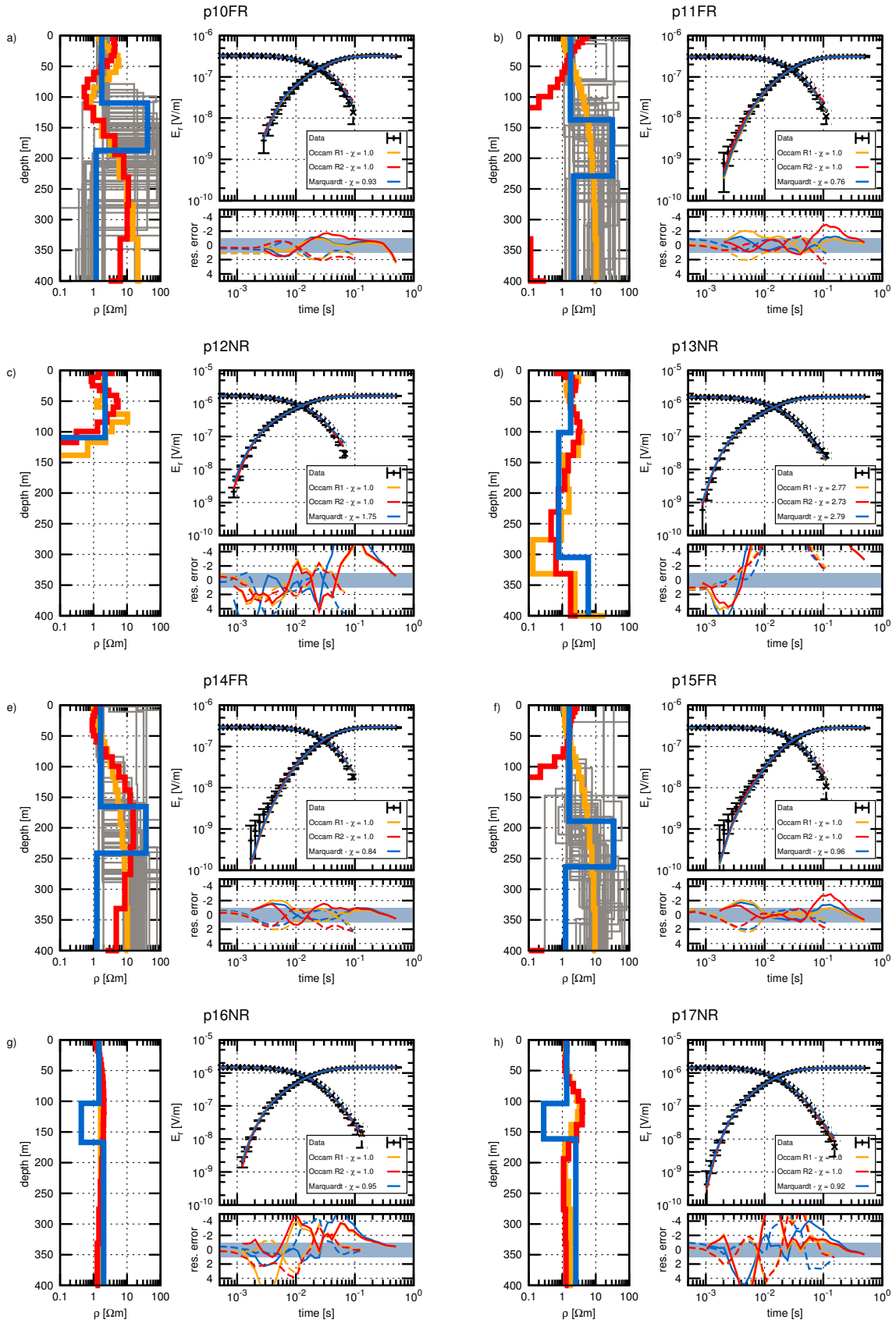


Figure B.6: Joint-Inversion models of step-on/off signals for stations p10FR through p17NR in (a) through (h), respectively.

2D Modelling of Field Data - Extended

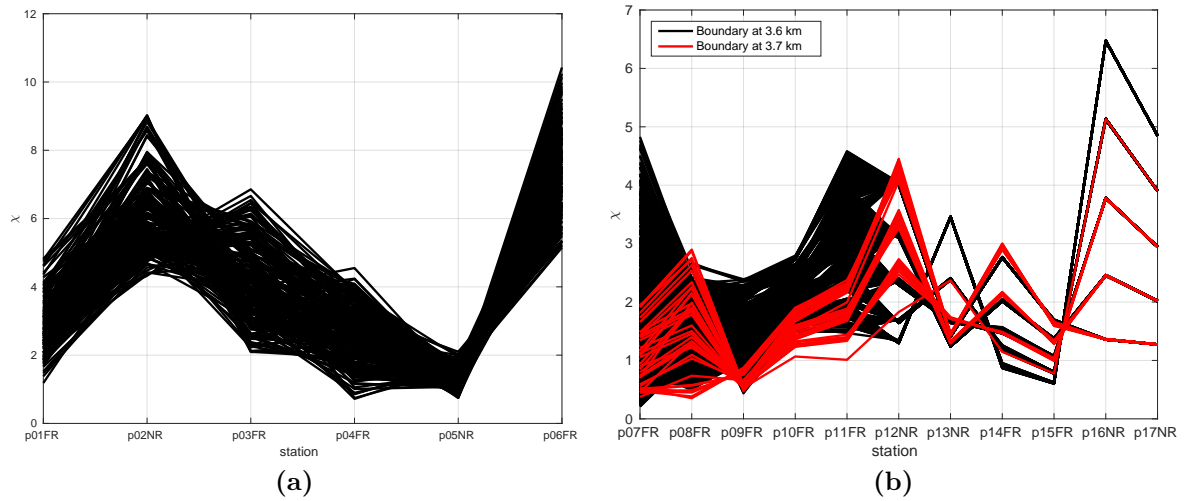


Figure C.1: χ -errors for all equivalent models along the profile. The black curves display the models for a boundary at 3600 m, the red lines a boundary at 3700 m.

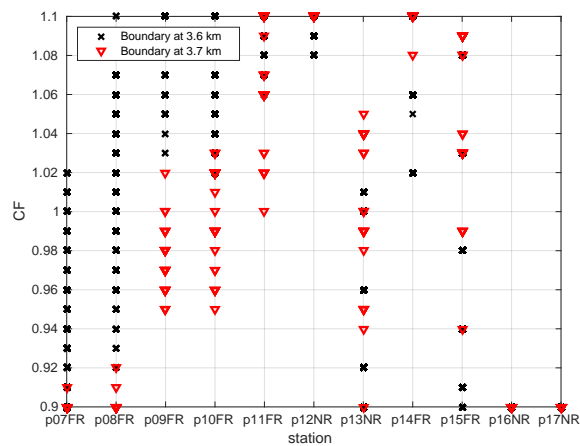


Figure C.2: Distribution of CF values at each station in Zone B. Red represent equivalent models for $x_a = 3700$ m, black for $x_a = 3600$ m.

Electric Fields of CED and DED

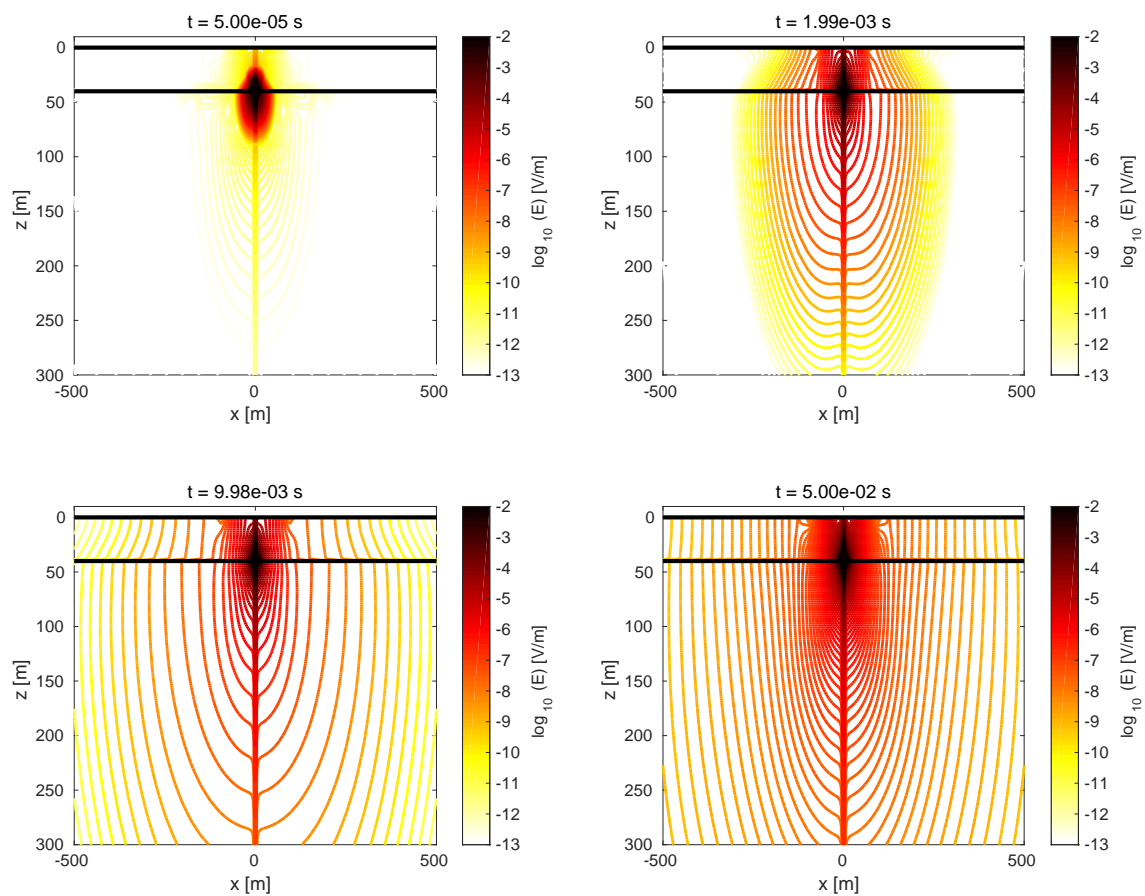


Figure D.1: Total electric field for CED step-on at selected times. The transmitter is located on the seafloor within a 40 m water column and a homogeneous half-space beneath.

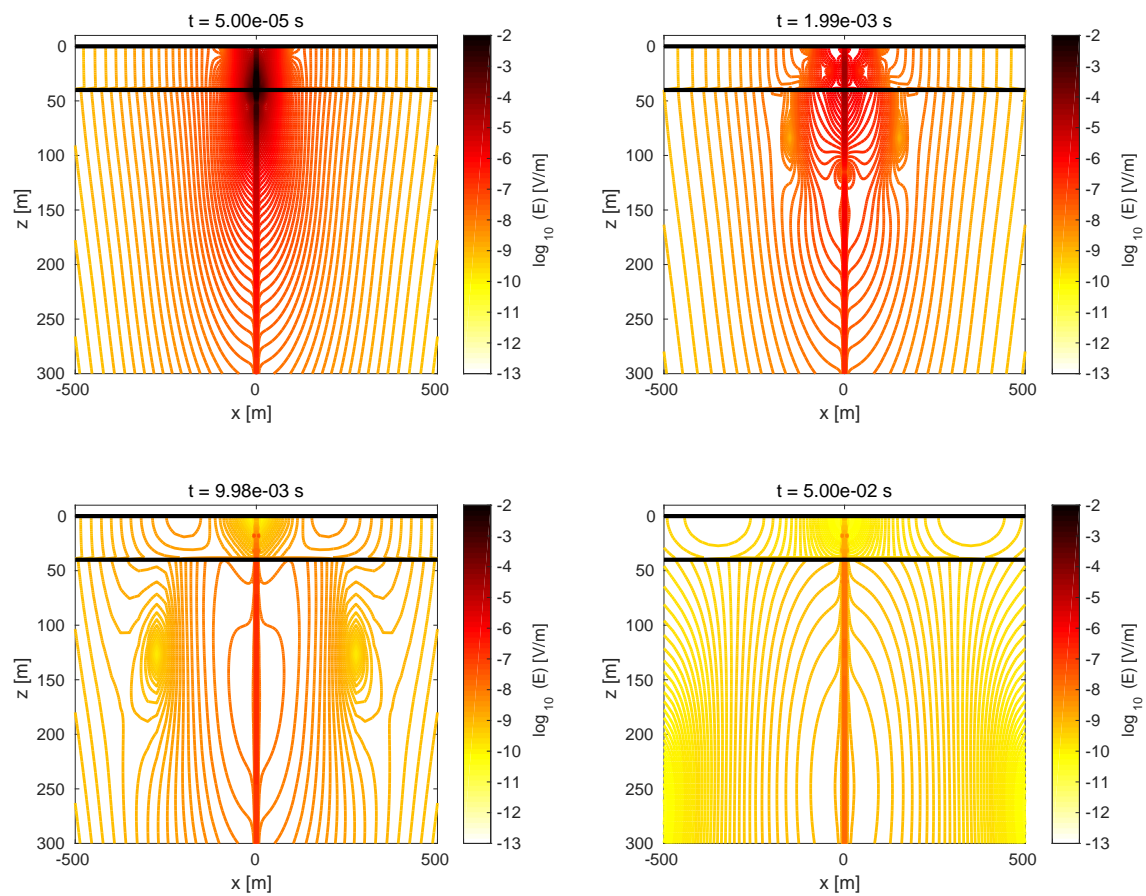


Figure D.2: Total electric field for CED step-off at selected times. The transmitter is located on the seafloor within a 40 m water column and a homogeneous half-space beneath.

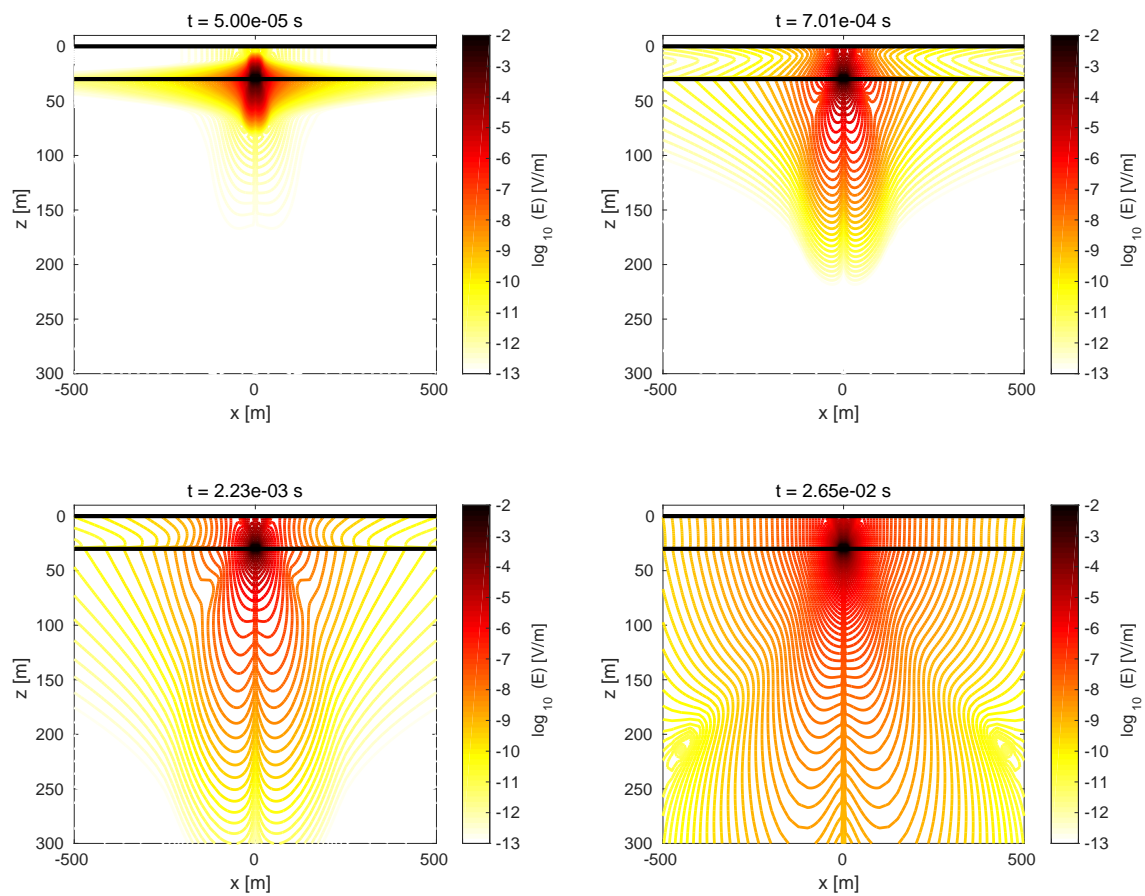


Figure D.3: Total electric field for DED step-on at selected times. The transmitter is located on the seafloor within a 30 m water column and a homogeneous half-space beneath.

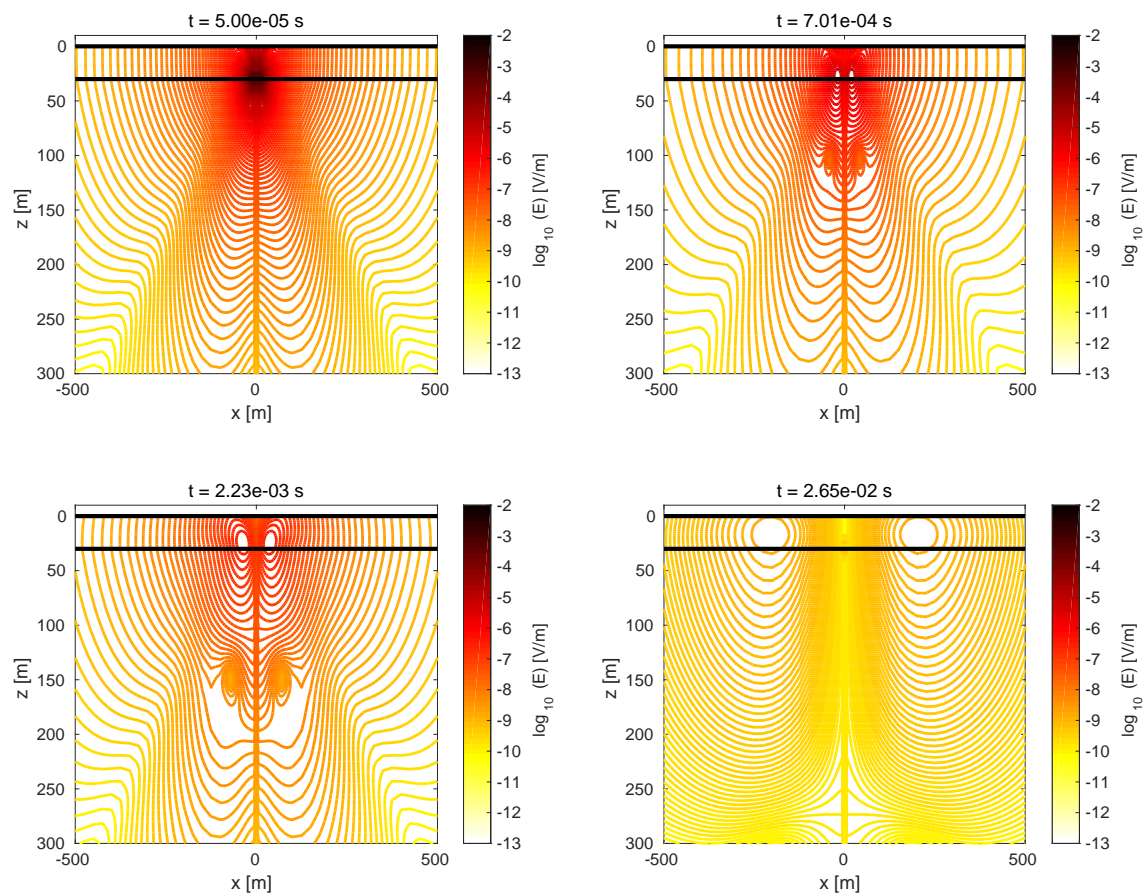


Figure D.4: Total electric field for DED step-off at selected times. The transmitter is located on the seafloor within a 30 m water column and a homogeneous half-space beneath.

Acknowledgements

I would like to thank

- Prof. Dr. B. Tezkan for the supervision of this thesis and for giving me the opportunity to follow my research interests of unconventional marine EM systems. His positive attitude towards life encouraged me in very difficult times.
- Prof. Dr. A. Junge for a very encouraging discussion at the EMTF 2015 and for appraising this thesis.
- Dr. M. Goldman for taking an active interest in me after my Master thesis and giving me the opportunity to work with him in Israel. Todah Rabah!
- Dr. K. Lippert for his friendship and assistance prior to, during, and after the field work. I hope that in future we manage to discuss about other subjects aside from marine TDEM.
- Itay Katzman, EcoOcean and the complete Crew of the Mediterranean Explorer for jumping in on very short notice to provide a research vessel after our project partners from the IOLR cancelled four weeks before the measurement due to technical difficulties.
- Andreas Busse, Michael Lohmer and Rainer Bergers for building the transmitter and their assistance in the planning phase of the field survey.
- Katrin Schwalenberg and BGR for her advice and the equipment. Sebastian Hölz (GEOMAR) for his advice regarding many practical issues prior to and after the measurement campaign. Tilman Hanstein (KMS Technologies) for countless discussions regarding the KMS-820 acquisition unit and TDEM data processing. Dr. C. Scholl for MARTIN and V. Mogilatov for his advice in the early stages of this work and his software package.
- Team Israel from the IGM Cologne: Janine Böckmann, Klaus Lippert, David Ossen, Nadine Pützer and Jan Wittke.
- Juliane Adrian, Klaus Lippert, Wiebke Mörbe, Marc Seidel and Dr. Pritam Yogeshwar for proof-reading the final version of this thesis.
- The rest of the Applied and Space Geophysics group members.

- My family
- My fiancée, Rosa for everything. This thesis would not have been possible without your constant encouragement and your indulgence for my unorthodox working hours.

Erklärung zur Dissertation

Ich versichere, dass ich die von mir vorgelegte Dissertation selbstständig angefertigt, die benutzten Quellen und Hilfsmittel vollständig angegeben und die Stellen der Arbeit – einschließlich Tabellen, Karten und Abbildungen –, die anderen Werken im Wortlaut oder dem Sinn nach entnommen sind, in jedem Einzelfall als Entlehnung kenntlich gemacht habe; dass diese Dissertation noch keiner anderen Fakultät oder Universität zur Prüfung vorgelegen hat; dass sie – abgesehen von unten angegebenen Teilpublikationen – noch nicht veröffentlicht worden ist sowie, dass ich eine solche Veröffentlichung vor Abschluss des Promotionsverfahrens nicht vornehmen werde.

Die Bestimmungen dieser Promotionsordnung sind mir bekannt. Die von mir vorgelegte Dissertation ist von Prof. Dr. B. Tezkan betreut worden.

Teilpublikationen:

- Haroon, A., M. Goldman and B. Tezkan (2013): *Marine Circular Electric Dipole (MCED): A new innovative electromagnetic technique for delineating resistive submarine targets*. Extended Abstract, MARELEC, Hamburg.
- Goldman, M., V. Mogilatov, A. Haroon, E. Levi and B. Tezkan (2015): *Signal detectability of marine electromagnetic methods in the exploration of resistive targets*. *Geophysical Prospecting*, 63(1), 192-210, doi:10.1111/1365-2478.12151
- Haroon, A., V. Mogilatov, M. Goldman, R. Bergers and B. Tezkan (2016): *Exploration of resistive targets within shallow marine environments using the Circular Electrical Dipole and the Differential Electrical Dipole Methods: A time-domain modelling study*. *Geophysical Journal International*, 205(2), 1032-1048, doi:10.1093/gji/ggw051

Ich versichere, dass ich alle Angaben wahrheitsgemäß nach bestem Wissen und Gewissen gemacht habe und verpflichte mich, jedmögliche, die obigen Angaben betreffenden Veränderungen, dem Dekanat unverzüglich mitzuteilen.

Köln, Oktober 2016

